

THE UNIVERSITY OF CHICAGO

MILLIMETER WAVE PHOTONS FOR HYBRID QUANTUM SYSTEMS

A DISSERTATION SUBMITTED TO  
THE FACULTY OF THE DIVISION OF THE PHYSICAL SCIENCES  
IN CANDIDACY FOR THE DEGREE OF  
DOCTOR OF PHILOSOPHY

DEPARTMENT OF PHYSICS

BY

AZIZA SULEYMANZADE

CHICAGO, ILLINOIS

AUGUST 2021

Dedicated to my parents, Lala and Mais

# TABLE OF CONTENTS

LIST OF FIGURES . . . . .	viii
LIST OF TABLES . . . . .	xxiv
ACKNOWLEDGMENTS . . . . .	xxv
ABSTRACT . . . . .	xxvii
1 INTRODUCTION . . . . .	1
1.1 Photons . . . . .	1
1.1.1 Powerful toolbox of cavity-QED . . . . .	4
1.2 Millimeter wave band for quantum technology . . . . .	10
1.3 Our hybrid cavity-QED systems . . . . .	12
1.3.1 Engineering strong interactions between single mm-wave and optical photons . . . . .	14
1.3.2 Optical to mm-wave transduction . . . . .	16
1.3.3 Large scale entanglement for quantum enhanced metrology . . . . .	16
1.4 Thesis Layout . . . . .	17
2 HARMONIC OSCILLATORS FOR HYBRID EXPERIMENTALISTS . . . . .	19
2.1 Mass on a spring . . . . .	19
2.2 Coupled masses on springs . . . . .	24
2.2.1 Cavity - Vacuum Rabi Splitting (VRS) . . . . .	25
2.2.2 Coupling Q of a cavity . . . . .	28
2.2.3 Cavity - Electromagnetically Induced Transparency (EIT) . . . . .	30
2.2.4 Dark states . . . . .	32

2.2.5	From susceptibility to impedance . . . . .	33
2.3	$N \rightarrow \infty$ masses on springs: from oscillations to waves . . . . .	36
2.3.1	Driving a HO with a chain of masses on springs . . . . .	38
2.4	RLC impedance analogy . . . . .	42
2.4.1	Linear response from the total impedance . . . . .	46
2.4.2	Impedance analogy vs. mobility analogy: limits of analogies . . . . .	47
2.5	Transmission Line Resonator . . . . .	49
2.5.1	Coupling to a $\lambda/4$ resonator . . . . .	51
2.6	Fabry Perot cavity: another transmission line resonator . . . . .	53
2.6.1	Single-port measurement of a cavity, S11. . . . .	54
2.6.2	Two-port measurement of a cavity: S21 and S11. . . . .	58
2.6.3	Calculation . . . . .	59
2.6.4	A Hanger measurement . . . . .	61
2.7	Conclusion . . . . .	63
3	HYBRID CAVITY QED . . . . .	64
3.1	From waves to photons . . . . .	69
3.1.1	Quantizing the classical fields . . . . .	70
3.2	Jaynes-Cummings model . . . . .	76
3.3	Perturbation theory for the non-Hermitian Hamiltonian . . . . .	81
3.4	Our hybrid cavity QED Hamiltonian . . . . .	89
3.4.1	Our matter couplers and their strengths . . . . .	90
3.4.2	Collective VRS and Rydberg EIT . . . . .	93
3.4.3	MM-wave and optical hybrid CQED system . . . . .	97
3.5	Tracking coherences in many degree linear systems . . . . .	100

3.5.1	Vacuum Rabi Splitting vs. N of atoms . . . . .	101
3.5.2	EIT Doppler broadening . . . . .	103
3.5.3	Mm-wave Autler-Townes Splitting . . . . .	105
3.6	Conclusion . . . . .	107
4	MILLIMETER WAVE QUANTUM TECHNOLOGY . . . . .	108
4.1	Mm-wave radiation in other fields . . . . .	109
4.2	Millimeter wave technology and its potential quantum applications . . . . .	112
4.3	Our Quantum devices . . . . .	116
4.4	3D $\lambda/4$ coaxial resonator . . . . .	118
4.5	Seamless millimeter-wave cavities . . . . .	122
4.5.1	Design . . . . .	123
4.6	Photonic crystals . . . . .	130
4.6.1	Design . . . . .	131
4.6.2	Fabricated chips . . . . .	133
4.6.3	Machined cavities . . . . .	135
4.7	Mm-wave circuit-QED . . . . .	139
4.7.1	Background . . . . .	139
4.7.2	Planar mm-wave devices . . . . .	142
4.7.3	Outlook on 2D mm-wave circuits . . . . .	144
4.8	Mm-wave Fabry-Perot Cavity . . . . .	144
4.8.1	Outlook . . . . .	146
5	APPARATUS: HOW TO BUILD A HYBRID QUANTUM SYSTEM FROM SCRATCH? 148	
5.1	System requirements . . . . .	148
5.2	Building components . . . . .	150

5.2.1	Optical Tables . . . . .	150
5.2.2	Cryostat . . . . .	151
5.3	Two-chamber design . . . . .	153
5.3.1	Cryogenic Requirements . . . . .	154
5.4	Cryogenic Magneto Optical Trap (MOT) . . . . .	161
5.4.1	Atom sources . . . . .	162
5.4.2	Grating Chip . . . . .	164
5.4.3	Accessories . . . . .	165
5.5	Hybrid Cavity . . . . .	166
5.6	Inside of the Science Chamber . . . . .	167
5.7	Optical Setup . . . . .	169
5.8	MM-wave setup for hybrid experiments . . . . .	170
6	EXPERIMENT: INTERFACING OPTICAL AND MM-WAVE PHOTONS USING RYDBERG ATOMS . . . . .	176
6.1	Experimental Sequence . . . . .	176
6.1.1	Trapping and cooling of $^{85}\text{Rb}$ . . . . .	177
6.1.2	$\lambda$ -enhanced Gray Molasses $^{85}\text{Rb}$ . . . . .	180
6.1.3	Lattice and transport . . . . .	180
6.2	Hybrid Interface for mm-wave and optical photons . . . . .	182
6.3	Optical Pumping and Meissner effect . . . . .	186
6.4	The first nonlinear signals from our hybrid system . . . . .	189
6.5	Conclusion . . . . .	192
7	OUTLOOK . . . . .	193
7.1	Mm-wave quantum platforms . . . . .	193

7.2 Hybrid Cavity-QED systems with mm-wave photons . . . . .	194
APPENDICES . . . . .	197
A INPUT/OUTPUT THEORY . . . . .	198
A.1 Quantized Coupled Cavities . . . . .	198
A.1.1 Coherent driving of a perfect cavity . . . . .	199
A.1.2 Cavity decay into the bath . . . . .	200
A.2 Input-Output theory of a cavity coupled to a bath . . . . .	201
A.2.1 Cavity Reflection . . . . .	204
A.2.2 Cavity Transmission . . . . .	205
A.2.3 Driven cavity . . . . .	206
A.3 Atom in a cavity . . . . .	207
B SEAMLESS MM-WAVE CAVITIES . . . . .	208
B.1 Etching of Nb seamless cavities . . . . .	208
B.2 Mechanical squeezing of Nb seamless cavities . . . . .	208
B.3 Room temperature filter cavity . . . . .	208
B.4 High-Tc superconductor seamless cavities . . . . .	208
B.5 Etching Cavities . . . . .	209
C MM-WAVE VECTOR NETWORK ANALYZER . . . . .	214
C.1 Schematic . . . . .	214
C.2 GUI . . . . .	216
REFERENCES . . . . .	218

# LIST OF FIGURES

1.1	Photons in the current Standard Model . . . . .	1
1.2	Thermal photon occupation at different temperatures <b>a.</b> Room temperature with a mark at 384 THz, which corresponds to our 780 nm optical photons and at 100 GHz. Single optical photons can be easily resolved at 300 K, but even the high-frequency mm-wave photons at 100 GHz would be overwhelmed by the bath of thermal photons at that frequency. <b>b.</b> At 1 K, we can resolve single mm-wave photons, but microwaves are still out of reach. <b>b.</b> 50 mK is a good temperature stage for resolving microwave photons at 4 GHz, and subsequently the mm-wave and optical photons. . . . .	2
1.3	Different light source produce of light with different statistics. From left to right: super-Poissonian - random number fluctuations in thermal light, Poissonian - the least random light that fits semi-classical description, sub-Poissonian - correlated quantum state of light . . . . .	3
1.4	Probability of number of photons in one mode with the same expectation number $\langle n \rangle = 4$ for: <b>a.</b> Thermal light from blackbody radiation, <b>b.</b> Coherent light from a laser or harmonic oscillator, <b>c.</b> Fock state from a nonlinear quantum system . . . . .	4
1.5	Diagrams of theoretical photon-photon interactions . . . . .	6
1.6	Different photonic regimes depending on the number of photons and the interaction strength per photon between them. Adapted from [1] . . . . .	7
1.7	A diagram of an emitter coupled to a photon in a cavity, with characteristic parameters $\kappa$ , $\gamma$ and $g$ . . . . .	8
1.8	Some of the variety of quantum hardware platforms . . . . .	10

1.9	Some of our mm-wave devices . . . . .	11
1.10	Hybrid cavity for interfacing mm-wave and optical photons using Rydberg atoms	12
1.11	Source of strong interactions in our hybrid cavity-QED system: <b>a.</b> the simplified diagram of $^{85}\text{Rb}$ energy levels used in generating strong interactions, <b>b.</b> parameter regime for single optical photons - single atom coupling, and single mm-wave photon single Rydberg atom coupling at 1 K, <b>c.</b> The signature optical cavity transmission with the EIT peak split due to coupling to the vacuum of the mm-wave cavity mode. . . . .	14
1.12	Inter-conversion of single mm-wave and optical photons: <b>a.</b> the simplified diagram of $^{85}\text{Rb}$ energy levels used in transduction, <b>b.</b> expected bandwidth and efficiency performance of the transducer . . . . .	15
1.13	Spin squeezing: one-axes twisting: <b>a.</b> our energy diagram for one-axes twisting with many Rydberg atom excitations. <b>b.</b> Wigner functions of a $N = 100$ twisted spin states as a function of the duration of the twisting Hamiltonian. The figure is incorporated from [2] . . . . .	17
2.1	Resonance of a underdamped driven HO with $X_0 = 1$ and $f_0 = 1$ for different $\kappa$	20
2.2	Mass, $m$ , on a spring with a spring constant, $k$ , and damping coefficient $c$ has all of the prerequisites of an oscillatory system: an equilibrium position - at the bottom of the potential, and a restoring force provided by a conservative (path-independent) potential. . . . .	21
2.3	Time response of a harmonic oscillator. <b>a.</b> Damped harmonic oscillator without the drive. <b>b.</b> Damped harmonic oscillator driven on resonance. <b>c.</b> Damped harmonic oscillator driven off resonance. . . . .	23

2.4	Mechanical analogs of: <b>a.</b> A high-Q single mode of a driven optical or microwave cavity <b>b.</b> A "very" weak drive of a two-level atom . . . . .	24
2.5	Diagrams of two coupled damped harmonic oscillators, where only the first one is driven by the external force: <b>a.</b> in usual mechanical terms <b>b.</b> converted into the cavity-QED terms . . . . .	26
2.6	Frequency response of two coupled harmonic oscillators, shown in Fig. 2.5: a single mode of a cavity driven by a periodic force with $\Omega_d = 0.001$ and a two-level atom. Everything is in units of MHz <b>a.</b> Avoided crossing as a function of the cavity detuning and relative atomic detuning with $\Gamma = 1$ , $\kappa = 2$ and $g = 5$ . <b>b.</b> Energy spectrum of the of the atom coupled to a cavity mode of the same frequency simulated by coupled harmonic oscillators. As we increase the coupling strength $g$ , the driven cavity transmission shows a "transparency" followed by a "Vacuum Rabi-like" feature. $\Gamma = .1$ , $\kappa = 2$ <b>b.</b> Same as <b>b.</b> , but the $\kappa = .1$ and $\Gamma = 2$ . We do not see the same transparency dip in the transmission. . . . .	28
2.7	Two coupled resonators . . . . .	28
2.8	<b>a.</b> Diagram of three damped harmonic oscillators for simulating Rydberg cavity-EIT <b>a.</b> Usual atomic physics diagram of the system. . . . .	31
2.9	Frequency response of three coupled harmonic oscillators, shown in Fig. 2.8: a single mode of a cavity driven by a periodic force with $\Omega_d = 0.001$ and a two-level atom. Everything is in units of MHz. The plots are made with $\Gamma = 1$ , $\kappa = 2$ and $g = 5$ . . . . .	31
2.10	A diagram of N pairs of HOs (atoms) coupled to a single mode of a driven cavity	32
2.11	Transmission lines made of: <b>a.</b> Masses on springs, <b>b.</b> Beads on a string, <b>c.</b> RLC circuits . . . . .	35

2.12	Applying boundary conditions to an infinite chain of masses on springs to derive physical systems. . . . .	39
2.13	Log of the Linear response of the first HO as the Nth HO is driven with $x_d e^{i\omega t}$ . Here the parameters used are $\omega_0 = 1$ and $\kappa = 0.0001$ . . . . .	40
2.14	Lossy transmission line: here the parameters used are $\omega_0 = 1$ and $\kappa = 0.01$ . . .	41
2.15	Analogy between components of the damped mass on a spring and a series RLC circuit . . . . .	43
2.16	RLC circuits for: <b>a.</b> Vacuum Rabi splitting from Fig. 2.5b, <b>b.</b> Rydberg Cavity-EIT from Fig. 2.8 . . . . .	45
2.17	Analogy between components of the damped mass on a spring and a parallel RLC circuit using mobility analogy instead of impedance analogy . . . . .	48
2.18	Series RLC transmission line with the length and characteristic impedance $Z_{line}$ , terminated with a real load impedance $R_L$ . . . . .	48
2.19	Capacitive coupling to the transmission line resonator, each time a wave encounters an impedance mismatch some of it gets reflected and some if it gets transmitted. 52	52
2.20	Reflection measurement of a FP cavity with the length L and internal loss per roundtrip $\gamma$ . . . . .	54
2.21	Reflection signal for a Fabry Perot with $\kappa_{coupl} = 0.001$ : undercoupled, critical coupled and over coupled regimes, respectively. . . . .	56
2.22	Transmission measurement of a FP cavity with the length L and internal loss per roundtrip $\gamma$ . . . . .	58

2.23	Transmission signal for a Fabry Perot with $\kappa_{coupl} = 0.001$ : undercoupled, critical coupled and over coupled regimes, respectively. . . . .	60
2.24	Hanger measurement of a FP cavity with the length $L$ and internal loss per roundtrip $\gamma$ . . . . .	61
2.25	Hanger transmissison signal for a Fabry Perot with $\kappa_{coupl} = 0.001$ : undercoupled, critical coupled and over coupled regimes, respectively. . . . .	63
3.1	Bosonic modes of our hybrid cavity-QED system: photons trapped in optical and mm-wave cavities . . . . .	64
3.2	Different CQED models used in our hybrid experiments: <b>a.</b> Rabi Model for a single two-level system coupled to a cavity mode. It turns into the Jaynes-Cummings Hamiltonian after the Rotating Wave Approximation, <b>b.</b> Dicke model for an ensemble of TLSs coupled to a cavity mode. It turns into the Tavis-Cummings Hamiltonian after the RWA, <b>c.</b> The beam-splitter Hamiltonian for two coupled harmonic oscillators. . . . .	65
3.3	Bosonic interaction Hamiltonians: <b>a.</b> linear beam-splitter interaction, <b>b.</b> nonlinear parametric interaction, <b>c.</b> nonlinear dispersive interaction . . . . .	67
3.4	Quantum emitters and their energy levels used in our system: <b>a.</b> Rydberg states of $^{85}\text{Rb}$ atoms, <b>b.</b> ensemble of $^{85}\text{Rb}$ atoms . . . . .	67
3.5	Various coupling regimes in CQED system . . . . .	68
3.6	The diagram for quantization of light inside of the optical cavity, where $a^\dagger$ and $a$ are creation and annihilation operators for the mode of the Fabry-Perot cavity, $d^\dagger$ and $d$ for the drive, and $b_j^\dagger$ and $b_j$ for the free space modes. . . . .	70

3.7	Single atom in a cavity for Jaynes-Cummings Hamiltonian: <b>a.</b> diagram of the losses and couplings, <b>b.</b> energy levels involved in the derivation . . . . .	76
3.8	Energy levels of the Jaynes-Cummings Hamiltonian: from the bare photon and bare atom energy levels to the nonlinear ladder of the dressed states of JCH for $\delta_{ac} = 0$ . . . . .	78
3.9	The connection between the Jaynes-Cummings nonlinearity and effective interactions between photons. Non-interacting systems: <b>a.</b> electromagnetic waves in free space, <b>b.</b> photons in an empty cavity. Strongly interacting systems: <b>c.</b> two-photon blockade from a strongly interacting CQED system, <b>d.</b> bouncing billiard balls . . . . .	81
3.10	Perturbation theory for Jaynes-Cummings Hamiltonian with loss and drive: <b>a.</b> Bare non-Hermitian Hamiltonian, <b>b.</b> the perturbation term, which corresponds to the probe beam, <b>c.</b> energy states involved in the system . . . . .	84
3.11	Left: Cavity transmission for the bare cavity and cavity with an atom in a JCH with $g = 0, 10, 15$ MHz, right: second order correlation function for photons with $g = 0, 10, 15$ MHz. Here the $\Gamma = 1$ MHz and $\kappa = 2$ MHz, and the $g_2(0)$ is plotted in $\log_{10}$ . . . . .	89
3.12	Properties of a hydrogenic atom as a function of a quantum number $n$ : <b>a.</b> the dipole moment, <b>b.</b> scattering rate, <b>c.</b> frequency (Larmor frequency) . . . . .	90
3.13	Many-atom VRS: <b>a.</b> Energy levels involved in the system, <b>b.</b> The VRS spectrum obtained using non-Hermitian perturbation theory. . . . .	94
3.14	Many-atom Rydberg EIT: <b>a.</b> Energy levels involved in the system, <b>b.</b> The EIT spectrum obtained using non-Hermitian perturbation theory. . . . .	96

3.15 Hybrid system with optical and mm-wave photons up to one excitation: <b>a.</b> Energy levels involved in the system, <b>b.</b> The diagonalized Hamiltonian, <b>c.</b> The perturbation . . . . .	97
3.16 The splitting of the EIT line due to coupling to the vacuum of the mm-wave cavity. Here the $\Gamma = 6$ MHz, $\kappa = 4$ MHz, $\kappa_{mm} = 0.1$ MHz, $\Gamma_R = \Gamma_{R2} = 0.04$ MHz. The inset shows one such spectrum with $g_{mm} = 6$ MHz. . . . .	98
3.17 The cavity spectrum and the $g_2(0)$ of the hybrid system for interfacing single mm-wave and optical photons obtained using the non-Hermitian perturbation theory for various single mm-wave photon-Rydberg atom couplings. . . . .	99
3.18 Replication of the results using the Master Equation formalism: <b>a.</b> Cavity transmission, <b>b.</b> Second order correlation function, <b>c.</b> the overlap of the cavity transmission with the $g_2(0)$ . . . . .	100
3.19 Second correlation function of photons at a time $\tau$ : the probability of detecting two photons leaking out of our cavity separated in time by $\tau$ . . . . .	101
3.20 Vacuum Rabi splitting as a function of number of atoms in the ensemble with $\Gamma_R = 25$ kHz, $\Gamma = 6$ MHz, $\kappa = 3.5$ MHz, $g_0 = 0.6$ MHz and $\delta_{ac} = 0$ . . . . .	102
3.21 The spectra of the electromagnetically induced transparency as a function of the temperature of the atomic cloud with $\Gamma_R = 25$ kHz, $\Gamma = 6$ MHz, $\kappa = 3.9$ MHz, $g_0\sqrt{N_{at}} = 8$ MHz, $\delta_R = 0$ , $\Omega_R = 2$ MHz and $\delta_{ac} = 0$ . . . . .	104
3.22 The energy states involved in the Autler-Townes splitting of the EIT by the mm-wave population in our hybrid optical/mm-wave system . . . . .	105

3.23	The simulated spectra in our hybrid system: bare cavity transmission, vacuum Rabi splitting, EIT and the Autler-Townes splitting with $\Gamma_R = 25$ kHz, $\Gamma = 6$ MHz, $\kappa = 3.9$ MHz, $g_0\sqrt{N_{at}} = 12$ MHz, $\Omega_R = 3.2$ MHz, $\Omega_{R2} = 1$ MHz, $\delta_{ac} = 0$ , $\delta_R = 0$ and $\delta_{R2} = 0$ . . . . .	106
4.1	Caption for LOF . . . . .	108
4.2	The mm-wave band lies between microwave and infrared bands in the Electromagnetic Spectrum. It is essential for many industries. . . . .	109
4.3	Applications in Chemistry: vibrational and rotational spectroscopy of molecules; Medicine: for imaging; Security: for metal detectors at the airport TSA. . . . .	110
4.4	Astronomy heavily relies on mm-wave detection both for Astrochemistry and studying the evolution of the Universe after the Big Bang . . . . .	111
4.5	Telecommunication industry has recently bought up the mm-wave band for larger bandwidth and lower latency in 5G . . . . .	112
4.6	Comparison between photonics at optical, mm-wave and microwave frequencies. To perform quantum manipulations, we need to have a blackbody photon occupation much less than 1, which corresponds to temperature of 26500K, 7K and 207 mK, respectively. . . . .	113
4.7	Various types of quantum emitters that can be used in the mm-wave band: <b>a.</b> Vibrational and rotational states of molecules. <b>b.</b> Cold atoms in Rydberg states. <b>c.</b> Lattice defects. <b>d.</b> Superconducting circuits [3]. <b>e.</b> Some types of fabricated mechanical membranes can be manufactured at 100 GHz, the figure shows an example of drum membrane at 7.5 GHz. <sup>1</sup> . . . . .	114

4.8	Conceptual sketch of modal multilayer microwave quantum computer, the figure is from T.Brecht et al 2016 [4] . . . . .	116
4.9	Conceptual implementation of a 3D mm-wave hybrid systems, from Fig. 4.1, including layered wavers, machined photonic crystals, lattices of cold atoms and Fabry-Perot cavities . . . . .	116
4.10	Diagram of a coaxial $\lambda/4$ cavity . . . . .	119
4.11	<b>a.</b> Electric field distribution of the fundamental mode of the coaxial cavity at 100 GHz simulated by HFSS. <b>b.</b> A picture of the top of the machined coaxial cavity with a WR-10 waveguide flange pattern. <b>c.</b> Zoomed in picture of the top of the coaxial cavity. <b>d.</b> Length-wise crossection of the coaxial cavity. . . . .	121
4.12	Reflection data from a Nb coax cavity. . . . .	122
4.13	Transmission properties of a 1.5 mm diameter hollow cylindrical waveguide: <b>a.</b> real and imaginary parts of $\beta$ , <b>b.</b> power loss in dB per 1 mm length . . . . .	123
4.14	$TE_{11}$ mode of a hollow cylindrical waveguide: <b>a.</b> Cutoff frequency as a function of a diameter of the cylinder, <b>b.</b> E and B field pattern in radial view, <b>c.</b> E and B field pattern in transverse view . . . . .	124
4.15	HFSS simulation of E field of three lowest modes of a cavity with tube sizes: 1.54 mm, 1.36 mm, 1.43 mm, <b>a.</b> 99.4 GHz, <b>b.</b> 102.4 GHz, <b>c.</b> 107.2 GHz . . . . .	125
4.16	Various cavities made using hollow tubes with diameter of 1.6 mm . . . . .	126

4.17	(a) Photograph of various tested mm-wave cavity geometries. (b) Reflection spectra from several cavities with varying frequencies and coupling Q values, resulting in different total Q values. (c) Internal Q as a function of the number of photons for the hybrid cavity. The constant trend indicates that the limiting loss mechanism is not power-dependent. (d) Internal Q (black) and fractional frequency change (red) as a function of temperature for the hybrid cavity. The deviation from Mattis–Bardeen curve at 2.3 K suggests that the resistivity of Nb does not limit the lifetime of the photons at the lowest temperatures. . . . .	127
4.18	Cryogenic frequency tuning of a high-Q mm-wave cavity. <b>a</b> Photograph of the piezoelectric actuator system attached to a test cavity. <b>b</b> Frequency shift of the cavity resonance as a function of the voltage of the piezo. . . . .	128
4.19	<b>a.</b> Schematic of the early version of the hybrid cavity. The superconducting mm-wave cavity was formed by the intersection of three evanescent waveguides. The x-axis waveguide was employed for atom transport, the y-axis waveguide for mm-wave coupling, and the z-axis waveguide for an optical Fabry–Perot cavity. Each side of the Fabry–Perot cavity included Invar spacers to prevent differential thermal contractions and a piezo actuator for tuning and locking the frequency of the optical cavity. <b>b.</b> Photograph of the assembled crossed mm-wave and optical cavity with wired piezos. <b>c.</b> Schematic reflection measurement setup for the mm-wave cavity. 100 GHz photons enter the coupling port of the cavity through a WR10 waveguide. . . . .	129
4.20	Fabricated Nb superconducting photonic crystal cavity . . . . .	130
4.21	Fabricated photonic crystals: <b>a.</b> 500 $\mu$ m Si wafer, <b>b.</b> Patterned PR using Heidelberg lithography, <b>c.</b> After deep Si etch + Nb sputtering <b>d.</b> Prepared devices: two different bottoms and one top, <b>e.</b> Mounted bottom chip, <b>f.</b> Mounted chips . . . . .	132

4.22	Transmission data from a few different fabricated photonic crystals, with different designed coupling Qs . . . . .	132
4.23	Design of a hexagonal lattice PC: <b>a.</b> From a conventional geometry of holes in a dielectric to a two-piece metal design, <b>b.</b> An example of a set of parameters for a functional PC cavity at 100 GHz, <b>c.</b> Different geometries for varying coupling Q	133
4.24	Diagram of the fabrication sequence: <b>a.</b> 500 $\mu$ m Si wafer, <b>b.</b> Patterning the PR using Heidelberg lithography, <b>c.</b> Deep Si etch, <b>d.</b> Sputtering Nb, <b>d.</b> Assembling (snapping two pieces together). . . . .	134
4.25	<i>26 GHz machined Aluminum PC:</i> <b>a.</b> HFSS simulation of the lowest mode of the PC, <b>b.</b> AutoCad model of the device, <b>d.</b> Machined Al device; <i>13GHz machined Aluminum PC:</i> <b>c.</b> HFSS simulation of the lowest mode of the PC, <b>e,f.</b> Machined Al device: hooked up for the measurement and seprated bottom part. . . . .	136
4.26	Design of a machined Nb photonic crystal cavity . . . . .	136
4.27	Photos of a machined mm-wave photonic crystal cavity: <b>a.</b> The assembled aluminum cavity for room temperature measurement, <b>b., c.</b> The machined Nb cavity before the etch . . . . .	137
4.28	HFSS simulation of the PC cavity . . . . .	138
4.29	Reflection data from the leaky seamless cavity without the PC and with the PC	139
4.30	SEM images of a mm-wave lumped element Nb resonator made by A.Anferov and K-H. Lee: <b>a.</b> a single resonator zoomed in, <b>b.</b> A chain of six resonators on one chip, <b>c.</b> lumped element circuit of the device . . . . .	142

4.31	2D nonlinear device for mm-wave para-amp. The figure is taken from [3] made by A.Anferov: <b>a.</b> mm-wave measurement setup with a copper box for the sapphire chip, <b>b.</b> Image of a mounted chip with the top waveguide removed, <b>c.</b> SEM image of one NbN resonator: wire width $4 \mu\text{m}$ and film thickness, <b>d.</b> RLC diagram of the device with the coupling impedance included . . . . .	143
4.32	HFSS simulation of a mm-wave Fabry-Perot with a Gaussian excitation: <b>a.</b> transverse slice of the mode, <b>b.</b> axial slice . . . . .	144
4.33	Photos of a machined mm-wave Fabry-Perot cavity: <b>a.</b> The assembled aluminum cavity for room temperature measurement, <b>b.</b> The machined Al mirrors . . . . .	145
4.34	A preliminary scan of one of the modes of the FP. The image on the right shows a there-and-back scans through the cavity mode volume in the radial direction . . . . .	146
5.1	How it began... . . . . .	148
5.2	Newport optical table with an 18" hole . . . . .	150
5.3	A two-stage pulse tube refrigerator: <b>a.</b> drawing <b>b</b> diagram . . . . .	152
5.4	The design of the overall two-chamber system . . . . .	154
5.5	<i>Cryomech PT410 CPA289C series</i> capacity curves. . . . .	154
5.6	35K shield: <b>a.</b> First, we drill hole patterns in the aluminum sheet and roll it into a cylinder, <b>b.</b> we cover the surface of the shield with several repeated layers of Mylar and insulator . . . . .	156
5.7	The Fridge chamber: <b>a.</b> design, <b>b.</b> picture of the internal structure . . . . .	159
5.8	Internal design of the Science chamber . . . . .	160

5.9	Thermal connectors: <b>a.</b> Science chamber with the cold arm and copper braids connectors, <b>b.</b> Fridge chamber connected to the cold arm of the Science chamber through braids connectors, 45 K, and copper foil connectors, 4K . . . . .	160
5.10	Animation of a grating MOT: <b>a.</b> Atoms are released from the source behind the getter, <b>b, c, d</b> Atoms are loaded, trapped and cooled in the trap . . . . .	161
5.11	Homemade grating Mot with commercial gratings, Rb atom sources and magnetic coils attached . . . . .	161
5.12	Cryogenic GMOT assembly including the atom source box and the atomic beam	162
5.13	Pictures of the GMOT assembly: <b>a.</b> getters mounted on maycore inside of the room temperature aluminum box, <b>b</b> Assembled MOT with a grating (here the coil spools are made of stainless steal, later they were updated to copper) . . . .	163
5.14	A fluorescence image of the GMOT structure with the trapped atoms inside of the cryostat . . . . .	164
5.15	Upgrade of the hybrid cavity: <b>a.</b> The old hybrid cavity with mirrors and piezos glued to the Nb cavity, <b>b.</b> Frequency response of the mechanical vibrations of the optical cavity with dramatic resonances at low frequencies, <b>c.</b> New hybrid cavity with mirrors spring-loaded to the Nb cavity, without glue, <b>d.</b> Frequency response of the mechanical vibrations of the new optical cavity with significantly improved performance. . . . .	166
5.16	ANSYS mechanical vibrations simulation for the hybrid cavity structure . . . .	167
5.17	New superconducting cavity: <b>a.</b> The picture of the Nb cavity, <b>b.</b> Resonance frequency of the cavity after each subsequent etches and squeezes, <b>c.</b> Reflection measurement of the final cavity at 1K . . . . .	168

5.18	New superconducting cavity: <b>a.</b> The picture of the Nb cavity, <b>b.</b> Resonance frequency of the cavity after each subsequent etches and squeezes, <b>c.</b> Reflection measurement of the final cavity at 1K . . . . .	168
5.19	Interior of the Science Chamber: <b>a.</b> only including the mm-wave circuitry, <b>b.</b> with everything inside . . . . .	169
5.20	Diagram of the MOT laser setup (the figure is made by M.Stone ) . . . . .	170
5.21	Diagram of the setup for locking 780 nm laser for optical cavity probe (the figure is made by M.Stone ) . . . . .	171
5.22	Images of the main optical table with the hybrid experiment . . . . .	171
5.23	MM-wave measurement setup for our hybrid experiment: <b>a.</b> using VDI TRx modules, <b>b,c,d</b> using VDI AMC modules . . . . .	172
5.24	The schematic for the MM-wave measurement setup for our hybrid experiment. . . . .	175
6.1	Our experimental sequence for interfacing mm-wave and optical photons using cold atoms. . . . .	176
6.2	Grating MOT and laser cooling . . . . .	177
6.3	<sup>85</sup> Rb <i>D</i> <sub>2</sub> line energy levels used in: <b>a.</b> MOT and PGC cooling, <b>b.</b> λ-enhanced Gray Molasses. . . . .	178
6.4	Time of flight fluorescence images of the atomic cloud after MOT, PGC and Gray molasses . . . . .	179
6.5	Fano signature of Gray Molasses cooling at different $\Delta_{GM}$ . . . . .	181

6.6	Lifetime of the atomic cloud in a lattice as a function of the transport distance from the MOT . . . . .	181
6.7	Transport of the atoms in the lattice . . . . .	182
6.8	Fluorescent images of atoms trapped in a lattice with a falling under gravity MOT	183
6.9	Interfacing optical and mm-wave photons with Rydberg atoms . . . . .	183
6.10	Bare optical cavity transmission measurement: <b>a.</b> Cartoon of the system, <b>b.</b> Data and fit, <b>c.</b> The excitations involved in the spectrum . . . . .	184
6.11	Vacuum Rabi splitting measurement: <b>a.</b> Cartoon of the system, <b>b.</b> Data and fit, <b>c.</b> The excitations involved in the spectrum . . . . .	184
6.12	Electromagnetically Induced Transparency measurement: <b>a.</b> Cartoon of the system, <b>b.</b> Data and fit, <b>c.</b> The excitations involved in the spectrum . . . . .	184
6.13	Autler-Townes splitting due to mm-wave photons in the superconducting cavity: <b>a.</b> Cartoon of the system, <b>b.</b> Data and fit, <b>c.</b> The excitations involved in the spectrum . . . . .	185
6.14	EIT spectrum as a function of B field: <b>a.</b> Above $T_c$ , <b>b.</b> Below $T_c$ . . . . .	187
6.15	EIT spectrum: <b>a.</b> Before optimizing optical pumping above $T_c$ , <b>b.</b> After optimizing the optical pumping . . . . .	188
6.16	EIT spectrum: <b>a.</b> Before optimizing optical pumping above $T_c$ , <b>b.</b> After optimizing the optical pumping . . . . .	190
6.17	Raw data . . . . .	191
7.1	The 297 nm UV laser for the mm-wave to optical inter-conversion . . . . .	195

A.1	Coupled cavities . . . . .	198
A.2	A cavity with quantized field coupled to one with classical field inside . . . . .	199
A.3	A cavity coupled to a bath . . . . .	200
A.4	A cavity with one port with a decay rate $\kappa$ . . . . .	204
A.5	A cavity with two ports with decay rates $\kappa/2$ . . . . .	205
B.1	Data from several etching calibration runs . . . . .	209
B.2	Mechanical deformation in different direction corresponds to different signs of frequency shifts for different modes. . . . .	210
B.3	Mechanical deformation calibration. . . . .	211
B.4	Room temperature seamless cavity used as a band-pass filter: <b>a.</b> HFSS simulation of the filter mode, <b>b.</b> CAD 3D, model, <b>c.</b> Machined Al cavity, <b>d.</b> A typical transmission through the cavity . . . . .	212
B.5	High-Tc superconductor seamless cavities: <b>a.</b> YBCO, <b>b.</b> BSCCO . . . . .	213
C.1	Mm-wave VNA schematic . . . . .	215
C.2	Mm-wave VNA GUI before the measurement . . . . .	216
C.3	Mm-wave VNA GUI with the loaded data right after the measurement . . . . .	217

## LIST OF TABLES

4.1	Common Quantum resonators . . . . .	118
5.1	System requirement . . . . .	149
5.2	Gas composition of air [5] . . . . .	157
5.3	MM-wave measurement circuit components . . . . .	174

## ACKNOWLEDGMENTS

I have been lucky to have had a unique experience as a PhD student. I have built a novel experimental machine from the ground up and saw it give its first data. I have worked on pushing an unexplored frequency band into the quantum playground. I have trapped atoms, aligned lasers, nanofabricated superconducting chips, built vacuum chambers and designed cryostats. I have machined too many parts to remember, etched metal in hydrofluoric baths, soldered electrical circuits, set up plumbing, and occasionally got sunburned from welding vacuum chamber parts. And I loved every part of this journey. I have truly embraced the hybrid nature of my work, as it has become the defining feature of my PhD experience.

My hybrid journey was only possible due to the incredibly talented and supportive scientific community I have been part of in my two labs and beyond. I would not be where I am without all of their contributions, so I would like to extend my thanks to:

**Jonathan Simon and David Schuster** - my advisors. Their constant support and wisdom were an integral part of my PhD experience. Jon's excitement about science has always been contagious, and his guidance through tough numerics, tricky locking circuitry, or pondering on big scientific questions were essential for my growth as a scientist. I have never left a conversation with Dave without a new idea and full-hearted support in whatever new wild project I was interested in. They have instilled in me the desire and confidence to be an independent scientist.

**My hybrid team:** Mark Stone, Ash Kumar, Lavanya Taneja - are the best teammates I could ask for. Mark joined our project when I was in my second year, and together we kept building our hybrid system for five years. We have been through a lot of challenges together, and it created a strong bond, which was maintained by excessive amounts of pop-tarts and never-ending physics conversations. Ash and Lavanya have been a blessed addition to the team. Ash, with his wisdom and kindness, has been an incredible first postdoc. And Lavanya

is a brilliant scientist and the funniest lab partner. I can not wait to work more in the future with this team.

**Mm-wave crew:** I would like to thank Alexander Anferov for being a great partner in many of my mm-wave frequency projects. It has been a pleasure to work with such an enthusiastic person and a great scientist. It is exciting to see that the mm-wave effort is expanding with the great addition of Kan-Heng Lee. I would also like to thank Andrew Oriani for being an essential resource of my education on cryogenics and incredibly useful for engineering advice.

**Simon and Schuster labs:** I would like to thank current and past members of my labs for teaching me their tools and scientific worldview, inspiring in me the excitement about their projects sometimes as much as about my own, and most importantly being an incredible supportive science family through happy times and challenging moments.

**University of Chicago community:** the University of Chicago has given me a diverse academic community that made my PhD experience extremely rewarding. This includes an incredibly supportive physics department that gave me a wider physics community and scientific worldview. And the ballroom dance community, which I have been lucky to be part of as a competitor and a coach. The dance allowed me to stay physically active and inspired about many things outside of my lab work.

**Family and friends:** None of this would have been possible without the support of my parents. They never fail to be excited about my scientific adventures, no matter how far they are or how long they have not seen me. I would like to thank my friends and my partner, Diego, for making me a kinder and happier person every day.

# ABSTRACT

The advancements in quantum technology resulted in the development of a wide range of different quantum hardware platforms, including superconducting qubits, trapped ions, Rydberg atom arrays, and photonics chips. These powerful platforms have unique advantages and shortcomings, but they all use photons for one purpose or another. Photonic hybrid systems could leverage individual strengths of the constituent platforms for the implementation of novel functionalities or compensation of individual weaknesses. As advantageous as they are theoretically, hybrid systems are extremely challenging to build.

In this thesis, I will report on the development of a new hybrid quantum system for interfacing single optical and millimeter-wave photons using Rydberg atoms as mediators. At the heart of our system is a cloud of laser-cooled Rb85 atoms loaded into a crossed 3D superconducting mm-wave cavity with an optical Fabry-Perot Cavity. Through Rydberg excitations of our atomic cloud, we hope to generate strong interactions between light particles, entangle optical and mm-wave photons and transduce quantum information from single optical to mm-wave photons. Moreover, the strong interactions between mm-wave photons and atoms in our systems could open up new opportunities for many-atom entanglement and generation of spin squeezed states useful for quantum-enhanced metrology. I will describe the development of our system from its humble beginnings and finish with the exciting recent results.

In addition, I will discuss my work on developing mm-wave quantum technology beyond our Rydberg Cavity-QED system. The mm-wave band has unique advantages for quantum information technology: modest  $\approx 1K$  cryogenic requirement, wide availability of quantum emitters, and flexibility of design. Despite this, potential mm-wave photons are not heavily utilized in the quantum fields. I hope this work encourages more interest in the mm-wave frequency band and its potential applications in science and technology.

# CHAPTER 1

## INTRODUCTION

### 1.1 Photons

Photons have become essential building blocks in quantum systems due to their wide availability, coherence, and ease of control. They are ubiquitous “on-shell” - like packets of electromagnetic radiation, as well as “off-shell” - holding charges and magnets together, popping in and out of the vacuum.

As someone who started their research in particle physics, I always thought of photons as force carrier gauge bosons [6]. They obey Bose-Einstein statistics, have zero mass, no charge, spin one, and act as their own antiparticle, as shown in Fig. 1.1. Most importantly, it was a force carrier particle of one of the most successful quantum field theories to this date - Quantum Electrodynamics. In particle physics, QED is revered as the suc-

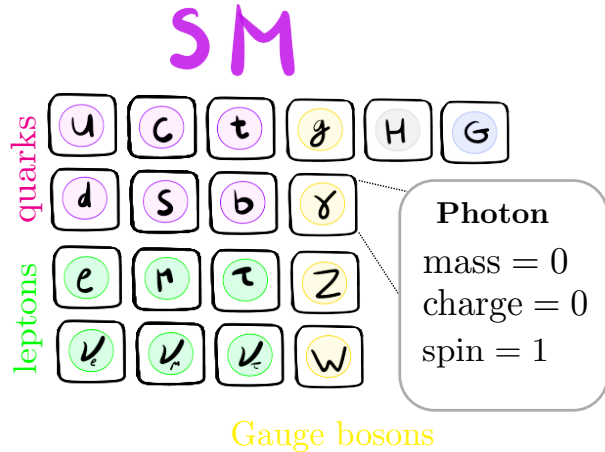


Figure 1.1: Photons in the current Standard Model

cess of quantum field theory of Standard model and a successful unification of two forces, Weak and Electromagnetic, into one - which has been a holy grail for the remaining forces in and out of the Standard Model. At the same time, due to its success, it might have been one of the least exciting objects in the particle zoo at the time of discovery of the Higgs boson, searches for new dark matter particles, and investigation of neutrinos.

However, in the fields of AMO and cavity-QED physics, photons were at the heart of every

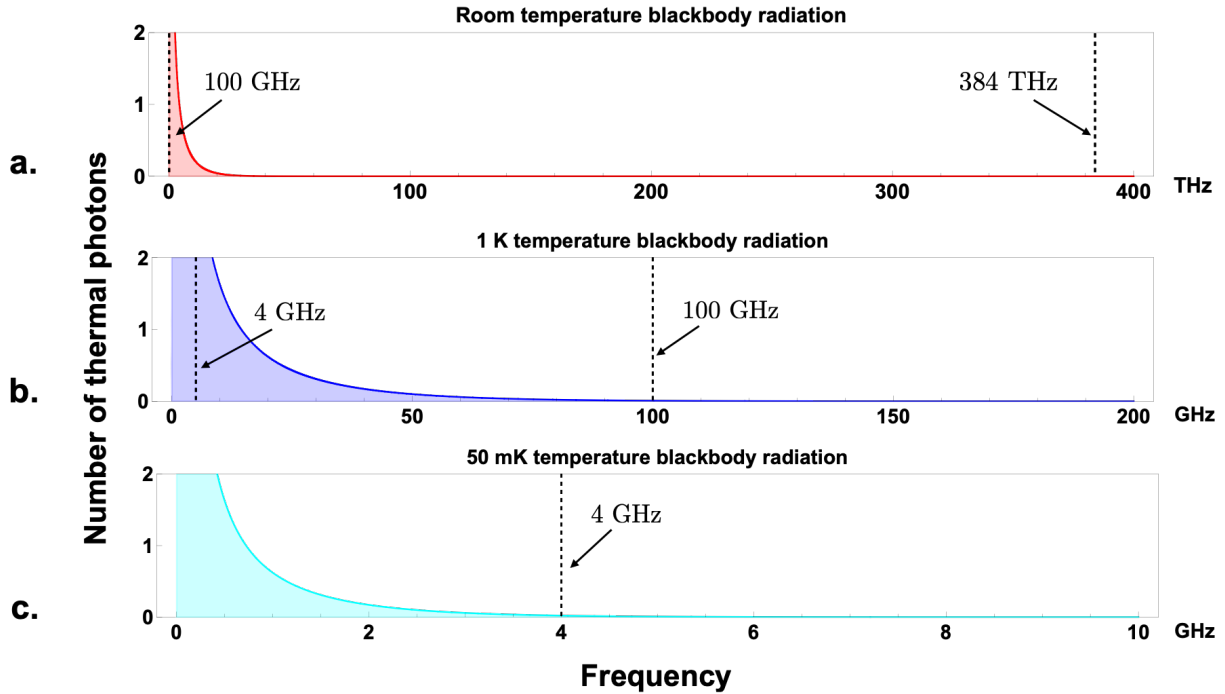


Figure 1.2: Thermal photon occupation at different temperatures **a.** Room temperature with a mark at 384 THz, which corresponds to our 780 nm optical photons and at 100 GHz. Single optical photons can be easily resolved at 300 K, but even the high-frequency mm-wave photons at 100 GHz would be overwhelmed by the bath of thermal photons at that frequency. **b.** At 1 K, we can resolve single mm-wave photons, but microwaves are still out of reach. **b.** 50 mK is a good temperature stage for resolving microwave photons at 4 GHz, and subsequently the mm-wave and optical photons.

system I encountered. The well-understood fundamental particles have been heavily utilized as a workhorse of rapidly developing fields of quantum optics, engineering of synthetic quantum materials for simulations [7], quantum computing [8], and quantum information technology [9]. Photons have had a unique historical advantage to be at the center of quantum technology. Scientists have debated whether light is a wave or made up of particles for centuries [10, 11, 12, 13]. As a society, we have developed an infrastructure to study and utilize radiation in technology as waves, ray beams, and particles. After all, the electromagnetic force is the most common force we experience in nature through daylight, shadows, friction, and even neural sensations such as touch. Even the uncertainty principle for light particles doesn't seem bizarre since we are very comfortable with Fourier transforms of elec-

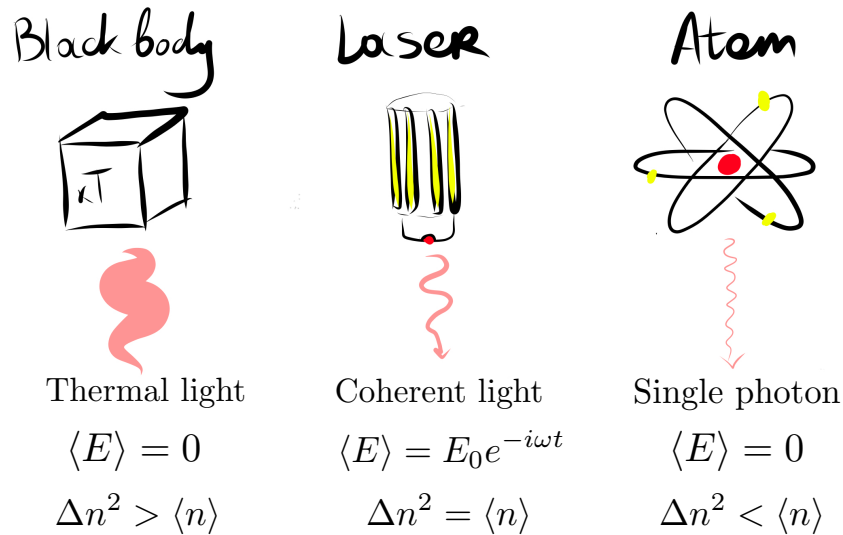


Figure 1.3: Different light source produce of light with different statistics. From left to right: super-Poissonian - random number fluctuations in thermal light, Poissonian - the least random light that fits semi-classical description, sub-Poissonian - correlated quantum state of light

tromagnetic waves. So by the time Plack's solution to the UV catastrophe [14] cemented the particle nature of light in quantum mechanical theory, scientists and engineers were ready to embrace the wave-particle duality of light.

Even though the historical and natural advantage might explain the proliferation of photons in modern quantum systems, it is a strikingly odd object in a quantum lab. Most of the quantum objects we use in the lab, including atoms, electrons, and other artificially engineered quantum objects, enter the quantum regime at ultracold temperatures as they acquire sizable de Broglie [15] wavelengths and corresponding wave-like behavior. Photons behave like waves classically. It is quite a challenge to get photons to act as a particle, especially interacting particles. The reasons for this challenge and how cavity- and circuit-QED tools attempt to solve it are described below.

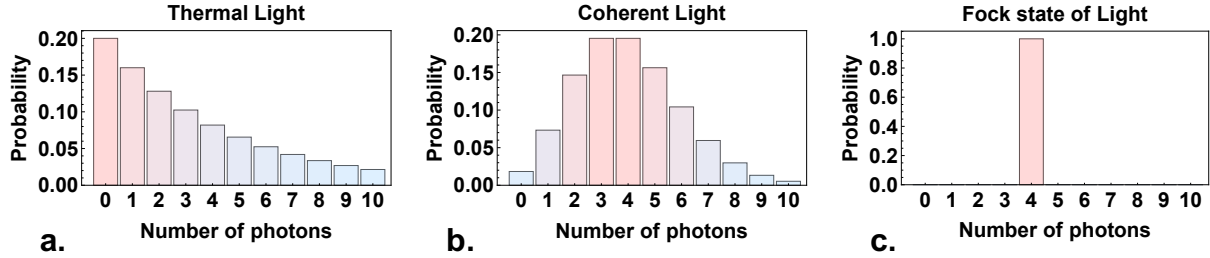


Figure 1.4: Probability of number of photons in one mode with the same expectation number  $\langle n \rangle = 4$  for: **a.** Thermal light from blackbody radiation, **b.** Coherent light from a laser or harmonic oscillator, **c.** Fock state from a nonlinear quantum system

### 1.1.1 Powerful toolbox of cavity-QED

**“Conservation of the number of particles”:** First step in the “wave-to-particle” transformation is mimicking the conservation of particle number, which photons do not obey since, unlike leptons or baryons, photons are their own antiparticles. In the QED regime, the virtual photons can pop in and out of a vacuum, leading to measurable pressure such as seen in Casimir effect [16, 17]. Even classically, the most we can do is to prepare a particular expectation value of photons by using thermal and coherent state of light as shown in Fig. 1.3.

In cavity [18] and circuit-QED [19], we achieve a constant expectation number of photons by carefully engineering an empty box, which we call a cavity. The temperature is crucial for ensuring that in the steady-state and without a drive, the cavity, on average, is empty [14].

1

$$n_{ph} = \frac{1}{e^{\frac{h\nu}{k_B T}} - 1} \approx 0 \quad (1.1)$$

---

1. Note that in any thermal state of light, the most likely number of photons is zero, but the expectation number of thermal photons can still be high depending on temperature.

The cavity is designed to have a specific density of states which maintains photons of interest and avoids others. The interplay between losses and drive is an important challenge in our field, which can also be used as a tool for building driven and dissipative photonic quantum systems [20, 21].

More often, we prefer to avoid thermal photons entirely by cooling down the system. As shown in Fig. 1.2 depending on the frequency of the photons used, the pristine thermal background is hard to achieve. Optical photons, like ours at 780 nm, can be used in room temperature experiments, while microwaves require dilution refrigerators to get down to mK. In our experiment, we use mm-wave photons at 100 GHz to operate a complex hybrid system at a few K in a quantum regime both for optical and mm-wave photons.

The temperature and the design of density of states of the cavity take care of the allowed frequencies of the photons and get rid of the thermal light. But how do we prepare a precise number of photons in a cavity? The development of coherent RF technology and lasers have made coherent states of radiation widely available as drives. We use coherent sources to populate cavities with photons. As a result we prepare coherent states of light inside of the cavities with a desired expectation number of photons. Coherent states are quantum by definition, since they involve number of photon states, but behave very similar to a linear harmonic oscillator in classical physics:

$$\begin{aligned}
 |\alpha\rangle &= e^{-\frac{|\alpha|^2}{2}} \sum_{n=0}^{\infty} \frac{\alpha^n}{\sqrt{n!}} |n\rangle \\
 \langle n\rangle &= (\Delta n)^2 = |\alpha|^2 \\
 \langle x(t)\rangle &= \sqrt{\frac{2\hbar}{m\omega}} \text{Re}[\alpha(t)] = |\alpha(0)| \sqrt{\frac{2\hbar}{m\omega}} \cos(\omega t)
 \end{aligned} \tag{1.2}$$

The understanding of wave phenomena and coherence is necessary for developing photonics.

That is why I dedicated a whole Chapter. 2 to linear phenomena that can be described using harmonic oscillators we leverage in the lab. But to fully explore the quantum properties of photons as particles, we need to prepare states that cannot be described by classical electromagnetism. This implied preparing a specific number of photons - Fock states, and correlated quantum states such as Bell states and squeezed states. The comparisons between sources and produced types of light are shown in Fig. 1.3 and Fig. 1.4. To generate particle states of light, we need nonlinearity in the system. In other words, we need interactions that lead to entanglement.

**“Interactions”**: As discussed above, reducing the expectation number of the coherence state of photons to a few is not enough to fully explore quantum phenomena. Quantum mechanics becomes powerful when both coherence of the wave phenomena and entanglement created through interactions are combined. To explore entanglement, especially on large scales, we need nonlinear quantum systems, which display phenomena that depend on the number of

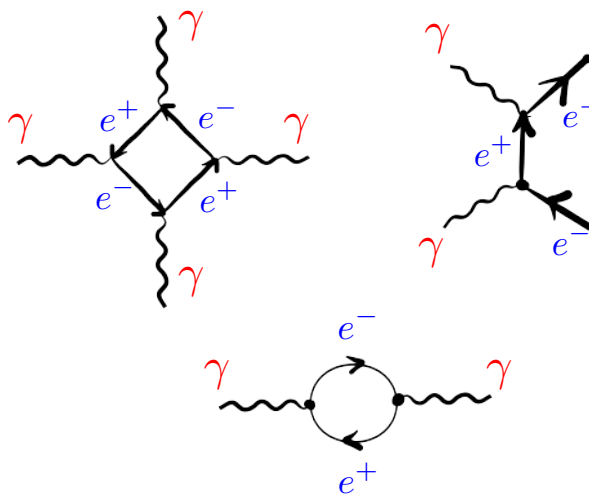


Figure 1.5: Diagrams of theoretical photon-photon interactions

particles in the system. Entanglement is a quantum correlation between particles that gives rise to quantum enhancement in metrology, quantum supremacy in computing, and emergent strongly correlated quantum many-body phenomena that classical machines and our analytic tools are inadequate at describing. Strongly interacting particles display nonlinear phenomena. For example, classically, electric charges interact through EM fields which decay with  $\propto 1/r$  Coulomb potential. In QED, we think of charged particles interacting with each other through an exchange of virtual photons, which are "off-shell" bosonic excitations of the quantum EM field. A lone particle has a different energy than particles in a tight

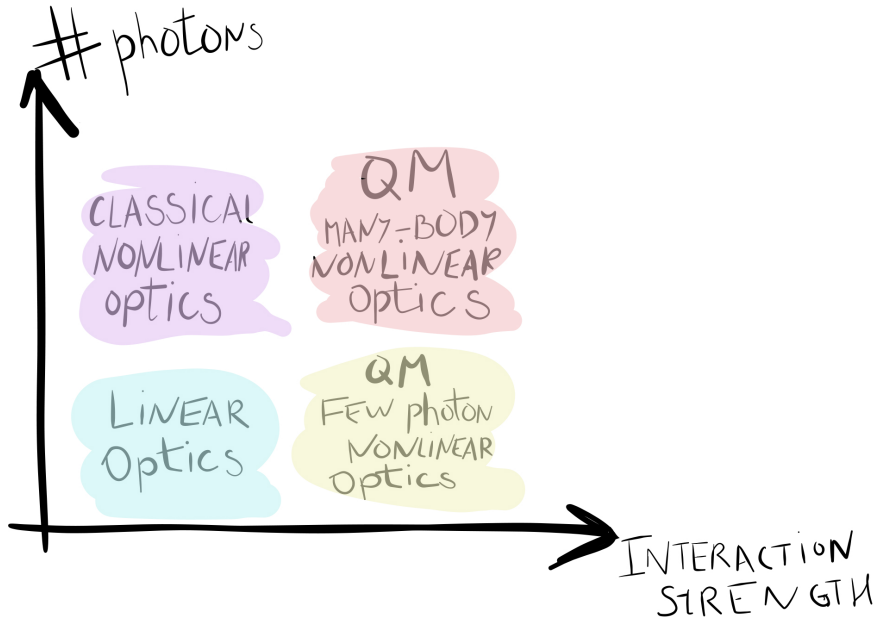


Figure 1.6: Different photonic regimes depending on the number of photons and the interaction strength per photon between them. Adapted from [1]

group. The stronger the inter-particle interactions, the more “grainy” the quantum behavior of the group appears. If the difference in energy is already apparent when we go from one particle to two, we consider this system strongly nonlinear or strongly interacting. Whereas if the difference in energy only becomes apparent every several orders of magnitude, we refer to it as weakly interacting. If we want to explore nonlinear quantum many-body photonic systems, we need many photons to interact strongly with each other, as shown in Fig. 1.6.

The issue is that photons do not interact with each other. Classically, the linearity of Maxwell’s equations tells us that each individual photon doesn’t change its energy or color because of the presence of another. And from QED, we know that since photons do not have a charge, they only interact indirectly and with tiny scattering probabilities, as shown in Fig.1.5. Photon-photon scattering is an incredibly rare event, which requires the production of an electron-positron pair in exact right conditions. And it needs the photons to be energetic enough to produce two massive particles. This means that it is more likely to happen for gamma rays of  $E > mc^2$ , and even then, it is extremely rare. So if our goal is to

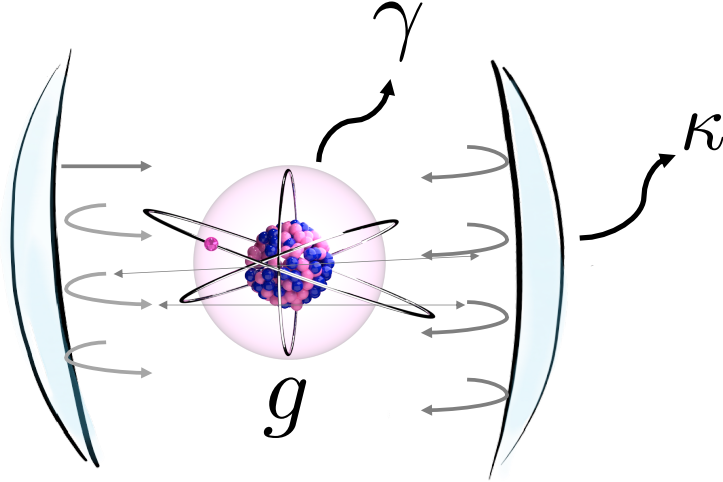


Figure 1.7: A diagram of an emitter coupled to a photon in a cavity, with characteristic parameters  $\kappa$ ,  $\gamma$  and  $g$ .

create strongly interacting photons, we cannot rely on naturally occurring coupling.

Cavity-QED framework allows us to engineer effective light interactions by implanting cavities with nonlinear mediators that couple photons to each other. Unlike ones used in classical nonlinear optics these mediators can provide a large interaction per photon energy as shown in Fig. 1.6. Examples of these mediators can be Rydberg atoms [22, 23, 24], Josephson junctions [25] and solid state defects [26, 27, 28]. A lot of recent effort in cavity and circuit-QED has been dedicated to push the interaction strength as high as possible to reach strong interaction regime. As illustrated in Fig. 1.7, the main parameters of a cavity-QED system are:

$$\begin{aligned}
f_0 & \text{ frequency of the light, units = Hz} \\
\Gamma & \text{ linewidth of the quantum emitter, units = Hz} \\
\kappa & \text{ linewidth of the cavity, units = Hz}
\end{aligned}
\tag{1.3}$$

$$g = E \cdot d \text{ single photon coupling strength to the emitter, units = Hz}$$

$$\eta = \frac{g^2}{\kappa\Gamma} \text{ single photon cooperativity, unitless}$$

The  $g$  coupling parameter quantifies how strongly a single photon in a mode volume of the cavity couples the mediator.<sup>2</sup> The  $g$  can be maximized by making the cavity mode smaller, engineering stronger dipole moment of the emitter, and even using collective excitations of an ensemble of mediators. The cooperativity,  $\eta$ , determines what interaction regime we are in: weak coupling  $\eta < 1$  or strong coupling  $\eta > 1$ . It’s a measure of how many interactions an emitter and a photon will have in a coherence lifetime of the system, e.g. before the photon leaks out of the cavity or the emitter loses coherence.

Technological advances in optimizing these parameters have revolutionized the field of quantum optics. It is still technologically challenging, but the ability to create effective strong interactions between photons allows us to harness entanglement and prepare specific number states of photons with no classical counterpart.

**“Shaping”** Cavity and circuit-QED tools also provide us tools to imbue other matter-like properties on photons. We can localize photons in tight spaces using boundary conditions of cavities [29, 30] and waveguides [31]. We can shape their potentials to give them mass and apply magnetic fields [32]. Many-body photonic systems can be in discrete lattices [33, 34] or continuous [24]. And we can even engineer the interactions between photons to be

---

<sup>2</sup> The interaction doesn’t have to be dipolar, but it is the most commonly occurring in the cold atoms community

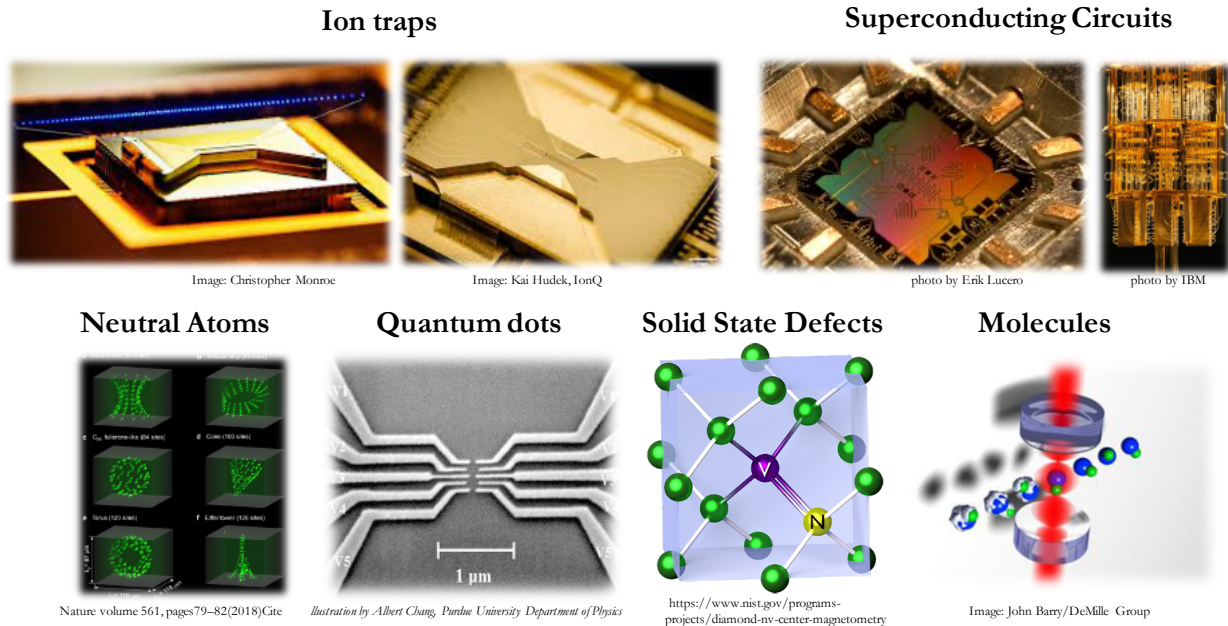


Figure 1.8: Some of the variety of quantum hardware platforms

repulsive [22, 34] or attractive [35]. Finally, we can leverage their loss and dissipation to explore non-equilibrium quantum many-body systems [36]. I hope the reader got a little flavor of how odd the photon is like a “lego” piece of quantum engineering and, at the same time, how powerful it can be once incorporated into cavity-QED platforms. As a PhD student, I have been lucky to be part of two significant scientific advances in quantum photonics. One is the exploration of the mm-wave frequency band for quantum technology. And the other one is developing a new type of hybrid cavity-QED system for interfacing single mm-wave and optical photons using Rydberg atoms.

## 1.2 Millimeter wave band for quantum technology

The mm-wave photons with frequencies between 75 and 100 GHz have been at the heart of my PhD research. As I will thoroughly discuss in Chapter. 4, mm-wave photons offer unique advantages as a frequency band for cavity and circuit-QED, including negligible thermal photon background at 1 K temperatures, variety of coherent quantum emitters, and

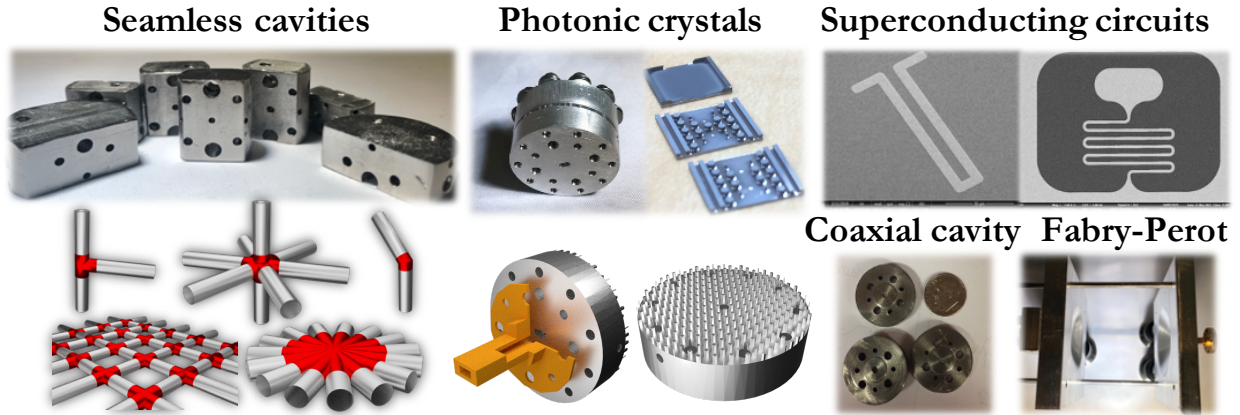


Figure 1.9: Some of our mm-wave devices

flexibility in design and fabrication of devices, some of which are shown in Fig. 1.9.

Before our efforts, the mm-wave band was not widely used in modern quantum platforms, but mm-waves have played an essential role in pioneering the fields of the cavity and, eventually, circuit-QED [37]. After Purcell’s idea in 1946 that spins can spontaneously decay faster if coupled to resonant circuits [38], the first inhibited spontaneous emission of a Rydberg atom was observed in a 340 GHz mm-wave superconducting cavity in 1983 [39]. The atom shifts due to atom-cavity vacuum interactions were even measured in 1.9 THz cavities due to van der Waals interactions in 1992 [40] and at 50 GHz due to Lamb shift in 1993 [41]. The  $\sqrt{N}$  enhancement from coupling to  $N$  Rydberg atoms in a cavity was shown at 82 GHz in 1983 [42]. The first single-atom robust coupling regime achieved in a 21 GHz cavity-QED system led to the realization of a single atom maser in 1983 [43]. All of these early efforts have been powered by a combination of favorable interactions between mm-waves and Rydberg atoms and mild cryogenic requirements needed for cavities to reach extremely high-quality factors. This revolution culminated in physical confirmation of quantum phenomena with single photons [44, 45, 46] that directly confirmed quantum theory and jump-started cavity-QED based quantum technology.

Our work attempts to bring the mm-wave band back into the quantum playground on a

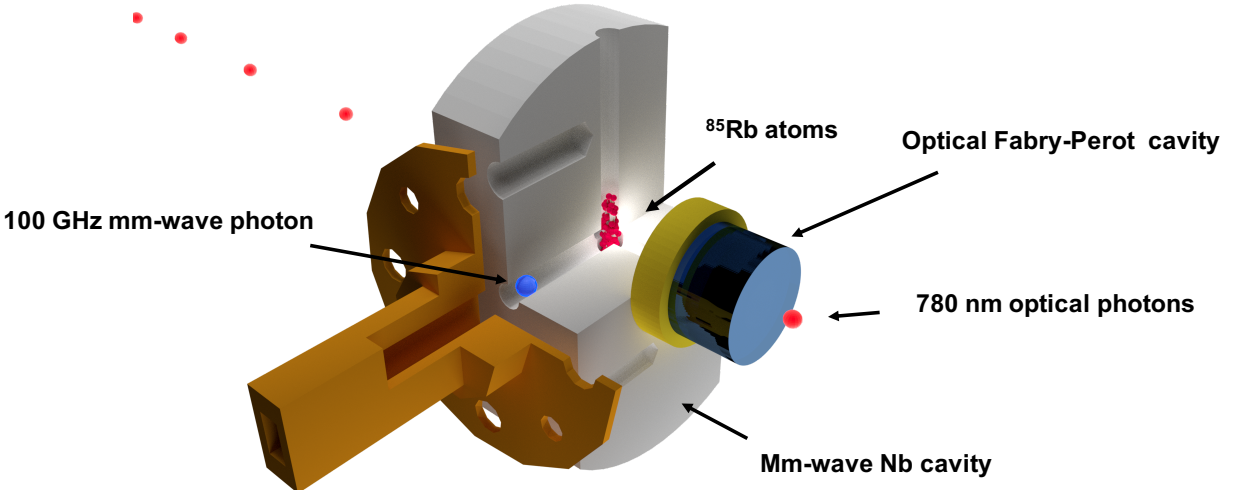


Figure 1.10: Hybrid cavity for interfacing mm-wave and optical photons using Rydberg atoms

new level. We have started to explore the capabilities of mm-wave photons for many-body quantum platforms with strong interactions in hybrid configurations, cavity-QED systems, and superconducting circuit-QED systems. I hope that our work would impact the future development of scalable quantum technology and contribute to the realization of extended quantum networks leveraged by more flexible quantum design.

All of my work in mm-wave quantum technology covered in Chapter. 4 has led to my main project as a PhD student, which is the development of a novel hybrid cavity-QED system for interfacing single mm-wave and optical photons using Rydberg atoms.

### 1.3 Our hybrid cavity-QED systems

The rapid progress of cavity and circuit-QED tools for manipulating photons has been concurrent with the advancement of quantum information technology. As shown in Fig. 1.8, scientists have developed an incredible variety of hardware platforms for quantum computing including superconducting circuits [47, 48], trapped ions [49, 50], cold atoms [51, 52] and

photonic chips [53, 54]. All of them have specific strengths and drawbacks, which have pointed scientists towards the possibility that the future of quantum technology could be hybrid. Hybrid systems aim to combine disparate physical platforms to leverage their individual strengths for the implementation of novel functionalities [55, 56, 57]. Since all of the current platforms rely on photons for manipulating and reading out quantum information, and some even use photons as qubits, photonics could become hybrid as well.

There is, currently, a lot of effort in hybrid photonic systems attempting to interface single optical and microwave photons [58, 59, 60, 61, 62, 63, 64]. Most of them are concerned with the transduction of quantum information between microwave to optical bands. Our system for interfacing single optical and mm-wave photons is uniquely versatile for a diverse set of photonic experiments and novel technologies, including quantum transduction.

At the heart of the experiment is an optical Fabry-Perot cavity crossed with a 3D superconducting mm-wave cavity, which contains an ensemble of cold  $^{85}\text{Rb}$  atoms as shown in Fig. 1.10. The  $^{85}\text{Rb}$  atoms act as mediators of effective interactions between optical and mm-wave photons at an extremely high efficiency opening up several powerful opportunities opportunity. First, our system allows for efficient and coherent inter-conversion between optical and mm-wave photons. Second, due to high cooperativity, our system has a unique ability to create strong nonlinear interactions between optical and mm-wave photons. This opens up a new field of nonlinear hybrid quantum optics applicable both as a quantum computing platform and as a tool for simulating exotic many-body quantum states with light. Finally, we can also create strong all-to-all interactions between atoms through coupling to the mm-wave photon. This can generate large-scale entanglement in an ensemble of atoms beneficial for quantum-enhanced metrology and precision measurement.

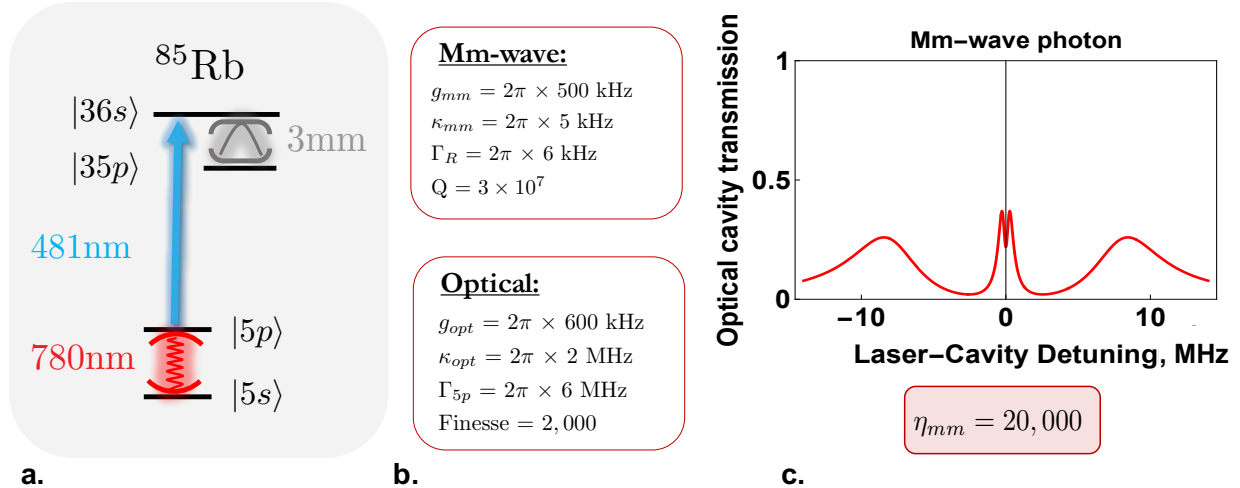


Figure 1.11: Source of strong interactions in our hybrid cavity-QED system: **a.** the simplified diagram of  $^{85}\text{Rb}$  energy levels used in generating strong interactions, **b.** parameter regime for single optical photons - single atom coupling, and single mm-wave photon single Rydberg atom coupling at 1 K, **c.** The signature optical cavity transmission with the EIT peak split due to coupling to the vacuum of the mm-wave cavity mode.

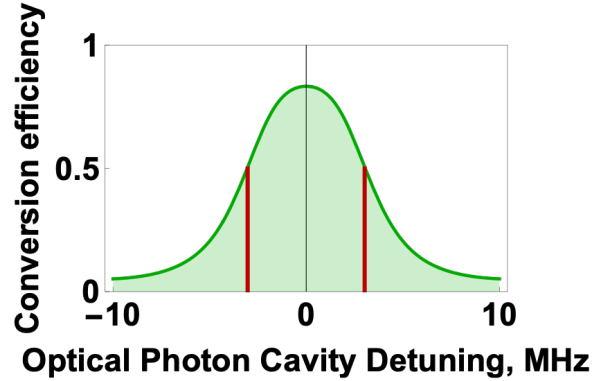
### 1.3.1 Engineering strong interactions between single mm-wave and optical photons

The key strength of our experiment is strong interactions between single optical and mm-wave photons. As shown in Fig. 1.11a, the simplified energy structure of  $^{85}\text{Rb}$  provides a coherent medium for coupling to both 780 nm (384 THz) optical photon when the atom transitions between ground states  $|5s\rangle \rightarrow |5p\rangle$  and to 3 mm (100 GHz) mm-wave photon when atom transitions between Rydberg states  $|36s\rangle \rightarrow |35p\rangle$ . To optimize the strength of effective photons interactions, we enhance the photon-atom coupling in both frequency regimes. We trap a 780 nm photon in a Fabry-Perot cavity and couple it to an ensemble of  $N$  atoms on the optical side. The high-Finesse of the cavity increases the lifetime of the photon, where the  $N$  atoms provide a  $\sqrt{N}g_{opt}$  enhancement to the single optical single ground state atom coupling. On the mm-wave side, we trap photons in a tight mode volume of a superconducting cavity. The high-quality factor of the superconducting cavity increases the coherence time of the mm-wave photon. And the tight mode volume magnifies the  $g_{mm}$ ,



**a.**

$$H_{int} \Rightarrow G_{eff}(a_{opt}^\dagger a_{mm} + a_{opt} a_{mm}^\dagger)$$



$$BW \approx 7MHz$$

**b.**

Figure 1.12: Inter-conversion of single mm-wave and optical photons: **a.** the simplified diagram of  $^{85}\text{Rb}$  energy levels used in transduction, **b.** expected bandwidth and efficiency performance of the transducer

which is a single mm-wave - single Rydberg atom coupling.

The nonlinearity in our system comes from Jaynes-Cummings Hamiltonian [65, 66] generated by strong coupling of the mm-wave photon to the Rydberg excitation of the atomic ensemble. This excitation is created using cavity EIT (Electromagnetically Induced Transparency) by coupling the  $|5p\rangle \rightarrow |36s\rangle$  with an intense 481 nm blue beam. This is an essential tool not only for bridging the two frequency transitions but also for allowing us to use the dark Rydberg-polariton excitation, which is decoupled from the broad  $|5p\rangle$  state and has a significantly longer coherence time. For parameters at 1 K temperature, as shown in Fig. 1.11b and c, our experiment is expected to reach single mm-wave- single atom cooperativities of over 20000. This puts us in a strong interaction regime in a unique hybrid photonics platform.

### 1.3.2 *Optical to mm-wave transduction*

Even though the mm-wave band is not widely used in quantum technology yet, it has the potential to be an exciting quantum platform on its own and as a part of a hybrid quantum system [67, 68]. Since optical frequencies are the most robust quantum buses, especially across a long distance, transduction of quantum information across the mm-wave and optical band is necessary. Moreover, since the research on microwave-to-optical transduction is still ongoing, the demonstration of high-efficiency optical-to-mm-wave transduction would be a milestone for the field.

Our inter-converter requires the addition of the UV beam to transfer the atomic excitation back to the ground state as shown in Fig. 1.12a. In the low excitation manifold, the interaction Hamiltonian can be linearized to take the beam-splitter form for coherently exchanging information from mm-wave to optical regime. As shown in Fig. 1.12b, we expect to have a high-performance transducer with a few MHz of bandwidth at  $\approx 75\%$  efficiency.

### 1.3.3 *Large scale entanglement for quantum enhanced metrology*

One last thing to mention is a different perspective and, hence, a new opportunity for our cavity-QED system. Instead of a hybrid experiment for leveraging strong interactions and efficient interconversion between photons, we can treat it as a strong all-to-all entanglement generator for a cloud of atoms inside the mm-wave cavity. A cloud of Rydberg atoms in a mm-wave cavity at 1 K would have extremely high single-atom single-photon cooperativities,  $\eta$  up to 22000. Most importantly, due to the large wavelength of the cavity photons compared to the size of the atomic cloud, a uniform all-to-all interaction can be achieved. This entanglement can be used to create squeezed state, for moderate cooperativities  $\eta < N$ , and even more dramatically correlated quantum states of matter such as Cat states, for high cooperativities  $\eta > N$  as shown in Fig. 1.13. Spin squeezed states have

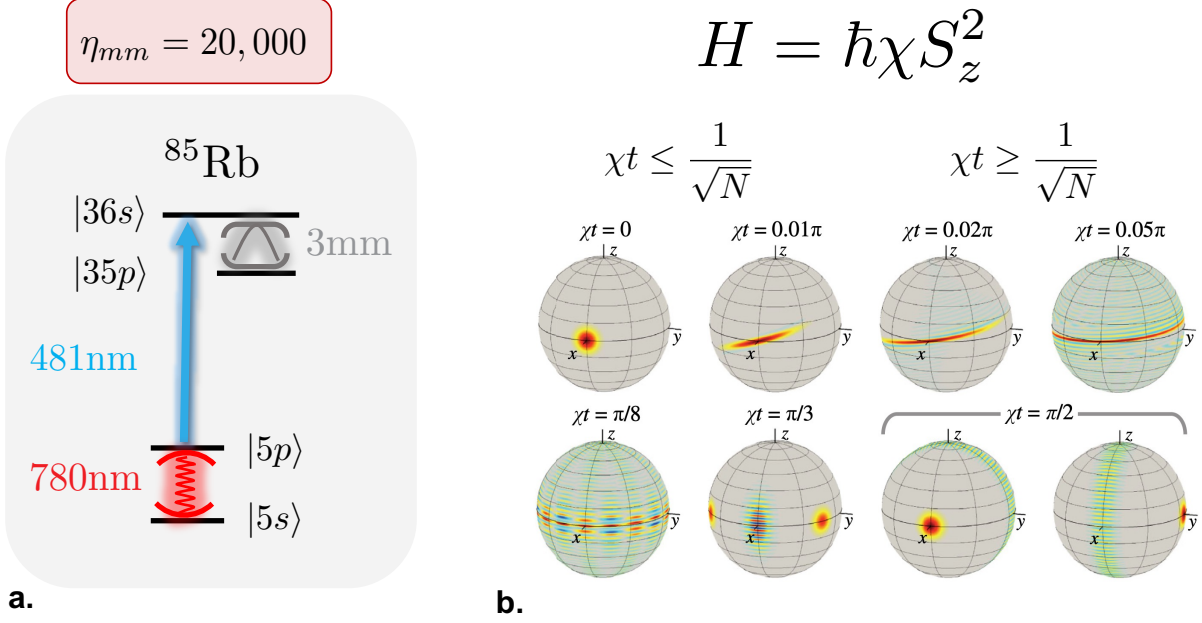


Figure 1.13: Spin squeezing: one-axes twisting: **a.** our energy diagram for one-axes twisting with many Rydberg atom excitations. **b.** Wigner functions of a  $N = 100$  twisted spin states as a function of the duration of the twisting Hamiltonian. The figure is incorporated from [2]

already been demonstrated in cavity-QED experiments [69, 70, 71]. This effort is motivated by quantum-enhanced metrology, which attempts to measure many-body quantum effects at an uncertainty level beyond classical noise limit  $\propto \frac{1}{\sqrt{N}}$  towards the Heisenberg limit  $\propto \frac{1}{N}$ . This field would greatly benefit from a strong uniform coupling that our system can provide. It is worth noting that there is a peculiar regime in our experiment where we could generate interaction between Rydberg atoms both through the coupling to the same mode of the cavity and through leveraging Rydberg-Rydberg interactions that occur at closer inter-particles distances and high Rydberg  $n$  states. It would be a fascinating regime to explore.

## 1.4 Thesis Layout

I will begin with an overview of linear wave physics that underpins most of the tools we use in our lab in Chapter. 2. I will attempt to connect multiple coherent phenomena, including

resonant cavities and atomic transitions, in the common language of coupled Harmonic oscillators. In the Chapter. 3, I will cover the quantum treatment of light in cavities and the non-Hermitian perturbation theory we use to describe our hybrid system. I will also cover other numerical and analytical tools which are useful to make predictions about our complex Cavity-QED system.

Chapter. 4 will describe my work in the mm-wave band, starting from the background of the frequency regime, current progress, and future for quantum technology. I will describe the devices I have developed during my Ph.D. and will use concepts from Chapter 2 to characterize the results.

Chapter. 5 will describe the details behind our experimental system. I will go over the main challenges we faced while designing and building this hybrid system and the solutions we came up with.

Then, in Chapter. 6 I will describe the experiment. I will go over some interesting aspects of our experiment, such as the Meissner effect for Optical pumping,  $^{85}\text{Rb}$  Gray Molasses, and the experimental sequence for the hybrid-CQED experiment. I will show our latest results, which show the mm-wave optical interface using Rydberg atoms and the first signs of nonlinear physics in our platform.

Finally, Chapter. 7 will go over our short and long-term scientific plans as well as the apparatus improvements. And I will review the impact our system has had in the field and describe potential future directions for exploration using the tools we have developed.

## CHAPTER 2

# HARMONIC OSCILLATORS FOR HYBRID EXPERIMENTALISTS

By the end of the advanced graduate coursework, every physics student starts wondering why so many concepts in physics seem like abstract interpretations of a harmonic oscillator. In addition to this, as an experimental physicist in the hybrid cavity and circuit-QED fields, I have found myself trying to understand, develop and manipulate single and many harmonic oscillators in the lab: from microwave resonators and optical cavities to atomic lines and lasers. It turns out that a phenomenon of resonance is at the heart of the field since a big part of the quantum advantage of our systems comes from coherence. So to harness coherence in both linear and nonlinear systems, we have to deeply understand a harmonic oscillator - the star of linear systems.

This chapter attempts to translate some practical terminology that describes the phenomenon of resonance in the circuit- and cavity-QED experiments that could be useful for interdisciplinary experimental physics students like me. We will explore a few things: what is resonance, how to think about loss, coupling, linear vs. nonlinear systems, and quantum treatment of light. And we will try to get an intuitive understanding of key resonator concepts, such as resonance frequency  $f_0$ , Quality factor,  $Q$ , external and internal  $Q$  and linewidth  $\kappa$ .

### 2.1 Mass on a spring

We will start from a Newton's  $2^{nd}$  law for a periodically driven damped harmonic oscillator (DHO) shown in Fig. 2.2.

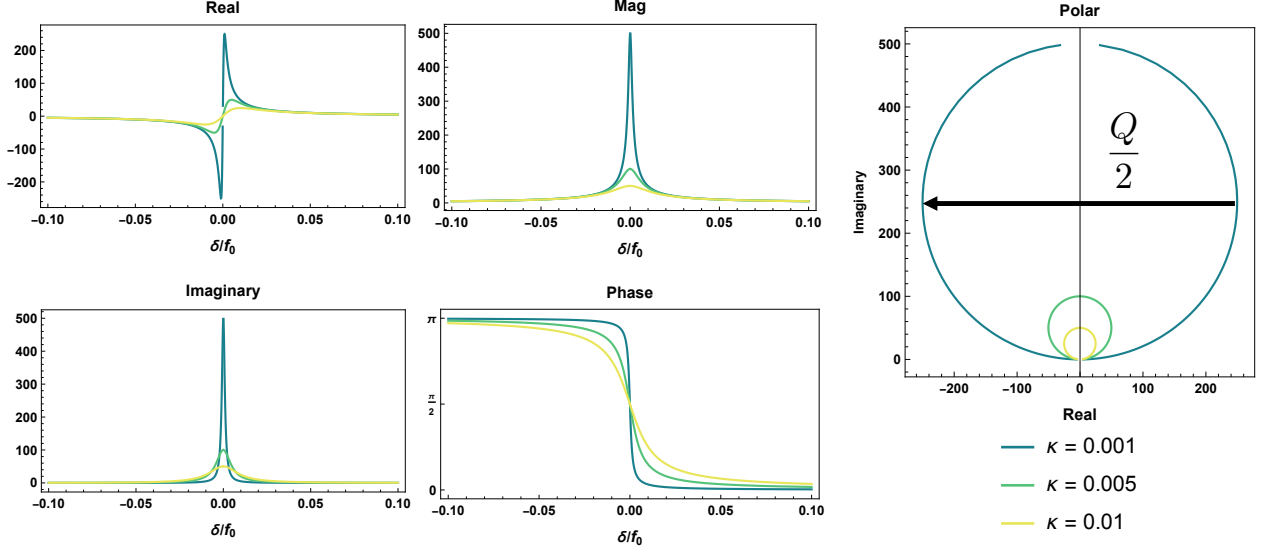


Figure 2.1: Resonance of an underdamped driven HO with  $X_0 = 1$  and  $f_0 = 1$  for different  $\kappa$

$$\begin{aligned}
 m\ddot{x} + c\dot{x} + kx &= F(t) \\
 \ddot{x} + 2\vartheta\omega_0\dot{x} + \omega_0^2x &= \omega_0^2X_0e^{i\omega t}
 \end{aligned} \tag{2.1}$$

where  $\omega_0 = \sqrt{\frac{k}{m}}$  is a natural angular resonance frequency of the system and  $\vartheta = \frac{c}{2\sqrt{mk}}$  is the dimensionless damping ratio <sup>1</sup>. In the lab, that would correspond to shining a CW tone at a fixed frequency into the resonator with some intrinsic loss.

In the frequency domain, the oscillatory driving force becomes a Dirac delta function, and the differential equation transforms into the algebraic equation, which is much easier to solve.

---

1. Note that the damping force is not conservative and leads to dissipation, which is similar to dissipation in atom-light systems. The frictional non-conservative force, in reality, is a result of a complex interplay of conservative electromagnetic forces, which we sweep under the rug in this picture. Similarly, in atomic systems, a lot of the time, we include damping or loss, but in reality, if we could write the equations for the entire system of all atomic states we are coupled to, there would not be this "magical" loss term.

$$\begin{aligned}
-\omega^2 x(\omega) + i\omega\omega_0 2\vartheta x(\omega) + \omega_0^2 x(\omega) &= \omega_0^2 X_0 \delta(\omega) \\
\tilde{Y}(\omega) = \frac{x(\omega)}{\delta(\omega)} &= \frac{X_0}{\frac{\omega^2}{\omega_0^2} - i2\vartheta \frac{\omega}{\omega_0} - 1}
\end{aligned} \tag{2.2}$$

The frequency response of the ideal oscillator, let's call it  $\tilde{Y}(\omega)$  for now, is shown in Fig. 2.1. Familiarity with these curves comes in handy when we need to fit the transmission data to extract parameters such as  $f_0$  and  $Q$ . I prefer fitting both imaginary and real parts to get the best fit. Note that real devices tend to have some asymmetries and offsets in the data from various reflections

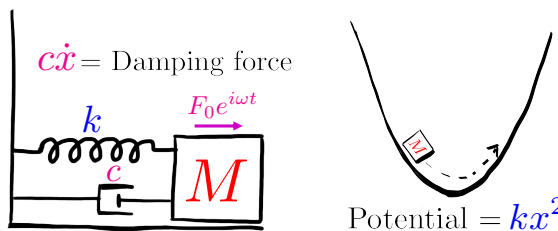


Figure 2.2: Mass,  $m$ , on a spring with a spring constant,  $k$ , and damping coefficient  $c$  has all of the prerequisites of an oscillatory system: an equilibrium position - at the bottom of the potential, and a restoring force provided by a conservative (path-independent) potential.

and leakages of signals to the ports that are not included in the model, which will be discussed later in the chapter.

We can apply Fourier transform to Eq. 2.2 to get the time response of our oscillator, which is:

$$x(t) = x_0 e^{i\omega t + \phi} = \left| \tilde{Y}(\omega) \right| e^{i\omega t + \phi_\omega}, \text{ where } \phi_\omega = \arg(\tilde{Y}(\omega)) + \pi n \tag{2.3}$$

$$x(t) = \frac{X_0}{\sqrt{\left(1 - \frac{\omega^2}{\omega_0^2}\right)^2 + 4\left(\vartheta \frac{\omega}{\omega_0}\right)^2}} e^{i\omega t + \phi}, \text{ where } \phi = \tan^{-1}\left(\frac{\vartheta}{\frac{\omega}{\omega_0} - \frac{\omega_0}{\omega}}\right) + \pi n \tag{2.4}$$

This means that the mass on a spring will oscillate at the frequency of the drive with an amplitude and phase lag dependent on the detuning of the drive from the resonance of the

oscillator. The maximum response is at  $\omega_0$ , with  $\frac{x_0}{X_0} = \frac{1}{2\vartheta} = Q$ , which is the Quality factor of a DHO or the bandwidth of the excitation:

**Underdamped harmonic oscillator:** Since we work with cavities and resonators which exhibit oscillations, we only care about the very underdamped case of the harmonic oscillator with  $\vartheta \ll 1$  or equivalently with very high  $Q$ . This allows us to make a few simplifications:

Without the drive:

- An underdamped HO oscillates at a slightly lower frequency than the undamped one:  $\omega_1 = \omega_0\sqrt{1 - \vartheta^2}$ . But when the  $Q$  is very high we can assume that  $\omega_1 \approx \omega_0(1 - \frac{\vartheta^2}{2})$  or even  $\omega_1 \approx \omega_0$ . This makes sense for our uses since our  $Q$ s can get to  $10^7$  or  $\vartheta = 10^{-7}$ , whereas the natural frequencies are in the order of  $10^{11}$  or  $2\pi \cdot 100$  GHz.
- The oscillations would decay exponentially as  $e^{-\vartheta\omega_0 t}$ , where the linewidth of our oscillator is  $\kappa = \frac{1}{2\pi}\vartheta\omega_0$
- The Quality factor can be calculated as follows:

$$Q = 2\pi \frac{\text{Energy stored}}{\text{Energy loss per cycle}} = \pi \frac{KE + PE}{\Delta E_{1cycle}} = 2\pi \frac{\frac{1}{2}m\dot{x}^2 + \frac{1}{2}kx^2}{\int_{\frac{\phi}{\omega_1}}^{\frac{2\pi+\phi}{\omega_1}} -m2\vartheta\omega_0\dot{x}^2 dt} = \frac{\omega_1}{2\vartheta\omega_0} \approx \frac{f_0}{\kappa} \quad (2.5)$$

Finally, for very underdamped driven HO near resonance,  $\omega = \omega_0 + \delta$ :

$$\tilde{Y}(\omega) = \frac{X_0 f_0}{2(\delta - i\kappa(1 + \frac{\delta}{f_0}))} \quad (2.6)$$

$$x(t) = \frac{X_0 f_0}{2\sqrt{\delta^2 + \kappa^2}} e^{i\omega t + \phi}, \text{ where } \phi = \tan^{-1}\left(\frac{2\pi\kappa}{2\delta}\right) + \pi n$$

Before we move on, it's important to note that the Eq. 2.1 is a second order ODE, which

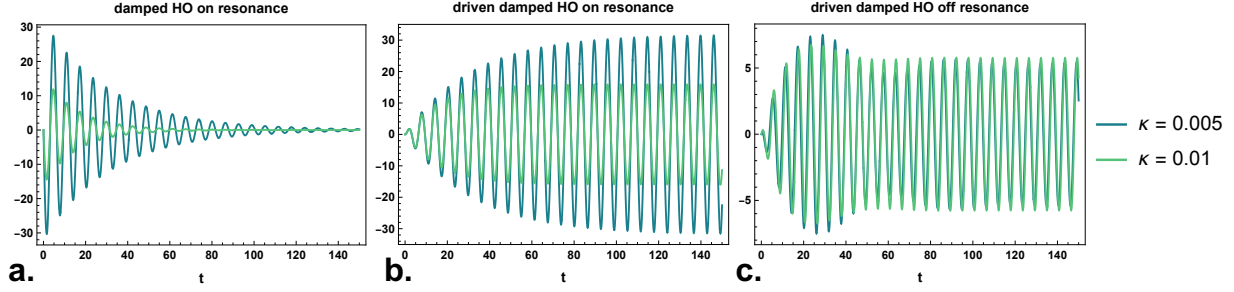


Figure 2.3: Time response of a harmonic oscillator. **a.** Damped harmonic oscillator without the drive. **b.** Damped harmonic oscillator driven on resonance. **c.** Damped harmonic oscillator driven off resonance.

means that its solution should have two arbitrary constants. But our solution in Eq. 2.4 has no arbitrary constants, implying that it can not be the most general solution to the equation. It is, in fact, the steady-state solution - which is usually what we are looking for in lab when working with resonators. To find the transient solution notice that any solution to the undriven HO oscillator is also a solution to a DHO. The time response of a damped harmonic oscillator is shown in Fig. 2.3a. Then the full solution is a sum of the steady state and transient solutions:

$$\begin{aligned}
 x(t) &= x_{ss}(t) + x_{tr}(t) \\
 &= \frac{X_0 f_0}{2\sqrt{\delta^2 + \kappa^2}} e^{i\omega t + \phi} + A e^{-2\pi\kappa t} e^{i\omega_0 t} + B e^{-2\pi\kappa t} e^{i\omega_0 t}
 \end{aligned} \tag{2.7}$$

As the name suggests, this piece is transient in time and dependent on the initial conditions. It only lasts a short period of time. For a high-Q mm-wave cavity with a total Q of 100000, the transient part would decay within a microsecond, but this dynamics is important for understanding the cavity drive.

For the DHO initially in an equilibrium  $x(0) = \dot{x}(0) = 0$  and driven on resonance, the time evolution follows:

$$x(t) \approx X_0(1 - e^{-2\pi\kappa t})e^{i\omega_0 t} \quad (2.8)$$

which is shown in Fig 2.3b. You can see that within  $1/\kappa$  time period, the oscillation amplitude builds up in the HO and stay constant afterward when power provided by the drive is equal to the power dissipated in the DHO. This applies to our cavities as well. When we turn on the laser and send it into the Fabry-Perot, it would not make sense if the far mirror of our cavity knew instantaneously about the frequency of our photon that was just imparted on the front mirror - it needs time. In a steady state, both mirrors are "aware of" the frequency of the light.

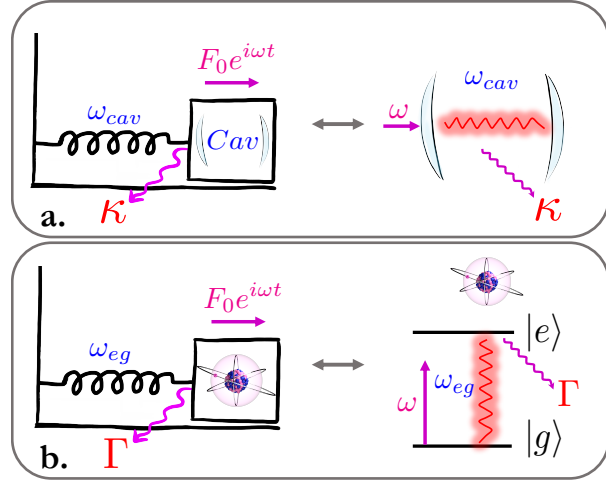


Figure 2.4: Mechanical analogs of: **a.** A high-Q single mode of a driven optical or microwave cavity **b.** A "very" weak drive of a two-level atom

Even stranger thing happens when the DHO initially in equilibrium is driven off-resonance. As shown in Fig 2.3c. there is a short period of time  $1/\kappa$  where there is a beating between two frequencies  $\omega$  and  $\omega_0$  and, eventually, the oscillations settle at a lower amplitude but the drive frequency.

## 2.2 Coupled masses on springs

The underdamped HOs are everywhere in a cavity- or circuit-QED lab. A simple mass on a spring is a good starting point for describing a single mode of a microwave or optical cavity

or a semi-classical description of a weakly driven two-level atom and any other resonant RLC circuit you might find in the lab.

To see some useful applications [72, 73], Fig.2.4 translates our mechanical HO in Fig. 2.2 in terms that are more familiar in cavity-QED systems. Note that the two-level atom here is linear, which is odd since we use a two-level atom and its intrinsic inharmonicity to get interactions between photons. Think about it this way: if you are only coupling less than one photons per  $\Gamma$ , your atom decays to the ground state before the next photon comes in. This means that this "two-level" atom can be a zoomed-in view of two levels of a quantum harmonic oscillator for our purposes. When you drive the transition  $|g\rangle \rightarrow |e\rangle$  harder, a second photon can arrive and try to re-excite your atom while it is still in the excited state. We know that quantum mechanically that that would actually de-excite the atom back into the  $|g\rangle$  state, rendering our linear HO treatment nonsensical. Basically, any two-level system driven very weakly or below saturation can be simulated using linear HOs.

### 2.2.1 Cavity - Vacuum Rabi Splitting (VRS)

Let us consider a pair of coupled HOs, one representing a mode of a cavity and another our "linear" atom shown in Fig. 2.5. Similar to the previous section, we start with a Newton's  $2^{nd}$  law, but now for a pair of the harmonic oscillator (DHO) shown in Fig. 2.5a, and only one of them being driven by a periodic force.

$$\begin{aligned} m\ddot{x}_1 + c_1\dot{x}_1 + k_1x_1 + k_{12}(x_1 - x_2) &= F_0e^{i\omega t} \\ m\ddot{x}_2 + c_2\dot{x}_2 + k_2x_2 + k_{12}(x_2 - x_1) &= 0 \end{aligned} \tag{2.9}$$

Following [72], I will transform parameters in the equations used in Fig. 2.5a. for usually

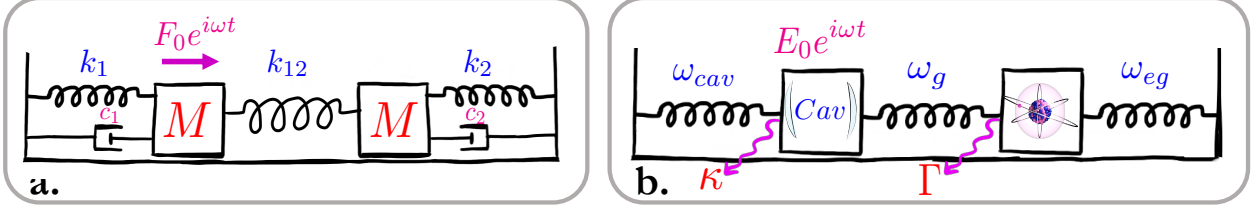


Figure 2.5: Diagrams of two coupled damped harmonic oscillators, where only the first one is driven by the external force: **a.** in usual mechanical terms **b.** converted into the cavity-QED terms

mechanical oscillators into cavity-QED language in Fig. 2.5. Specifically:  $\omega_{cav} = \sqrt{\frac{k_1+k_{12}}{m}}$ ,  $\omega_{eg} = \sqrt{\frac{k_2+k_{12}}{m}}$ ,  $\omega_g = \sqrt{\frac{k_{12}}{m}}$ ,  $2\kappa = \frac{c_1}{m}$  and  $2\Gamma = \frac{c_2}{m}$  will transform our coupled differential equations into:

$$\begin{aligned} \ddot{x}_1 + 2\kappa\dot{x}_1 + \omega_{cav}^2 x_1 - \omega_g x_2 &= \tilde{F}_0 e^{i\omega t} \\ \ddot{x}_2 + 2\Gamma\dot{x}_2 + \omega_{eg}^2 x_2 - \omega_g x_1 &= 0 \end{aligned} \quad (2.10)$$

Note that frequencies of our cavity and atomic resonances have shifted from their bare values  $\omega_{eg}^b = \sqrt{\frac{k_2}{M}}$  and  $\omega_{cav}^b = \sqrt{\frac{k_1}{M}}$  not just from damping, but from the interaction. So we will consider resonances around these values instead of bare frequencies. It's analogous to considering our cavity-QED system in the dressed state. Indeed, you will notice that our future calculations only make sense if the two or three resonators have similar resonance frequencies, which is not the case before transferring into the dressed picture.

Since in our hybrid experiments we drive and probe the cavity, I set up this toy model to be analogous. As shown in Fig. 2.5b, we are only driving the cavity oscillator with  $F_0 e^{i\omega t}$ , which corresponds to sending low power coherent light into the cavity and we are solving for  $x_1(t)$ , since in our setup we can only measure the cavity response. As always, we Fourier transform the equations or, equivalently, pick an ansatz to be  $x_1 = \tilde{Y}_1(\omega) e^{i\omega t}$ , to get:

$$\tilde{Y}_1(\omega) = \frac{x_1(\omega)}{\delta(\omega)} = \frac{\tilde{F}_0/m}{\omega_{cav}^2 - \omega^2 - i2\kappa\omega - \frac{\omega_g^4}{\omega_{eg}^2 - \omega^2 - i2\Gamma\omega}} \quad (2.11)$$

Now, we make an assumption that both oscillators are very underdamped and close to each other in frequency, and look for solutions near the resonance  $\omega = \omega_{cav} - \Delta_{cav}$  and  $\omega = \omega_{eg} - \Delta_{eg}$  :

$$\begin{aligned} \tilde{Y}_1(\omega) &\approx \frac{\frac{2\tilde{F}_0}{m\omega_{cav}}(\Delta_{eg} - i\Gamma)}{4(\Delta_{cav} - i\kappa)(\Delta_{eg} - i\Gamma) - \frac{\omega_g^4}{\omega_{cav}\omega_{eg}}} \\ &= \frac{\Omega_d X_1(\Delta_{eg} - i\Gamma)}{(\Delta_{cav} - i\kappa)(\Delta_{eg} - i\Gamma) - g^2} \end{aligned} \quad (2.12)$$

where  $\frac{2\tilde{F}_0}{m\omega_{cav}} = 2\Omega_d X_1$ , with  $\Omega_d$  is the Rabi frequency of the drive and  $X_1$  a coefficient with a unit of length, and  $\frac{\omega_g^2}{\sqrt{\omega_{cav}\omega_{eg}}} = 2g$ , with  $g$  is the Rabi frequency of the coupling to the two-level atoms.

In the limit of low atomic excitation or weak probe the Eq. 2.13 is identical to the steady state expectation value of the cavity field annihilation operator, which can be derived using master equation and Janes-Cummings Hamiltonian:

$$\langle a \rangle = \frac{\varepsilon(\Delta_{eg} - i\Gamma)}{(\Delta_{cav} - i\kappa)(\Delta_{eg} - i\Gamma) - g^2} \quad (2.13)$$

This simple derivation can simulate phenomena we associate with quantum systems such as avoided crossing in Fig. 6.11a., the "dark state," and the Vacuum Rabi Splitting in

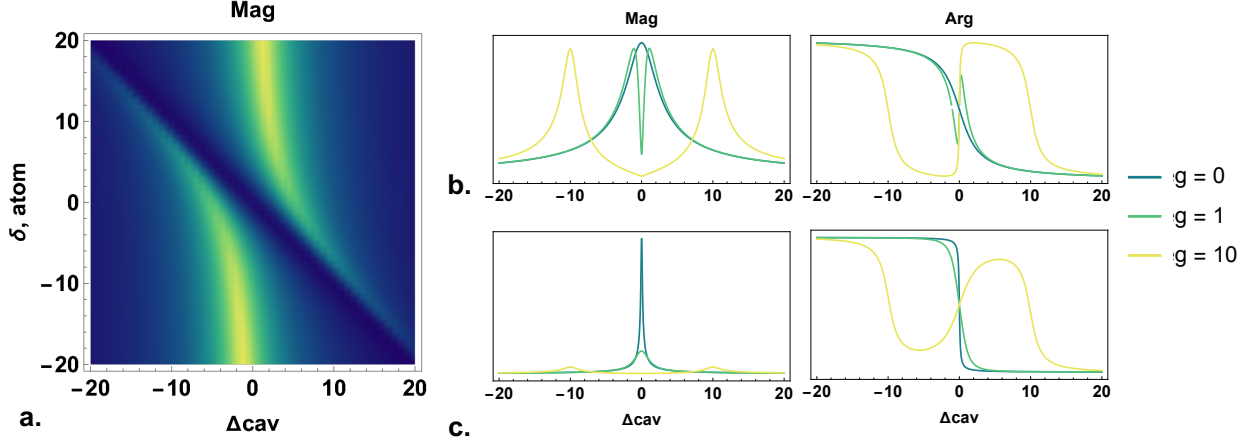


Figure 2.6: Frequency response of two coupled harmonic oscillators, shown in Fig. 2.5: a single mode of a cavity driven by a periodic force with  $\Omega_d = 0.001$  and a two-level atom. Everything is in units of MHz **a.** Avoided crossing as a function of the cavity detuning and relative atomic detuning with  $\Gamma = 1$ ,  $\kappa = 2$  and  $g = 5$ . **b.** Energy spectrum of the of the atom coupled to a cavity mode of the same frequency simulated by coupled harmonic oscillators. As we increase the coupling strength  $g$ , the driven cavity transmission shows a "transparency" followed by a "Vacuum Rabi-like" feature.  $\Gamma = .1$ ,  $\kappa = 2$  **b.** Same as **b.**, but the  $kappa = .1$  and  $\Gamma = 2$ . We do not see the same transparency dip in the transmission.

Fig. 6.11b. In fact, for the driven cavity case, as long as the drive strength is much less than the coupling,  $\Omega_d \ll g$ , and atomic loss is much less than the cavity loss  $\Gamma \ll \kappa$  the quantum and classical treatments give identical results, shown in Fig. 6.11. Note that the "dark state" or the transparency is only observed when  $\Gamma \ll \kappa$ .

### 2.2.2 Coupling $Q$ of a cavity

Another neat application of two coupled harmonic oscillators is a simulation of "loading" of the internal  $Q$  of a cavity by coupling to the external world. We will discuss this later in the context of trans-

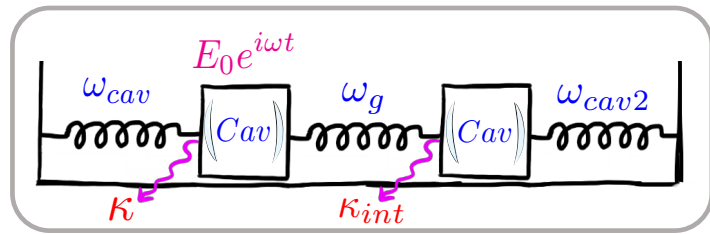


Figure 2.7: Two coupled resonators

mission lines and traveling waves, which is more natural for this topic, but it is interesting to

see the analogy in this simple model. Consider exactly the same system we solved to show the Vacuum Rabi splitting but with relabeled parameters, as shown in Fig. 2.7. Now we have two coupled cavities with no atoms, and we drive the first one with a harmonic force and measure the response of the second cavity.

From Eq. 2.6, we know that if we drive the second cavity directly, the linear response function would be:

$$\tilde{Y}(\omega) = \frac{\Omega_d}{2(\delta - i \cdot \kappa_{int})} \quad (2.14)$$

with the linewidth of  $\kappa_{int}$  and the quality factor  $Q = \frac{f_0}{\kappa_{int}}$ .

Now, what happens if we drive directly the first cavity and it is in turn driving the second cavity. We have tools from previous section to solve it, but instead of calculating  $\tilde{Y}_1(\omega)$ , we want  $\tilde{Y}_2(\omega)$ :

$$\begin{aligned} \tilde{Y}_2(\omega) &= \frac{\omega_g^2}{\omega_2 - \omega^2 - 2i\kappa_{int}\omega} \tilde{Y}_1(\omega) \\ &= \frac{g\Omega_d X_1}{\omega_1(\Delta_{cav1}\Delta_{cav2} - i\kappa_{int}\Delta_{cav1} - i\kappa\Delta_{cav2} - \kappa_{int}\kappa - g^2)} \end{aligned} \quad (2.15)$$

To see how relative detuning and coupling affects the linewidth of the second cavity, lets set  $\Delta_{cav1} = 0$  and  $\Delta_{cav2} = \delta$ . The  $\Delta_{cav1} = 0$  is primarily to transfer all of the power from the drive to the  $x_1(t)$ , since we don't want to know the overall attenuation of the power cause by the first cavity, but its effect of the linear response function of the second cavity. With these assumption, we get:

$$\tilde{Y}_2(\omega) = \frac{\tilde{\Omega}_d X_1 \frac{g^2}{\kappa}}{\delta - i(\kappa_{int} + \frac{g^2}{\kappa})} = \frac{\tilde{\Omega}_d X_1 \kappa_{ext}}{\delta - i(\kappa_{int} + \kappa_{ext})} \quad (2.16)$$

where  $\tilde{\Omega}_d = \frac{-i\Omega_d}{g\omega_1}$

So not only did the resonance frequency of the second cavity has shifted from  $\omega_{cav}^b = \sqrt{\frac{k_2}{M}}$  to  $\omega_{cav} = \sqrt{\frac{k_2+k_{12}}{M}}$ , but its linewidth increased to  $\kappa_{tot} = \kappa_{int} + \kappa_{ext} = \kappa_{int} + \frac{g^2}{\kappa}$  and quality factor decreased to  $Q_{tot} = \frac{Q_i Q_{ext}}{Q_i + Q_{ext}}$ .

In conclusion, we see that coupling to resonance through another device can significantly alter its linear response function. In this system, it is not terribly surprising since we coupled the masses to create interesting linear effects. In practice, this happens by accident or as an inconvenience, which we need to worry about. The more conventional way to couple power to resonators is via transmission lines, we do not have tools yet to describe them, but we will soon.

### 2.2.3 Cavity - Electromagnetically Induced Transparency (EIT)

The simulation of our "linear" cavity-QED systems using coupled harmonic oscillators can be extended further to the intra-cavity Rydberg EIT with a single three-level atom, as shown in Fig. 2.8. Solving three coupled differential equations from Newton's  $2^nd$  law for three harmonic oscillators, we get:

$$\tilde{Y}_{CEIT}(\omega) \approx \frac{\Omega_d X_1 (\Delta_{eg} - i\Gamma)(\Delta_R - i\Gamma_R) + \Omega_d \Omega_b^2}{(\Delta_{eg} - i\Gamma)(\Delta_R - i\Gamma_R)(\Delta_{cav} - i\kappa) - \Omega_b^2(\Delta_{cav} - i\kappa) - g^2(\Delta_R - i\Gamma_R)} \quad (2.17)$$

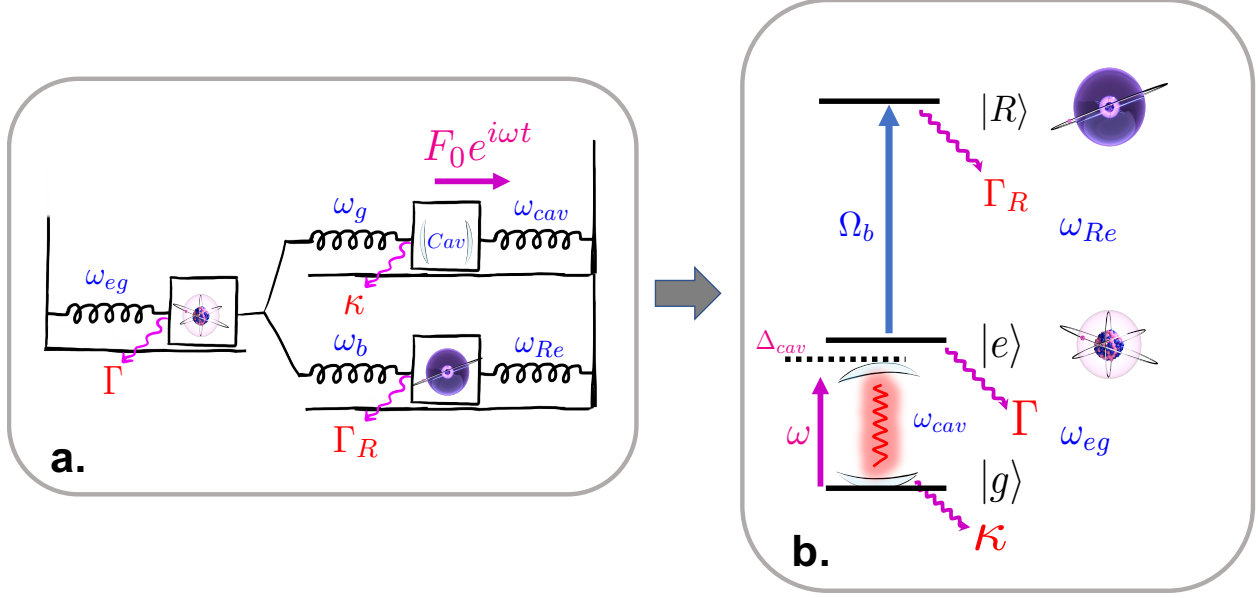


Figure 2.8: **a.** Diagram of three damped harmonic oscillators for simulating Rydberg cavity-EIT **a.** Usual atomic physics diagram of the system.

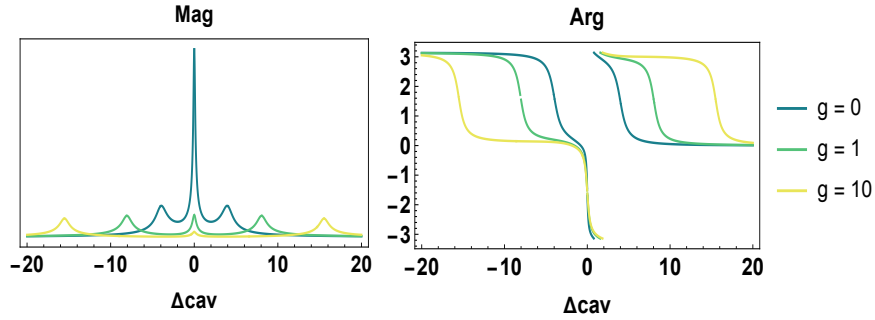


Figure 2.9: Frequency response of three coupled harmonic oscillators, shown in Fig. 2.8: a single mode of a cavity driven by a periodic force with  $\Omega_d = 0.001$  and a two-level atom. Everything is in units of MHz. The plots are made with  $\Gamma = 1$ ,  $\kappa = 2$  and  $g = 5$ .

where  $\Omega_d$  and  $g$  are defined the same way as in Eq. 2.13, and  $\frac{\omega_g^2}{\sqrt{\omega_{cav}\omega_{eg}}} = 2\Omega_b$  with  $\Omega_b$  as the blue Rabi frequency which couples excited and Rydberg states. The typical response of the weakly driven CEIT system, where the atomic levels are in resonance,  $\Delta_R = \Delta_{eg} = \Delta_{cav}$ , is shown in Fig. 2.9.

To mimic our hybrid system, we can go even further and simulate the many-atom intra-cavity EIT, as shown in Fig. 2.10. Note that, in the low excitation manifold, the collective excitation of our atomic ensemble of  $N$  atoms, the result in Eq. 2.17 gets modified only

slightly, by  $g^2 \rightarrow Ng^2$ .

### 2.2.4 Dark states

In atomic systems, we usually call dark states the transitions that "normally" absorb the radiation but do not under the condition of destructive interference. This condition can occur when there are three or more states, and two of them are coupled. For example, in Fig. 2.8b. if the  $\Delta_{cav} = 0$ , the optical photon resonant with  $|g\rangle \rightarrow |e\rangle$  is usually absorbed and then spontaneously emitted through decay  $|e\rangle \rightarrow |g\rangle$ . However, with the resonant blue beam on, two processes can occur: a. the usual absorption and spontaneous emission, only involving  $|g\rangle$  and  $|e\rangle$  states, b. a two-photon absorption and spontaneous decay involving the Rydberg state. Since these two paths are equivalent for the photon, they interfere. And for the particular parameters in the system, this leads to the destructive interference, where the photon in resonance with  $|g\rangle \rightarrow |e\rangle$  transition passes through the system unimpeded. We also call it - transparency, so if we measure the light leaking out of the cavity, we would measure a narrow peak where the system used to be opaque but now is transparent. Note that the transparency is narrow compared to the lossy excited state because, in the dressed picture, it doesn't involve these states.

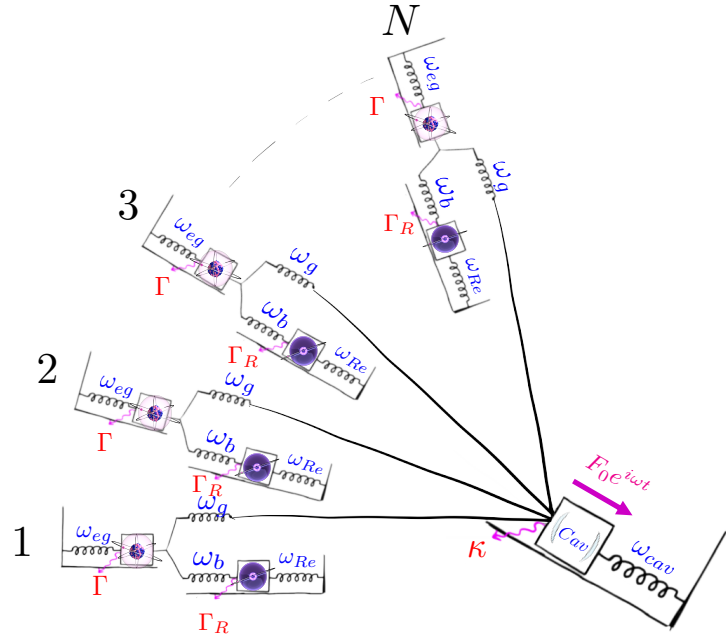


Figure 2.10: A diagram of  $N$  pairs of HOs (atoms) coupled to a single mode of a driven cavity

Figure 2.10: A diagram of  $N$  pairs of HOs (atoms) coupled to a single mode of a driven cavity. The diagram shows  $N$  pairs of atoms, each with three energy levels:  $|g\rangle$ ,  $|e\rangle$ , and  $|R\rangle$ . The atoms are coupled to a cavity mode with frequency  $\omega_{cav}$  and wavevector  $k$ . The atoms are also coupled to external fields with frequencies  $\omega_{eg}$ ,  $\omega_b$ , and  $\omega_{Re}$ , and decay rates  $\Gamma$ ,  $\Gamma_R$ , and  $\Gamma_R$  respectively. The diagram is labeled with 1, 2, 3, and  $N$ , indicating the number of atoms in each pair.

I think classical dark states could shed some light on these phenomena. Since we were able to simulate EIT with couples masses on springs, it is fair to assume that there is some classical analogy to EIT in the case of masses. In fact, there is! For coupled HOs, e.g., in Fig. 2.5 - there exist normal modes of the system,  $X_-$  and  $X_+$ , that can interfere in such a way that even when you are driving the mass 1 with a harmonic force - the mass one does not move. This is incredible since all of the power you provide to the mass one gets transferred into the oscillation of the mass 2. And since the damper - aka loss - of the mass one doesn't contribute to the system if the mass is motionless, that loss doesn't show up in the frequency response. This is directly analogous to the narrow linewidth of the transparency peak in EIT in comparison to the linewidth of the lossy excited state. This lossy state just does not participate in the dynamics under destructive interference.

This analogy highlights the fact that dark states and Fano resonances are wave phenomena that do not require quantum mechanics to observe. The quantum nature comes in only when you realize that at these low intensities of the probe power, our photons act as particles while they constructively and destructively interfere.

### 2.2.5 *From susceptibility to impedance*

Before we move on from atomic systems to other fun resonances we work with in the lab lets, try to figure out what exactly is the  $\tilde{Y}$  from Eq. 2.6, 2.11 and 2.17. In general, we can call it a linear response function. But since this chapter aims to connect some jargon, let's explore what this  $\tilde{Y}$  is called in various systems.

For the cavity-QED systems we have covered, the  $\tilde{Y}$  usually correspond to the expectation values of field and spin operators. Classically, we usually call the  $\tilde{Y}$  an electric susceptibility,  $\chi_e$ :

$$\mathbf{D} = \epsilon_0 \mathbf{E} + \mathbf{P} = \epsilon_0 \mathbf{E} + \epsilon_0 \chi_e \mathbf{E} \quad (2.18)$$

where  $\mathbf{D}$  is the displacement field, the  $\mathbf{P}$  is the polarization density,  $\mathbf{E}$  is the applied electric field and  $\epsilon_0$  is the vacuum electric permittivity. Note that susceptibility is related to the relative permittivity of the matter through:

$$\epsilon_r = \chi_e + 1 \quad (2.19)$$

and to the refractive index,  $n$ , through:

$$n = \sqrt{\mu_r \epsilon_r} = \sqrt{\chi_e + 1} \quad (2.20)$$

for non-magnetic material  $\mu_r = 1$ .

The term susceptibility is also used in an optomechanical system, which also exhibits all of the phenomena mentioned above, including the VRS and EIT [74].

From Maxwell's equations, we know that the intrinsic wave impedance of a medium is:

$$Z = \sqrt{\frac{\mu}{\epsilon}} = \sqrt{\frac{\mu_0}{\epsilon_0} \frac{1}{n}} = Z_0 \frac{1}{n} \quad (2.21)$$

for non-magnetic material  $\mu_r = 1$ . So when we find a linear response function of a linear system: we find its susceptibility, permittivity, or impedance. Depending on our physical

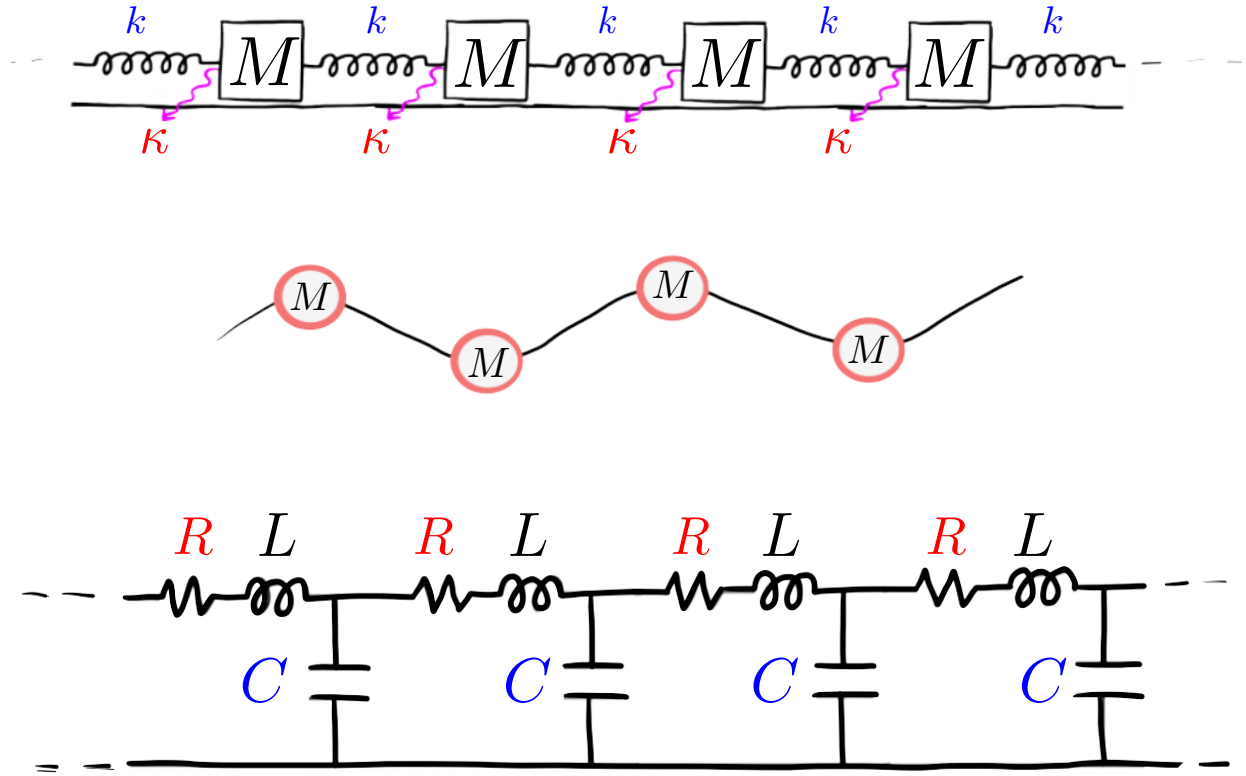


Figure 2.11: Transmission lines made of: **a.** Masses on springs, **b.** Beads on a string, **c.** RLC circuits

system and the specifics of the drive and response we want to measure, it makes sense to pick the term that describes your system best. In some sense, it is about choosing the extrinsic and intrinsic variables in your setup or, equivalently, picking the force and the coordinate. Even though thermodynamically, it is crucial to know what part of the system is performing the work and which one responds, as the systems and their geometries get more complex - we should be careful with defining the effect of the drive and the response [75].

Now that we have mentioned waves, it is helpful to see how they emerge in our HO picture.

### 2.3 $N \rightarrow \infty$ masses on springs: from oscillations to waves

As we couple more and more masses together, we begin to simulate more complex systems with many normal modes of oscillations. In all of these systems, there is one specific limit we haven't discussed - the wavelength of the oscillations has to be larger than the size of the oscillator. This becomes, frankly, impossible in the lab, where we need to measure the linear response of the superconducting cavity inside of the cryostat using a Vector Network Analyzer meters away. At 100 GHz frequency, the wavelength is around 3 mm, so we definitely can't simulate our measurement systems as two resonators coupled together by a spring. Things get even worse at optical frequencies. We sent 485 nm light through meters of fiber before it reaches the atomic ensemble inside of the system. Even for superconducting microwave circuits with a wavelength of centimeters, this assumption breaks apart as soon as you attach a wire to your chip. To address and manipulate resonant systems in the lab, we have to extend our oscillators into systems of non-zero length scales. This brings us to the concept of a transmission line, shown in Fig. 2.11, and traveling waves.

Consider an infinite chain of masses on springs in Fig. 2.11a. All of the linear systems we have covered have the time translation invariance. Here we will encounter a new symmetry - space translational symmetry. Following a beautiful derivation in [76], we will use the translational symmetry of our system to find the normal modes of the entire system. I had hinted at normal modes when we discussed dark states of two and three coupled masses on springs. Normal modes are the ones where all  $x_i$  are moving with the same frequency - so the motion is collective. In fact, without loss, all of them move in phase; this changes with damping, which is what we are interested in. Another way to think about it is a coordinate transformation from each mass being a single degree of freedom to all of the masses in a normal mode being a collective degree of freedom. In a matrix form, the equation of motion looks like the following:

$$\ddot{\vec{x}} = -M^{-1}K\vec{x} - \vec{C}\dot{\vec{x}} \quad (2.22)$$

$$\text{where } \vec{x} = \begin{pmatrix} x_1(t) \\ x_2(t) \\ x_n(t) \\ \dots \end{pmatrix}, M^{-1}K = \begin{pmatrix} \frac{2k}{M} & -\frac{k}{M} & 0 & \dots \\ -\frac{k}{M} & \frac{2k}{M} & -\frac{k}{M} & \dots \\ 0 & -\frac{k}{M} & \frac{2k}{M} & \dots \\ \dots & \dots & \dots & \dots \end{pmatrix} \text{ and } \vec{C} = \begin{pmatrix} \kappa & 0 & 0 & \dots \\ 0 & \kappa & 0 & \dots \\ 0 & 0 & \kappa & \dots \\ \dots & \dots & \dots & \dots \end{pmatrix}$$

Because of the translational symmetry, using our previous nomenclature:

$$\begin{aligned} \tilde{Y}_{i+i} &= \beta \tilde{Y}_i = e^{ika} \tilde{Y}_i \\ \tilde{Y}_{i+n} &= \beta^n \tilde{Y}_i = e^{inka} \tilde{Y}_i \end{aligned} \quad (2.23)$$

where  $a$  is the distance between the masses and  $k$  is a wave number. In frequency regime, we get:

$$\left[ -\omega^2 - i\vec{C}\omega + M^{-1}K \right] Y_i^k = 0 \quad (2.24)$$

since due to translational invariance, the  $\tilde{Y}$  is an eigenvector of both  $M^{-1}K$  and  $\vec{C}$ , we get an eigenvalue equation which corresponds to a dispersion relation or a relation between a frequency of the normal mode and its  $k$  wave number, which correspond to "wiggleness" in time and space, respectively:

$$\omega^2 = \omega_0^2(k) - i\kappa\omega \quad (2.25)$$

where  $\omega_0$  is frequency from from a dispersion relationship of an undamped infinite system of harmonic oscillators:

$$\begin{aligned} \omega_0^2 &= \frac{2k}{m} - \frac{k}{m}e^{ika} - \frac{k}{m}e^{-ika} \\ &= \frac{2k}{m}(1 - \cos(ka)) = 4\frac{k}{m}\sin^2\left(\frac{ka}{2}\right) \end{aligned} \quad (2.26)$$

so our final dispersion relation is:

$$\omega(k)^2 = 4\frac{k}{m}\sin^2\left(\frac{ka}{2}\right) - i\kappa\omega \quad (2.27)$$

Dispersion relation comes up everywhere when we treat extended many-body systems: material lattices, transmission lines, photonic crystals, etc. No system is truly infinite in real life, and we always apply boundary conditions, which give us the exact eigenvalues and eigenvectors. However, their dispersion relations only depend on the underlying infinite system.

### *2.3.1 Driving a HO with a chain of masses on springs*

Using the symmetry of the system, we found the normal modes of the infinite chain of HOs and the dispersion relation. Applying boundary conditions correspond to finding the right

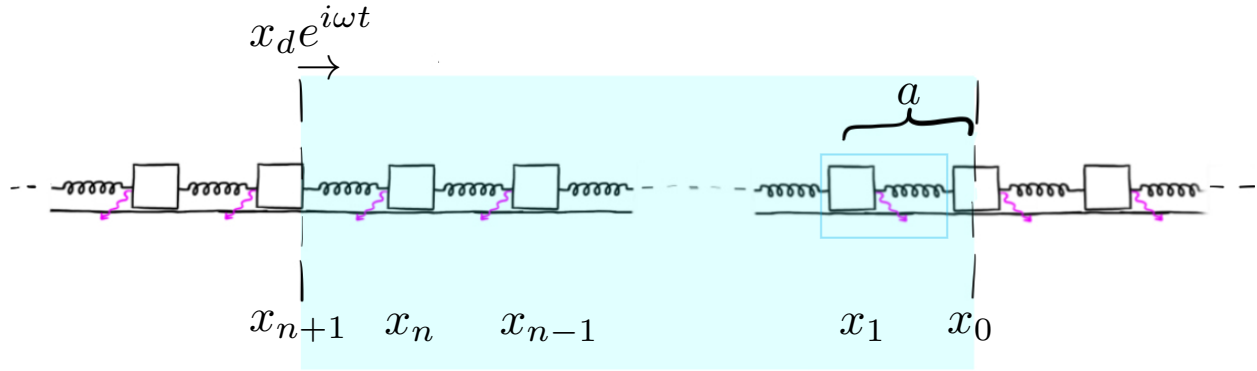


Figure 2.12: Applying boundary conditions to an infinite chain of masses on springs to derive physical systems.

linear combination of normal modes that satisfy these boundary conditions. Let's consider a system of  $N$  HOs where, as shown in Fig. 2.12: the 0th mass is a wall - so it doesn't move, the 1st mass is the one we considered at the beginning of this chapter, and  $(N+1)$ th mass oscillating as  $x_d e^{i\omega t}$ . Note that instead of driving a mass directly with force  $F_0 e^{i\omega t}$ , we are moving the end of the  $(N+1)$  spring, which exerts a force on the  $N$ th mass. We do this for symmetry purposes, and it won't change the physics significantly aside from changing the resonance frequency of our DUT - device under test, which is the 1st mass in our chain.

First, since we are driving our damped system at frequency  $\omega$ , we are looking for normal modes that in the steady state oscillate at  $\omega$ . Using Eq. 2.27, for mode frequency  $\omega$  the wave number  $k$  (a pair of them) is:

$$k = \frac{2}{a} \sin^{-1} \left( \pm \sqrt{\frac{\omega^2 + i\kappa\omega}{4k/m}} \right) \quad (2.28)$$

For  $x_0 = 0$  and  $x_{n+1} = \text{Re}[x_d e^{i\omega t}]$ , the following conditions have to hold:

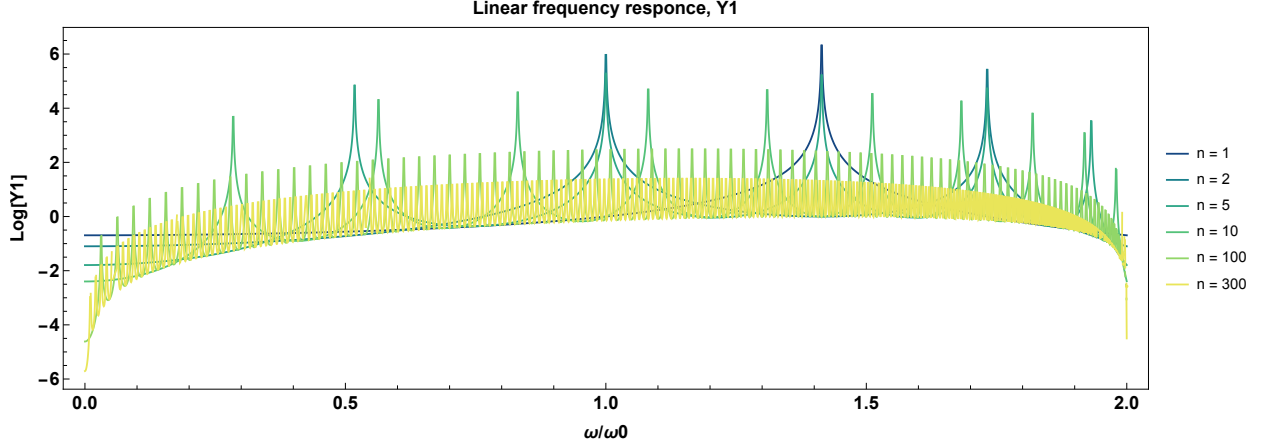


Figure 2.13: Log of the Linear response of the first HO as the Nth HO is driven with  $x_d e^{i\omega t}$ . Here the parameters used are  $\omega_0 = 1$  and  $\kappa = 0.0001$ .

$$\begin{aligned}
 x_1 - x_{-1} &= \tilde{Y}_1 - \tilde{Y}_{-1} = 0 \\
 \tilde{Y}_{n+2} - \tilde{Y}_n &= x_d e^{i\omega t}
 \end{aligned}
 \tag{2.29}$$

This gives a solution for overall system to be:

$$\tilde{Y}(x) = A e^{i\omega t} \frac{\sin(kx)}{\sin k(N+1)a}
 \tag{2.30}$$

where  $x = na$ . The linear response of the 1st HO is:

$$\tilde{Y}(a) = \tilde{Y}_1 = A e^{i\omega t} \frac{\sin(ka)}{\sin k(N+1)a}
 \tag{2.31}$$

Fig. 2.13 shows the frequency response of the 1st mass. The case with  $n=1$  corresponds to our original system considered in Fig. 2.2 with a shifted frequency due to an extra spring.

As the number  $N$  of HOs goes up, there are more and more resonances all the way to the continuum. At this point, our chain of masses becomes a transmission line that continuously transfers information at all frequencies between  $0$  <sup>2</sup> and coupling frequency,  $\omega_c = \sqrt{\frac{4k}{m}}$ . Also, note that the plot shows that with a larger  $N$  or longer chain, the amplitude of the oscillations of the 1st mass goes down - the longer transmission lines are lossier.

The parameters used in Fig. 2.13 correspond to a transmission line with a very low. In real life at very large  $N$ , it's impossible to resolve each separate peak, so the realistic *continuous* lossy transmission line transfers frequencies smoothly to the target in its band as shown in Fig.2.14.

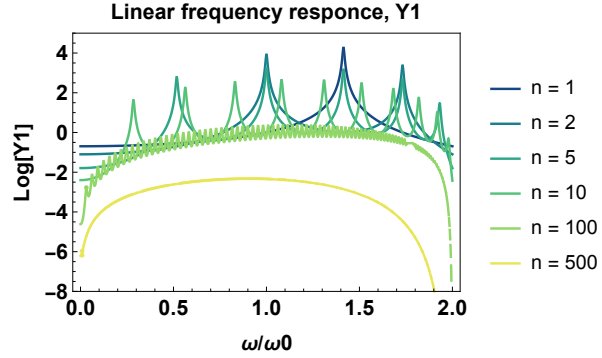


Figure 2.14: Lossy transmission line: here the parameters used are  $\omega_0 = 1$  and  $\kappa = 0.01$ .

The long chain of HO oscillators turns out to be a useful model to simulate a transmission line which transfers longitudinal mechanical waves. The solution in Eq. 2.30 is our first encounter with travelling waves as shown below:

$$\tilde{Y}(x) = Ae^{i\omega t} \frac{\sin(kx)}{\sin k(N+1)a} = \frac{A}{2i \sin k(N+1)a} \left( e^{i(kx+\omega t)} - e^{-i(kx+\omega t)} \right) \quad (2.32)$$

In the rest of the chapter, we will use the transmission line in two ways:

1. **As a mode of transferring power to the device.** Here, we need to be careful about coupling the high-Q devices to a lossy transmission line. As in the case of two

---

2. there is a spontaneously broken symmetry in our system, leading to a Goldstone boson - the 0 energy excitation of our system.

coupled harmonic oscillators in Fig. 2.7, the total quality factor of the device can be lowered by strongly coupling into the transmission line, in this case. So by engineering an *impedance mismatch* with the coupling, the power can be delivered to the DUT without increasing its  $Q$

2. **As a cavity** If instead of using lossy continuous lines to deliver excitation to the device, we are engineering high  $Q$  transmission lines, by carefully designing the boundary conditions, we can make high-quality devices that resonate at wavelengths smaller than their corresponding length scale.

With that note, I will conclude the purely "masses on the spring" part of this chapter and jump into the electromagnetic devices that we encounter in the lab most of the time. These mechanical derivations will come in handy not just as an analogy but also as a foundation for our understanding of resonance and wave phenomena.

## 2.4 RLC impedance analogy

I have briefly mentioned in the previous chapters the concept of impedance and how it relates to the linear response function. Even though it is ubiquitous in systems that can support and impede waves, shown in Fig. 2.11, the most common places where the concept of impedance pops up is Electromagnetism and Circuits. Conveniently, it's also the most common manifestation and language of HO that we work on in circuit and cavity-QED labs. Maybe, it would have been wiser to just derive everything from RLC circuits - but I just personally really like masses on spring. And, translating from one language to another will help us get a better intuition for the framework.

As shown in Fig. 2.15, our damped mass on a spring has three components: mass, spring, and a damper. Each of them has a different phase response for the same drive. The mass

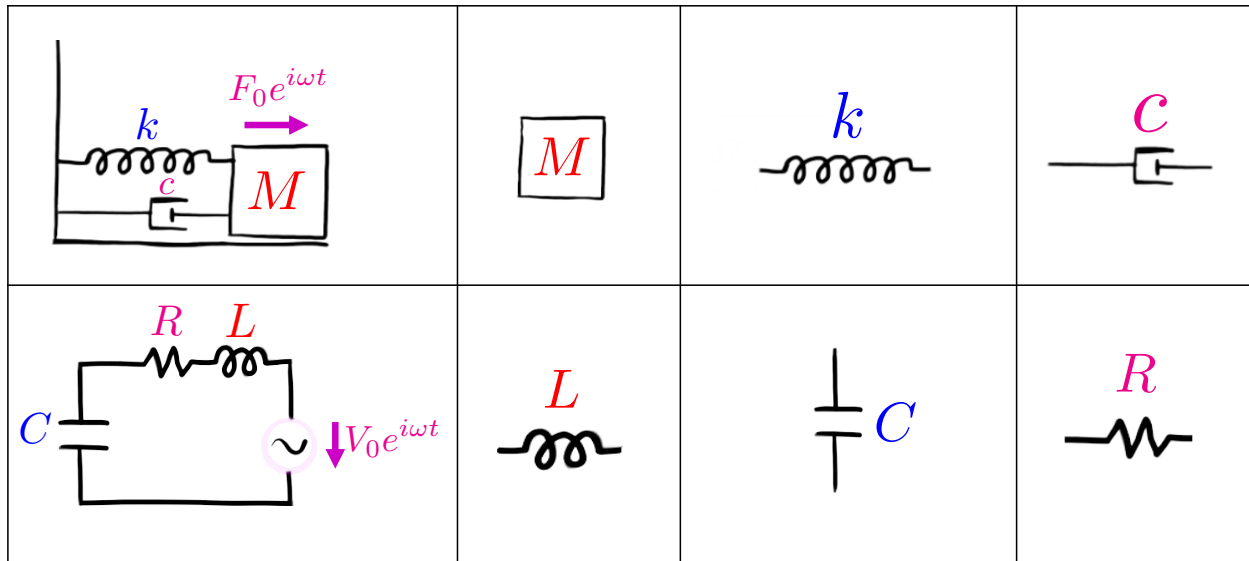


Figure 2.15: Analogy between components of the damped mass on a spring and a series RLC circuit

oscillations lead in phase with the drive, the spring lags in phase, and the damper oscillates in phase with the drive. So the net effect is not just an arithmetic sum of responses of each of the elements, but the vector sum - which results in fascinating phenomena of constructive and destructive interference. This is why when you apply a force that is constant in frequency and what, you end up with the response that varies in frequency.

Let's introduce lumped element circuit terminology - impedance,  $Z(\omega)$ , and admittance,  $Y(\omega)$ :

$$Z(\omega) = \frac{V(\omega)}{I(\omega)} = \frac{V(\omega)}{\dot{q}(\omega)}, \text{ and } Y(\omega) = \frac{I(\omega)}{V(\omega)} = \frac{\dot{q}(\omega)}{V(\omega)} = \frac{1}{Z(\omega)} \quad (2.33)$$

where I and V are current and voltage in a linear lumped circuit. Similarly, we can define impedance and admittance for a mass on a spring system:

$$Z(\omega) = \frac{F(\omega)}{\dot{x}(\omega)}, \text{ and } Y(\omega) = \frac{\dot{x}(\omega)}{F(\omega)} = \frac{1}{Z(\omega)} \quad (2.34)$$

Now, this impedance analogy is a hint that there is a way to build an RLC circuit that behaves like a damped mass on a spring. But what is the geometry? Well, if current,  $I$ , is constant, then it should be a series circuit, but if the voltage,  $V$ , is constant, it should be in parallel. In the case of Fig. 2.2, the constant was  $x$  or similarly  $\dot{x}$  - so it seems that the analogous circuit is a series RLC circuit shown in Fig. 2.15.

Let's confirm this hypothesis. In Fig. 2.2 we apply a periodic drive force, and solve for the ansatz  $x_0 e^{i\omega t}$ . Because of the geometry of the system, if the position of the mass is  $x_0 e^{i\omega t}$ , this position also corresponds to the stretching of the spring and the motion of the damper. But the forces are different in each component.

$$\begin{aligned} F_{mass} &= M\ddot{x} = -M\omega^2 x_0 e^{i\omega t} \\ F_{spring} &= kx = kx_0 e^{i\omega t} \\ F_{damper} &= c\dot{x} = ci\omega x_0 e^{i\omega t} \end{aligned} \quad (2.35)$$

which correspond to following impedances:

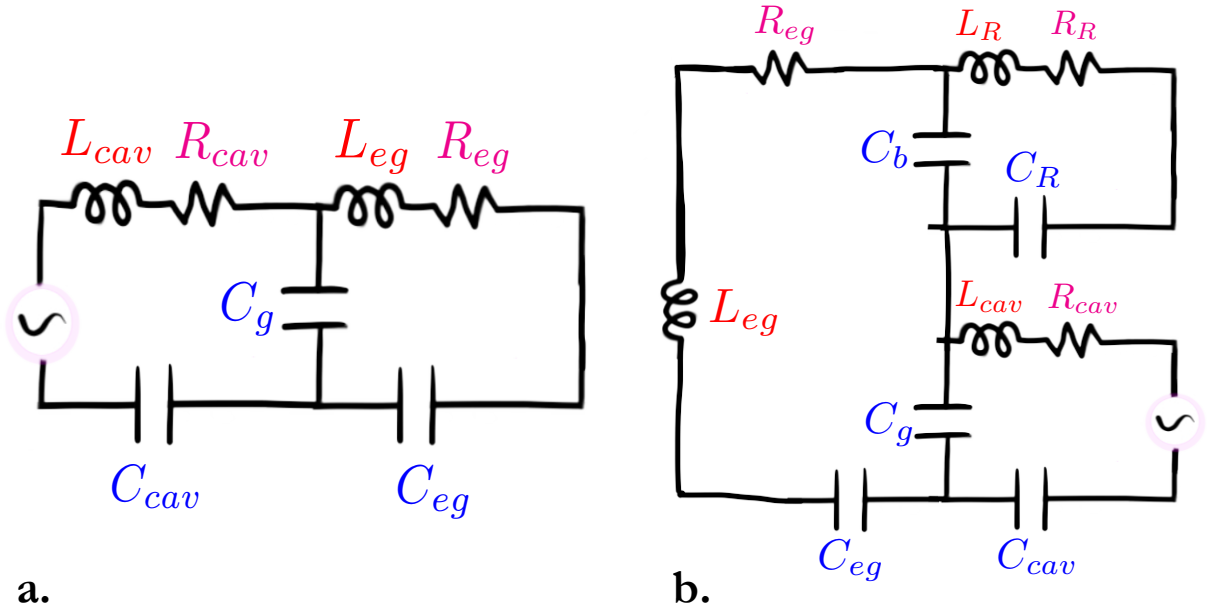


Figure 2.16: RLC circuits for: **a.** Vacuum Rabi splitting from Fig. 2.5b, **b.** Rydberg Cavity-EIT from Fig. 2.8

$$\begin{aligned}
 Z_{mass} &= \frac{F}{\dot{x}} = im\omega \\
 Z_{spring} &= \frac{k}{i\omega} \\
 Z_{damper} &= c
 \end{aligned}
 \tag{2.36}$$

As shown in Fig. 2.15, the mass, spring, and damper impedances have a direct correspondence to the impedances of an inductor, capacitor, and a resistor, respectively in the series RLC circuit.

This is great, since now we can make circuit HOs from Fig.2.15, the transmission line of RLC circuits from Fig.2.11 and even analogous circuits of coupled harmonic oscillators for Vacuum Rabi Splitting and Cavity EIT from Fig.2.16 [77, 73]

### 2.4.1 Linear response from the total impedance

To confirm the analogy, let's see if we can derive the Eq. 2.6 of a weakly damped HO from the total impedance. We can calculate the total impedance of the underdamped "circuit" of mass on a spring, which in this case is elements in series, since the  $x(t)$  (I for RLC) is the same for every element but  $F(t)$  (V for RLC) varies:

$$Z(\omega) = Z_{mass} + Z_{spring} + Z_{damp} = im\omega + \frac{k}{i\omega} + c \approx \frac{2\delta - i2\kappa(1 + \frac{\delta}{\omega_0})}{i\omega/m\omega_0^2}$$

$$Y(\omega) \approx \frac{i\omega/m\omega_0^2}{2\delta - i2\kappa(1 + \frac{\delta}{\omega_0})}$$
(2.37)

note that up to a constant  $m\omega_0$  of normalization in our equation  $Y(\omega) = i\omega\tilde{Y}(\omega)$ . Which makes sense, since we were evaluating  $\tilde{Y}(\omega) = \frac{F}{x}$  and not  $\frac{F}{\dot{x}}$ . This is a neat observation, but since we are considering underdamped systems, our answer further simplifies into:

$$Z(\omega) \approx 2\delta - i2\kappa(1 + \frac{\delta}{\omega_0})$$

$$Y(\omega) \approx \frac{1}{2\delta - i2\kappa(1 + \frac{\delta}{\omega_0})}$$
(2.38)

This also means that in a series RLC circuit:

$$\omega_0 = \sqrt{\frac{k}{M}} = \sqrt{\frac{1}{LC}}$$

$$\kappa = \frac{1}{2\pi} \frac{c}{\sqrt{Mk}} \omega_0 = \frac{1}{2\pi} \frac{R}{L}$$
(2.39)

### 2.4.2 Impedance analogy vs. mobility analogy: limits of analogies

Analogies in physics are great. They simplify calculations, help to understand unfamiliar subjects, and tie together many unrelated topics. But as all analogies do, our impedance analogy has a limit. Before you start applying the tools here to every linear system you encounter, note that the series RLC circuit was not the only one that we could have made in analogy to the HO configuration in Fig. 2.2.

The idea goes back to being careful with defining the effect of the drive and the response. For the the mass on a spring in Fig. 2.2 we defined that at a point object, the mass in this case,  $\sum Forces = 0$ , and we correlated it to  $\sum Voltage = 0$  in a circuit loop. And that's how we got the equivalence of a "parallel" mass on a spring system to the "series" RLC circuit. Here, the voltage sources were the force generators, and the potential current source was the velocity input.

The other approach is to correspond the  $\sum Forces = 0$  to a  $\sum Current = 0$  at a circuit node. Here, the voltage sources are velocity inputs, and the current sources are force generators. Leading to our equivalent circuit being a parallel RLC as shown in Fig. 2.17 with

$$Z(\omega) = \left( \frac{1}{R} + \frac{1}{i\omega L} + i\omega C \right)^{-1} \approx \frac{1}{1/R + 2iC\delta} \quad (2.40)$$

$$\begin{aligned} \omega_0 &= \sqrt{\frac{1}{LC}} \\ \kappa &= \frac{1}{2\pi} \frac{R}{C} \end{aligned} \quad (2.41)$$

The moral of the story is that to fully utilize analogy it's important to know their full

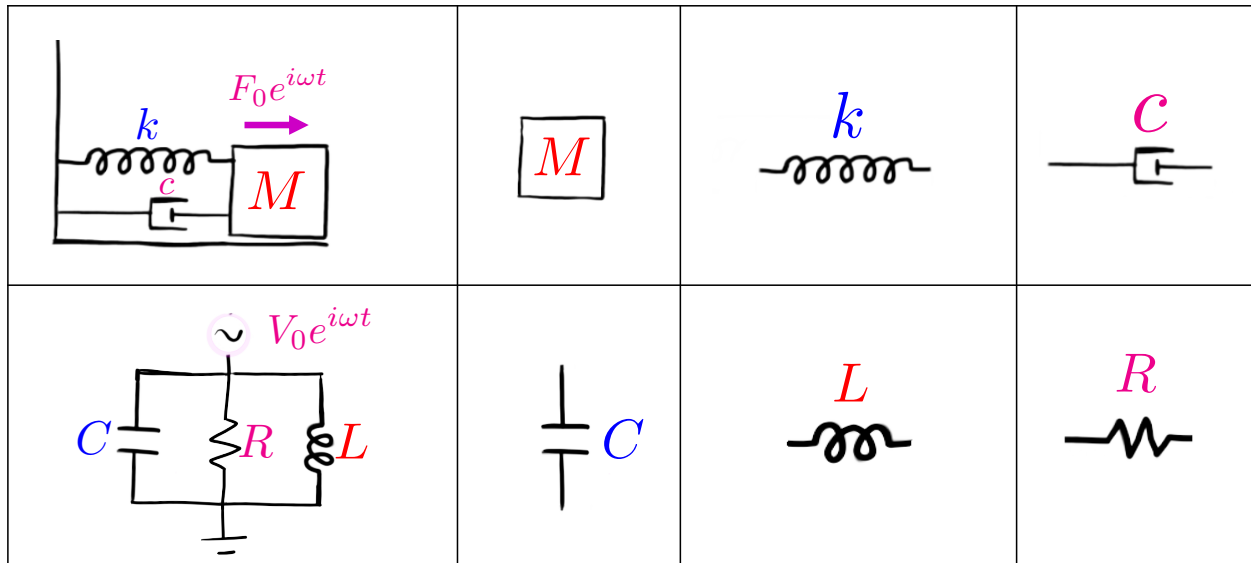


Figure 2.17: Analogy between components of the damped mass on a spring and a parallel RLC circuit using mobility analogy instead of impedance analogy

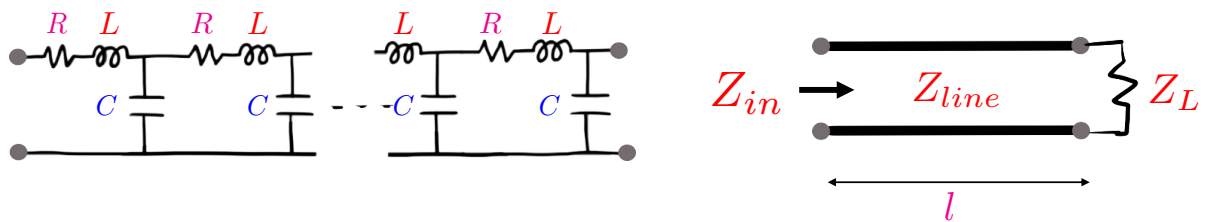


Figure 2.18: Series RLC transmission line with the length and characteristic impedance  $Z_{line}$ , terminated with a real load impedance  $R_L$

potential and limitations. For a single mass on a spring in Fig. 2.2 there is no difference between mobility and impedance analogies, but for a more complicated circuit, there will be. For example, when calculating the kinetic energy of the mass, we use the velocity with respect to the ground. Similarly, for the mobility analogy, it is convenient when the capacitor is attached to the ground. On the other hand, for the impedance analogy to work, it's convenient for only one current to be flowing through the indicator [78].

## 2.5 Transmission Line Resonator

Now that we have a better understanding of RLC circuits and masses on springs let's get back to the transmission lines in Fig. 2.11c. Similar to Eq. 2.27, the dispersion relation of a chain of L,C,R components is:

$$\omega(k)^2 = 4 \frac{1}{LC} \sin^2 \left( \frac{ka}{2} \right) - i \frac{R}{L} \omega \quad (2.42)$$

or in a continuous limit:

$$\begin{aligned} \omega(k)^2 &= 4 \frac{l^2}{LC} k^2 - i \frac{R}{L} \omega \\ k &= \pm \sqrt{\frac{LC}{l^2} (\omega^2 + i \frac{R}{L} \omega)} = k_r + ik_i \end{aligned} \quad (2.43)$$

where now the L, C, R are the total inductance, capacitance, and resistance of the transmission line with the length  $l$ . For the sake of being able to translate the jargon, I should note that  $k$ ,  $k_i$ ,  $k_r$  in the language of the wavenumber framework are identical to  $\gamma$ ,  $\alpha$  and  $\beta$ , respectively, in the language of transmission lines in Pozar [79].

Following Pozar [79] and [19], the impedance of a transmission line of a series RLC circuits terminated with an arbitrary load is:

$$Z_{in} = \frac{R_L + iZ_{line} \tanh kl}{Z_{line} + iR_L \tanh kl} \quad (2.44)$$

where  $R_L$  is the impedance of the load and  $Z_{line}$  is the characteristic impedance of the transmission line with a length  $l$ . Note that I assume there is no dielectric loss in the transmission line, although it can easily be included through a resistive impedance parallel to the capacitor.

In our 2D nonlinear millimeter wave resonators, we used the  $\lambda/4$  design, where the load impedance is a short. So for our device the input impedance was:

$$Z_{in} = Z_{line} \tanh kl = Z_{line} \frac{\tanh k_r l + i \tan k_i l}{1 + i \tanh k_r l \tan k_i l} \quad (2.45)$$

Since it is a  $\lambda/4$  design, our  $l = \frac{\lambda}{4}(n + 1)$ , and for the low loss superconducting circuit we can assume  $R$  is small and  $\tan k_i l \approx k_i l$ . As always we want to figure out the linear response function close to the resonance, so for  $\omega = \omega_0 + \Delta\omega$ , the  $k_r = \frac{\pi}{2}(n + 1)(1 + \frac{\delta}{\omega_0})$ . Finally, our  $\lambda/4$  resonator has an impedance of:

$$Z_{in} = \frac{1}{1/R + 2i\delta C} \quad (2.46)$$

where  $R = \frac{Z_{line}}{k_i l}$ ,  $C = \frac{\pi(n+1)}{4\omega_0 Z_{line}}$  and  $L = \frac{1}{\omega_0^2 C}$ . Incidentally, it looks exactly like the impedance of the parallel RLC circuit from before, while allowing oscillations with small wavelengths, unlike the physical lumped element circuit.

### 2.5.1 Coupling to a $\lambda/4$ resonator

In the previous section on coupling Quality factor in Fig. 2.7, we saw that one needs to be careful when sending power to the resonator to characterize it. The reason is that to measure the device, we have to couple to it, which inevitably changes the performance of the device both in frequency and in line width. So the best we can do is to minimize the effect and to be able to include it in our analysis.

To couple power to the  $\lambda/4$  resonator, we have to build a device that uses our chain of RLC circuits in two forms: a resonator and a transmission line. We can't attach them back to back directly because then all of the power would leak out immediately. So we need to create a "mirror" that would leak some light in, but not all of it. In RLC circuits, we can do it using a capacitor, which acts to change an impedance at the boundary between the device and the transmission line as shown in Fig. 2.19.

If we consider this circuit using lumped element circuit analogy, we can see that the input impedance  $Z_{in}$  will now include a capacitor,  $C_{in}$ , that will shift down the frequency of the modes and an effective parallel resistor  $\omega^2 C_{in}^2 Z_0$  which will affect the total quality factor.

But we can also look at this circuit from the point of transmitted and reflected waves at the impedance mismatch boundary, as shown in Fig. 2.19. Here, the  $\Gamma$  is the reflection coefficient and  $T$  is the transmission coefficient. For this systems:

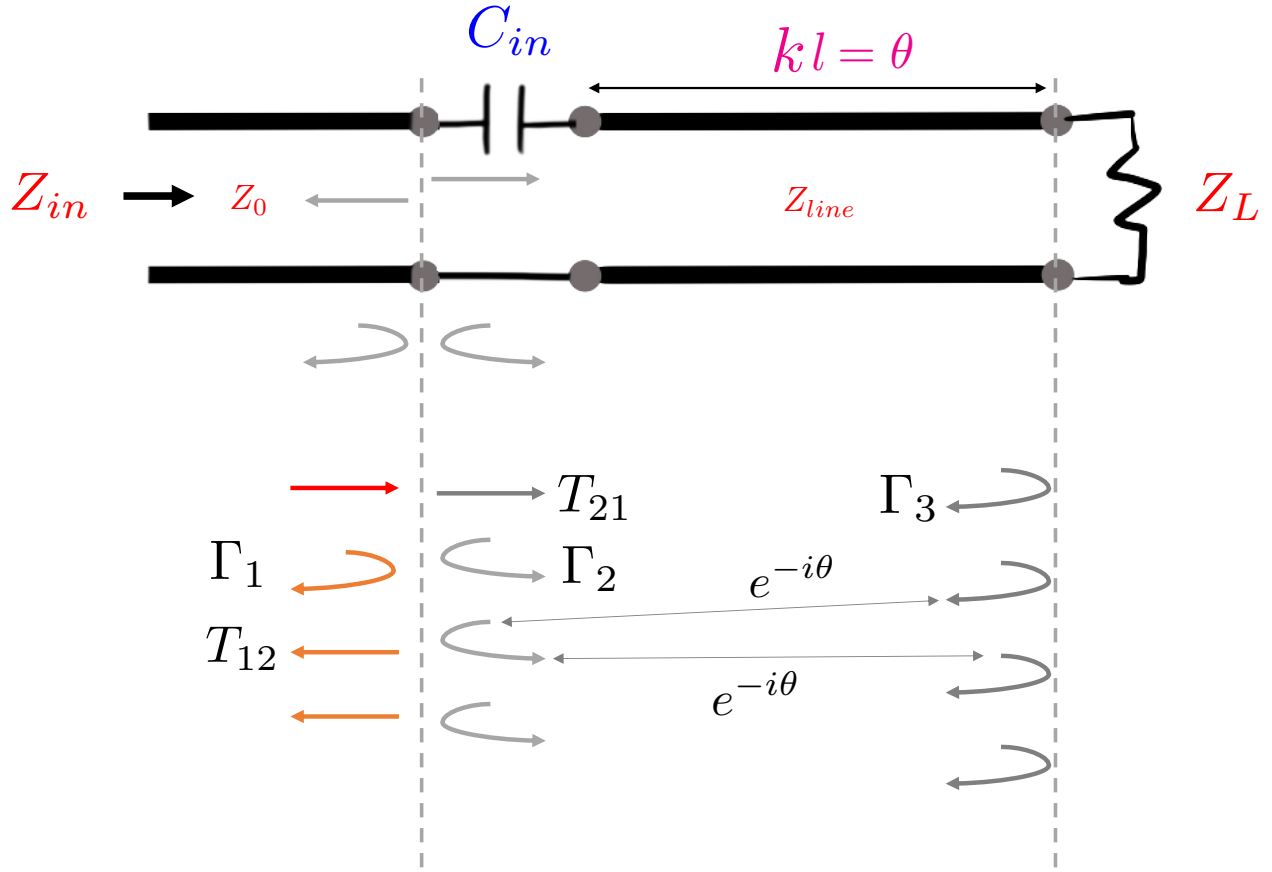


Figure 2.19: Capacitive coupling to the transmission line resonator, each time a wave encounters an impedance mismatch some of it gets reflected and some if it gets transmitted.

$$\begin{aligned}
 \Gamma_1 &= \frac{Z_2 - Z_1}{Z_2 + Z_1} = \frac{\frac{1}{i\omega C_{in}} + Z_{\lambda/4} - Z_0}{\frac{1}{i\omega C_{in}} + Z_{\lambda/4} + Z_0}. \\
 \Gamma_2 &= -\Gamma_1 \\
 \Gamma_3 &= \frac{Z_L - Z_2}{Z_L + Z_2} = -1 \\
 T_{12} &= 1 + \Gamma_1 \\
 T_{21} &= 1 + \Gamma_2
 \end{aligned} \tag{2.47}$$

where  $Z_{\lambda/4}$  is the  $Z_{in}$  for a  $\lambda/4$  resonator,  $Z_0$  is the impedance of the transmission line

feeding in the signal, and  $C_{in}$  is the coupling capacitor.

The total reflection coefficient,  $\Gamma_{tot}$ , in this case is just the some of all of the waves that make it out of our device past the coupling capacitor:

$$\begin{aligned}
 \Gamma_{tot} &= \Gamma_1 + T_{12}T_{21}\Gamma_3e^{-2j\theta} + T_{12}T_{21}\Gamma_3^2\Gamma_2e^{-4j\theta} + .. \\
 &= \Gamma_1 + T_{12}T_{21}\Gamma_3e^{-2j\theta} \sum_{n=0}^{\infty} \Gamma_3^n\Gamma_2^n e^{-2jn\theta} \\
 &= \frac{\Gamma_1 - e^{-2i\theta}}{1 - \Gamma_1e^{-2i\theta}}
 \end{aligned} \tag{2.48}$$

This is neat because now we can treat the transmission line circuit in two different waves. In fact, the impedance mismatch perspective leads quite nicely into my favorite cavity in the optical spectrum - the Fabry Perot cavity.

## 2.6 Fabry Perot cavity: another transmission line resonator

In the optical regime, our ideal reflective boundaries tend to be a thin stack of dielectric mirrors. It is currently the best material to reflect light for affordable and usable devices. So to make a high-quality resonator, we will make our optical transmission line cavity out of two spaced flat reflective mirrors. Note that in this section, we will ignore the radial modes and the effects produced by the mirrors' curvature.

The idea of this section is to use optical elements to derive three types of measurements we usually perform:

- The single port reflection,  $S_{11}$

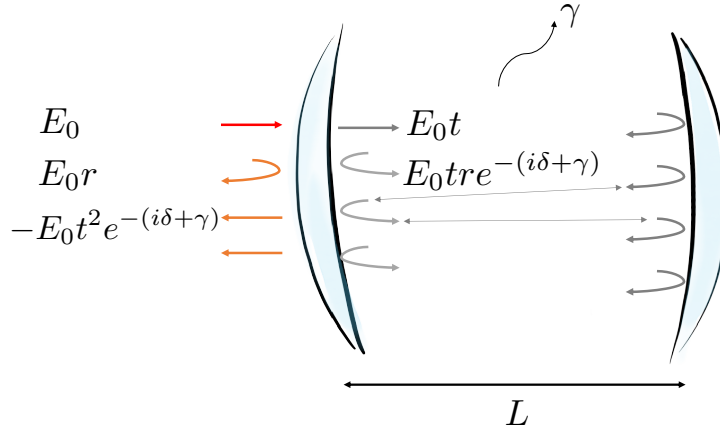


Figure 2.20: Reflection measurement of a FP cavity with the length  $L$  and internal loss per roundtrip  $\gamma$

- Two port transmission,  $S_{21}$
- Two port hanger measurement,  $S_{21}^*$

These are the most performed measurements used in all frequency regimes, and the formulas can be used in any systems involving measuring a resonance.

### 2.6.1 Single-port measurement of a cavity, $S_{11}$ .

#### Setup

The overall setup is shown in Fig 2.20. To imitate a single-port measurement, we will send input electric field  $E_0$  into a FB cavity of length  $L$  with one transmissive mirror at the input with reflection and transmission coefficients  $r$  and  $t$ , respectively, and one perfect mirror at the back. It is important to note that reflection and transmission coefficients from the back and front of the mirror are related by Stokes relations

$$r = -r' \quad (2.49)$$

$$r^2 + tt' = 1 \quad (2.50)$$

which is a result of a time reversal symmetry [80]. The  $r$  and  $t$  coefficients are going to determine the coupling quality factor  $Q_{coupl}$  of our resonator, similar to the previous capacitive coupling in the microwave regime. The internal quality factor  $Q_{int}$  will be determined by a loss coefficient  $\gamma$ , where the electric field and energy reduces per round trip by  $e^{-\gamma}$  and  $e^{-2\gamma}$  respectively. The  $\gamma$  represents any loss that we cannot measure. In the optical regime, it could include diffraction and absorption by mirrors; in the microwave regime, it could include surface resistance (absorption) or loss in seams.

## Calculation

As shown in in Fig 2.20., we trace the electric field as it gets reflected, transmitted, attenuated and acquires a phase proportional to the traveled distance. The reflected field is an infinite sum

$$\begin{aligned} E_{refl} &= E_0 r - E_0 t^2 e^{i\delta - \gamma} - E_0 r t^2 e^{i2\delta - 2\gamma} - E_0 r^2 t^2 e^{i3\delta - 3\gamma} + \dots \\ &= E_0 \left( r - t^2 e^{i\delta - \gamma} \sum_0^{\infty} r e^{i\delta - \gamma} \right) = \\ &= E_0 \left( r - \frac{t^2 e^{i\delta - \gamma}}{1 - r e^{i\delta - \gamma}} \right) \end{aligned} \quad (2.51)$$

Next, we make a couple of approximations. Since  $\gamma \ll 1$  and we are only interested in the behavior around resonance  $f_0$ , we can expand the exponent

$$\delta = -\frac{2\pi 2Lf}{c} = -\frac{2\pi n\lambda_0 f}{c} = -\frac{2\pi n f}{f_0} = -\frac{2\pi n(f_0 + df)}{f_0} \quad (2.52)$$

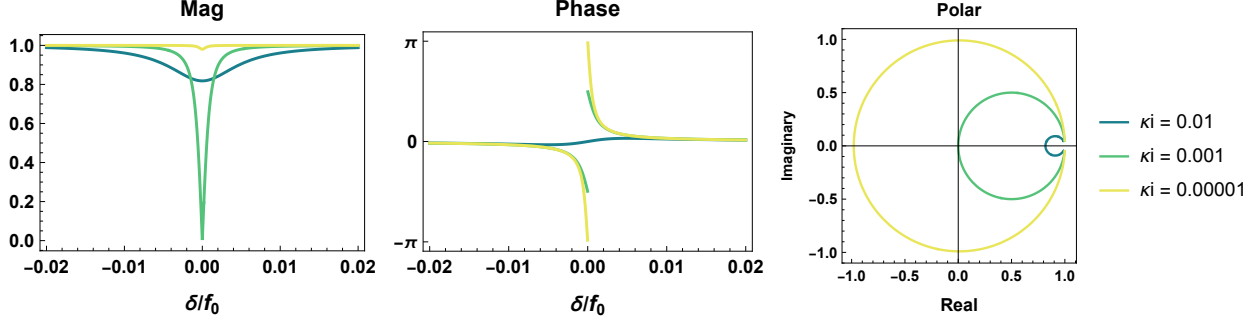


Figure 2.21: Reflection signal for a Fabry Perot with  $\kappa_{coupl} = 0.001$ : undercoupled, critical coupled and over coupled regimes, respectively.

$$e^{-i\delta+\gamma} = e^{i\frac{2\pi n d f}{f_0}} e^{\gamma} \approx 1 + \gamma + i2\pi n \frac{d f}{f_0} \quad (2.53)$$

We will use  $n = 1$  throughout for the convenience. And using  $r = \sqrt{1-t^2} \approx 1 - \frac{t^2}{2}$ , we can write out the frequency dependent expression for the reflected field.

$$\begin{aligned} E_{refl} &= E_0 \left( r - \frac{t^2}{e^{-i\delta+\gamma} - r} \right) = E_0 \left( 1 - \frac{t^2}{2} - \frac{t^2}{e^{-i\delta+\gamma} - 1 + \frac{t^2}{2}} \right) \\ &= E_0 \left( 1 - \frac{t^2}{2} - \frac{t^2}{1 + \gamma + i2\pi \frac{d f}{f_0} - 1 + \frac{t^2}{2}} \right) = E_0 \left( 1 - \frac{t^2}{2} - \frac{t^2}{\gamma + i2\pi \frac{d f}{f_0} + \frac{t^2}{2}} \right) \\ &= E_0 \left( 1 - \frac{t^2 \gamma f_0 + i2\pi d f t^2 + t^4 f_0 / 2 + 2t^2 f_0}{2\gamma f_0 + i4\pi d f + t^2 f_0} \right) \approx E_0 \left( 1 - \frac{2t^2 f_0}{2\gamma f_0 + i4\pi d f + t^2 f_0} \right) \end{aligned} \quad (2.54)$$

Note: we neglect  $-\frac{t^2}{2}$  term since it is small.

Finally, we derive expressions for Quality factors. We can do it in two ways.

1. We know that  $Q = \frac{2\pi \text{Energy Stored}}{\text{Energy dissipated per cycle}}$ . Lets call Energy Stored  $E_{tot}$ , then the energy after one cycle is  $E_{tot} e^{-2\gamma} \approx E_{tot} (1 - 2\gamma)$  and resulting energy loss is  $2\gamma E_{tot}$ .

Using this the internal quality factor and linewidths are

$$Q_{int} = \frac{2\pi E_{tot}}{E_{tot}2\gamma} = \frac{\pi}{\gamma} \quad \kappa_{int} = \frac{f_0}{Q_{int}} = \frac{f_0\gamma}{\pi} \quad (2.55)$$

similarly, coupling loss per cycle is  $E_{tot}t^2$  and total loss is  $E_{tot}(t^2 + 2\gamma)$  giving us following expressions

$$\begin{aligned} Q_{coupl} &= \frac{2\pi E_{tot}}{E_{tot}t^2} = \frac{2\pi}{t^2} & \kappa_{coupl} &= \frac{f_0t^2}{2\pi} \\ Q_{tot} &= \frac{2\pi}{2\gamma + t^2} & \kappa_{tot} &= \frac{f_0(2\gamma + t^2)}{2\pi} \end{aligned} \quad (2.56)$$

2. We can also calculate the exponential decay times of the field intensity (or equivalently energy) inside of the cavity [81]. After  $m = \frac{ct}{2L}$  roundtrips, the intensity inside FB is

$$I = I_0(r^2e^{-2\gamma})^m = I_0e^{-\frac{t}{t_{tot}}} = I_0e^{-2\pi t\kappa_{tot}} \quad (2.57)$$

$$\begin{aligned} \kappa_{tot} &= -\frac{c}{2L2\pi} \ln(r^2e^{-2\gamma}) = -\frac{c}{2L2\pi} (\ln r - 2\gamma) = -\frac{c}{2L2\pi} (\ln(1 - \frac{t^2}{2}) - 2\gamma) \\ &= -\frac{c}{2L2\pi} (-\frac{t^2}{2} - 2\gamma) = \frac{c}{2L2\pi} (\frac{t^2}{2} + 2\gamma) = \frac{f_0}{2\pi} (\frac{t^2}{2} + 2\gamma) \end{aligned} \quad (2.58)$$

Note:  $\frac{c}{2L}$  is a free spectral range in optics, which is the separation in frequency between successive resonant features. We can think about it as the inverse of the roundtrip time of a photon in the cavity. We cannot think about it in this way in the microwave regime since the path that photon takes is not as ray-like when the length of the cavity is comparable with the wavelength of the resonance.

Result

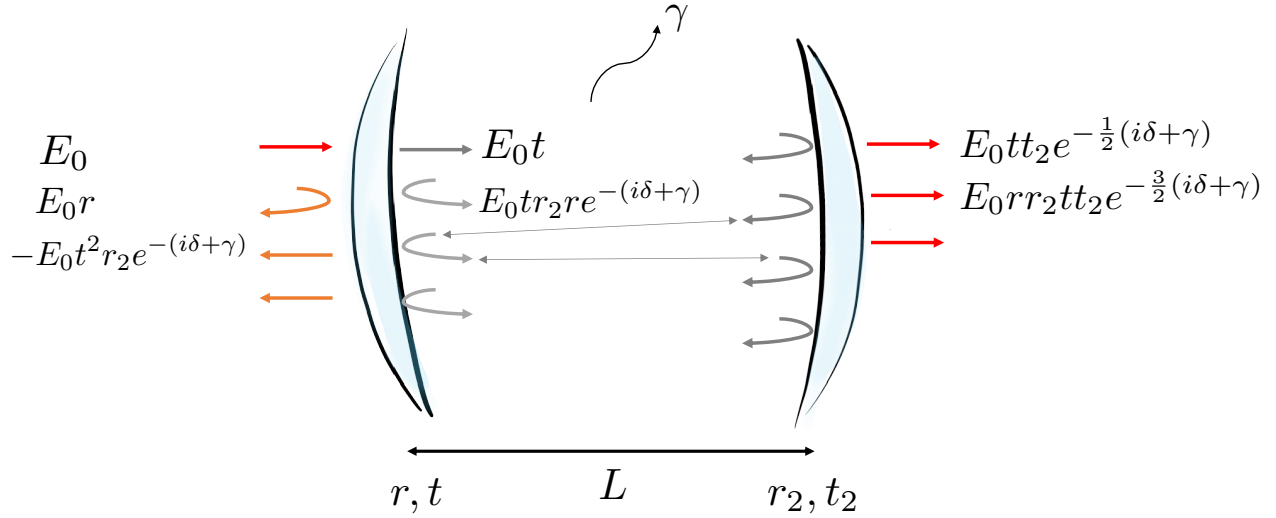


Figure 2.22: Transmission measurement of a FP cavity with the length  $L$  and internal loss per roundtrip  $\gamma$

Finally, we get

$$\begin{aligned}
 E_{refl} &= E_0 \left( 1 - \frac{2t^2 f_0}{2\gamma f_0 + i4\pi df + t^2 f_0} \right) = E_0 \left( 1 - \frac{2\kappa_{coupl}}{\kappa_{int} + i2df + \kappa_{coupl}} \right) \\
 &= E_0 \left( 1 - \frac{2Q_{int}}{Q_{coupl} + i2\frac{df}{f_0} Q_{coupl} Q_{int} + Q_{int}} \right)
 \end{aligned} \tag{2.59}$$

Using these expressions, it is helpful to take a look at typical spectra of the measurement for under-coupled, critically coupled and over-coupled regimes shown in Fig. 2.21.

### 2.6.2 Two-port measurement of a cavity: $S_{21}$ and $S_{11}$ .

#### Setup

The more general setup for the two-port measurement includes a second imperfect mirror with the reflectivity  $r_2$  and transmissivity  $t_2$ , as shown in Fig 2.22. Here, I flipped the sign of  $\delta$  for convenience. Using logic from previous section, this system has following parameters:

$$\begin{aligned}
Q_{int} &= \frac{\pi}{\gamma} & \kappa_{int} &= \frac{f_0}{Q_{int}} = \frac{f_0\gamma}{\pi} \\
Q_{cin} &= \frac{2\pi}{t^2} & \kappa_{cin} &= \frac{f_0 t^2}{2\pi} \\
Q_{cout} &= \frac{2\pi}{t_2^2} & \kappa_{cout} &= \frac{f_0 t_2^2}{2\pi} \\
Q_{tot} &= \frac{2\pi}{2\gamma + t^2 + t_2^2} & \kappa_{tot} &= \frac{f_0(2\gamma + t^2 + t_2^2)}{2\pi}
\end{aligned} \tag{2.60}$$

### 2.6.3 Calculation

$$\begin{aligned}
E_{refl} &= E_0 \left( r - \frac{t^2 r_2}{e^{i\delta + \gamma} - r r_2} \right) = E_0 \left( 1 - \frac{t^2}{2} - \frac{t^2(1 - \frac{t_2^2}{2})}{1 + \gamma + i2\pi \frac{df}{f_0} - (1 - \frac{t^2}{2})(1 - \frac{t_2^2}{2})} \right) \\
&\approx E_0 \left( 1 - \frac{2t^2 f_0}{2\gamma f_0 + i4\pi df + t^2 f_0 + t_2^2 f_0} \right) \\
&= E_0 \left( 1 - \frac{2\kappa_{cin}}{\kappa_{int} + i2df + \kappa_{cin} + \kappa_{cout}} \right) = E_0 \left( 1 - \frac{2\kappa_{cin}}{\kappa_{tot} + i2df} \right) \\
&= E_0 \left( 1 - \frac{2Q_{int}Q_{cout}}{Q_{cin}Q_{cout} + i2\frac{df}{f_0}Q_{cin}Q_{cout}Q_{int} + Q_{cin}Q_{int} + Q_{cout}Q_{int}} \right) \\
&= E_0 \left( 1 - \frac{2Q_{tot}}{Q_{cin} + i2\frac{df}{f_0}Q_{cin}Q_{tot}} \right)
\end{aligned} \tag{2.61}$$

Note: As a check, when the second mirror is perfect  $t_2 = 0$  and  $\kappa_{cout} = 0$ , which reduces Eq 2.63 to Eq 2.59 for single-port measurement. And, for identical mirrors or  $\kappa_{cin} = \kappa_{cout} = \kappa_{coupl}$

$$E_{refl} = E_0 \left( 1 - \frac{2\kappa_{coupl}}{\kappa_{int} + i2df + 2\kappa_{coupl}} \right) = E_0 \left( 1 - \frac{2Q_{int}}{Q_{coupl} + i2\frac{df}{f_0}Q_{coupl}Q_{int} + 2Q_{int}} \right) \tag{2.62}$$

Now we derive the S21 expression for this setup

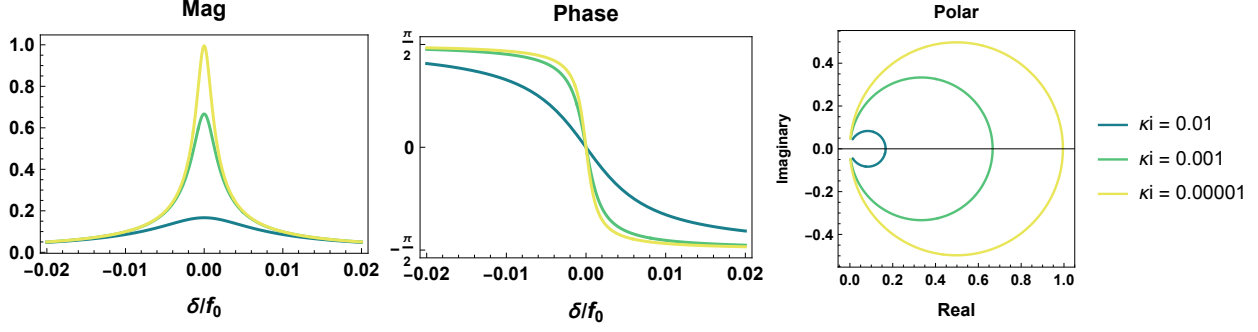


Figure 2.23: Transmission signal for a Fabry Perot with  $\kappa_{coupl} = 0.001$ : undercoupled, critical coupled and over coupled regimes, respectively.

$$\begin{aligned}
E_{transm} &= E_0 \frac{tt_2 e^{-\frac{1}{2}(i\delta+\gamma)}}{1 - rr_2 e^{-(i\delta+\gamma)}} = E_0 \frac{tt_2(1 - i\pi\frac{df}{f_0} - \frac{\gamma}{2})}{1 - (1 - \frac{t_2^2}{2})(1 - \frac{t_2^2}{2})(1 - i2\pi\frac{df}{f_0} - \gamma)} \\
&\approx E_0 \frac{2f_0 tt_2}{t^2 f_0 + t_2^2 f_0 + i4\pi df + 2\gamma f_0} \\
&= E_0 \frac{2\sqrt{\kappa_{cin}\kappa_{cout}}}{\kappa_{int} + i2df + \kappa_{cin} + \kappa_{cout}} = E_0 \left( \frac{2\sqrt{\kappa_{cin}\kappa_{cout}}}{\kappa_{tot} + i2df} \right) \\
&= E_0 \left( \frac{2Q_{int}\sqrt{Q_{cout}Q_{cin}}}{Q_{cin}Q_{cout} + i2\frac{df}{f_0}Q_{cin}Q_{cout}Q_{int} + Q_{cin}Q_{int} + Q_{cout}Q_{int}} \right)
\end{aligned} \tag{2.63}$$

Similar to reflection, for identical mirrors

$$E_{transm} = E_0 \left( \frac{2\kappa_{coupl}}{\kappa_{int} + i2df + 2\kappa_{coupl}} \right) = E_0 \left( \frac{2Q_{int}}{Q_{coupl} + i2\frac{df}{f_0}Q_{coupl}Q_{int} + 2Q_{int}} \right) \tag{2.64}$$

Note: In order to get  $Q_{int}$  from only transmission measurement, the background need to be calibrated/known.

Here are some typical spectra of the transmission measurement for undercoupled, critically coupled, and overcoupled regimes.

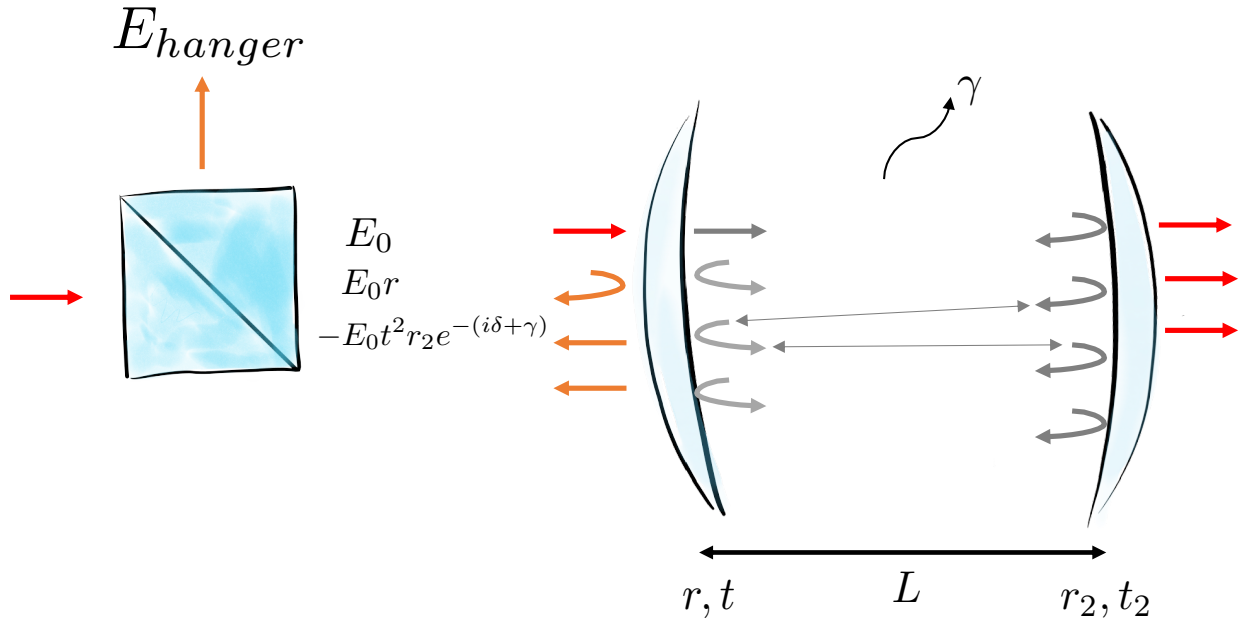


Figure 2.24: Hanger measurement of a FP cavity with the length  $L$  and internal loss per roundtrip  $\gamma$

#### 2.6.4 A Hanger measurement

In order to derive the expression for two-port Hanger measurement, we need to add a beam splitter to the setup as shown in Fig 2.24.

#### Beamsplitter relations

For a 50/50 beam splitter, the input and output port fields are related by the following expressions

$$\begin{bmatrix} E_1 \\ E_2 \end{bmatrix} = \frac{1}{\sqrt{2}} \begin{bmatrix} 1 & -i \\ -i & 1 \end{bmatrix} \begin{bmatrix} E_3 \\ E_4 \end{bmatrix}$$

$$\begin{bmatrix} E_3 \\ E_4 \end{bmatrix} = \frac{1}{\sqrt{2}} \begin{bmatrix} 1 & i \\ i & 1 \end{bmatrix} \begin{bmatrix} E_1 \\ E_2 \end{bmatrix}$$

which can be derived from energy conservation principles.

We use these relations to trace the electric field as it enters and leaves the beams splitter.

$$\begin{aligned} \begin{bmatrix} E_{3out} \\ E_{4out} \end{bmatrix} &= \frac{1}{\sqrt{2}} \begin{bmatrix} 1 & i \\ i & 1 \end{bmatrix} \begin{bmatrix} E_0 \\ 0 \end{bmatrix} = \frac{E_0}{\sqrt{2}} \begin{bmatrix} 1 \\ i \end{bmatrix} \\ E_{3in} \rightarrow -E_{3in} &= -\frac{E_0}{\sqrt{2}} \\ E_{4in} \rightarrow \frac{i}{\sqrt{2}} E_{refl} &= \frac{i}{\sqrt{2}} E_0 \left( 1 - \frac{2\kappa_{coupl}}{\kappa_{int} + i2df + \kappa_{coupl}} \right) \end{aligned} \quad (2.65)$$

$$\begin{bmatrix} E_{1out} \\ E_{2out} \end{bmatrix} = \begin{bmatrix} E_{1out} \\ E_{Hanger} \end{bmatrix} = \frac{1}{\sqrt{2}} \begin{bmatrix} 1 & -i \\ -i & 1 \end{bmatrix} \begin{bmatrix} E_{3in} \\ E_{4in} \end{bmatrix} = \frac{E_0}{2} \begin{bmatrix} -1 + \left( 1 - \frac{2\kappa_{coupl}}{\kappa_{int} + i2df + \kappa_{coupl}} \right) \\ i + i \left( 1 - \frac{2\kappa_{coupl}}{\kappa_{int} + i2df + \kappa_{coupl}} \right) \end{bmatrix}$$

Therefore the S21 Hanger measurement expression is

$$\begin{aligned} E_{Hanger} &= E_0 i \left( 1 - \frac{\kappa_{coupl}}{\kappa_{int} + i2df + \kappa_{coupl}} \right) \\ &= E_0 i \left( 1 - \frac{Q_{int}}{Q_{coupl} + i2\frac{df}{f_0} Q_{coupl} Q_{int} + Q_{int}} \right) \end{aligned} \quad (2.66)$$

Here are some typical spectra of the hanger measurement for undercoupled, critically coupled, and overcoupled regimes.

Even though the only difference between reflection and hanger formulas is a factor of 2, the qualitative differences are very significant for a measurement. The size of the dip for the

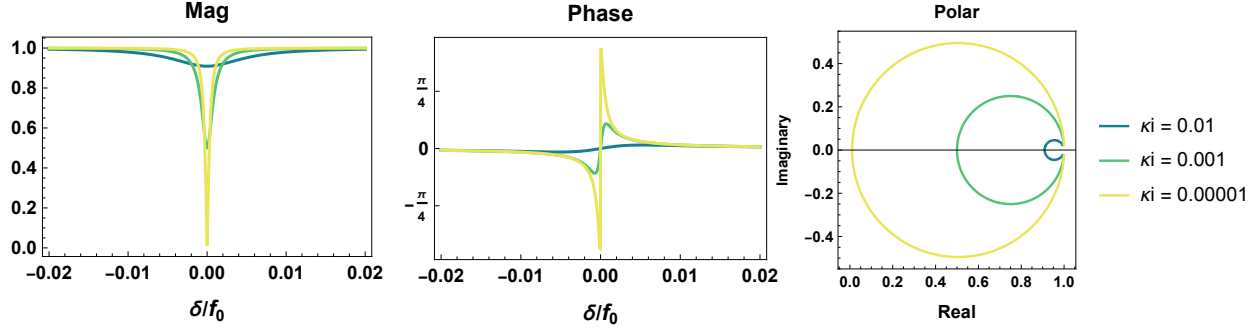


Figure 2.25: Hanger transmission signal for a Fabry Perot with  $\kappa_{coupl} = 0.001$ : undercoupled, critical coupled and over coupled regimes, respectively.

reflection measurement is maximized for critical coupling,  $\kappa_{int} = \kappa_{coupl}$ , while for the hanger, the dip is half-max at critical coupling and keeps increasing as  $\kappa_{int}$  decreases. Moreover, the phase difference past critical coupling for the reflection measurement is  $2\pi$ , whereas for the hanger measurement, the phase tends to  $\pi$  as  $\kappa_{int}$  decreases past  $\kappa_{coupl}$ .

## 2.7 Conclusion

This chapter offered an overview of some of the resonant phenomena common in a quantum lab. I find thinking in different "languages" about harmonic oscillators helpful for a deeper understanding of coherence, which helps design and build more complex systems for cavity and circuit-QED experiments. Conceptually, understanding the classical phenomena originating from purely linear wave physics allows us to identify the purely quantum phenomena that could not be replicated in classical systems. In the following chapter, we will use the concepts discussed here for treating emergent nonlinear quantum phenomena in hybrid systems.

## CHAPTER 3

### HYBRID CAVITY QED

In Chapter. 2 we covered the wave phenomena of classical electromagnetism such as resonance, coherence, and interference used in quantum technology. Now, we are ready to make the “wave-to-particle transition” and start treating photons as particles in order to build strongly-interacting photonic systems using cavity- and circuit-QED formalism. There are three main building blocks of CQED systems we use to build tailored photonic Hamiltonians:

**Photons:** At the heart of every CQED system, there is a bosonic mode,  $\hat{a}, \hat{a}^\dagger$ , trapped inside of a resonator<sup>1</sup>. Our work concentrates on photons or electromagnetic excitations in optical Fabry-Perot and superconducting mm-wave cavities. CQED tools extend beyond photonics. Optomechanical systems use mechanical resonators with very high-quality factors to trap phonons for hybrid quantum experiments [82]. The size, shape, and dimensionality of

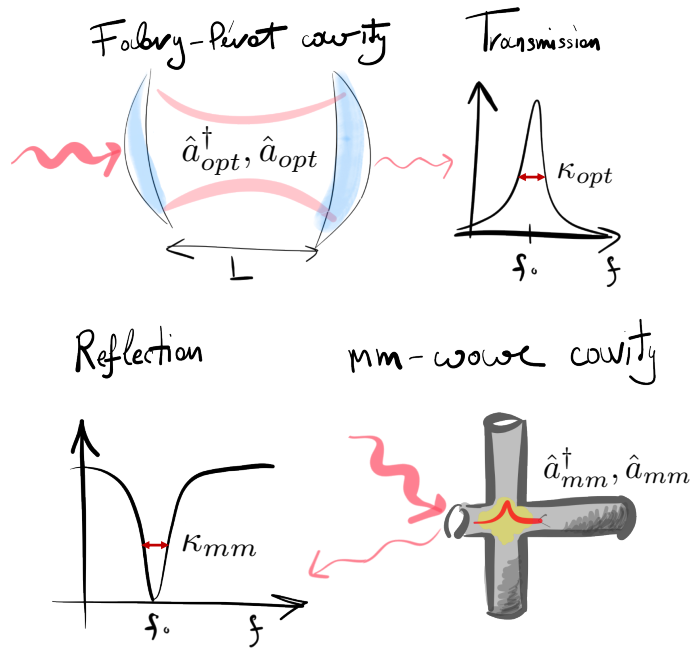


Figure 3.1: Bosonic modes of our hybrid cavity-QED system: photons trapped in optical and mm-wave cavities

the resonator determine the frequency,  $f_0$ , mode volume,  $V_0$ , and density of states of photons stored. Chapter. 4 covers many examples of high-Quality factor 2D, quasi-2D, and 3D resonators I have worked on for quantum systems at mm-wave frequencies throughout my

---

1. This is why I dedicated a whole Chapter. 2 to harmonic resonators

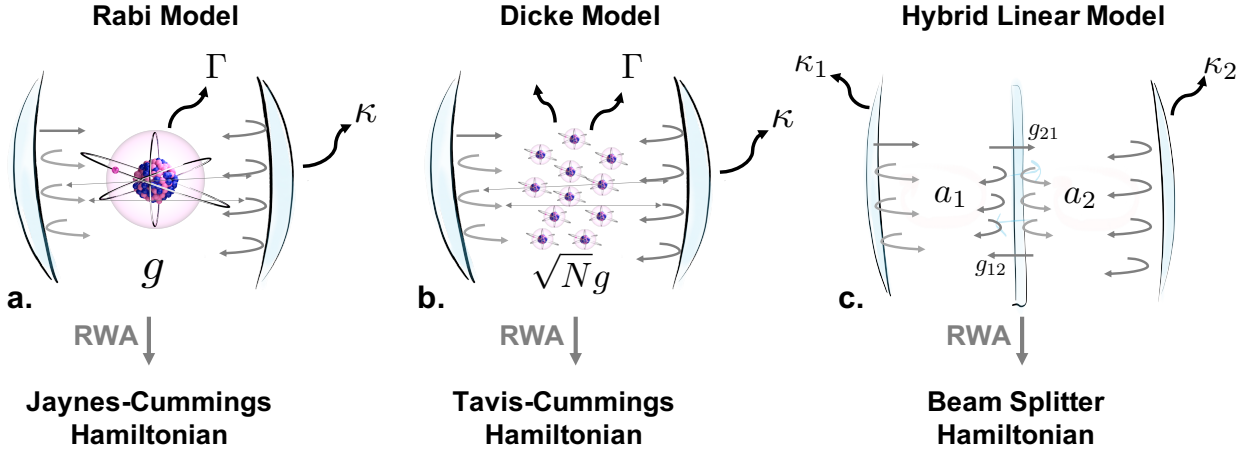


Figure 3.2: Different CQED models used in our hybrid experiments: **a.** Rabi Model for a single two-level system coupled to a cavity mode. It turns into the Jaynes-Cummings Hamiltonian after the Rotating Wave Approximation, **b.** Dicke model for an ensemble of TLSs coupled to a cavity mode. It turns into the Tavis-Cummings Hamiltonian after the RWA, **c.** The beam-splitter Hamiltonian for two coupled harmonic oscillators.

PhD.

**matter couplers:** Photons do not interact with each other. In order to manipulate bosonic excitations and build many-body systems out of light, we need mediators. Mediators allow us to engineer effective interactions between photons through matter-light interactions.

Matter couplers can be microscopic quantum emitters such as atoms [83], molecules and Josephson Junctions [84], or larger linear mediators such as beam splitters, semi-transparent mirrors [85] or mechanical membranes [86]. The macroscopic objects tend to be easier to couple to but have low coupling strength per photon,  $g_0$ . An example of such a system is two coupled cavities, shown in Fig. 3.2c, with linear beam-splitter interactions shown in Fig. 3.3a. The linearity comes from the fact that a large piece of dielectric like a beam splitter couples to  $n$  or  $n + 1$  photons with the same strength. This is ideal for swapping excitations between different bosonic modes [85]. In our quantum hybrid system, we use the beam-splitter Hamiltonian for the transduction of quantum information between optical and mm-wave photons.

The quantum emitters tend to be microscopic and harder to couple to. However, they can provide a strong nonlinearity per photon because they get affected easily by small amounts of energy. This ability to respond to the “graininess” of the electromagnetic field makes them essential for engineering nonlinear photonic systems. The most commonly used quantum emitter is a two-level system (TLS). The Hamiltonian which describes the photon coupled to a single TLS is the Jaynes-Cummings Hamiltonian [65], as shown in Fig. 3.2a. As we will see later in the chapter, JCH is nonlinear in the number of excitations. We use JCH as a primary tool for engineering effective nonlinear interactions between photons by utilizing the nonlinearity of TLS. In our case, the TLS is a  $^{85}\text{Rb}$  atom or an excited Rydberg state of a  $^{85}\text{Rb}$  atom, shown in 3.4. The coupling strength per photon,  $g_0$ , and the natural resonance frequencies of the emitter,  $f_{opt}$  and  $f_{mm}$ , determine the interaction between the coupler and the photon.

Another important Hamiltonian we employ in our experiment is the Tavis-Cummings Hamiltonian [87], shown in Fig. 3.2b. The TCH describes the energy spectrum of an ensemble of TLSs coupled to a single mode of a cavity. We use an ensemble of  $N$   $^{85}\text{Rb}$  atoms coupled to an optical photon for the collective enhancement in the coupling strength,  $\sqrt{N}g_0$ . Even though the ensemble of TLSs can provide up to 1000x higher coupling strength per photon, the distribution of a single excitation among many TLSs takes away the nonlinearity from the Hamiltonian in the low number of excitations manifold. In other words, in the weak probe regime, the ensemble of atoms in a cavity acts as a linear coupler or as a harmonic oscillator instead of a two-level dipole [88]. For our transduction experiments, this is not an issue since we want a linear beam-splitter Hamiltonian. For our nonlinear hybrid experiments, we overcome this issue by using the JC nonlinearity in the Rydberg manifold, which will be described later in this chapter. The ability to harness both linear and nonlinear phenomena in the same setup is a manifestation of flexibility and potential of Hybrid CQED experiments [89, 90]. We can use different properties of our matter-light interactions in the optical and mm-wave regime to optimize the functionality and tailor the desired quantum

# Bosonic Interactions

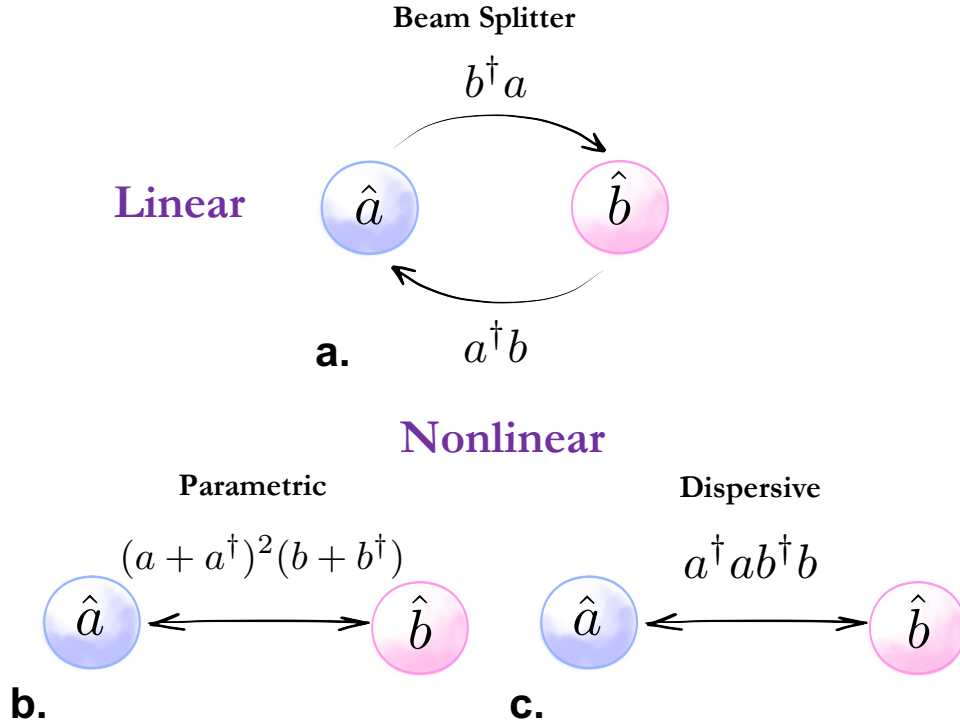


Figure 3.3: Bosonic interaction Hamiltonians: **a.** linear beam-splitter interaction, **b.** non-linear parametric interaction, **c.** nonlinear dispersive interaction

systems.

**Dissipation:** The last important aspect of every CQED system is the dissipation. The resonators we build have the internal dissipation due to surface losses and external dissipation due to the coupling of the bosonic mode to the environment, both thoroughly covered in

Chapter. 2. These losses combined determine the linewidths of the res-

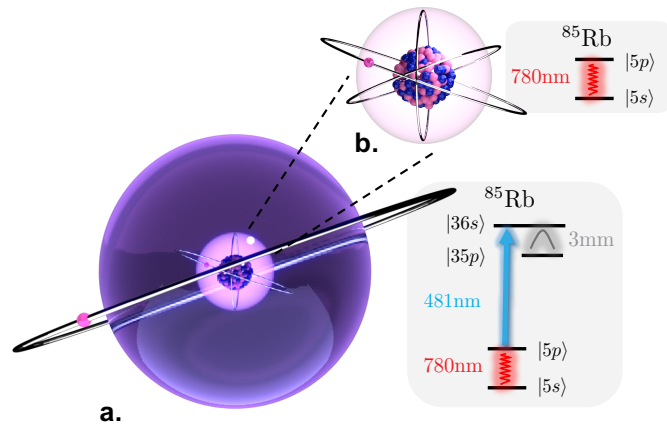


Figure 3.4: Quantum emitters and their energy levels used in our system: **a.** Rydberg states of  $^{85}\text{Rb}$  atoms, **b.** ensemble of  $^{85}\text{Rb}$  atoms

onators,  $\kappa_{mm}$  and  $\kappa_{opt}$ . Our goal

is always to reduce the internal losses and have robust control over the external losses. The matter couplers also exhibit dissipation, which leads to a non-zero linewidth of the energy transitions. In our case, the  $^{85}\text{Rb}$   $|5P\rangle$  state has  $\Gamma/2\pi = 6$  MHz and the  $|36S\rangle$  state has  $\Gamma_R/2\pi \approx 5$  kHz [91].

The linewidth of the elements involved in a CQED system determine the coherence of the systems and the coupling regime that can be achieved.

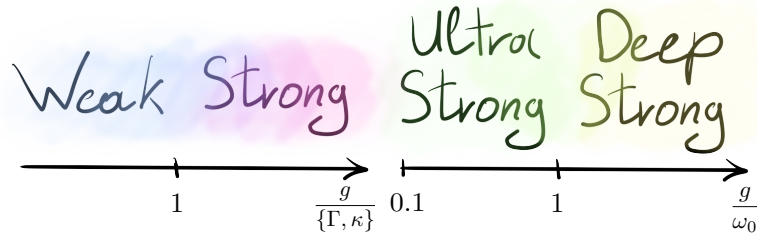


Figure 3.5: Various coupling regimes in CQED system

As shown in Fig. 3.5, a CQED system can operate in several regimes [92]. Our goal is to be in the strong coupling regime in both optical and mm-wave bands of our hybrid CQED. This requires the cooperativity [90], which is defined as:

$$\eta = \frac{g^2}{\kappa\Gamma} \quad (3.1)$$

to be greater than 1 for both a single mm-wave photon coupling to the Rydberg state and a single optical photon coupling to an ensemble of ground state  $^{85}\text{Rb}$  atoms. The strong coupling regime ensures that an excitation can be swapped between the cavity and the emitter before it decays. The higher the cooperativity, the effective interactions could be made stronger between the optical and mm-wave photons. It is worth noting that if the coupling strength  $g$  is large in comparison to the frequency of the photon, we can reach ultra-strong and deep strong coupling regimes, as shown in Fig. 3.5. Here, the frequency of the exchange of excitations is comparable or higher than the frequency of the excitation itself. This renders the perturbative approach ineffective [92] and opens a whole new area of possibilities to explore for nonlinear quantum physics. In our system, the excitation energies

are significantly higher than the coupling strengths, so we are not worried about these higher-order effects. As I mentioned above, the main goal is to reach the strong coupling regime for higher nonlinearities and effective exchange of excitations between single mm-wave and optical photons.

### 3.1 From waves to photons

The EM fields are essential in our system. On one side, we have the quantized photons, which play the leading role in our Hamiltonian. On the other hand, we have a myriad of supporting classical EM fields across many frequency bands that are crucial for controlling, dressing, locking, and manipulating our quantum degrees of freedom. By pushing the irrelevant atomic states out of the energy band of interest, locking and tuning the signals to the proper transitions, they significantly simplify the main picture and enable us to only analytically treat the critical states of light and matter. I will start by discussing the general quantum treatment of light using an example of an optical cavity.

The approach here works best for high-finesse cavities. We know classically that for the perfect cavity, EM fields vanish at the boundaries (mirrors), so expanding the fields inside the cavity in terms of discrete modes implies perfect or close to ideal cavity walls. However, the transmissivity of the mirrors induces losses, resulting in a deviation from the perfectly quantized field inside the cavity. We will ignore this since our cavities have very high finesse.

### 3.1.1 Quantizing the classical fields

As described in [93], we first quantize the EM field in a cavity. Note that the B field should really be H field in general, but to avoid confusion with Hamiltonian we will call it B.

$$E_x(z, t) = \sum_j A_j q_j(t) \sin(k_j z) \quad (3.2)$$

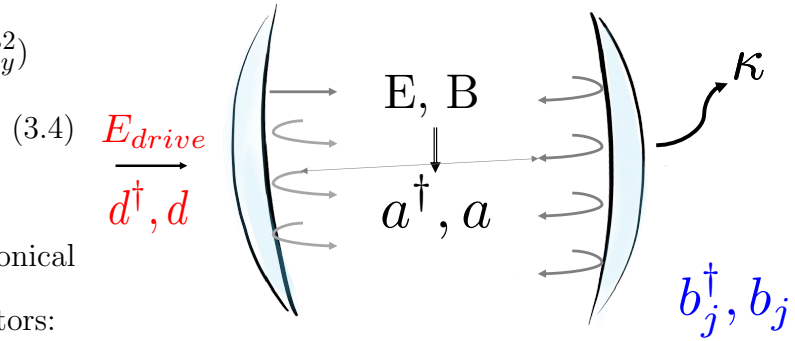
and

$$B_y(z, t) = \sum_j A_j \frac{\dot{q}_j(t) \epsilon_0}{k_j} \cos(k_j z) \quad (3.3)$$

where  $A_j = (\frac{2\nu_j^2 m_j}{V\epsilon_0})^{1/2}$ ,  $\nu_j = j\pi c/L$ ,  $m_j$  is a constant with a dimension of mass <sup>2</sup> and  $q_j(t)$  is a normal mode amplitude with dimension of a length.

The Hamiltonian is:

$$H = \frac{1}{2} \int_V d\tau (\epsilon_0 E_x^2 + \mu_0 B_y^2) \quad (3.4)$$



To quantize we make a canonical transformations to the operators:

$$a_j e^{-i\nu_j t} = \frac{1}{\sqrt{2m_j \hbar \nu_j}} (m_j \nu_j q_j + i p_j) \quad (3.5)$$

Figure 3.6: The diagram for quantization of light inside of the optical cavity, where  $a^\dagger$  and  $a$  are creation and annihilation operators for the mode of the Fabry-Perot cavity,  $d^\dagger$  and  $d$  for the drive, and  $b_j^\dagger$  and  $b_j$  for the free space modes.

---

2. The constant  $m_j$  is included only to make an analogy with the harmonic oscillator of mass  $m$

$$a_j^\dagger e^{-i\nu_j t} = \frac{1}{\sqrt{2m_j \hbar \nu_j}} (m_j \nu_j q_j - ip_j) \quad (3.6)$$

Then the QM Hamiltonian becomes:

$$H = \hbar \sum_j \nu_j (a_j^\dagger a_j + \frac{1}{2}) \quad (3.7)$$

The commutation relations are:

$$[a_j, a_{j'}^\dagger] = \delta_{jj'} \quad (3.8)$$

,

$$[a_j, a_{j'}] = [a_j^\dagger, a_{j'}^\dagger] = 0 \quad (3.9)$$

So the fields in QM picture become:

$$E_x(z, t) = \sum_j \mathcal{E}_j (a_j e^{-i\nu_j t} + a_j^\dagger e^{i\nu_j t}) \sin(k_j z) \quad (3.10)$$

$$B_y(z, t) = -i\epsilon_0 c \sum_j \mathcal{E}_j (a_j e^{-i\nu_j t} - a_j^\dagger e^{i\nu_j t}) \cos(k_j z) \quad (3.11)$$

where  $\mathcal{E}_j = \sqrt{\frac{\hbar \nu_j}{\epsilon_0 V}}$

Now, for the free field we have, classically, the following:

$$E(\vec{r}, t) = \sum_k k \hat{\epsilon}_k \mathcal{E}_k (\alpha_{k,\lambda} e^{-i(\nu_k t - \vec{k} \cdot \vec{r})} + \alpha_{k,\lambda}^* e^{i(\nu_k t - \vec{k} \cdot \vec{r})}) \quad (3.12)$$

$$B(\vec{r}, t) = \frac{1}{\mu_0} \sum_k \frac{k \times \hat{\epsilon}_k}{\nu_k} \mathcal{E}_k (\alpha_{k,\lambda} e^{-i(\nu_k t - \vec{k} \cdot \vec{r})} + \alpha_{k,\lambda}^* e^{i(\nu_k t - \vec{k} \cdot \vec{r})}) \quad (3.13)$$

The Hamiltonian for a single photon in the high-finesse cavity (in rotating wave approximation) is [88]:

$$H = \hbar w_c a^\dagger a + \hbar \sum_j (w_j b_j^\dagger b_j + g_j (a^\dagger b_j + b_j^\dagger a)) \quad (3.14)$$

where  $w_c$  is the cavity frequency,  $a/a^\dagger$  are photon annihilation and creation operators in the single mode of the cavity,  $w_j$  is the frequency of the  $j$ th mode of the open space, and  $b_j/b_j^\dagger$  are photon annihilation and creation operators for the open space outside of the cavity. It is basically a continuum, but we will treat it as a spectrum of discrete close-spaced states for now. Note that this Hamiltonian is in Heisenberg picture, the states are stationary Fock states, but operators are varying in time.

$$\dot{a} = \frac{i}{\hbar} [H, a(t)] \quad (3.15)$$

$$\dot{a} = -i w_c a(t) - 2i \sum_j g_j b_j \quad (3.16)$$

$$\dot{b}_j = \frac{i}{\hbar} [H, b_j(t)] \quad (3.17)$$

$$\dot{b}_j = -i g_j a - i w_j b_j \quad (3.18)$$

Next we integrate  $b_j$  over time in Eq. 3.18:

$$b_j = i g_j \int a(t) dt - i w_j \int b_j(t) dt \quad (3.19)$$

where the general solution (from non-homogeneous PDE method) is:

$$b_j = b_j(0)e^{-iw_j t} - ig_j \int a(t')e^{-iw_j(t-t')} dt' \quad (3.20)$$

insert Eq. 3.20 into Eq. 3.16:

$$\begin{aligned} \dot{a} &= -iw_c a - 2i \sum g_j (b_j(0)e^{-iw_j t} - ig_j \int a(t')e^{-iw_j(t-t')} dt) \\ &= -iw_c a - 2 \sum g_j^2 \int a(t')e^{-iw_j(t-t')} dt' + f(t) \end{aligned} \quad (3.21)$$

where

$$f(t) = -2i \sum g_j b_j(0)e^{-iw_j t} \quad (3.22)$$

It is convenient now to move into a rotating frame with  $\tilde{a}(t) = a(t)e^{iw_c t}$ , then Eq. 3.21 becomes:

$$\dot{\tilde{a}}(t) = -2 \sum g_j^2 \int_0^t \tilde{a}(t')e^{-i(w_j - w_c)(t-t')} dt' + \tilde{f}(t)w \quad (3.23)$$

here

$$\tilde{f}(t) = -2i \sum g_j b_j(0)e^{-(w_j - w_c)t} \quad (3.24)$$

is the noise operator that depends on the initial occupation of the free space modes  $b_j(0)$ . Since the modes of the open space make up a continuum spectrum of states, we can turn the sum in Eq. 3.23 into an integral with

$$\sum_j = \frac{2V}{(2\pi)^2} \frac{1}{c^3} \int d\phi \int d\theta \sin(\theta) \int \frac{dw}{c} \frac{w^2}{c^2} \quad (3.25)$$

with the assumption that coupling constant  $g_j = g_k = g(w = kc)$ . The Eq. 3.23 becomes:

$$\dot{\tilde{a}} = -\frac{2Vw_c^2}{\pi^2 c^3} \int g^2(w)e^{-(w-w_c)(t-t')} dw \int \tilde{a}(t') dt' + \tilde{F}(t) \quad (3.26)$$

the exponent in the integral oscillates fast away from  $w \approx w_c$ , so we can make Wigner-Weisskopf approximation and get:

$$\begin{aligned}
\dot{\tilde{a}} &= -\frac{2Vw_c^2}{\pi^2c^3}g^2(w_c) \int e^{-(w-w_c)(t-t')}dw \int \tilde{a}(t')dt' + \tilde{F}(t) \\
&= -\frac{4Vw_c^2}{\pi c^3}g^2(w_c) \int \delta(t-t')\tilde{a}(t')dt' + \tilde{F}(t) \\
&= -\frac{4Vw_c^2}{\pi c^3}g^2(w_c)\tilde{a}(t) + \tilde{F}(t) \\
&= -\pi g^2(w_c)\rho(w_c)\tilde{a}(t) + \tilde{F}(t)
\end{aligned} \tag{3.27}$$

where  $\rho(w_c) = \frac{4Vw_c^2}{\pi^2c^3}$  is the density of states of the free-space at  $w_c$ . Inspired by Fermi's Golden rule we can specify the decay constant of the cavity:  $\kappa = 2\pi\rho(w_c)g^2(w_c)$  and we arrive at:

$$\dot{\tilde{a}}(t) = -\frac{1}{2}\kappa\tilde{a}(t) + \tilde{F}(t) \tag{3.28}$$

which is a manifestation of fluctuation-dissipation theorem. Going back to the lab frame, we get:

$$\dot{a}(t) = -i(w_c - i\frac{\kappa}{2})a(t) + F(t) \tag{3.29}$$

Phenomenologically,  $a$  is a non-Hermitian operator that corresponds to the annihilation of our photon in the cavity. Therefore, we can see that the emission probability of the photon from the cavity is an exponential decay  $\propto e^{-\frac{t}{2\kappa}}$  with a lifetime  $2/\kappa$ . A steady-state solution  $\langle \dot{a}(t) \rangle = 0$  of this equation gives us 0, which means eventually photon escapes from the lossy cavity. Note, that time average of the fluctuation noise operator  $F(t)$  is 0 for our operators. Now, to get a transmission spectrum of the cavity from our Hamiltonian we need to add a drive field, which in this case is a monochromatic laser field of frequency  $w_l$  inside of our cavity. The Hamiltonian of this field is:

$$H_{drive} = i\hbar(d^\dagger(k)\mathcal{E}e^{-i\omega_l t} - d(k)\mathcal{E}^*e^{i\omega_l t}) \tag{3.30}$$

It is important to note that  $d(k)$  creation and annihilation operators are not the same as ones in the cavity. The  $d(k)$  is an operator of the free space that also follow the usual commutator relations  $[d^\dagger(k), d(k)] = 1$  and  $[d^\dagger(k'), d(k)] = \delta(k - k')$ .

The Heisenberg operator evolution  $[H_{drive}, a_k(t)] = -i\hbar e^{-i\omega_l t} \mathcal{E}$  and  $[H_{drive}, b_j(t)] = 0$  mean that  $b_j$  operators remain unchanged but the evolution equation Eq. 3.29 of the cavity annihilation operator becomes:

$$\dot{a}(t) = -i(w_c - i\frac{\kappa}{2})a(t) + \mathcal{E}e^{-i\omega_l t} + F(t) \quad (3.31)$$

Going into the frame of reference rotating with phase of the laser light  $\bar{a}(t) = e^{i\omega_l t} a(t)$ , the above Eq. 3.31 becomes:

$$\dot{\bar{a}}(t) = -i(\Delta - i\frac{\kappa}{2})\bar{a}(t) + \mathcal{E} \quad (3.32)$$

where  $\Delta = w_c - w_l$  and  $F(t)$  is omitted since it does not contribute to the expectations values of our operators.

Here, we are more interested in the steady state solution  $\langle \dot{\bar{a}}(t) \rangle = 0$ , which gives  $\langle \bar{a}(t) \rangle = \frac{\mathcal{E}2}{i\frac{\Delta^2}{\kappa} + 1}$ . This leads to the final transmission of the cavity, which is the exact solution that classical calculation of the transmission of the cavity gives:

$$E_{out} \propto Re(\langle \tilde{a}(t) \rangle) = \frac{2\mathcal{E}}{\kappa} \frac{1}{1 + \frac{4\Delta^2}{\kappa^2}} \quad (3.33)$$

I derived this result classically in Chapter. 2 with significantly less math. However, the machinery for solving empty cavity transmission becomes relevant in the following sections, where I will derive transmission of the cavity with atoms addressed by various electromagnetic fields. We will see that the physics becomes much more interesting and “grainy” or quantum mechanical with the addition of our nonlinearity.

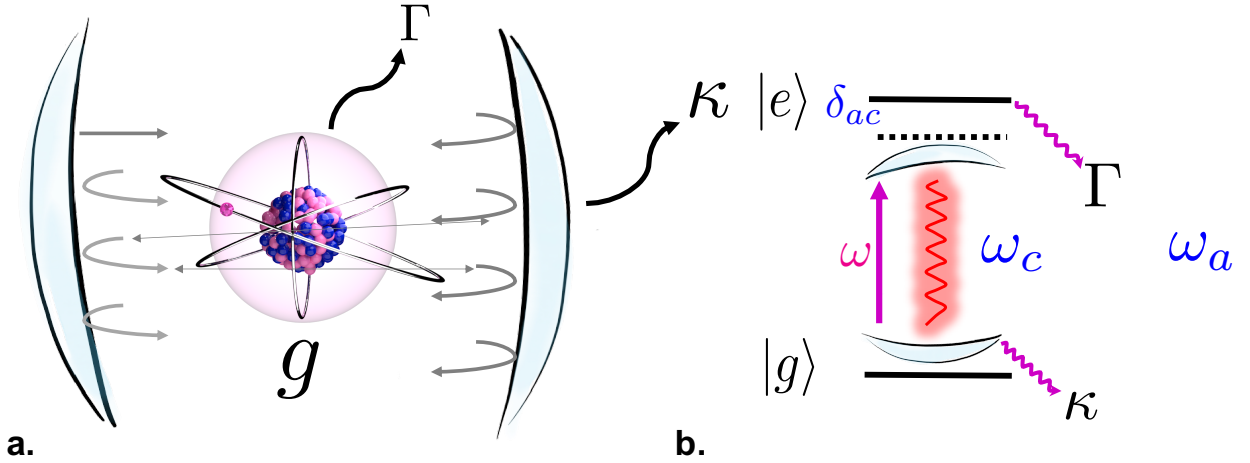


Figure 3.7: Single atom in a cavity for Jaynes-Cummings Hamiltonian: **a.** diagram of the losses and couplings, **b.** energy levels involved in the derivation

An alternative derivation of transmission and reflection of a cavity in quantum regime can be found in Appendix. A. The input and output theory is used, which is a very useful formalism for solving linear systems like coupled harmonic oscillators.

### 3.2 Jaynes-Cummings model

Now, it is time to couple a single two-level atom to the mode of the cavity discussed above. The Hamiltonian of the system without the dissipation has three parts:

$$H = H_{cav} + H_{atom} + H_{int} \quad (3.34)$$

The  $H_{cav}$  is an energy associated with the photons of a single cavity mode with creation and annihilation operators  $a$  and  $a^\dagger$ :

$$H_{cav} = \hbar\omega_c a^\dagger a \quad (3.35)$$

The  $H_{atom}$  is the energy of the atom in the cavity. The atom has only two states: ground  $|g\rangle$

and excited  $|e\rangle$ , and we set the energy level of the ground state to 0. Then the only relevant energy contribution  $\hbar\omega_a$  is from the excited state:

$$H_{atom} = \hbar\omega_a |e\rangle \langle e| \quad (3.36)$$

The last term is the coupling between photon modes of the cavity and the atomic energy states. To the lowest order, the coupling can be modeled as a dipole interaction  $\mu_{at} \cdot E_{cav}$  at the location of the electron  $\vec{r}_0$  of the atom:

$$H_{int} = -e\vec{r} \cdot \vec{E}(\vec{r}_0) \quad (3.37)$$

We will set  $\vec{r}_0 = 0$ , and derive  $\vec{E}(0)$  in Coulomb gauge:

$$\vec{E}(0) = \frac{\partial A}{\partial t} = \frac{\partial(A_0 a^\dagger \hat{e} e^{i(\vec{k} \cdot \vec{r}_0 - w_c t)} + A_0^* a \hat{e} e^{-i(\vec{k} \cdot \vec{r}_0 - w_c t)})}{\partial t} = i w_c (-A_0 a^\dagger \hat{e} e^{-i w_c t} + A_0^* a \hat{e} e^{i w_c t}) \quad (3.38)$$

Lets call the dipole moment operator of the atomic transition  $\hat{\mu} = \mu |g\rangle \langle e| + \mu^* |e\rangle \langle g|$ , where  $\mu = \mu^* = \langle e| e\vec{r} \cdot \hat{e} |g\rangle$

The complete Hamiltonian is

$$H = \hbar\omega_c a^\dagger a + \hbar\omega_a |e\rangle \langle e| - i\mu(|g\rangle \langle e| + |e\rangle \langle g|)(E_0 a^\dagger e^{-i w_c t} - E_0^* a e^{i w_c t}) \quad (3.39)$$

From the bare Hamiltonian we know that the excited energy evolves like  $|e\rangle e^{-i\omega_a t}$ . We can use this to ignore the counter-propagating terms (fast oscillating at  $\omega_a + \omega_c$ ) and arrive at:

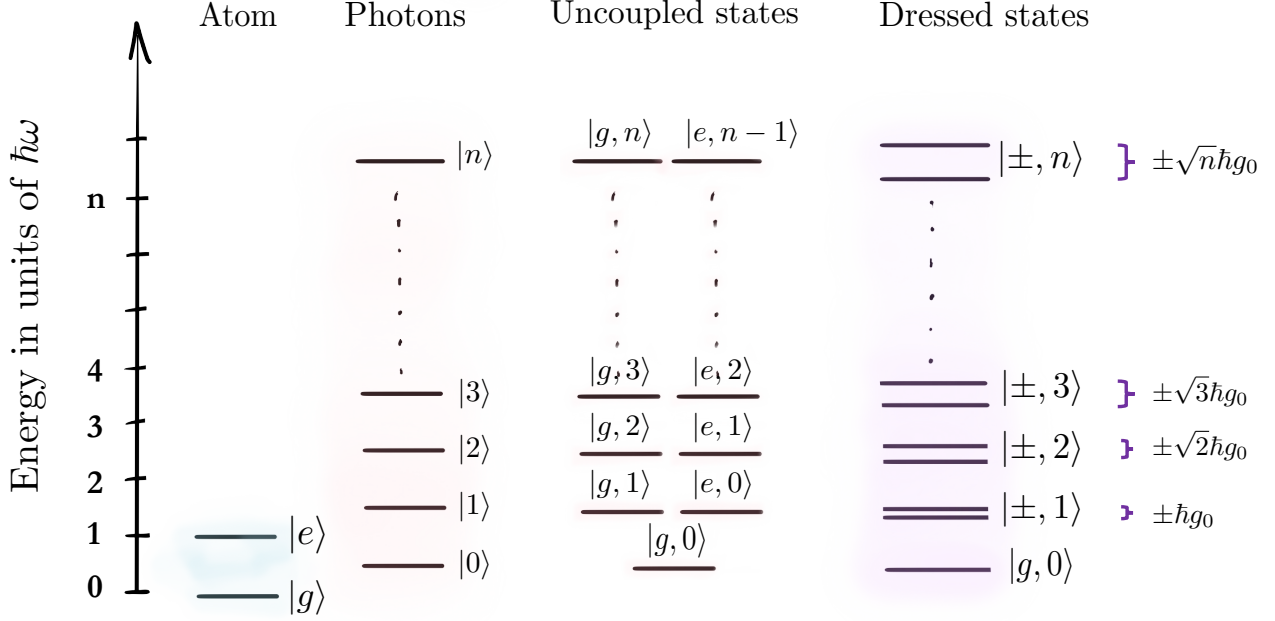


Figure 3.8: Energy levels of the Jaynes-Cummings Hamiltonian: from the bare photon and bare atom energy levels to the nonlinear ladder of the dressed states of JCH for  $\delta_{ac} = 0$

$$H = \hbar\omega_c a^\dagger a + \hbar\omega_a |e\rangle \langle e| - i\mu E_0 (-|g\rangle \langle e| a^\dagger e^{-i(\omega_c - \omega_a)t} - a e^{i(\omega_c - \omega_a)t} |e\rangle \langle g|) \quad (3.40)$$

where  $g = \frac{\mu E_0}{\hbar}$ .

To simplify the notation we introduce operators for the atom:  $|e\rangle \langle g| = \sigma_{eg}$ ,  $|g\rangle \langle e| = \sigma_{ge}$  and  $|e\rangle \langle e| = \sigma_{ee}$ . The  $\sigma_+$  and  $\sigma_-$  are the Pauli spin raising and lowering operators with fermionic anti-commutator relationship.

The Hamiltonian transforms into the following form:

$$H = \hbar\omega_c a^\dagger a + \hbar\omega_a \sigma_{ee} + g\hbar(\sigma_{ge} a^\dagger e^{-i(\omega_c - \omega_a)t} + a e^{i(\omega_c - \omega_a)t} \sigma_{eg}) \quad (3.41)$$

Note that ignoring the counter propagating terms is only viable close to the resonance or for weak coupling.

Our analysis of the cavity transmission with an atom will start from solving the exact Jaynes-Cummings Hamiltonian back in the Schrodinger picture after the RWA written below.

$$H = \hbar w_c a^\dagger a + \hbar w_a \sigma_{ee} + g\hbar(\sigma_{ge} a^\dagger + a \sigma_{eg}) \quad (3.42)$$

Of course, there is no cavity transmission yet. The transmission implies a lossy cavity, and we have not included any dissipation in our system. The picture here is this: we have a perfect atom with no dissipation inside a perfect cavity, which interacts with a photon that was somehow “placed” perfectly into the mode of the cavity.

Without the dipole interaction the Nth pair of eigenstates of the Hamiltonian are  $|e, N - 1\rangle$  and  $|g, N\rangle$  with energies  $E_{|e, N-1\rangle} = \hbar\omega_a + \hbar w_c(N - 1)$  and  $E_{|g, N\rangle} = \hbar w_c N$ . These are the collective excitation energies of the system comprised of an atomic excitation number (0 or 1 - "fermion") and photonic excitation number N. The interaction term introduces coupling between pair of states which conserve total excitation number  $|e, N - 1\rangle$  and  $|g, N\rangle$ . Rewriting the Hamiltonian for the nth pair in this collective basis, we get:

$$H = \hbar \begin{pmatrix} w_c N & \frac{g\sqrt{N}}{2} \\ \frac{g\sqrt{N}}{2} & w_c(N - 1) + \hbar w_a \end{pmatrix} = \hbar \begin{pmatrix} w_c(N - 1) & \frac{g\sqrt{N}}{2} \\ \frac{g\sqrt{N}}{2} & w_c(N - 1) + \delta_{ac} \end{pmatrix} \quad (3.43)$$

where  $\delta_{ac} = w_a - w_c$

After diagonalizing the matrix, we find dressed states to be:

$$|N+\rangle = \cos \theta_n |e, N - 1\rangle + \sin \theta_n |g, N\rangle \quad (3.44)$$

$$|N-\rangle = \cos \theta_n |g, N\rangle - \sin \theta_n |e, N - 1\rangle \quad (3.45)$$

$$\cos \theta_n = \frac{G + \delta_{ac}}{\sqrt{(\delta_{ac} + G)^2 + G_0^2}} \quad (3.46)$$

$$\sin \theta_n = \frac{G_0}{\sqrt{(\delta_{ac} + G)^2 + G_0^2}} \quad (3.47)$$

where  $G_0 = g\sqrt{N}$  and  $G^2 = G_0^2 + \delta_{ac}^2$ .

The corresponding energies are:

$$E_{N,+} = \hbar N w_c + \frac{1}{2} \hbar (\delta_{ac} - G) \quad (3.48)$$

$$E_{N,-} = \hbar N w_c + \frac{1}{2} \hbar (\delta_{ac} + G) \quad (3.49)$$

For  $n = 0$ , no photons in the cavity, we have three states  $|e, 0\rangle$ ,  $|g, 1\rangle$  and  $|g, 0\rangle$ . In the dressed picture they become  $|+1\rangle$ ,  $|-1\rangle$  and  $|g, 0\rangle$ . Notice that  $|g, 0\rangle$  is "dark", unaffected by the interaction term.

For an arbitrary number of photons  $n$ , without the interaction and at resonance, we have a ladder of equally separated states with energy gap  $= \hbar w_c$ , as shown in Fig. 3.8. In this case,  $E_{N,+}$  and  $E_{N,-}$  are degenerate. The interaction lifts the degeneracy by introducing a gap between  $E_{N,+}$  and  $E_{N,-}$  states equal to  $G = G_0 = g\sqrt{N}$ . The diagram in Fig. 3.8 shows the final ladder of dressed states which have the characteristic nonlinearity.

The nonlinear dependence of the energy of the dressed state on the number of excitation is the main tool used for creating effective interactions between photons. To make the connection a bit clearer, it helps to think about the phenomena of a blockade in a cavity. Photons in an empty cavity similar to the electromagnetic waves in free space pass through each other with mere interference. In a CQED system with strong nonlinearity, the photons resemble the colliding billiard balls. Since there is a significant difference in energy between one photon

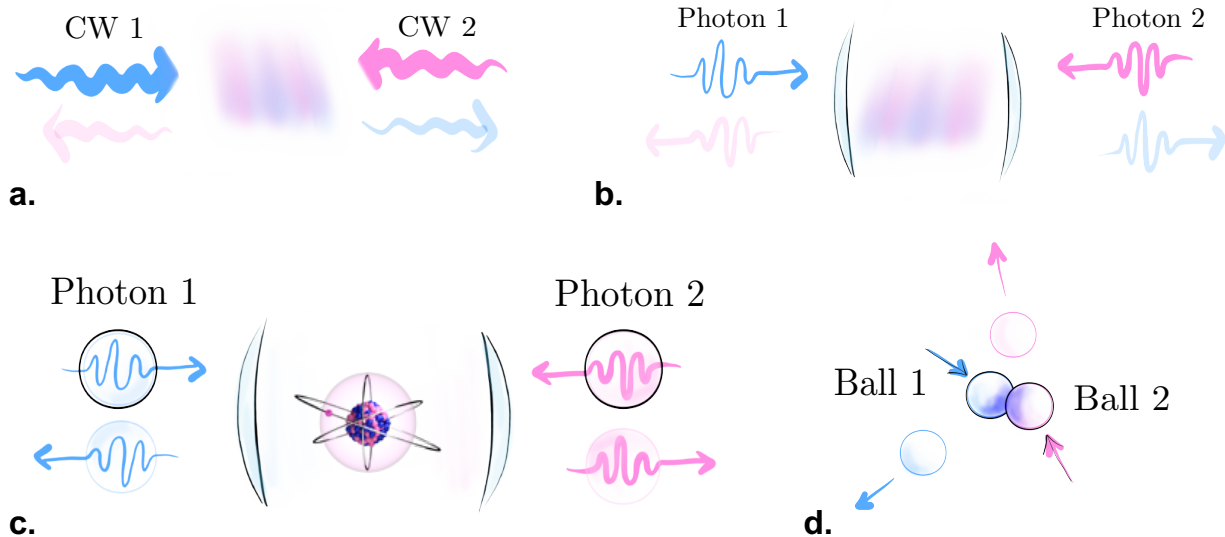


Figure 3.9: The connection between the Jaynes-Cummings nonlinearity and effective interactions between photons. Non-interacting systems: **a.** electromagnetic waves in free space, **b.** photons in an empty cavity. Strongly interacting systems: **c.** two-photon blockade from a strongly interacting CQED system, **d.** bouncing billiard balls

in a cavity vs. two photons in a cavity simultaneously, see the Figure. 3.8, at the frequency of one photon in a cavity, two photons cannot enter the cavity due to the blockade. In other words, two-photon and one-photon processes are not co-resonant with each other. In this sense, it is very similar to two solid balls colliding since they cannot occupy the same space. This intuitive idea is pictured in Figure. 3.9. One of the experimental measurements that can demonstrate the blockade, and therefore the nonlinearity, is the  $g^2(0)$  known as the second correlation function. It is the probability to measure two photons at the same time,  $\tau = 0$ . For the classical states of light including the coherent state  $g^2(0) = 1$ , for non-classical light the statistics should be sub-Poissonian or  $g^2(0) < 1$ .

### 3.3 Perturbation theory for the non-Hermitian Hamiltonian

The JCH described above is at the heart of our hybrid quantum system. However, without the dissipation included, it is not realistic, which makes it not useful for experimental in-

vestigation. To be able to observe the nonlinearities of the JC model (the sensitivity of the system to the "graininess" of the photon field), something measurable has to come out of the "cavity-atom" box. In fact, the intuition behind using JCH to create photons bouncing off each other in Figure. 3.9 only makes sense if photons can enter and leave the cavity. Therefore, not only is dissipation important for the Hamiltonian to be realistic, but part of it is essential for our technology to work. The distinction between the loss we have to deal with and the dissipation we engineer for the measurement is critical for designing a quantum experiment.

Let's go back to our cavity transmission story. It is time to introduce realistic dissipation in the JC model. We saw in Section 3.1 that solving a system where one discrete mode is coupled to a "quasi-continuum" of modes was equivalent to adding a purely imaginary part to the operator. We can do a similar trick here. Instead of just the cavity coupling to the continuum of the outside world, our excited atomic state undergoes a similar decay process due to spontaneous emission.

Including complex energy terms into the Hamiltonian is equivalent to accepting the inevitable loss of probability that we will get with a time evolution operator  $e^{iHt}$  when H is complex. This is what we mean by loss - the loss of information. Of course, we could have avoided it and tracked all of the "bath modes" this probability could leak into, and then it wouldn't look like loss. Similar to how friction is not a conservative force in Chapter. 2 unless you are willing to get into microscopies of the friction which comes from electromagnetism.

In addition to the loss, we add a cavity drive term with a small amplitude  $\Omega$ , which will enable us to probe the system. Our new "realistic" JCH with ability to probe the system is:

$$H_{JC}^r = \hbar(w_a + i\frac{\Gamma}{2})\sigma_{ee} + \hbar(w_c + i\frac{\kappa}{2})a^\dagger a + g\hbar(\sigma_{ge}a^\dagger + a\sigma_{eg}) + \hbar\Omega(t)(a^\dagger + a) \quad (3.50)$$

where  $\Gamma$  and  $\kappa$  are one over the lifetime of the excited state of the atom and the cavity mode, respectively [88]. Note that the JCH state with two photons has twice as large of a decay rate as a state with one photon. This makes sense since the two-photon state can decay into two different one-photon states, each with a decay rate  $\kappa$ . These states, in turn, can decay into a vacuum state, each with a decay rate  $\kappa$ . However, the time it takes to decay by  $1/e$  is still fundamentally the same  $= \kappa$ . A counter-intuitive fact that is connected to statistics more than to quantum mechanics.

Physically the Eq. 3.50 means the following: the first two terms are the energies of the bare atom and the number of photons in the cavity. The third term is the strong coupling within the same excitation number manifolds. And the last term is the small perturbation that couples the excitation manifolds that are uncoupled in the regular JCH shown in Figure. 3.8. So if we are probing weakly,  $\Omega \ll 1$ , we can use the perturbation theory to find the new energy spectrum of an atom in a cavity probed with a very weak field.

The only complication in this logic is the fact that our Hamiltonian is no longer Hermitian. The Hermiticity of the Hamiltonian is required in perturbation theory to guarantee that the new perturbed Hamiltonian has an orthonormal basis [88, 34]. Thankfully, this issue is avoidable, as I will show below. The reader might be more concerned about the fact that the non-Hermiticity of our Hamiltonian could mean that the spectrum of our perturbed Hamiltonian is not real, hence not observable. While it is true that we will get the perturbed ground state which is complex, and we are used to real observables, this complexity can be interpreted as a loss in an open system. As a side note, in general, the Hamiltonian does not have to be Hermitian to have real eigen energies, as long as it has PT-symmetry or pseudo-Hermiticity. Here are a few interesting discussions about a whole class of non-Hermitian Hamiltonians, including the modified JCH, and fascinating consequences such as exceptional points and their use in optics [94, 95, 96, 97, 98, 99].

To derive the transmission spectrum of the cavity for a weakly probed JCH we rewrite the

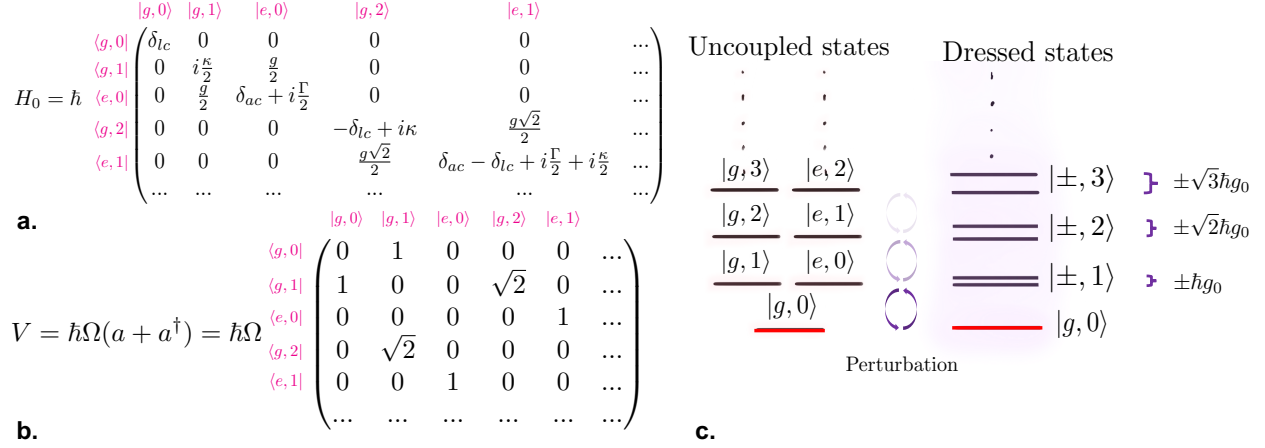


Figure 3.10: Perturbation theory for Jaynes-Cummings Hamiltonian with loss and drive: **a.** Bare non-Hermitian Hamiltonian, **b.** the perturbation term, which corresponds to the probe beam, **c.** energy states involved in the system

Eq. 3.50 in the uncoupled JCH basis shown in Fig. 3.10. It is very useful to write out the full Hamiltonian,  $H_0$ , and operators on a physically intuitive basis. It helps determine the smallest number of excitations needed to be included in  $H_0$  to extract the information we need from the experimental system. We will see that for the observation of the vacuum Rabi splitting, we only need the 0th and 1st excitation manifolds, while the first sign of nonlinearity can only be observed with the inclusion of the two-excitation manifold.

Another important note is about the rotating frame transformation, not to be confused with the Rotating Wave Transformation (RWA). As the Hamiltonians grow in complexity and we add more energy levels to the system, we need to be careful about getting rid of the time dependencies in the Hamiltonian by moving into the frame rotating with the probe light. For example, to arrive at the Hamiltonian in Fig. 3.10 from the time-dependent driven Hamiltonian in Eq. 3.50, I used the following transformation [100]:

$$\tilde{H} = i\frac{\partial U}{\partial t}U^\dagger + UH_0U^\dagger \quad (3.51)$$

where

$$U = \begin{pmatrix} 1 & 0 & 0 & 0 & 0 & \dots \\ 0 & e^{i\omega_1 t} & 0 & 0 & 0 & \dots \\ 0 & 0 & e^{i\omega_1 t} & 0 & 0 & \dots \\ 0 & 0 & 0 & e^{i2\omega_1 t} & 0 & \dots \\ 0 & 0 & 0 & 0 & e^{i2\omega_1 t} & \dots \\ \dots & \dots & \dots & \dots & \dots & \dots \end{pmatrix} \quad (3.52)$$

This transformation takes care of the time dependence that the perturbation  $V$  adds to the overall Hamiltonian:

$$V(t) = \hbar\Omega \begin{pmatrix} 0 & e^{i\omega_1 t} & 0 & 0 & 0 & \dots \\ e^{-i\omega_1 t} & 0 & 0 & \sqrt{2}e^{i\omega_1 t} & 0 & \dots \\ 0 & 0 & 0 & 0 & 0 & \dots \\ 0 & \sqrt{2}e^{-i\omega_1 t} & 0 & 0 & 0 & \dots \\ 0 & 0 & 0 & 0 & 0 & \dots \\ \dots & \dots & \dots & \dots & \dots & \dots \end{pmatrix} \quad (3.53)$$

I hope this pedantic note is helpful for a reader trying to make sense of her complex Hamiltonians. Now we are ready to apply the perturbation theory around the ground state of the system  $|\psi_0\rangle = |g, 0\rangle$  [88]. This means that the total Hamiltonian,  $H_{tot} = H_t = H_0 + V$ , has eigenstates  $|\psi_t\rangle$  and eigen energies  $E_t$ :

$$\begin{aligned}
|\psi_t\rangle &= \sum_n \Omega^n |\psi_n\rangle \\
E_t &= \sum_n \Omega^n E_n
\end{aligned}
\tag{3.54}$$

where  $n$  is the perturbation order parameter. We are going to be interested in  $t = 0$  state of the perturbed system and its changes due to different orders of perturbation, mostly  $n = 1$  and 2. As usual for the perturbation theory:

$$\begin{aligned}
H_t |\psi_t\rangle &= E_t |\psi_t\rangle \\
\Omega^m : H_0 |\psi_m\rangle + V |\psi_{m-1}\rangle &= \sum_{n=0}^m E_n \psi_{m-n}
\end{aligned}
\tag{3.55}$$

The tricky part is that the  $|\psi_m\rangle$  states need not be orthonormal since our Hamiltonian is not Hermitian. And as the Hamiltonians get more complex and hybrid, we won't usually know what the unperturbed states are. A useful tool is to find a state  $|\psi_{0*}\rangle$ , such that:

$$\begin{aligned}
\langle \psi_{0*} | \psi_0 \rangle &= 1 \\
\langle \psi_{0*} | \psi_n \rangle &= 0
\end{aligned}
\tag{3.56}$$

which exists since  $H_0$  is invertible and diagonalizable.

When we apply  $\langle \psi_{0*} |$  to Eq. 3.55 we get the recursive relations for energies and states of our unperturbed Hamiltonian:

$$\begin{aligned}
E_n &= \langle \psi_{0*} | V | \psi_{n-1} \rangle - \sum_{m=1}^{n-1} E_m \langle \psi_{0*} | \psi_{n-m} \rangle \\
|\psi_n\rangle &= \frac{1}{H_0 - E_0 \cdot \mathbb{I}} \left( \sum_{m=0}^{n-1} E_{n-m} |\psi_m\rangle - V |\psi_{n-1}\rangle \right)
\end{aligned} \tag{3.57}$$

For the JCH up to the second order in perturbation we get:

$$\begin{aligned}
E_1 &= \langle \psi_{0*} | V | \psi_0 \rangle = \langle g, 0 | (a + a^\dagger) | g, 0 \rangle = 0 \\
E_2 &= \langle \psi_{0*} | V Q \frac{1}{H_0 - E_0 \cdot \mathbb{I}} Q V | \psi_0 \rangle = \frac{K_4}{K_1} \\
|\psi_1\rangle &= \frac{1}{H_0 - E_0 \cdot \mathbb{I}} Q V | \psi_0 \rangle = \left( 0, \frac{K_4}{K_1}, \frac{2g}{K_1}, 0, 0 \right) \\
|\psi_2\rangle &= \frac{1}{H_0 - E_0 \cdot \mathbb{I}} Q V \frac{1}{H_0 - E_0 \cdot \mathbb{I}} Q V | \psi_0 \rangle = \left( 0, 0, 0, -\frac{2\sqrt{2}K_4K_3}{K_1K_2}, \frac{4igK_4}{K_1K_2} \right)
\end{aligned} \tag{3.58}$$

where

$$\begin{aligned}
K_1 &= g^2 + (2\delta_{lc} - i\kappa)(i\Gamma + 2\delta_{ac} - 2\delta_{lc}) \\
K_2 &= g^2 + (2\delta_{lc} - i\kappa)(i\Gamma + 2\delta_{ac} - 4\delta_{lc} + i\kappa) \\
K_3 &= g^2 - (\Gamma - 2i(\delta_{ac} - \delta_{lc})) \\
K_4 &= \Gamma - 2i\delta_{ac} + 4\delta_{lc} + \kappa
\end{aligned} \tag{3.59}$$

and  $Q = \mathbb{I} - |\psi_0\rangle \langle \psi_0|$  is an operator which projects onto the subspace orthogonal to the state  $|\psi_0\rangle$ . In other words, we apply the inverse operator only to the strongly coupled manifold, since with the  $|\psi_0\rangle$  included, the  $H_0$  is a singular matrix.

The ground state becomes:

$$\begin{aligned}
|\psi_t\rangle &= |g, 0\rangle + |\psi_1\rangle + |\psi_2\rangle + \dots \\
E_t &= \delta l c + E_1 + E_2 + \dots
\end{aligned}
\tag{3.60}$$

In the lab, we would like to measure the cavity transmission and two-photon correlation function,  $g_2(0)$ , of an empty cavity,  $g = 0$ , and the cavity with an atom,  $g \neq 0$ , in the weak probe limit. The first order perturbation theory with the Hamiltonian  $H_0$  written in the one excitation manifold, can already show the vacuum Rabi splitting of the bare cavity transmission as shown in Fig. 3.11. The second order perturbation theory with the Hamiltonian  $H_0$  written in the two excitation manifold reveals the intrinsic nonlinearity of the JCH with the sub-Poissonian  $< 1$  probability of observing two-photons leaking out of the cavity at the same time. This is the signature of the cavity blockade we have discussed before. The cavity transmission and the  $g_2(0)$  can be found using our previous results from the non-Hermitian perturbation theory:

$$\begin{aligned}
T &\propto \langle \psi_t | a^\dagger a | \psi_t \rangle \propto \langle g, 1 | \psi_t \rangle^2 \\
g_2(0) &\propto \frac{\langle \psi_t | a^\dagger a^\dagger a a | \psi_t \rangle}{\langle \psi_t | a^\dagger a | \psi_t \rangle^2} \propto \frac{\langle g, 2 | \psi_t \rangle^2}{\langle g, 1 | \psi_t \rangle^4}
\end{aligned}
\tag{3.61}$$

These expressions are applicable up to their respective excitation manifolds. The Fig. 3.11 shows example spectra for a weakly probed JCH.

This method of approximating the cavity transmission and photon statistics is extremely useful since it does not require us to know the full spectrum of states for the  $H_0$  and allows for dissipation. In addition, it allows for the addition of many more states to the Hamiltonian, as long as we can treat the coupling to those states perturbatively and recursively through

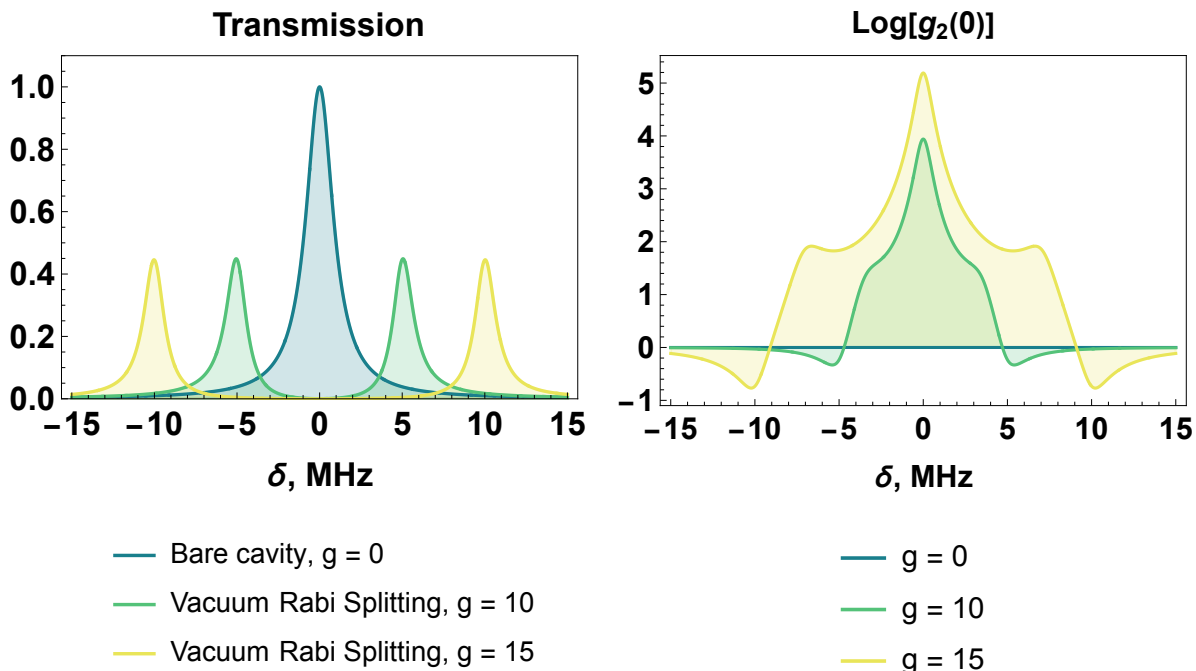


Figure 3.11: Left: Cavity transmission for the bare cavity and cavity with an atom in a JCH with  $g = 0, 10, 15$  MHz, right: second order correlation function for photons with  $g = 0, 10, 15$  MHz. Here the  $\Gamma = 1$  MHz and  $\kappa = 2$  MHz, and the  $g_2(0)$  is plotted in  $\log_{10}$

the application of our method above. We will use it below to derive the expression for cavity transmission and  $g_2(0)$  for our hybrid CQED, which has thousands of atoms with more than two levels and an additional quantized mode for mm-wave photons.

### 3.4 Our hybrid cavity QED Hamiltonian

In this section, we will apply the tools we have learned to construct a Hamiltonian for our experiment and calculate its spectrum. Our goal is to entangle and inter-convert single optical and mm-wave photons, which requires the strong interaction regime  $g > \sqrt{\Gamma\kappa}$  for both optical and mm-wave modes. Before using the non-Hermitian perturbation theory on our hybrid system, it is useful to overview a hydrogenic atom in the CQED context.

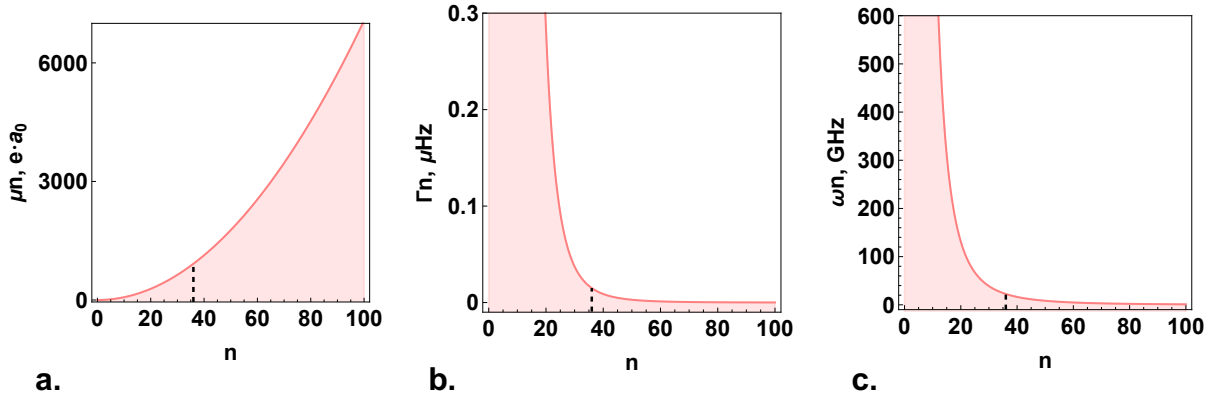


Figure 3.12: Properties of a hydrogenic atom as a function of a quantum number  $n$ : **a.** the dipole moment, **b.** scattering rate, **c.** frequency (Larmor frequency)

### 3.4.1 Our matter couplers and their strengths

The matter coupler we use in our system is a  $^{85}\text{Rb}$  atom. There are a lot of advantages of using neutral atoms in cavity-QED systems: they are identical by nature, commercially available, and have useful transitions. The  $^{85}\text{Rb}$ , specifically, is an alkali atom with an approximately hydrogenic structure, which helps to keep the calculations relatively simple. It has a high natural abundance and a well-documented spectrum of closed and open transitions matched with commercially available lasers. Note that  $^{87}\text{Rb}$  has been historically more popular in comparison to  $^{85}\text{Rb}$  in cold atoms experiments, primarily due to its scattering length for producing BECs and more resolved hyperfine structure for laser cooling. But for us, the  $^{85}\text{Rb}$  is a perfectly convenient choice of an atom.

The drawback of using neutral atoms in CQED systems is their weak dipole coupling strength. The coupling between the 780 nm optical photon and a single  $^{85}\text{Rb}$  atom transition  $|5s\rangle \rightarrow |5p\rangle$  is limited by the fundamental fact that the fine structure constant,  $\alpha \approx \frac{1}{137}$ , is a small number [101].

For a hydrogenic atom in a quantum state  $n$ , the dipole moment, the scattering rate and Larmor frequency of the transition  $n \rightarrow n + 1$  are:

$$\begin{aligned}
\mu_n &= \left( \frac{e\hbar}{m_e c \sqrt{2}} \right) \frac{n^2}{\alpha} \\
\Gamma_{n \rightarrow n+1} &= \left( \frac{2 m_e c}{3 \hbar} \right) \frac{\alpha^5}{n^5} \\
\omega_{n \rightarrow n+1} &= \left( \frac{m_e c^2}{\hbar} \right) \frac{\alpha^2}{n^3}
\end{aligned} \tag{3.62}$$

where the atom is assumed to be in a circular state with  $l = n - 1$  and  $m = l$  [102]. Fig. 3.12 illustrates the trends in  $\mu_n$ ,  $\Gamma_{n \rightarrow n+1}$  and  $\omega_{n \rightarrow n+1}$  as a function of quantum number  $n$ . These scalings are incredibly important for designing experiments that reach a specific parameter space. For example, we aimed at the highest possible dipole moment - for strong atom-light interaction; high frequency of the transition - for low thermal background; and lowest decay rate of the transition - for high cooperativity.

If we fix the volume of the cavity mode to be  $V_0 = (\lambda/2)^3$ , the electric field due to a single photon in this mode volume is:

$$E_0 = \sqrt{\frac{\hbar \omega_n}{\epsilon_0 V_0}} = \sqrt{\frac{\hbar^2 \omega_n 4\pi c \alpha}{e^2 V_0}} = \left( \frac{2m_e^2 c^3}{\pi \hbar} \right) \frac{\alpha^{9/2}}{n^6} \tag{3.63}$$

Then the coupling strength is:

$$g_0 = \frac{\mu_n E_0}{\hbar} = \left( \frac{2c^2 m_e}{\pi \hbar} \right) \frac{\alpha^{7/2}}{n^4} \tag{3.64}$$

which has a dimension of frequency. In order to evaluate the size of this coupling, we need to compare it to another parameter of the same unit. For some experiments, it is helpful to

compare  $g_0$  to the bare frequency of the transition  $w_n$ . This is the case for experiments trying to reach ultra-strong coupling and deep-strong regimes. In that case, the new dimensionless coupling strength is:

$$\tilde{g} = \frac{g_0}{\hbar\omega_n} \propto \frac{\alpha^{3/2}}{n} \quad (3.65)$$

Eq. 3.65 clearly shows how small the coupling parameter is, fundamentally, since  $\alpha$  is raised to a positive power  $> 1$ . So the  $n \rightarrow n + 1$  transitions of cold atoms even in high Rydberg states are not the way to reach the ultra-strong coupling regime. The Josephson Junctions, however, can do this due to lower dimensionality of  $\alpha$  in the coupling strength, as shown in this work [101].

As I have mentioned before, to reach the strong coupling regime what we need is  $\eta = \frac{g_0^2}{\kappa\Gamma} > 1$ . Since it is not straightforward to evaluate the unloaded quality factor of a superconducting cavity  $\propto 1/\kappa$ , we will look at the following quantity:

$$\tilde{g}_0 = \frac{g_0}{\Gamma_{n \rightarrow n+1}} \propto \frac{n}{\alpha^{3/2}} \quad (3.66)$$

which also needs to be  $> 1$  for Rabi oscillations to be resolvable. The  $\tilde{g}_0$  in contrast to  $\tilde{g}$  can easily be larger than one. And as long as  $\kappa$  is comparable to  $\Gamma$ , the cooperativity of this system can be  $> 1$ , signifying the strong coupling regime.

The Eq. 3.62 was derived using Bohr's atomic orbital picture followed by Kepler's equations, and they can only be applied to high  $n \gg 1$  circular Rydberg orbits. The conclusion from this exercise is that the dipole moment of the atom-light interaction is low by nature. But

with some sophisticated engineering, we can reach the strong coupling regime through the following routes:

**Decreasing the mode volume  $V_0 < (\lambda/2)^3$ :** It can be done either by reducing the dimension  $3D \rightarrow 2D$  of the cavity or by engineering exotic cavities, see Chapter. 4. Note that the polarizability of Rydberg states is  $\propto n^7$ , so as the mode volume of the cavity decreases, the Rydberg atoms are getting closer to the cavity surfaces. This makes them more susceptible to AC stark shifts and broadening.

**Going to higher Rydberg states:** this route also has a limit of dephasing from the polarizability close to surfaces.

**Using more than one atom:** Since all of the atoms are identical, and their size is  $< \lambda$ , the collective excitation of many atoms can be used to couple to a photon in a cavity, leading to a  $\sqrt{N_{at}}$  boost in the coupling strength

### 3.4.2 *Collective VRS and Rydberg EIT*

On the optical side our coupling,  $g_0$ , is  $\approx 600$  kHz and the decay rate,  $\Gamma$ , is  $\approx 6$  MHz <sup>3</sup>. To achieve the strong-coupling regime on this transition we utilize a collective coupling of an ensemble of  $N$  atoms to a single mode of the cavity. As shown in Fig. 3.13, in the weak probe limit a probability of a single-atom excitation is multiplied by  $\sqrt{N}$  [103]. This is another manifestation of interference. Since all of the atoms are equivalent to the photon, which atom gets excited is not relevant as long as there is a single excitation in the system. In this collective excitation basis, we can rewrite the non-Hermitian JCH as follows:

---

3. Here, the factors of  $2\pi$  are omitted

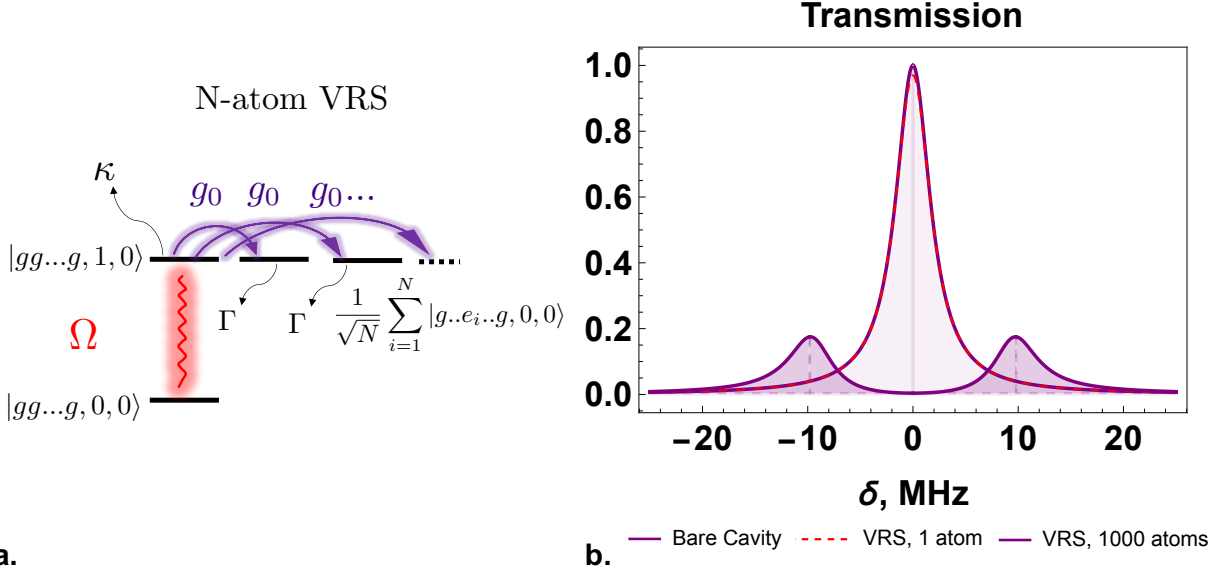


Figure 3.13: Many-atom VRS: **a.** Energy levels involved in the system, **b.** The VRS spectrum obtained using non-Hermitian perturbation theory.

$$\begin{aligned}
 H_{col} = & \hbar(w_a + i\frac{\Gamma}{2})\Sigma_{EE} + \hbar(w_c + i\frac{\kappa}{2})a_{opt}^\dagger a_{opt} + \hbar g_0 \sqrt{N}(\Sigma_{GE} a_{opt}^\dagger + a_{opt} \Sigma_{EG}) \\
 & + \hbar \Omega(t)(a_{opt}^\dagger + a_{opt})
 \end{aligned} \tag{3.67}$$

where  $\Sigma_{AB} = \frac{1}{\sqrt{N}} \sum_N |A\rangle \langle B| = \frac{1}{\sqrt{N}} \sum_N \sigma_{AB}^i$ . To make our lives easier we will define all collective linear operators with respect to the collective ground state. Then the Hamiltonian simplifies to:

$$\begin{aligned}
 H_{col} = & \hbar(w_a + i\frac{\Gamma}{2})\Sigma_E^\dagger \Sigma_E + \hbar(w_c + i\frac{\kappa}{2})a_{opt}^\dagger a_{opt} + \hbar g_0 \sqrt{N}(\Sigma_E a_{opt}^\dagger + a_{opt} \Sigma_E^\dagger) \\
 & + \hbar \Omega(t)(a_{opt}^\dagger + a_{opt})
 \end{aligned} \tag{3.68}$$

It is worth noting that, even though the  $\sigma_{eg}$  is a spin operator for a two-level atom which leads to the nonlinearity of a JCH, the collective spin operator  $\Sigma_{EG}$  is linear and resembles

a harmonic oscillator as  $N \rightarrow \infty$ . So even though we gain a lot in coupling strength  $g_0 \rightarrow g_0\sqrt{N}$ , which can be seen in significantly larger VRS in Fig. 3.13b, we lose the nonlinearity. This means that the system is not sensitive to the number of photons in a cavity since everything scales linearly like in classical wave physics. And, therefore, there is no blockade that could lead to effective interactions between photons.

We resolve our loss of nonlinearity in the optical domain, by gaining it back in the mm-wave domain, where our system goes back to resembling the JCH. As we will see below, with the use of the Rydberg Electromagnetically Induced Transparency (EIT) we not only hybridize the two frequency bands but also translate the nonlinearity from the mm-wave band into the optical one. Let's review the EIT in a three-level atom we covered in Chapter. 2 classically, now in a system with an ensemble of atoms using the non-Hermitian perturbation theory. For clarity, I included a co-rotating frame transformation matrix I used in diagonalizing our matrix in a collective basis below:

$$U_{EIT} = \begin{pmatrix} 1 & 0 & 0 & 0 & \dots \\ 0 & e^{i\omega_l t} & 0 & 0 & \dots \\ 0 & 0 & e^{i\omega_l t} & 0 & \dots \\ 0 & 0 & 0 & e^{i(\omega_l + \omega_B)t} & \dots \\ \dots & \dots & \dots & \dots & \dots \end{pmatrix} \quad (3.69)$$

We use the Rydberg-EIT mechanism for two main reasons in our experiment. First, it gives us access to the Rydberg states, which have high dipole coupling strength with mm-wave photons. Second, the EIT scheme allows us to eliminate the broad linewidth of the  $|5p\rangle$  state. As shown in Fig. 3.14, using a classical blue beam that couples to the desired Rydberg state, we can get a “dark” state polariton at zero detuning with significantly smaller linewidth than the  $|5p\rangle$  state or the bare cavity. This is due to the fact that, to the first order, the

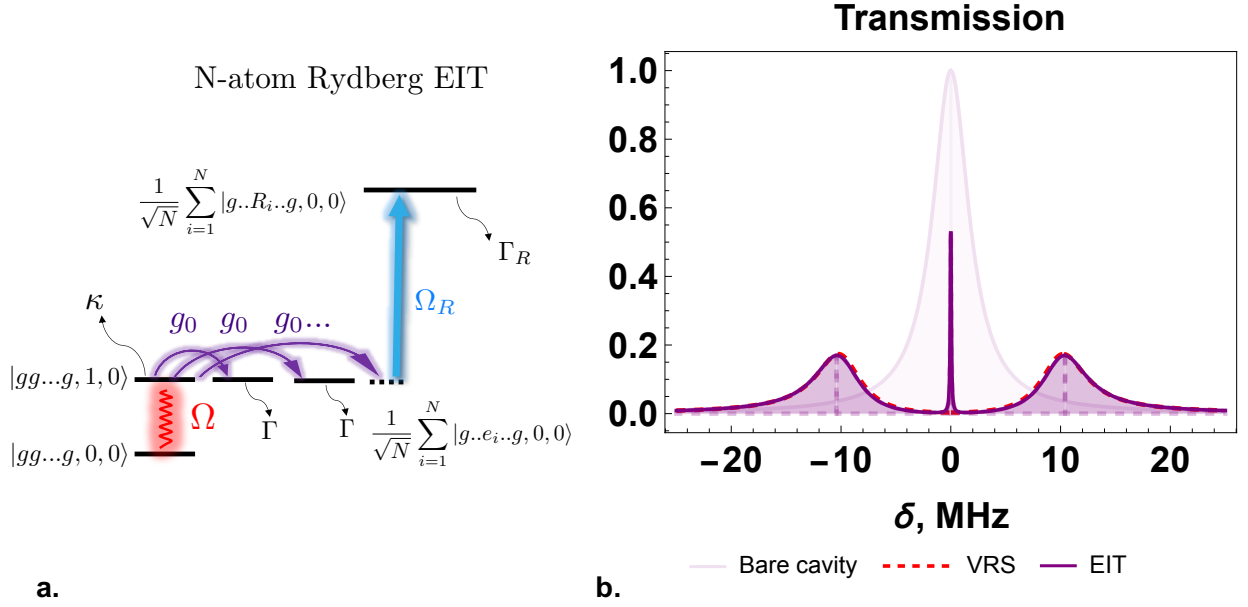


Figure 3.14: Many-atom Rydberg EIT: **a.** Energy levels involved in the system, **b.** The EIT spectrum obtained using non-Hermitian perturbation theory.

linewidth of the dark state is:

$$\Gamma_D = \kappa \cos^2 \theta_D + \Gamma_R \sin^2 \theta_D \quad (3.70)$$

where  $\tan \theta_D = \frac{g}{\Omega_b}$ ,  $g$  is the collective coupling,  $\Omega_b$  is the Rabi frequency of the blue beam, and  $\Gamma_R$  is the linewidth of the Rydberg state, which tends to be very narrow as we saw in our derivations above. By changing the  $\theta_D$  we can rotate the dark polariton from being more "photon-like" to more "Rydberg-like", as a result changing its linewidth or lifetime in the system. This fact is used for quantum information technology, especially if one wants to utilize Rydberg-Rydberg interactions between the polaritons, which can then be mapped onto photon-photon interactions.

With the blue beam and the EIT mechanism included, our full linear Hamiltonian now becomes:

### Hybrid system, 1 excitation

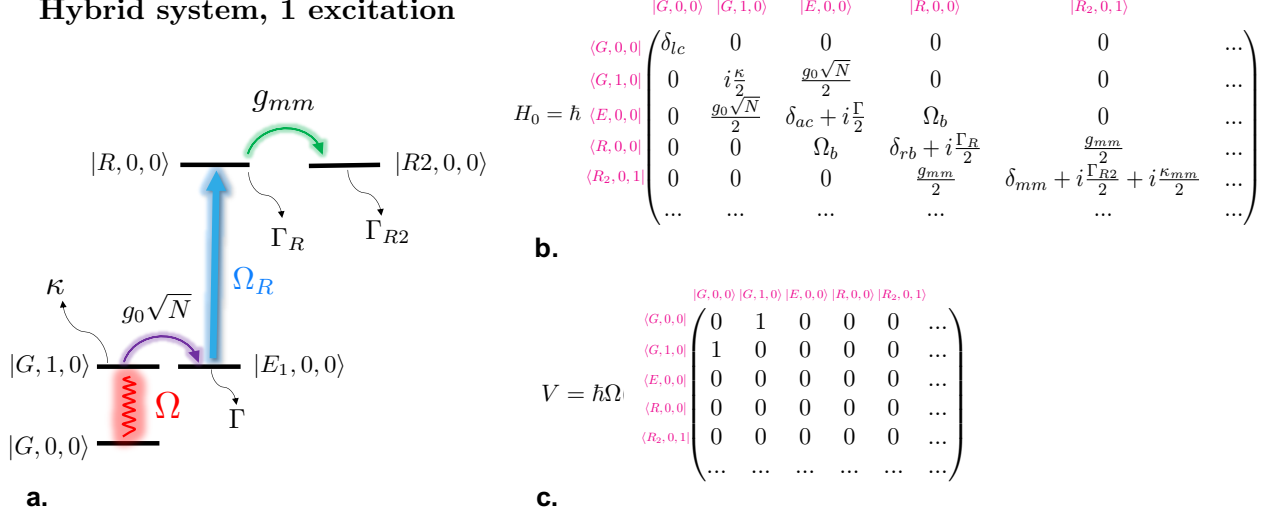


Figure 3.15: Hybrid system with optical and mm-wave photons up to one excitation: **a.** Energy levels involved in the system, **b.** The diagonalized Hamiltonian, **c.** The perturbation

$$\begin{aligned}
H_{col} = & \hbar(w_a + i\frac{\Gamma}{2})\Sigma_E^\dagger\Sigma_E + \hbar(w_R + i\frac{\Gamma_R}{2})\Sigma_R^\dagger\Sigma_R + \hbar(w_c + i\frac{\kappa}{2})a_{opt}^\dagger a_{opt} \\
& + \hbar g_0\sqrt{N}(\Sigma_E a_{opt}^\dagger + a_{opt}\Sigma_E^\dagger) + \hbar\Omega_b(t)(\Sigma_E\Sigma_R^\dagger + \Sigma_R\Sigma_E^\dagger) \\
& + \hbar\Omega(t)(a_{opt}^\dagger + a_{opt})
\end{aligned} \tag{3.71}$$

where  $\Sigma_R = \frac{1}{\sqrt{N}}\sum_N \sigma_{RG}^i$ . The only term in the Eq. 3.71 that can add and subtract photonic excitations to the systems without worrying about the atomic energy levels is the  $\hbar\Omega(t)(a_{opt}^\dagger + a_{opt})$ . All other terms require a change in the energy level of our collective "fuzzy" atom, and this is a key towards getting a nonlinear term with  $> 2$  harmonic oscillator operators in the next section.

### 3.4.3 MM-wave and optical hybrid CQED system

We are now ready to include the mm-wave mode into our system and construct the full Hamiltonian.

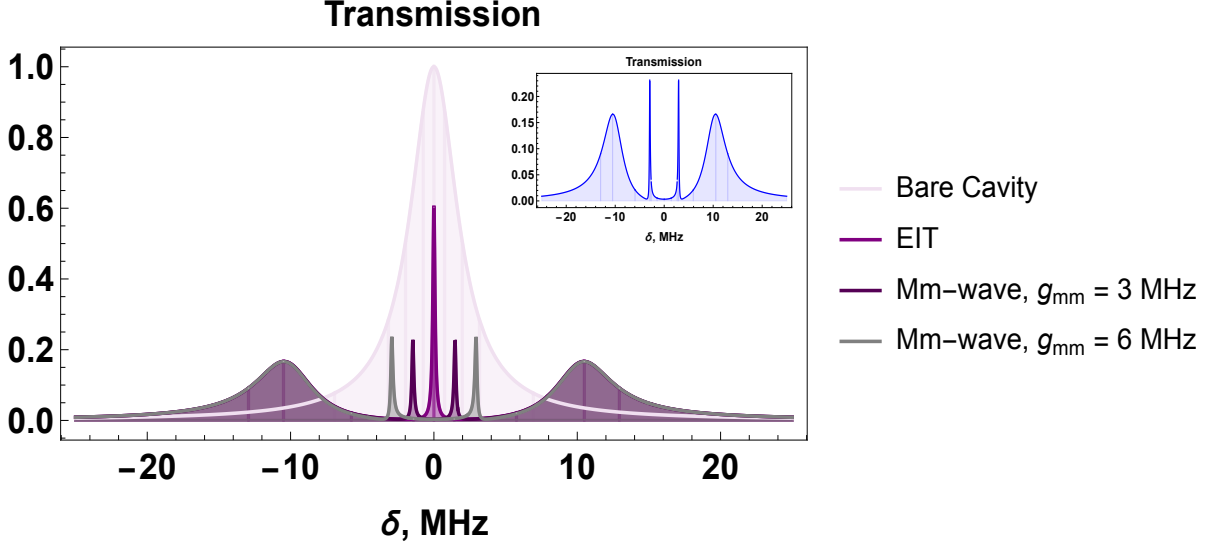


Figure 3.16: The splitting of the EIT line due to coupling to the vacuum of the mm-wave cavity. Here the  $\Gamma = 6$  MHz,  $\kappa = 4$  MHz,  $\kappa_{mm} = 0.1$  MHz,  $\Gamma_R = \Gamma_{R2} = 0.04$  MHz. The inset shows one such spectrum with  $g_{mm} = 6$  MHz.

$$\begin{aligned}
H_{mm} = & \hbar(w_a + i\frac{\Gamma}{2})\Sigma_E^\dagger\Sigma_E + \hbar(w_R + i\frac{\Gamma_R}{2})\Sigma_R^\dagger\Sigma_R + \hbar(w_{R2} + i\frac{\Gamma_{R2}}{2})\Sigma_{2R}^\dagger\Sigma_{2R} \\
& + \hbar(w_c + i\frac{\kappa}{2})a_{opt}^\dagger a_{opt} + \hbar(w_c^{mm} + i\frac{\kappa_{mm}}{2})a_{mm}^\dagger a_{mm} \\
& + \hbar g_0\sqrt{N}(\Sigma_E a_{opt}^\dagger + a_{opt}\Sigma_E^\dagger) + \hbar g_{mm}(\Sigma_R\Sigma_{R2}^\dagger a_{mm}^\dagger + a_{mm}\Sigma_R^\dagger\Sigma_{R2}) \\
& + \hbar\Omega_b(t)(\Sigma_E\Sigma_R^\dagger + \Sigma_R\Sigma_E^\dagger) + \hbar\Omega(t)(a_{opt}^\dagger + a_{opt})
\end{aligned} \tag{3.72}$$

The energy levels and the diagonalized Hamiltonian, including one excitation manifold, are displayed in Fig. 3.15. The corresponding cavity transmission spectrum of the system is shown in Fig. 3.16. The splitting of the EIT peak in this system is a result of strong coupling between the Rydberg atom and the mm-wave cavity mode. We don't need there to be a photon to see the splitting as long as the coupling is sufficiently strong. This is opposite to the Autler-Townes splitting due to the presence of mm-wave wave photons we will derive later, which is a consequence of linear physics.

Now, to see that we have regained the nonlinearity in our system, we diagonalize the Hamil-

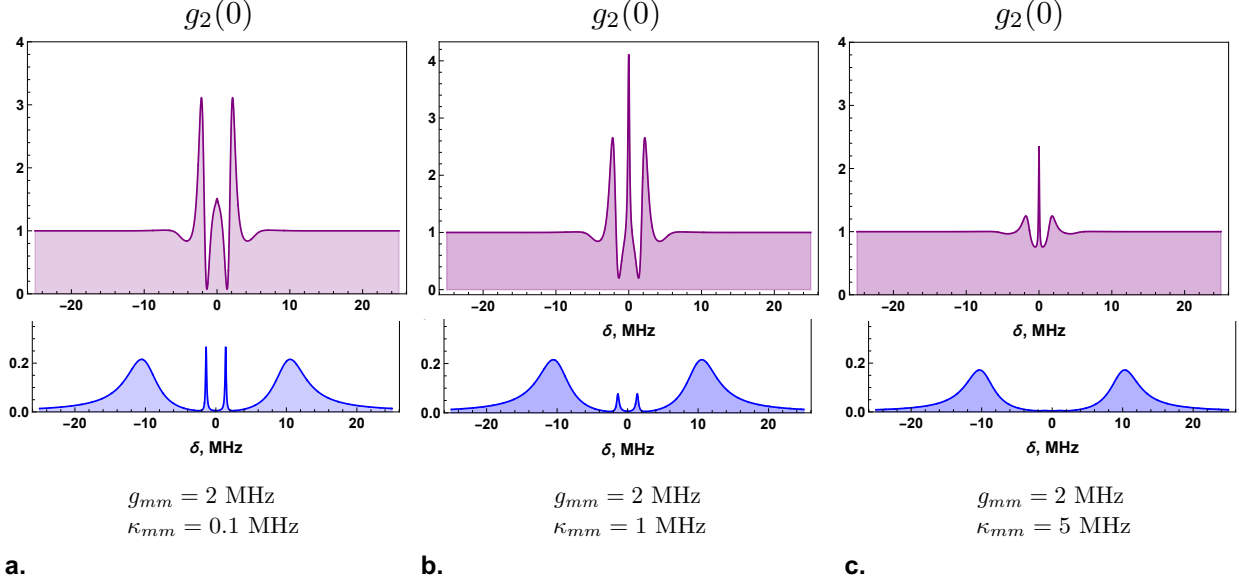


Figure 3.17: The cavity spectrum and the  $g_2(0)$  of the hybrid system for interfacing single mm-wave and optical photons obtained using the non-Hermitian perturbation theory for various single mm-wave photon-Rydberg atom couplings.

tonian and include the two-excitation manifold. The  $g_2(0)$  spectra in Fig. 3.17 were obtained using the non-Hermitian perturbation theory. As expected, we can see the sub-Poissonian photon statistics at frequencies that correspond to dark polaritons interacting with the mm-wave cavity. This effectively translates into optical photon-photon interactions since the nonlinearity in mm-wave manifold shifts linearly spaced optical energy levels. In Fig. 3.17 the linewidth of the mm-wave cavity,  $\kappa_{mm}$ , increases from a to c, while the coupling strength,  $g_{mm}$  is kept constant. This leads to a decrease in the cooperativity from a to c and, therefore, weaker interactions. This can be seen in the shallowness of the dip in  $g_2(0)$  in c vs. a. The code for generating these spectra and others in this chapter can be found here [104].

The perturbative approach to cavity-QED is extremely useful not only as a tool for calculations but also for gaining intuition on which energy states are relevant for the desired science. This is particularly important for hybrid systems like ours, which have a forest of energy states. A more formal treatment of the non-Hermitian perturbation method can be found in the resolvent method for solving open quantum systems [105].

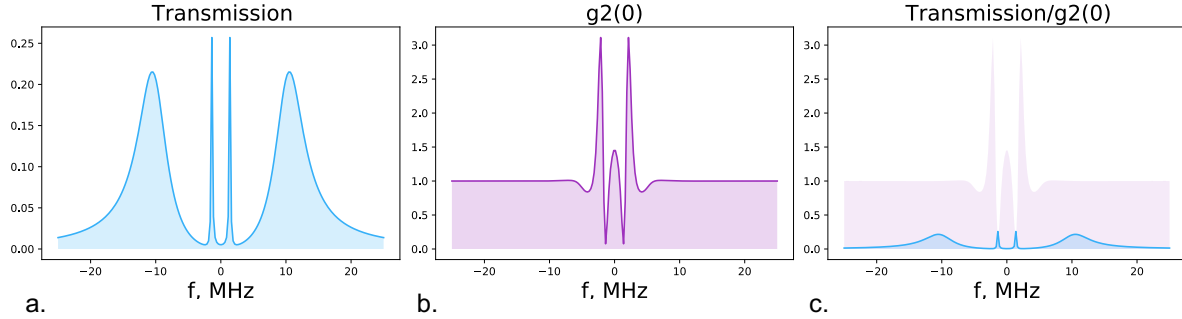


Figure 3.18: Replication of the results using the Master Equation formalism: **a.** Cavity transmission, **b.** Second order correlation function, **c.** the overlap of the cavity transmission with the  $g_2(0)$ .

Once we gained some intuition on engineering Hamiltonians for hybrid photonic systems perturbatively, it can be useful to use Master equation formalism to confirm our results and to explore the time dynamics of some observables. I attached the Qutip code for calculating the transmission spectra and  $g_2(0)$  for our system here [104]. Indeed, as shown in Fig. 3.18, the results match up with our perturbative approach. Moreover, the master equation approach allows for exploring the  $g_2(\tau)$  as a function of  $\tau$ , shown in Fig. 3.19c.

### 3.5 Tracking coherences in many degree linear systems

Another powerful tool for figuring out the cavity transmission spectra in a Hybrid linear quantum system involves tracking coherences of the basis states of the Hamiltonian before the decay, similar to Eq. 3.29. It is not a tool for a formal treatment of unknown Hamiltonian, but it can be used to numerically simulate all of the degrees of freedom in our setup since the system is linear. Please note that this method is not meant for deriving nonlinear effective interactions between photons. It is, however, incredibly intuitive and powerful for tracking changes due to variations in the number of atoms, temperature, or other forms of detuning. In this section, we will derive the spectra for the Vacuum Rabi splitting, Rydberg EIT, and Autler-Townes Splitting with the mm-wave light. We will show that the

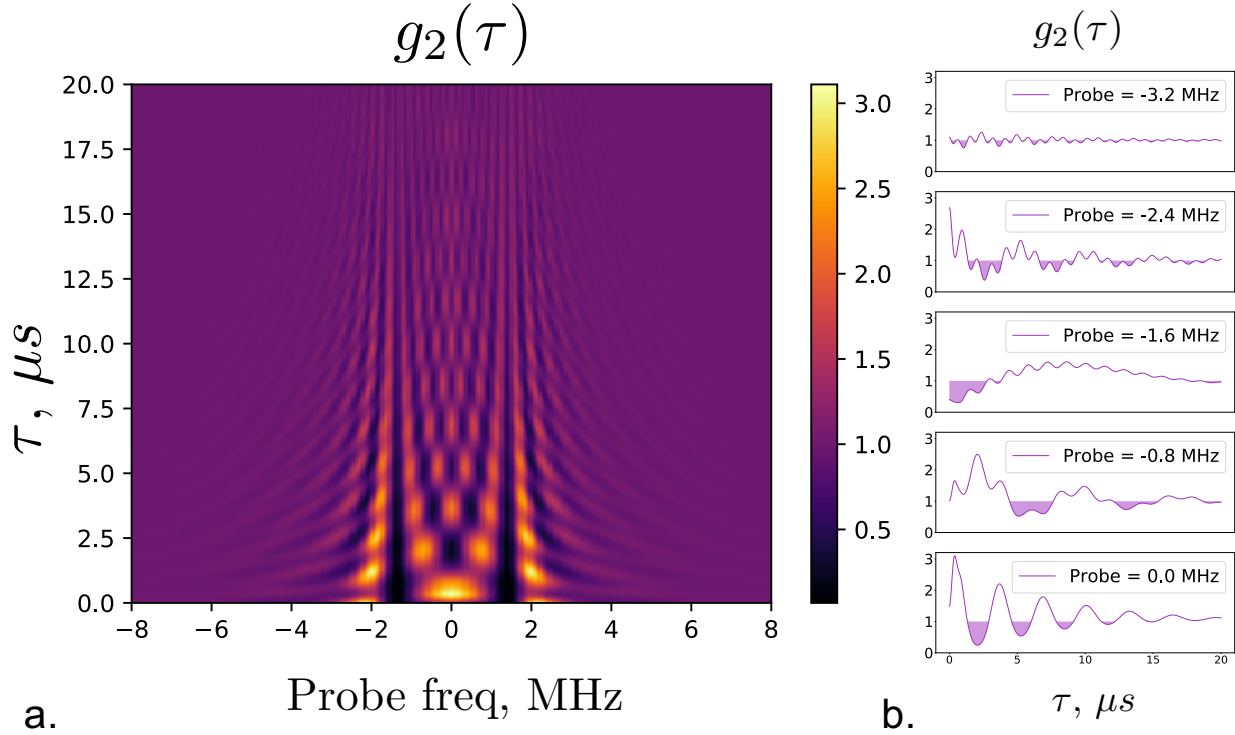


Figure 3.19: Second correlation function of photons at a time  $\tau$ : the probability of detecting two photons leaking out of our cavity separated in time by  $\tau$ .

$N$  atoms act as a harmonic oscillator with a coupling strength  $\sqrt{N}g_0$  and demonstrate how the variation in coupling strength and Doppler effect can manifest as broadening of our lines in the measurement. It is a great parallel to the classical derivations we did in Chapter. 2 but now applied to more complex systems and with the help of numerical calculations.

### 3.5.1 Vacuum Rabi Splitting vs. $N$ of atoms

This calculation only includes states within the 1st excitation manifold for coupling a single cavity mode to  $N$  two-level atoms. I will use the following convention:  $c(t) = |gg\dots g, 1\rangle$  and  $e_i(t) = |g\dots e..g, 0\rangle$  (e.g.  $e_2(t) = |geg\dots g, 0\rangle$ ). The equations which describe the dynamics of the coherences are below:

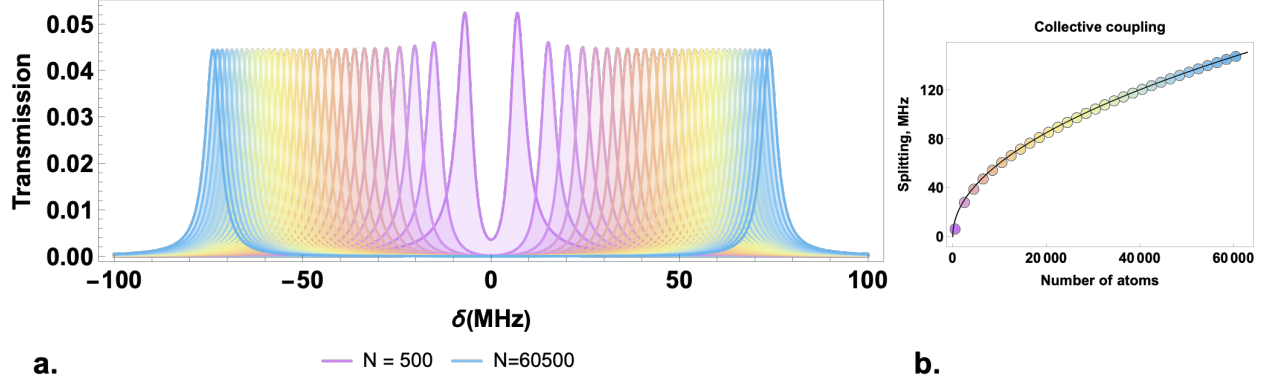


Figure 3.20: Vacuum Rabi splitting as a function of number of atoms in the ensemble with  $\Gamma_R = 25$  kHz,  $\Gamma = 6$  MHz,  $\kappa = 3.5$  MHz,  $g_0 = 0.6$  MHz and  $\delta_{ac} = 0$ .

$$\begin{aligned} \dot{c}(t) &= (i\delta_{lc} + \frac{\kappa}{2})c(t) + \Omega + i \sum_{i=1}^{N_{at}} \frac{g_i^*}{2} e_i(t) \\ \dot{e}_i(t) &= (i(\delta_{lc} + i\delta_{ac}^i) + \frac{\Gamma}{2})e_i(t) + i\frac{g_i^*}{2}c(t) \end{aligned} \quad (3.73)$$

To find the steady state solution, we set  $\dot{e}_i = 0$  and  $\dot{c} = 0$  and plug in the expression for  $e_i(t)$  in  $c(t)$ :

$$c_{ss}(t) = \frac{\Omega}{i\delta_{lc} + \frac{\kappa}{2} + \sum_{i=1}^{N_{at}} \frac{\frac{g_i^* g_i}{4}}{i(\delta_{lc} + \delta_{ac}^i) + \Gamma/2}} \quad (3.74)$$

where  $g_i$  and  $\delta_{ac}^i$  are the atom-light coupling strength and detuning of the  $i^{th}$  atom, respectively. The transmission spectra of the system is  $\propto |c(t)|^2$ , similar to Eq. 3.61.

The Fig. 3.20 shows the vacuum Rabi splitting as a function of the number of atoms. As expected, the splitting follows exactly the  $g_0\sqrt{N}$  with no fitting parameters. Note that the smaller the number of atoms more the splitting deviates from the expression, which is

expected since the collective excitation approaches a harmonic oscillator as  $N \rightarrow \infty$ .

### 3.5.2 EIT Doppler broadening

Here, we will simulate how the temperature of the atomic cloud leads to the broadening of the EIT line. This is a very important phenomenon for our system since the narrow linewidth of the EIT peak is essential to the science we are trying to observe.

Each atom in the ensemble is moving with some velocity  $v_i$  with a statistical probability from the Maxwell-Boltzmann distribution at a temperature  $T$ . Hence, each atomic has a Doppler detunings:

$$\begin{aligned}\delta_{ac}^i &= \frac{v_i}{c} \omega_{opt} \\ \delta_R^i &= \frac{v_i}{c} (\omega_{opt} + \omega_{blue})\end{aligned}\tag{3.75}$$

The equations of motion for an ensemble of three-level atoms coupled to a cavity mode are as follows:

$$\begin{aligned}\dot{c}(t) &= (i\delta_{lc} + \frac{\kappa}{2})c(t) + \Omega + i \sum_{i=1}^{Nat} \frac{g_i^*}{2} e_i(t) \rightarrow 0 \\ \dot{e}_i(t) &= (i(\delta_{lc} + \delta_{ac}^i) + \frac{\Gamma}{2})e_i(t) + i\frac{g_i^*}{2}c(t) + i\Omega_R r_i(t) \rightarrow 0 \\ \dot{r}_i(t) &= (i(\delta_{lc} + \delta_R^i + \frac{\Gamma_R}{2}))r_i(t) + i\Omega_R e_i(t) \rightarrow 0\end{aligned}\tag{3.76}$$

where  $r_i(t)$  corresponds to the Rydberg state of the  $i$ th excited atom. The steady state for the cavity photon is then:

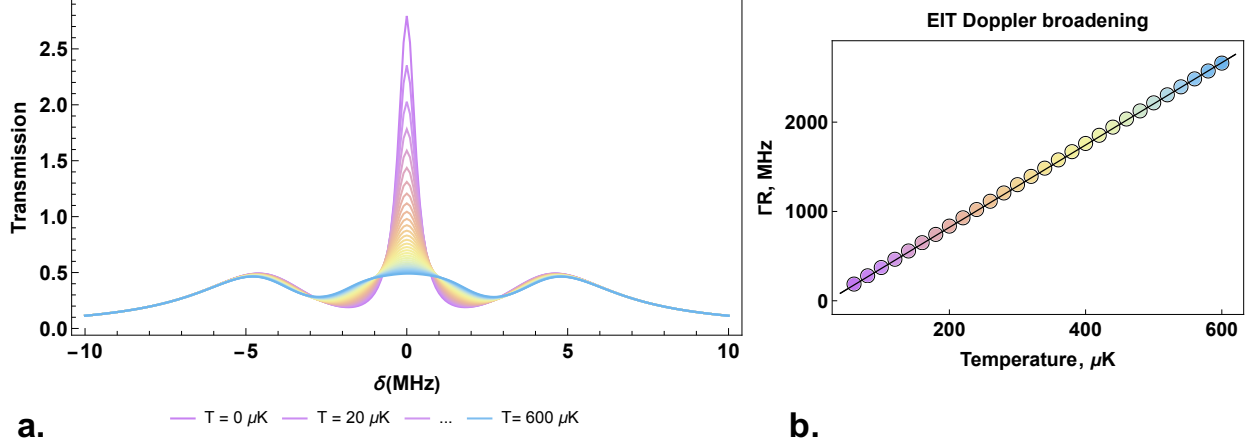


Figure 3.21: The spectra of the electromagnetically induced transparency as a function of the temperature of the atomic cloud with  $\Gamma_R = 25$  kHz,  $\Gamma = 6$  MHz,  $\kappa = 3.9$  MHz,  $g_0\sqrt{N_{at}} = 8$  MHz,  $\delta_R = 0$ ,  $\Omega_R = 2$  MHz and  $\delta_{ac} = 0$ .

$$c_{ss}(t) = \frac{\Omega}{i\delta_{lc} + \frac{\kappa}{2} + \sum_{i=1}^{N_{at}} \frac{\frac{g_i^* g_i}{4}}{\frac{\Omega_R^2}{i(\delta_{lc} + \delta_{ac}^i) + \frac{\Gamma_R}{2}} + i(\delta_{lc} + \delta_{ac}^i) + \Gamma/2}} \quad (3.77)$$

The Fig. 3.21 shows the broadening of EIT spectra as a function of the temperature of the atomic cloud. The relationship between the effective Rydberg linewidth acquired from the fit and the temperature is linear [106]. It is crucial to cool down the cloud before attempting any cavity-QED measurements in the strong interaction regime. In these plots, the bare Rydberg linewidth is  $\Gamma_R = 20$  kHz, and already at  $40\mu\text{K}$ , the broadening takes it up to  $\Gamma_R^* = 94$  kHz. At  $160\mu\text{K}$  the  $\Gamma_R^* = 650$  kHz, which would make it impossible to see any mm-wave splitting with  $g_m m < 400$  kHz. The collective suppression of Doppler broadening is

## Autler-Townes Effect

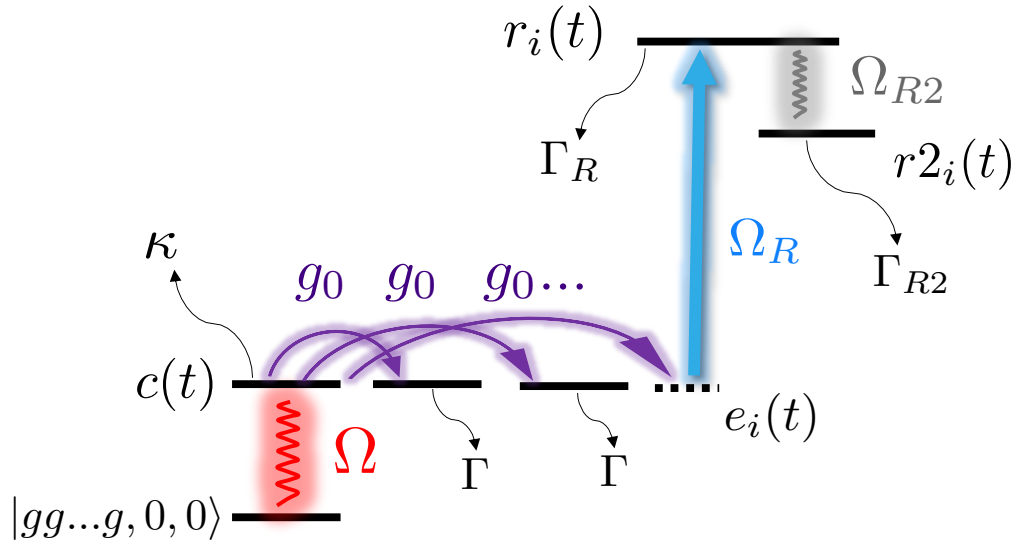


Figure 3.22: The energy states involved in the Autler-Townes splitting of the EIT by the mm-wave population in our hybrid optical/mm-wave system

### 3.5.3 Mm-wave Autler-Townes Splitting

We can also simulate the classical Autler-Townes Splitting of the EIT line due to the coupling of the Rydberg state to the coherent beam of mm-wave photons in our superconducting cavity. Note that this is not the quantum nonlinearity that caused the splitting of the EIT peak in the previous section. There is no cavity blockade involved in the process.

$$\begin{aligned}
 \dot{c}(t) &= (i\delta_{lc} + \frac{\kappa}{2})c(t) + \Omega + i \sum_{i=1}^{Nat} \frac{g_i^*}{2} e_i(t) \rightarrow 0 \\
 \dot{e}_i(t) &= (i(\delta_{lc} + \delta_{ac}^i) + \frac{\Gamma}{2})e_i(t) + i\frac{g_i^*}{2}c(t) + i\Omega_R r_i(t) \rightarrow 0 \\
 \dot{r}_i(t) &= (i(\delta_{lc} + \delta_R^i + \frac{\Gamma_R}{2}))r_i(t) + i\Omega_R e_i(t) + i\Omega_{R2} r2_i(t) \rightarrow 0 \\
 \dot{r2}_i(t) &= (i(\delta_{lc} + \delta_{R2}^i + \frac{\Gamma_{R2}}{2}))r2_i(t) + i\Omega_{R2} r_i(t) \rightarrow 0
 \end{aligned} \tag{3.78}$$

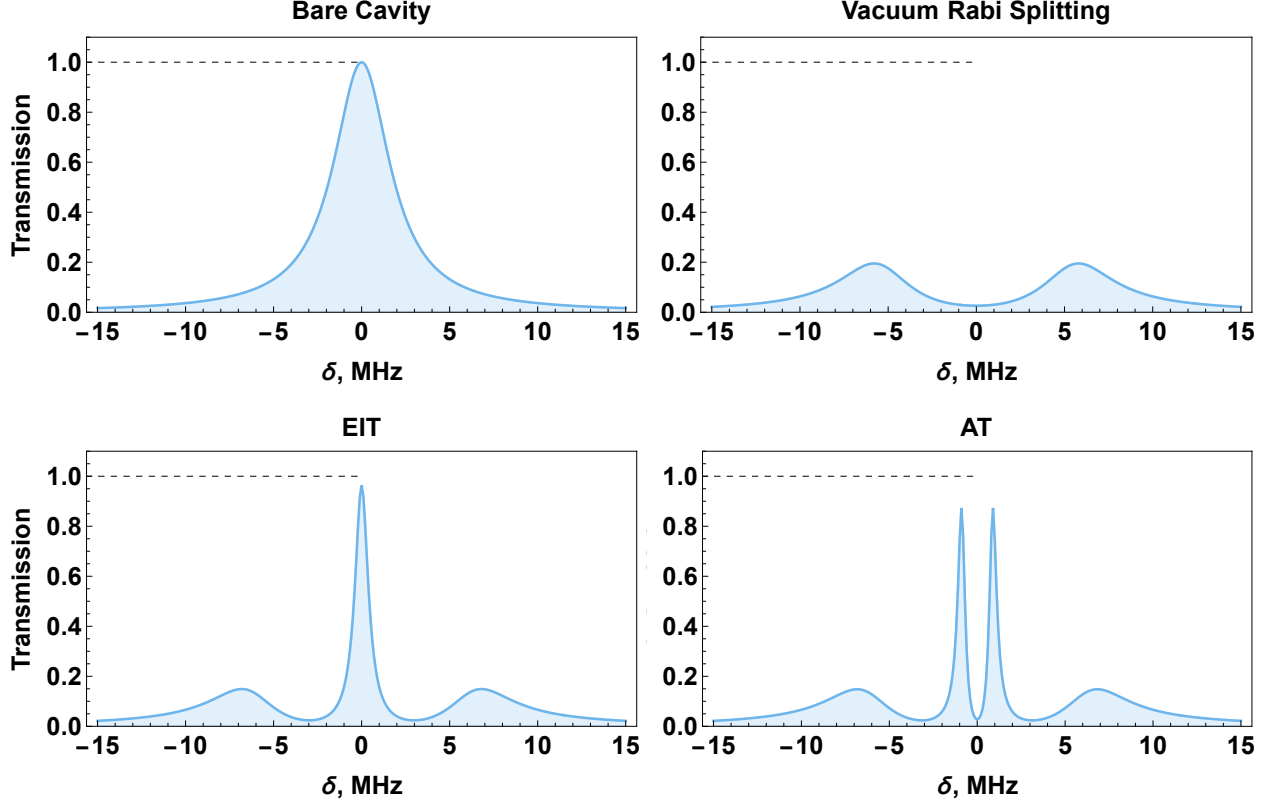


Figure 3.23: The simulated spectra in our hybrid system: bare cavity transmission, vacuum Rabi splitting, EIT and the Autler-Townes splitting with  $\Gamma_R = 25$  kHz,  $\Gamma = 6$  MHz,  $\kappa = 3.9$  MHz,  $g_0\sqrt{N_{at}} = 12$  MHz,  $\Omega_R = 3.2$  MHz,  $\Omega_{R2} = 1$  MHz,  $\delta_{ac} = 0$ ,  $\delta_R = 0$  and  $\delta_{R2} = 0$ .

The solution to the steady state of the cavity is:

$$c_{ss}(t) = \frac{\Omega}{i\delta_{lc} + \frac{\kappa}{2} + \sum_{i=1}^{N_{at}} \frac{ig_i^* g_i}{2(\Gamma + 2i(\delta_{lc} + \delta_{ac}^i)) \left(1 + \frac{4\Omega_R^2(\Gamma_R + 2i(\delta_{lc} + \delta_R^i))}{(2i(\delta_{lc} + \delta_{ac}^i) + \Gamma)((\Gamma_R + 2i(\delta_{lc} + \delta_R^i))(\Gamma_{R2} + 2i(\delta_{lc} + \delta_{R2}^i)) + 4\Omega_{R2}^2)}\right)}} \quad (3.79)$$

This expression can be used to get all of the linear spectra in our hybrid system: bare cavity transmission, vacuum Rabi splitting, EIT, and the Autler-Townes splitting, as shown in Fig. 3.23.

## 3.6 Conclusion

In this chapter, I covered the tools that one can use to gain intuition and tackle complex weakly probed systems involving interacting photons. I used non-Hermitian perturbation theory, Heisenberg, and Master equations to showcase how the same problems can be described using different formalisms. All of these tools have been tremendously useful for designing our experiment, tuning it as we build it up, and numerically exploring our current phase-space.

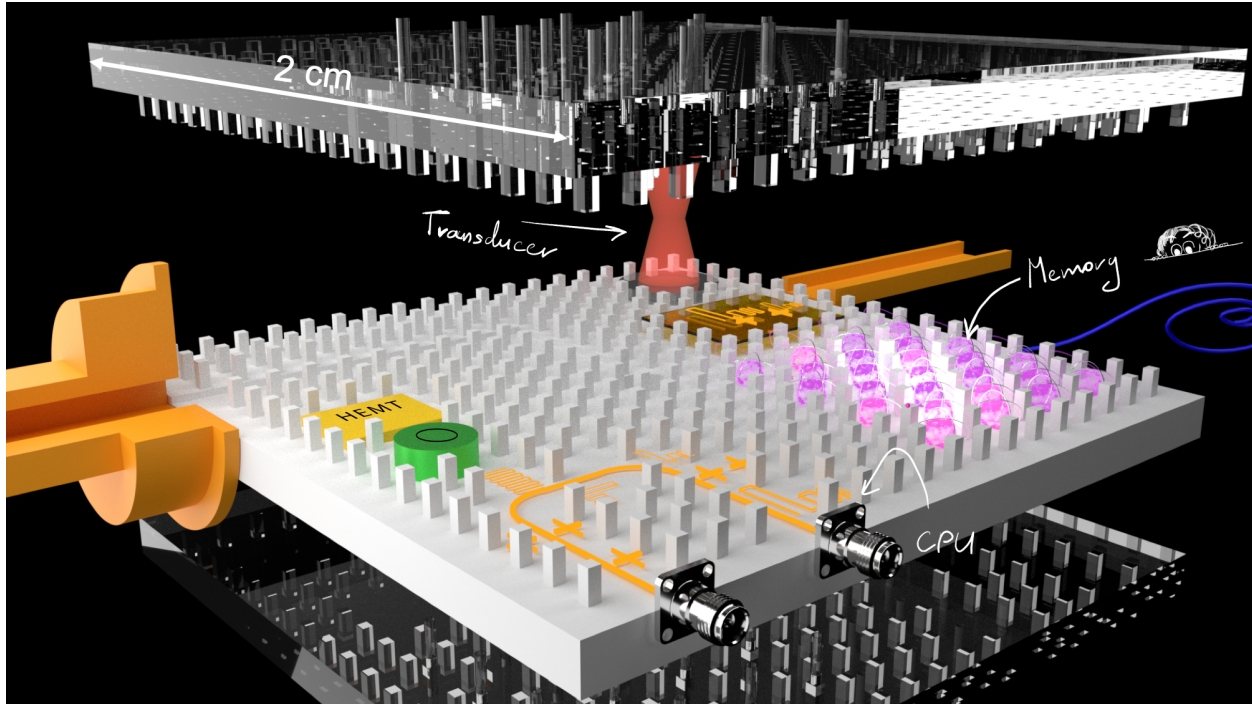


Figure 4.1: Conceptual art of a 3D hybrid quantum computer at 100 GHz. <sup>1</sup>

## CHAPTER 4

### MILLIMETER WAVE QUANTUM TECHNOLOGY

Our experiment is one of many hybrid quantum systems integrating multiple platforms to simultaneously harvest their complementary advantages. In our case, we bridge optical and mm-wave cavity-QED using cold  $^{85}\text{Rb}$  atoms. I have mentioned the utility of developing such hybrid systems. In this chapter, I would like to discuss how mm-wave technology made our system possible and how it has inspired a new wave of hybrid experiments in our group and beyond.

I begin by introducing the mm-wave band and discuss its current role in science and technology. Then, I highlight the advantages of the mm-wave photons for stand-alone and hybrid quantum platforms and outline possible applications beyond quantum information technol-

---

1. The overall scale is true, but some components, including the SMA connectors and circuit components, are resized for artistic convenience

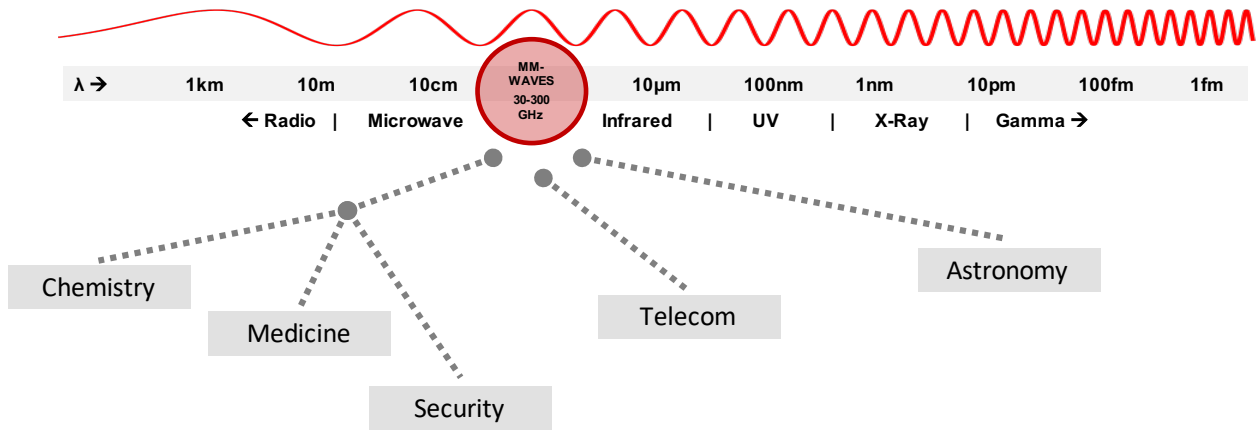


Figure 4.2: The mm-wave band lies between microwave and infrared bands in the Electromagnetic Spectrum. It is essential for many industries.

ogy. Finally, I describe the quantum mm-wave technology that I have developed for both hybrid cavity QED with atoms and circuit-QED experiments at mm-wave frequencies.

The mm-wave band lies in between infrared and microwave domains and usually includes electromagnetic radiation from 30 to 300 GHz and a corresponding wavelength of 1 to 10 mm. Even though it is not popular yet in quantum technology, mm-wave radiation is essential for many fields, as shown in Fig. 4.2.

## 4.1 Mm-wave radiation in other fields

Chemists use mm-wave radiation for vibrational and rotational spectroscopy since the energy scales of  $\sim 1$  meV are full of molecular transitions, as shown in Fig. 4.3. Medical professionals and engineers utilize mm-waves for cancer and body tissue imaging since 100 GHz radiation has a higher spatial resolution than microwaves,  $\sin \theta \approx 1.22 \frac{\lambda}{D}$ , able to penetrate the dielectrics such as clothing and skin for a few millimeters, but are not as harmful to humans as higher frequency waves [107, 108]. The devices in this band are also helpful for monitoring body vitals, such as blood glucose level, since their concentrations can be probed through changes in permittivity.

Mm-waves are also crucial for Astronomy. Our atmosphere has a transparency window in this band, Fig. 4.4. The astronomers find highly elevated and dry locations to build and operate powerful mm-wave telescopes to utilize this window and avoid any residual absorption of the light by water molecules. The large mm-wave array telescopes located in Northern Chile and Hawaii produce enormous data for Astrochemistry. As I mentioned before, a lot of molecules have mm-wave spectra. Astrochemists heavily use this to identify traces of molecules around stellar systems and other galaxies, which tells us about their age and evolution. For example, the recently debated discovery of Phosphine on Venus used mm-wave frequencies to identify the potential trace of the molecule. At this time, scientists are still arguing over the results and implications [109, 110]. Nevertheless, the earth-based mm-wave detectors are powerful tools that give us clues about interstellar evolution.

For astronomers, another important source of high-frequency microwaves is the Cosmic Microwave Background (CMB), which is relic radiation from the early Universe after the Big Bang. Since the CMB temperature is around 2.7 K, the blackbody radiation is high in the mm-wave band. To study the evolution of the early Universe, astronomers build large telescopes at the South Pole [111, 112]. Moreover, to optimize the detection of this faint signal, the telescope's circuitry is cooled down to 4K temperatures. This enables them to use superconducting circuits for efficient detection and maintain a low mm-wave thermal population due to the circuit's temperature.

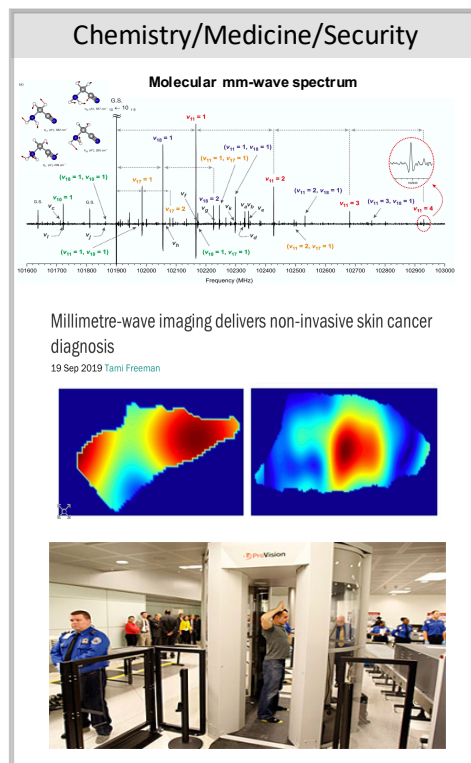


Figure 4.3: Applications in Chemistry: vibrational and rotational spectroscopy of molecules; Medicine: for imaging; Security: for metal detectors at the airport TSA.

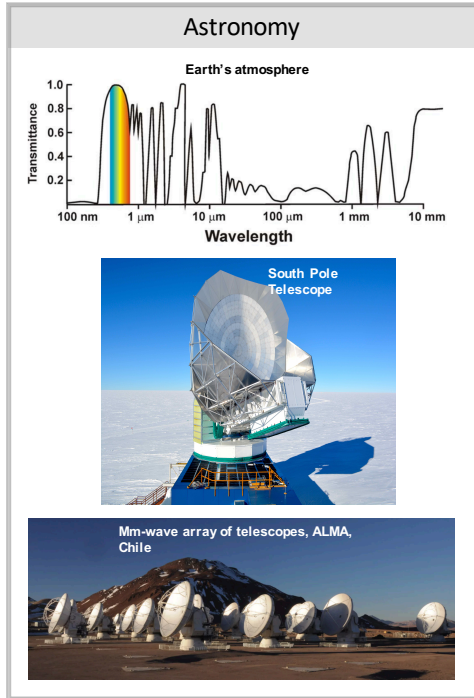


Figure 4.4: Astronomy heavily relies on mm-wave detection both for Astrochemistry and studying the evolution of the Universe after the Big Bang

In industry, mm-wave frequencies have been used for decades in radar technology and security. At the airports, we have all experienced TSA machines during pre-COVID times, utilizing mm-wave photons to reflect off metallic objects while not being too invasive for passengers. And the fact that hazardous chemicals have characteristic resonances in this frequency band has contributed to using mm-wave detectors for dangerous substance control.

Finally, the field that has made the most significant impact in mm-wave technology in recent years is the

Telecom [113, 114]. Communication companies have made the mm-wave band the new frontier. As connectivity became a big part of not only science and technology but also of our everyday life, big Telecom

companies realized that we are running out of bandwidth in LTE and 4G. And with our insatiable desire for speed and remote access, something drastic has to happen for technology to move forward. So this push towards higher bandwidths and low latency created our current race for 5G. As the communication band gets higher in frequency, it promises faster communication and widespread internet of things, smart cities, remote surgeries, safe self-driving cars. The last row of the Radio Spectrum of the United States Frequency Allocation, Fig. 4.5, has only been recently bought up in a bidding war between various companies.

One might ask: why do we care? The mm-wave technology was limited and prohibitively expensive until the recent interest of Telecom and progress in other fields have made the mm-wave technology more available even during the few years of my Ph.D. The technological advancement and broader availability of detectors and RF components are encouraging for

mm-wave quantum devices' future development.

## 4.2 Millimeter wave technology and its potential quantum applications

The mm-wave band is not very well explored in quantum systems. There have been pioneering works in the 80s all the way up to the 2000s by Heroche, Rempe [44, 45] and others in high-frequency microwave masers and quantum entanglement, which have revolutionized quantum science and jump-started the fields of Rydberg cavity-QED and eventually circuit-QED. Since then, the area has been relatively quiet, but not for long. Here are the few key advantages that mm-wave photons could bring for quantum platforms.

**More accessible temperature requirements:** At 7 K, there are less than one thermal photons at 100 GHz, and at 1 K, there is almost zero. This means that reaching a quantum regime or zero thermal photon background in the mm-wave band only requires modest cryogenic temperature. It could drastically reduce the cost of quantum systems by getting rid of dilution refrigerators, limiting the use of the non-renewable source of Helium which is depleting and expensive, and potentially democratize quantum science, which is currently only accessible to very few.

Operating at higher frequencies would be highly beneficial for current circuit-QED exper-

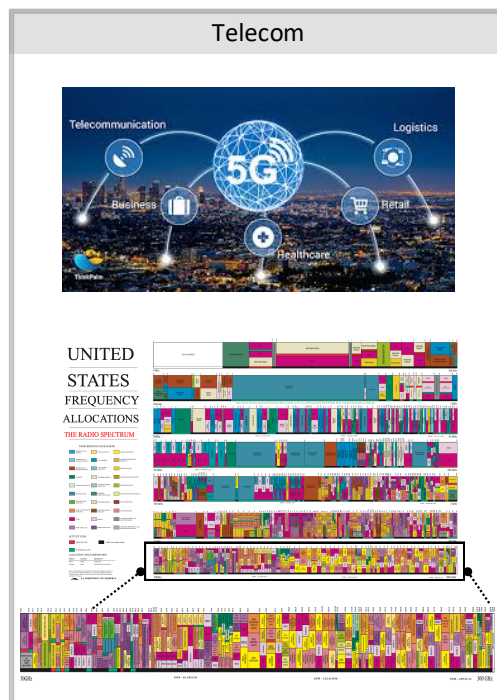


Figure 4.5: Telecommunication industry has recently bought up the mm-wave band for larger bandwidth and lower latency in 5G

iments, which normally run in the microwave regime. With the use of superconducting materials with higher  $T_c$  like Nb ( $T_c = 9.2\text{K}$ ), circuit-QED would benefit dramatically from orders of magnitude higher cooling power available in cryostats at 4K. We could build larger and more complex systems that bridge together disparate quantum platforms while maintaining low noise thermal background.

**Impact on other fields:** Quantum mm-wave devices would benefit numerous other areas of science and technology. High-efficiency parametric amplifiers, Josephson junctions, and other single-photon emitters would give astronomers, chemists and engineers access to quantum-limited precision technology.

**Diversity of promising hybrid platform:** Many existing quantum platforms already use mm-wave emitters. 100 GHz resonances with long coherence times are abundant among commonly used optical and microwave quantum emitters such as Rydberg atoms [115], molecules [116], spin defects [117] and even superconducting circuits [3, 67] and optomechanical membranes. They are rarely harnessed for quantum science due to the lack of both high-Q resonators with tight mode confinement and mature mm-wave manipulation technology. With the progress in our work and many new efforts in mm-wave technology, these emitters can be used both for stand-alone quantum platforms at mm-wave frequencies and as a part of novel hybrid systems bridging multiple platforms together.

Lower cryogenic requirements for mm-wave quantum technology would also allow for a higher complexity of hybrid platforms. The power dissipated from lasers, atomic sources, abundant optical access, and other electronics are hard to impossible to accommodate in systems

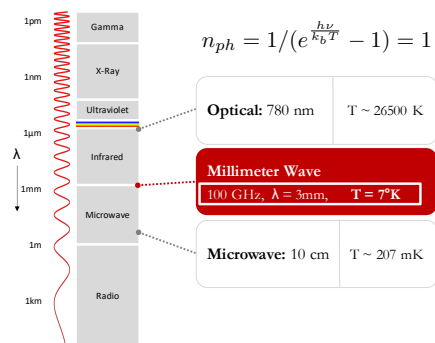


Figure 4.6: Comparison between photonics at optical, mm-wave and microwave frequencies. To perform quantum manipulations, we need to have a blackbody photon occupation much less than 1, which corresponds to temperature of 26500K, 7K and 207 mK, respectively.

requiring dilution refrigerators, which only provide a few hundreds of  $\mu W$ . This factor was a significant consideration for our cold atoms experiment with large optical access, more than seven lasers piercing through the cryostat, and an atomic source that heats up to 150 C.

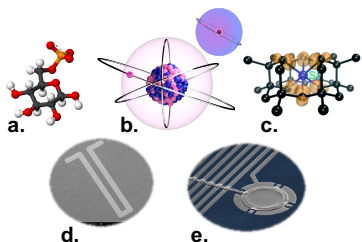


Figure 4.7: Various types of quantum emitters that can be used in the mm-wave band: **a.** Vibrational and rotational states of molecules. **b.** Cold atoms in Rydberg states. **c.** Lattice defects. **d.** Superconducting circuits [3]. **e.** Some types of fabricated mechanical membranes can be manufactured at 100 GHz, the figure shows an example of drum membrane at 7.5 GHz. <sup>2</sup>

**Quantum Interlinks:** The intermediate energy scale of mm-wave photons relative to optical and microwave energies makes them a promising interlink band for quantum communication. The quantum information stored in microwave regime in circuit-QED platforms could be easily transferred to mm-wave frequencies, which are much more suitable for longer distance travel [67]. On the other hand, the ideal long-distance bus of quantum internet would be the optical band, which is again much easier to transduce into the mm-wave band than the microwave band while maintaining low noise and low loss conditions.

**device manufacturing flexibility:** Finally, the intermediate length-scale of mm-waves enables the development of scalable, high Quality (high-Q) factor devices using both near and far-field wave engineering techniques. We can use ray optics for designing some devices and LCR circuits for others in the same frequency band. At the same time, these devices can be machined and fabricated, allowing for flexibility that is not common in other frequency bands.

**Hybrid multilayer quantum systems:** It is interesting to note that all of the above opportunities provided by the mm-wave band can be used to create multilayer or 3D hybrid

<sup>2</sup>. Note that usually mechanical membranes are used in the linear regime for beam splitter-like experiments. But intrinsically, they are also weakly nonlinear

quantum systems. Experts in circuit-QED systems have realized that as the 2D systems are rapidly scaling up, we are starting to run into the “volume” problems [4]. Miniaturizing the components as we do in classical computing is not very applicable in quantum hardware for several reasons.

- First, unlike the circuits in classical computers, quantum circuits interact very strongly with each other - this is why we use Josephson junctions in the first place. But their incredible strength is also a weakness when it comes to minimizing the unwanted cross-talk between different circuit components. For small systems, this is mitigated by spectral and spatial separation, but as the number of qubits grows, it gets significantly harder.
- Second, there is an issue of coherence. Larger components tend to be less sensitive to surface losses. Since the primary goal in the field is to maximize coherence and implement error correction, care has to be taken to avoid exacerbating the situation by miniaturizing the systems for purely larger scale chips.
- Third, the larger number of qubits require a larger number of connections for manipulation and readout. It becomes hard to pack all of the wirings in 2D, so there has already been considerable effort to expand control ports to 3D dimensions.
- Finally, larger chips require larger shielding boxes. These are crucial to protect the chips from coupling to the external environment. As the boxes grow in size, the mode frequencies get lower in frequency. So when the packaging becomes bigger than the wavelength  $\approx cm$ , the modes of the box would mediate detrimental couplings between circuit components.

The scientists and engineers in the circuit-QED community have been working to solve these problems and have made considerable progress towards mitigating potential future bottlenecks. For example, a more modular packaging approach and 3D tools used in engineering

MEMS devices have been proposed and implemented.[4, 118]. And it was suggested that as we scale up the number of qubits, the size, volume, and dimension of the systems will have to increase to maintain coherence and implement error-correction schemes.

The mm-wave circuit-QED systems will also have these problems in the future. But due to the length scale, multilayer systems could be easier to implement. We can machine the parts and fabricate them, build larger systems as we have more cooling power, and hybridize on-chip with other quantum platforms like cold atoms and cavity-QED systems as shown in Fig. 4.1. So the critical advantage of the mm-wave platform would be the access to scalable large hybrid systems.

### 4.3 Our Quantum devices

There are many applications for resonators in science and technology. We use them to harness the nonlinearity of quantum emitters in the mm-wave circuit- and cavity-QED systems. We usually optimize for the following parameters:

**Cooperativity:** To achieve a strong coupling regime between the emitter and a photon in a resonator, we usually optimize the cooperativity  $\eta = \frac{g^2}{\kappa\Gamma}$ , where  $g$  is the coupling strength,  $\kappa$  is the linewidth of the device and  $\Gamma$  is the linewidth of the emitter. For the device, this usually means that the coupling mechanism needs to be favorable - electric dipole vs. magnetic

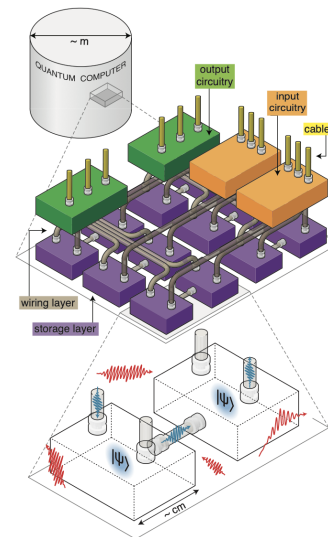


Figure 4.8: Conceptual sketch of modal multilayer microwave quantum computer, the figure is from T.Brecht et al 2016 [4]

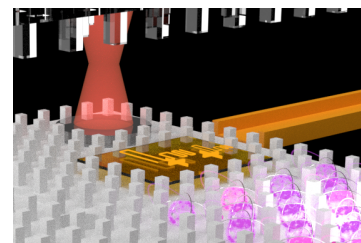
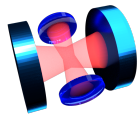
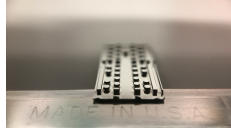

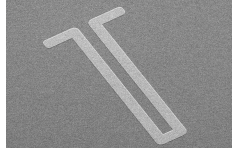


Figure 4.9: Conceptual implementation of a 3D mm-wave hybrid systems, from Fig. 4.1, including layered wavers, machined photonic crystals, lattices of cold atoms and Fabry-Perot cavities

coupling; the mode volume of the device needs to be small, and the device needs to be nearly lossless.

**Usability:** To be widely used, the devices need to be reproducible and allow for well-controlled coupling into and out of the device. These are not trivial tasks and tend to be one of the hardest hurdles to overcome to realize the technology. Usability also needs to satisfy specific needs of the experiment in hand: what is the size and the shape of the emitter, and how can it be conveniently placed in the cavity?

**Scalability:** Finally, it is essential to keep in mind the size and scalability of these devices, especially when it comes to systems that need to be cryogenically cooled. Not only does this come up when thinking about the future of the many-device quantum systems, but even in the single device systems. Even though Maxwell's equations are scale-invariant, the room in the fridge is not! We have limited cooling power and fridge space.

	Fabry-Pérot cavity	Photonic Crystal cavity	3D coaxial cavity	2D resonator
Device				
Frequency band	Optical		Microwave	
Materials	Dielectrics		Superconductors	
	Thin films SiO <sub>2</sub> /TiO <sub>2</sub>	Silicon Nitride Si <sub>3</sub> N <sub>4</sub>	Block of Al	Layer of Al
Manufacturing method	Sputtered coatings	Lithography and etching	Machining	Lithography and deposition
Figure of merit - loss	High Finesse	High Q		

	<b>Fabry-Pérot cavity</b>	<b>Photonic Crystal cavity</b>	<b>3D coaxial cavity</b>	<b>2D resonator</b>
<b>Common loss mechanisms</b>	Diffraction and Absorption in the coating	Dielectric loss tangent, TLS	Residual resistivity, other surface losses	TLS, dielectric loss tangent
<b>Figure of merit - field confinement</b>	Small waist	Strong confinement in the dielectric	Small mode volume	High zero-point V fluctuation
<b>Coupling</b>	Mode-matched Gaussian beam enters through the semi-transparent mirror	Fiber-to-waveguide	Wire antenna	Wire bonding

Table 4.1: Common Quantum resonators

This chapter will go over four primary device types: two commonly used in the optical domain - Fabry-Pérot and photonic crystal cavity, and two in the microwave - 3D coaxial cavity and 2D  $\lambda/2$  resonator. Table 4.3 describes their features in conventional use, and in the rest of the chapter, we will discuss how they apply in the mm-wave band.

#### 4.4 3D $\lambda/4$ coaxial resonator

My first attempt at an mm-wave cavity for the hybrid system was a 3D  $\lambda/4$  coaxial cavity, similar to ones frequently used at microwave frequencies. As eloquently described in [84], the design of this cavity relies on the combination of two waveguides machined out of the same piece of material. The bottom part is a coaxial waveguide shorted at one end and open at the other. This creates a  $\lambda/4$  resonant cavity. Finally, the top part of the cavity is

an open-ended cylindrical waveguide with a high-frequency cutoff  $f_{cutoff} \gg f_0$ . The outer diameter of this resonator determines the cutoff frequency and the amount of suppression of the field at the top of the cavity.

The coaxial cavity has a seamless design, which means it is made from one stock piece. This eliminates the losses that arise as the surface currents of the mode cross a nonuniform boundary transition. The suppression of the fields leaking to the top is  $e^{-\beta z}$ , so by choosing the proper aspect ratio of the cavity, the field can be suppressed by more than  $e^{-15}$ .

To make this cavity work in the mm-wave band, at first glance, all you need to do is to scale it down by a factor of  $\approx 10$  while maintaining the aspect ratio. This turns out to be quite difficult in practice. Below I will outline some common difficulties and how I have been dealing with them through my Ph.D. I hope it would be useful to anyone attempting to machine small features in this uncommon material.

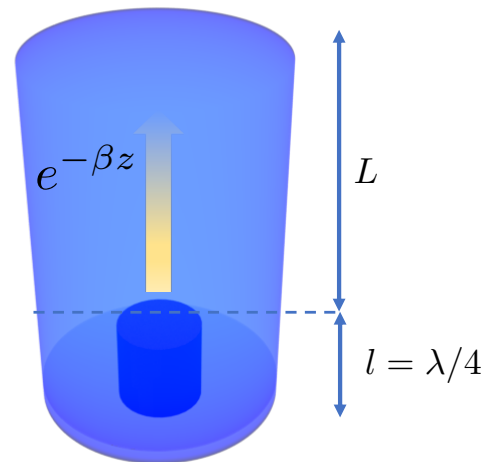


Figure 4.10: Diagram of a coaxial  $\lambda/4$  cavity

**Machining Nb:** I would have preferred my devices to be machined by professional companies. However,

Nb is not a common material, and the features I usually require are small. This meant that most of the time, I had to machine the devices myself. Nb is a tough material to machine. It is pretty hard and, somehow simultaneously, very “gummy”. The hardness means that it requires extremely sharp tools, but the tools wear out quite quickly since it’s gummy. So overall, it’s pretty hard to get a good finish without spending extra money on good finishing tools.

My general advice would be to:

- Always uses carbide tools for milling, and recheck if the tool has been worn out under a lens/microscope, even if used lightly or only once.
- For milling small features, make minimal cuts  $< 0.005$ . Cut at a reduced feed-rates of 1-3 in/min for end mill tools smaller than 0.1 in diameter at RPMs of 1000-5000. Use oil.
- Low RPMs around 600 for drilling small holes. Use tap magic at all times.
- After using oil, make sure that you have cleaned the surface thoroughly - sonicate using oil-removing cleaners, such as simple green. In the future steps, during chemical etching, the residues get in the way of achieving a low loss surface for trapping photons.

To machine this cavity, I had to manufacture a lathe tool myself by grinding down a regular milling tool. First, I drilled a hole in an Nb stock with a size of the cavities' outer diameter, followed by reaming for a better surface finish. Finally, the homemade lathe tool was used to cut out the bottom coax part of the cavity. Then the WR-10 waveguide flange pattern was machined on the top of the cavity surface.

This brings us to the next significant challenge with mm-wave devices - the coupling. Usually, in the microwave domain, the coupling to the coaxial  $\lambda/4$  cavity is accomplished by a coaxial SMA connector with a soldered longer wire antenna attached to a lid. It works pretty well because, to have reasonable control of a coupling  $Q$ , as mentioned in Chapter 2, we need to be able to control the integral over the overlap of the cavity mode and the mode of the incoming photon. The incoming photon usually enters a microwave cavity either through a transmission line or a waveguide. Here the coaxial mode of the SMA connector + the wire is co-aligned with the coaxial mode of the cavity resonance. Therefore, by changing the length of the wire, we can go smoothly from under-coupled to critical to over-coupled regimes.

This ideal coupling regime is not favorable when you scale the device down by a factor of 10

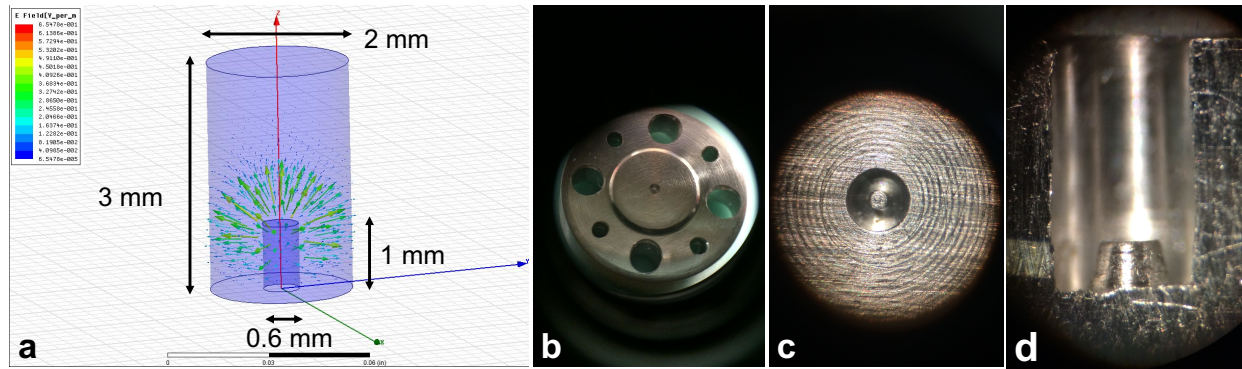


Figure 4.11: **a.** Electric field distribution of the fundamental mode of the coaxial cavity at 100 GHz simulated by HFSS. **b.** A picture of the top of the machined coaxial cavity with a WR-10 waveguide flange pattern. **c.** Zoomed in picture of the top of the coaxial cavity. **d.** Length-wise crosssection of the coaxial cavity.

since now the wire also has to be ten times shorter and thinner. Even if one can find such a wire, it is not usually feasible to solder it to the 100 GHz SMA connector and hope that it remains stationary and mechanically sound. Any perturbation of the length and position will change the frequency and the  $Q$ . If the perturbation is oscillatory, as in the case of vibrations - it could lead to broadening of the observed linewidth of the device.

The other option used in the microwave community is side coupling using an evanescent hole. Again, at a smaller scale, this becomes more difficult to machine. You can drill evanescent holes with a diameter of up to 1.4 mm, but they need to be extended to be evanescent, and they do change the shape and frequency of the original mode. We will use this to our advantage in the next section on the device, which happened to be a winner for our hybrid experiment.

So, after all of the considerations, we ended up coupling the top of the cavity to the regular rectangular WR-10 waveguide commonly used in the mm-wave band. You can see the manufactured device out of the niobium in Fig 4.11. Of course, the difficulty was the TE<sub>01</sub> mode of the rectangular cavity completely cancels the cylindrical symmetry of the mode, as shown in Fig. 4.11a. To overcome this, we shifted the alignment of the waveguide to the

alignment of the mode.

After machining, the cavity was cleaned in a sonicating bath in a sequence of Simple Green/Acetone/Isopropanol/DI. We achieved decent results with quality factors of up to 50000 at 4K, shown in Fig. 4.12. Note that we haven't attempted chemical etching of Nb at this time, so it's possible that the internal quality of the cavity was orders of magnitude higher.

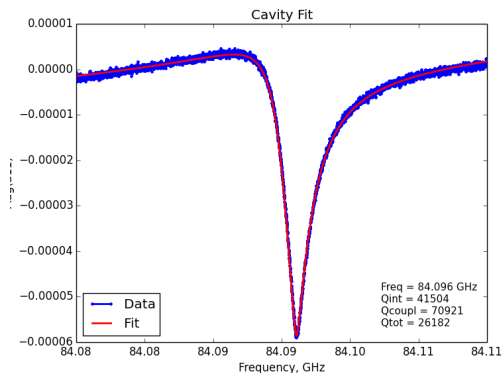


Figure 4.12: Reflection data from a Nb coax cavity.

Coaxial  $\lambda/4$  was a suitable test device to show that we could get a superconducting 100 GHz cavity out

of Nb. Still, it quickly became apparent that it wasn't performing well in the mm-wave band against the requirements for cavity-QED and circuit-QED we have mentioned. **Cooperativity:** Even though the mode volume of the cavity is quite small  $\approx 0.138\lambda^3$ , getting emitters inside the volume is nearly impossible without causing loss and mode shape change. **Usability:** The coupling problems due to wrong symmetry make the design unpredictable since we don't have great control over mode volume overlap. And the large aspect ratio of the features at mm scales makes it extremely difficult to machine while maintaining good surface roughness. **Scalability:** The design in principle is scalable, but due to the shortcomings mentioned above - it is not a redeeming quality.

## 4.5 Seamless millimeter-wave cavities

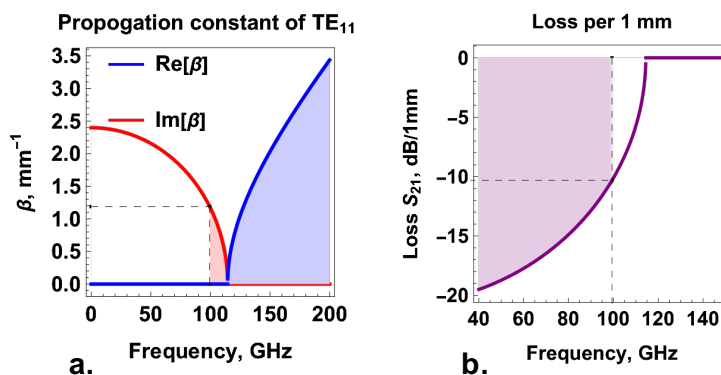
The Device I will describe in this section is at the heart of our hybrid experiment. The key is a seamless design uniquely suited for mm-wave length scales. This is unlike the coaxial cavity described above, which was well suited for microwave band, but has significant shortcomings

in the mm-waves.

Our cold atoms experiment uses thousands of  $^{85}\text{Rb}$  atoms to single interface mm-wave and optical photons trapped in respective cavities. To make this experiment work, I had to come up with a mm-wave cavity that would trap photons for a very long time in a tightest possible volume and allow line of sight access to the cloud of atoms as well as five different laser beams to manipulate the states of the hybrid system without ruining the performance of the cavity. It took over a decade for Heroche’s lab, together with a team of engineers, to develop a resonator at 50 GHz that would eventually lead to groundbreaking quantum experiments. My research was possible because of their work and many related efforts in high-Q microwave resonators.

#### 4.5.1 Design

The design idea is simple: instead of machining out a cavity mode and coupling to it using evanescent waveguides that only act as a small perturbation on the cavity - why not make the cavity mode out of the evanescent waveguides.



A hollow cylindrical waveguide of a diameter  $d$  can transmit infinitely many  $TE$  ( $E_z = 0$ ) and  $TM$  ( $H_z = 0$ ) modes but they all have a cutoff frequency. The lowest frequency mode this waveguide can transmit is  $TE_{11}$  shown in Fig 4.14.

Figure 4.13: Transmission properties of a 1.5 mm diameter hollow cylindrical waveguide: **a.** real and imaginary parts of  $\beta$ , **b.** power loss in dB per 1 mm length

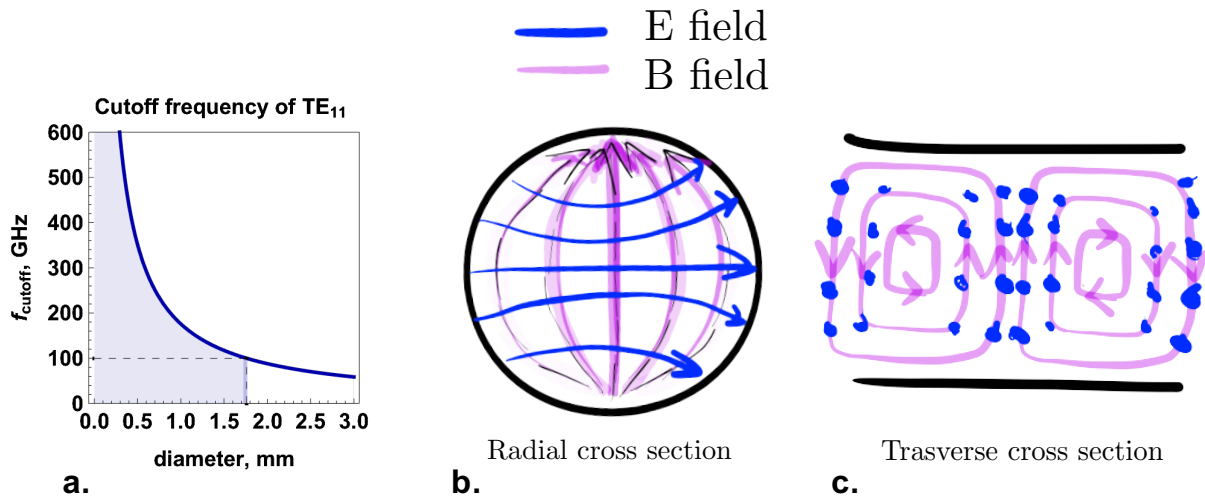


Figure 4.14:  $TE_{11}$  mode of a hollow cylindrical waveguide: **a.** Cutoff frequency as a function of a diameter of the cylinder, **b.** E and B field pattern in radial view, **c.** E and B field pattern in transverse view

$$f_{\text{cutoff}} = \frac{p_{11}c}{2\pi(d/2)} \quad (4.1)$$

where  $p_{11}$  is the root of the corresponding Bessel function.

The frequency we are interested in is the  $^{85}\text{Rb}$  atomic transition between Rydberg states  $|36s\rangle \rightarrow |35p\rangle$ , which is 99.43 GHz. This means that we want the diameter of the tubes to be below 1.77 mm to be effectively evanescent for a frequency of 99.43 GHz or wavelength of  $\lambda = 3$  mm.

The cylindrical waveguide is a transmission line, and as any other transmission line in Chapter.2, Section2.5, it has a dispersion relation with a complex propagation constant  $\beta$ :

$$\beta_{11} = \sqrt{k^2 - k_{cutoff}^2} = \sqrt{k^2 - \frac{p_{11}^2}{d/2}} \quad (4.2)$$

For our science cavity, the largest diameter cylinder we use is  $d = 1.5\text{mm}$ , the corresponding propagation constant as well as the loss per 1 mm length at 99.43 GHz is shown in Fig. 4.13

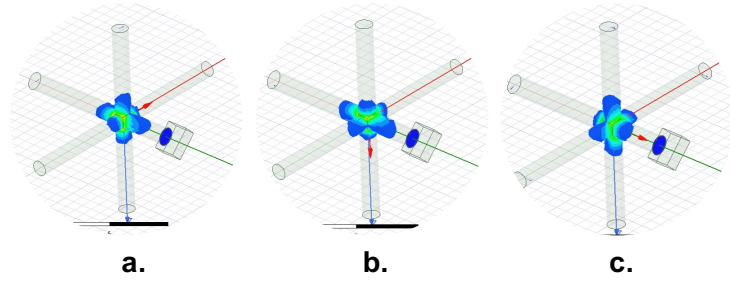


Figure 4.15: HFSS simulation of E field of three lowest modes of a cavity with tube sizes: 1.54 mm, 1.36 mm, 1.43 mm, **a.** 99.4 GHz, **b.** 102.4 GHz, **c.** 107.2 GHz

With this knowledge, we can construct resonators made of intersect-

ing evanescent waveguides at the desired frequency and coupling  $Q$ . As an example, Fig. 4.16 shows cavities with various frequencies one can build from identical tubes of 1.6 mm diameter. The simulated E field pattern of one of these cavities is shown in Fig. 4.15 using ANSYS HFSS software.

Below is the sequence of steps I used to make a cavity with the highest possible internal  $Q$  at 1K:

- Use a high-grade superconducting bulk Niobium stock, RRR = 300 from Ningxia (ADMAT refractory metals as a US distributor)
- Machining involves: machining the WR10 flange onto the cavity and machining the evanescent holes by drilling and reaming the holes for the best surface finish available
- After machining, the cavity is cleaned with Simple Green, Acetone, Isopropanol, DI water

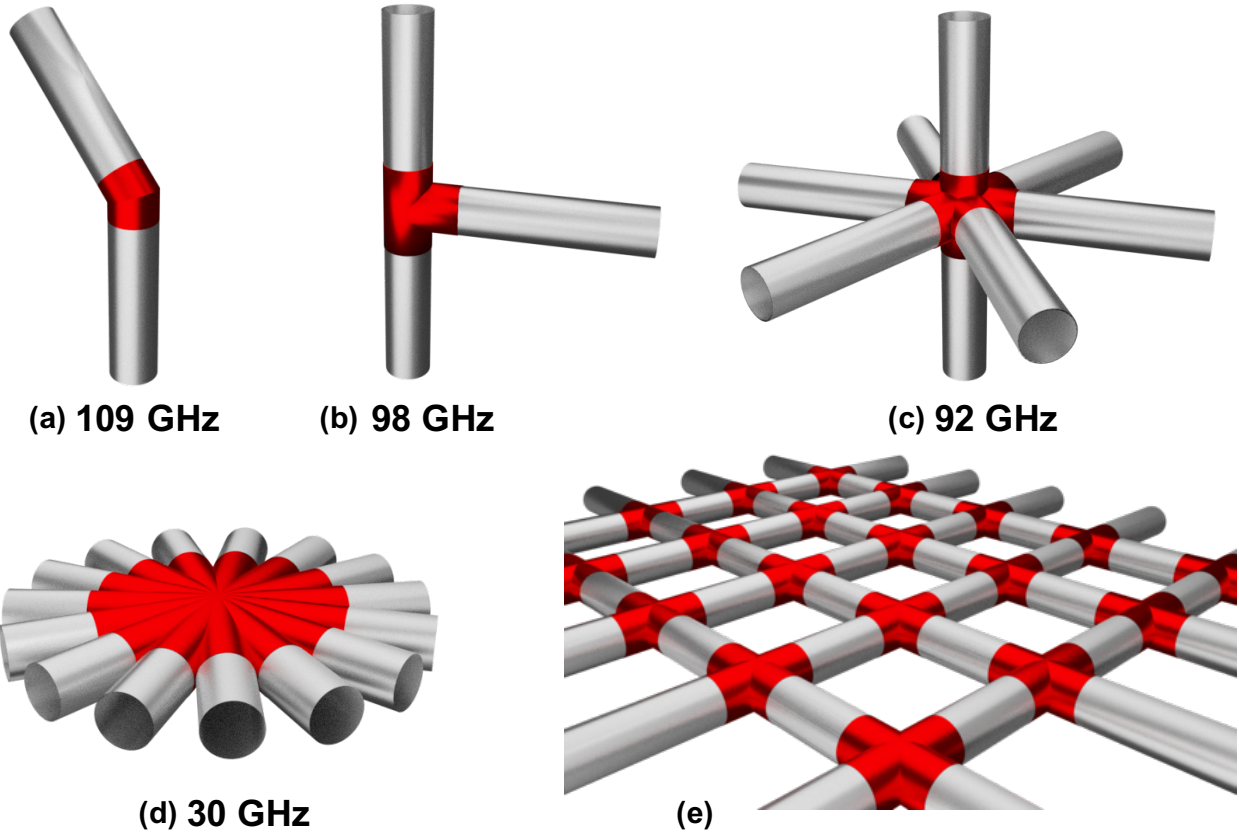


Figure 4.16: Various cavities made using hollow tubes with diameter of 1.6 mm

- The cavity is etched in a 2:1:1 solution of  $H_3PO_4$ :  $HNO_3$  :  $HF$ . Etch rate I get is usually about  $6 \mu\text{ m/min}$  in the steady-state. However, the first etch is usually more violent. The chemical etchant attacks sharp corners first, which round up, eventually leading to a more steady etch rate and behavior. Controlling the temperature and the concentration of the etchant could also make the etch process more predictable.

This sequence produced remarkably consistent and high-quality results. The devices and corresponding data at 1K are shown in Fig. 4.17 with internal Qs of 10s of millions. We also measured the cavity performance at different powers, all the way down to single-photon levels, and saw no strong indication of loss due to TLS - two-level systems. However, the internal Q measurement as a function of temperature did indicate that the Q was limited beyond the Mattis-Bardeen behavior of temperature-dependent conductivity as shown in

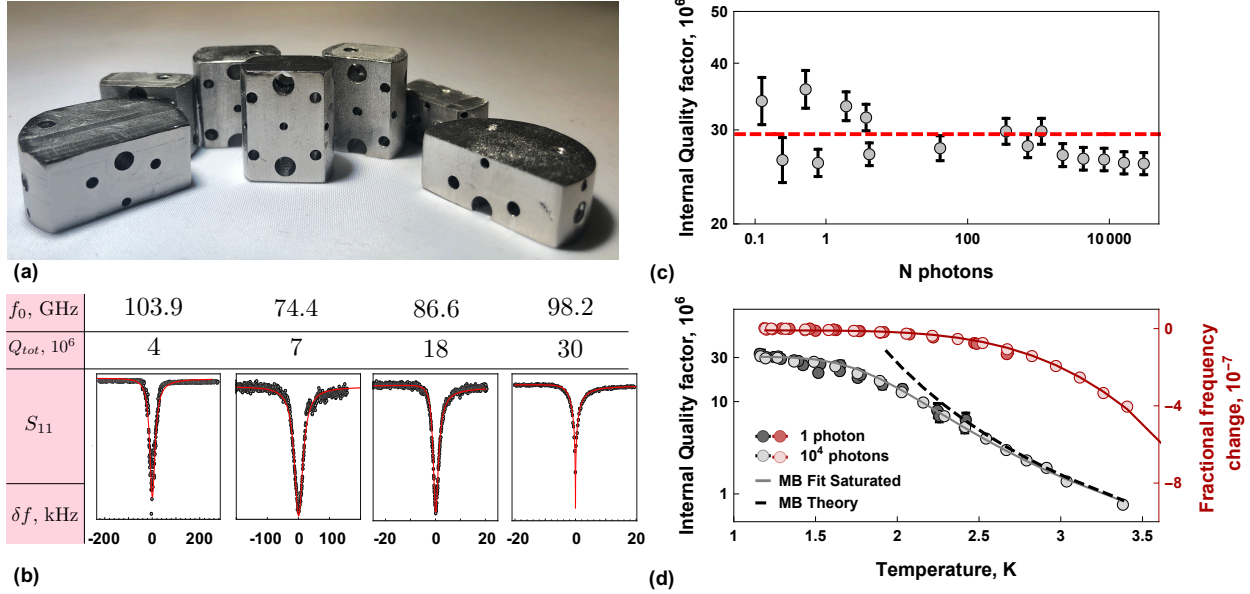


Figure 4.17: (a) Photograph of various tested mm-wave cavity geometries. (b) Reflection spectra from several cavities with varying frequencies and coupling  $Q$  values, resulting in different total  $Q$  values. (c) Internal  $Q$  as a function of the number of photons for the hybrid cavity. The constant trend indicates that the limiting loss mechanism is not power-dependent. (d) Internal  $Q$  (black) and fractional frequency change (red) as a function of temperature for the hybrid cavity. The deviation from Mattis–Bardeen curve at 2.3 K suggests that the resistivity of Nb does not limit the lifetime of the photons at the lowest temperatures.

Fig. 4.17 c,d.

Since the goal was to use this cavity for a hybrid cavity-QED experiment with cold atoms, we needed precise tuning of the resonator’s frequency. One way is to squeeze the cavity mode mechanically. The low-temperature (1 K) tuning is accomplished by displacing a pre-thinned cavity wall by 1–2  $\mu\text{m}$  using a piezo stack actuator. This pushes the mode farther out into the evanescent waveguides, effectively increasing the wavelength and decreasing the frequency of the lowest mode. At 1 K, the linear fit in Fig. 4.18 shows 0.1 MHz/V tunability, with a maximum frequency shift of 18 MHz. At room temperature, the increased piezo throw enables cavity tuning by a GHz. The inset shows that the piezo actuator introduced vibration, which broadened the resonance. For this reason, in the actual experiment, we decided to move towards turning the atoms to the cavity resonance instead of tuning the

cavity resonance. More on this is covered in Chapter. 6.

Aside from achieving the highest quality factor at 100 GHz [119], this design offered opportunities for our hybrid cavity-QED system with cold atoms. The evanescent tubes that made up the volume of the mode are all big enough to pass laser beams and a cloud of atoms in and out of the mode center without ruining the  $Q$  of the resonator or interfering with optics and atoms. Moreover, one of the tubes is used as a spacer for a Fabry-Perot cavity, which automatically aligns the optical and mm-wave modes to each other. An early version of the hybrid cavity is shown

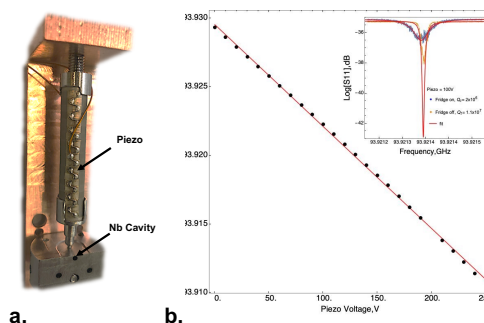


Figure 4.18: Cryogenic frequency tuning of a high- $Q$  mm-wave cavity. **a** Photograph of the piezoelectric actuator system attached to a test cavity. **b** Frequency shift of the cavity resonance as a function of the voltage of the piezo.

in Fig. 4.19 together with the minimal measurement setup for the mm-wave frequencies.

This cavity performed exceptionally well in terms of the quality factor, robustness regarding external elements such as laser beams, atoms, extra mechanical parts, and control over the parameters. In many cases, I can design several modes within the evanescent region to make several high- $Q$  modes. In fact, in our experiment, we use an auxiliary higher mode of the mm-wave cavity to tune Rydberg atoms into the resonance with the lower frequency “science” mode. And, finally, I was able to adjust the frequency of the cavity prior to the final cooldown to within 150 kHz of the atomic resonance using calibrated etching and mechanical squeezing using a hydraulic press with a pressure gauge. This is incredible considering 150 kHz is 1 part in a million precision in the cavity frequency.

Aside from using this device as a high- $Q$  superconducting resonator, I incorporated seamless mm-wave cavities in our measurement circuit as narrow band filters. An example of such a filter is shown in Appendix. B. These filters are extremely easy to machine out of aluminum. After machining and cleaning, we tune them either by drilling bigger through holes or by

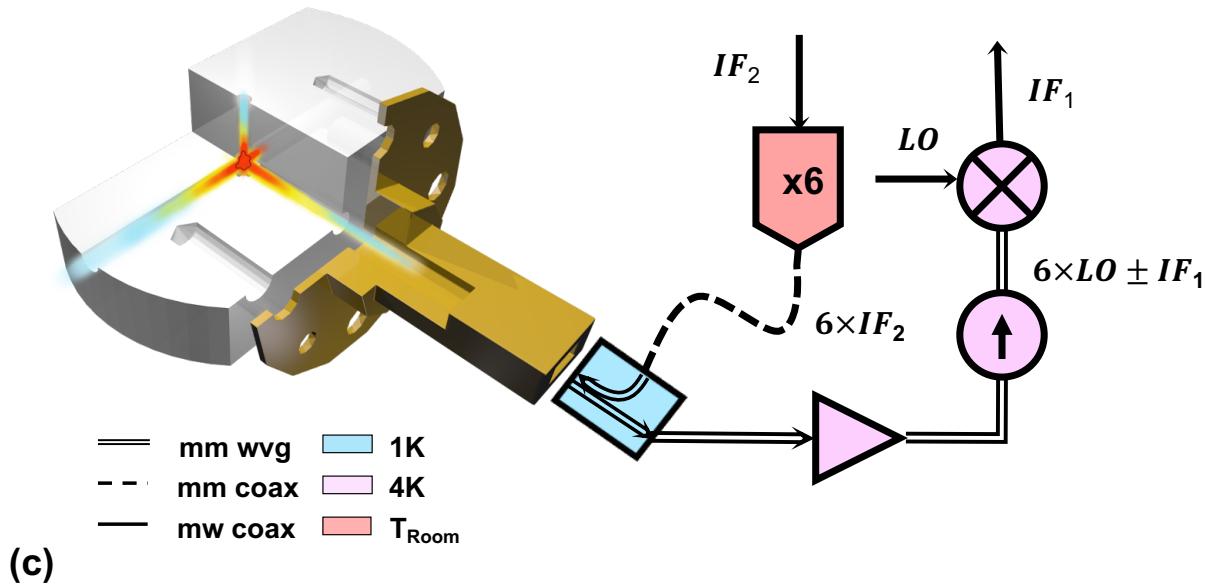
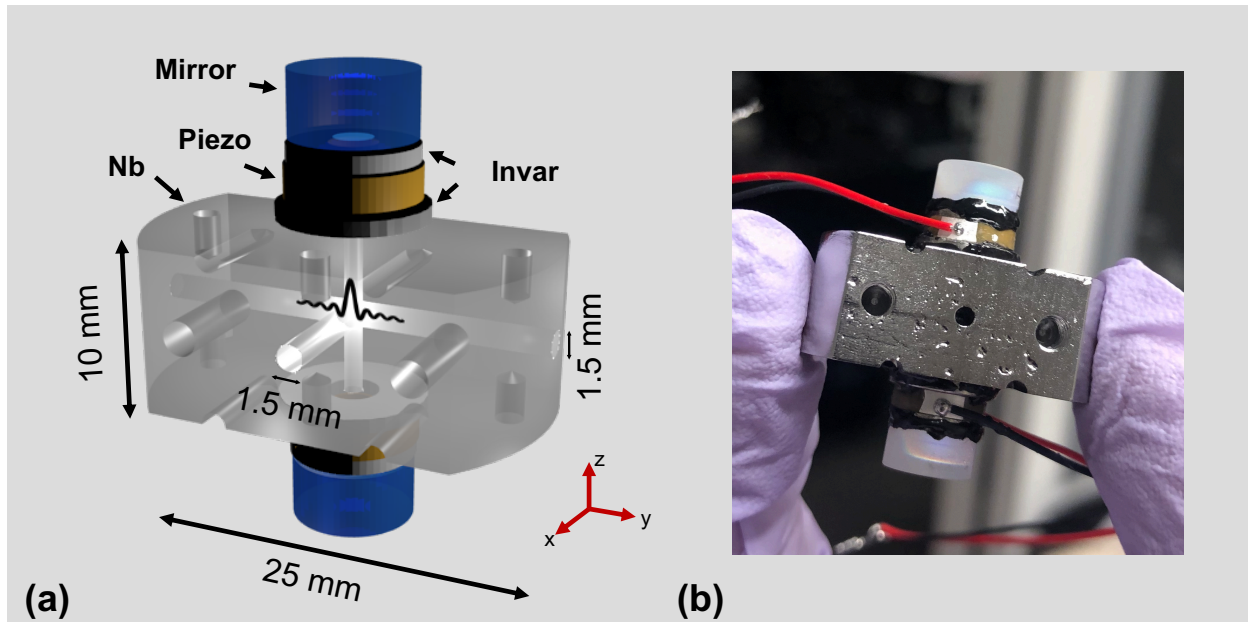


Figure 4.19: **a.** Schematic of the early version of the hybrid cavity. The superconducting mm-wave cavity was formed by the intersection of three evanescent waveguides. The x-axis waveguide was employed for atom transport, the y-axis waveguide for mm-wave coupling, and the z-axis waveguide for an optical Fabry–Perot cavity. Each side of the Fabry–Perot cavity included Invar spacers to prevent differential thermal contractions and a piezo actuator for tuning and locking the frequency of the optical cavity. **b.** Photograph of the assembled crossed mm-wave and optical cavity with wired piezos. **c.** Schematic reflection measurement setup for the mm-wave cavity. 100 GHz photons enter the coupling port of the cavity through a WR10 waveguide.

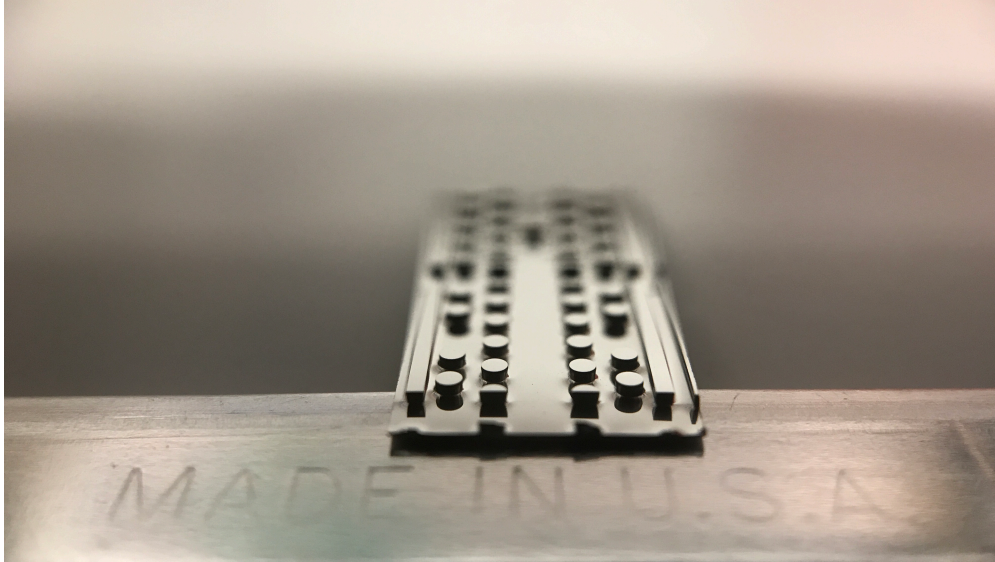


Figure 4.20: Fabricated Nb superconducting photonic crystal cavity

mechanically squeezing the structure along the axes of the cavity. Some tuning data is shown in Appendix. B.

With all of its advantages, this cavity does a drawback when it comes to use in other types of experiments. For example, it's not straightforward to use it for circuit QED experiments with fabricated chips. In the future, we would like to be able to use high-Q mm-wave cavities as memories for superconducting Josephson junctions at 100 GHz, but place a sapphire wafer inside of this cavity is difficult due to the size and geometry. This is one of the many reasons I was motivated to continue exploring other types of mm-wave cavities, as shown in the sections to follow.

## 4.6 Photonic crystals

The length scale of mm-waves allows for the creative application of both optical and microwave engineering techniques for manipulating light. For all of the resonant modes in the devices, we use two key principles: application of boundary conditions and light interference.

That's what creates standing wave patterns that we call modes. The transmission line cavities, including the Fabry-Perot, we have discussed in this chapter and Chapter. 2 were made by taking a waveguide that normally transmits light and applying boundary conditions that create an impedance mismatch. If light maintains its phase coherence at each impedance interface in a repeatable manner, we get a coherent superposition of the waves, which make up useful standing wave patterns.

Another way to create modes is through the interference of diffracted waves off of a periodic structure. Similar to how electron wavepackets propagate freely in the vacuum but in a lattice acquire a periodic wave function known as Bloch functions, we can create periodic wavefunction for our photonic plane waves in a photonic crystal. Here, we create the periodic potential through modulation of the impedance of the material. Optical photonic crystals are usually done by modulating the dielectric constant of the photonic crystal, e.g., etched holes in a dielectric slab. But it is also possible to make periodic structures using metals for microwave frequencies [120, 121, 122]. Here, I will describe a device I have made, which is a 2D superconducting photonic crystal at 100 GHz, both using machining techniques and fabrication.

#### *4.6.1 Design*

In both cases, the photonic crystal is made of two pieces of niobium: the bottom piece, which includes the cylindrical pins of radius  $r$  distance  $d$  apart, either in a rectangular or hexagonal lattice and a top which is just a flat plate of Nb. The lattice of pins creates a periodic potential that leads to a specific band structure. The strong modulation of the impedance of the propagation causes the band gaps to open. These bandgaps block the photons from propagating through the structure.

To turn the PC band filter into a high Q resonator, we take one pin out, effectively engineering

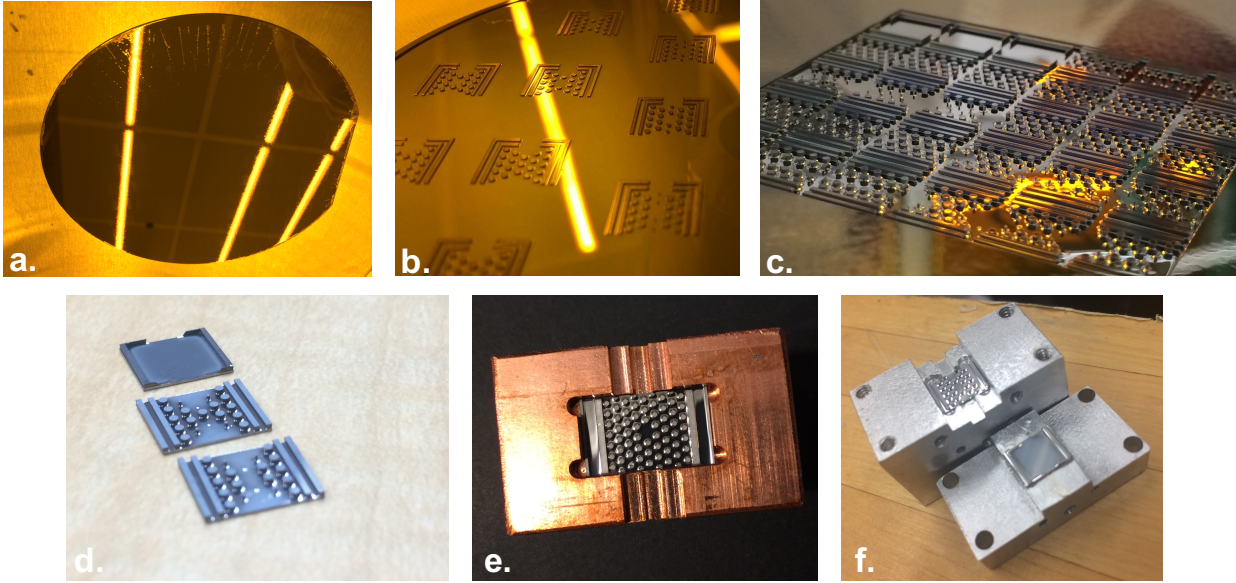


Figure 4.21: Fabricated photonic crystals: **a.**  $500\mu\text{m}$  Si wafer, **b.** Patterned PR using Heidelberg lithography, **c.** After deep Si etch + Nb sputtering **d.** Prepared devices: two different bottoms and one top, **e.** Mounted bottom chip, **f.** Mounted chips

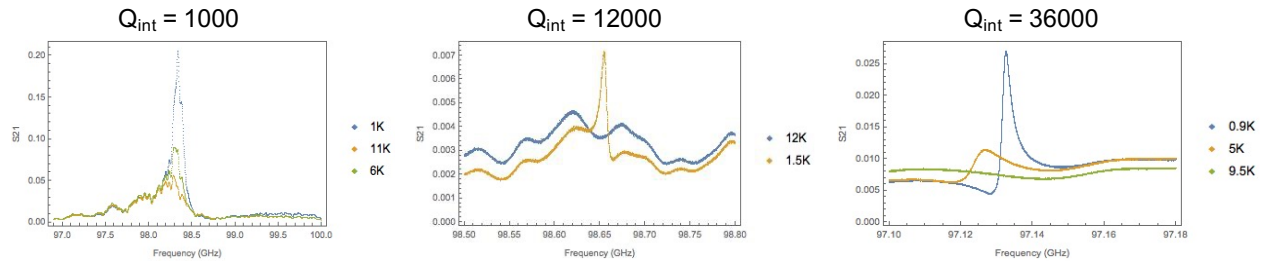


Figure 4.22: Transmission data from a few different fabricated photonic crystals, with different designed coupling  $Q_s$

a defect in the lattice. This defect in the lattice, given appropriate dimensions, can trap light at a frequency within the bandgap. Such a mode has a high-quality factor since the light can't leak out due to the bandgap of the remaining lattice. The main modes I consider here are TM modes, where the electric field is parallel to the cylinders

In most of the designs, the photons were fed into the resonator through evanescent waveguides engineered by taking out pins and varying the radii and the distances between the pins. I will describe a special case of a machined PC design later in this section, where the photons enter the cavity through a cylindrical evanescent waveguide perpendicular to the PC plane.

This cavity has a lot of advantages. First, since it is a quasi-2D crystal, the mode volume is quite small. We can make it arbitrarily small by decreasing the height of the pins. The design is flexible and allows for multiple cavities coupled together on the same small device. Finally, the aspect that I find most compelling is the two-piece design which allows the introduction of mini-wafers with circuits fabricated on them. The idea is that one can open the device, put a sapphire chip with a Josephson junction inside of the device and seal it without introducing loss through the seam due to photonic bandgap protection.

### 4.6.2 Fabricated chips

As I mentioned, the inspiration came from a dielectric photonic crystal for optical frequencies where a periodic pattern is etched into a dielectric material. As shown in Fig. 4.23a, by merely turning the layers inside out, one can make a metal photonic crystal for mm-wave photons. Here, the metal takes the place of the air/vacuum, and the air/vacuum takes the place of a dielectric.

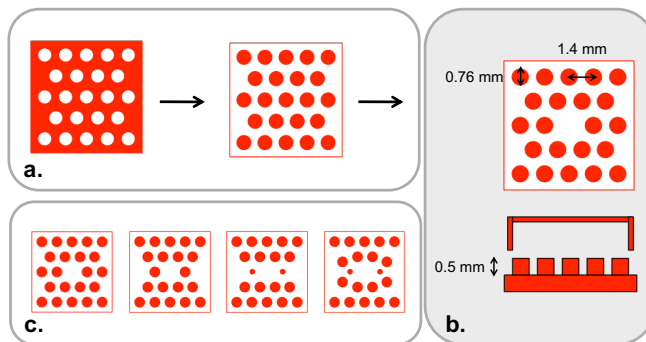


Figure 4.23: Design of a hexagonal lattice PC: **a.** From a conventional geometry of holes in a dielectric to a two-piece metal design, **b.** An example of a set of parameters for a functional PC cavity at 100 GHz, **c.** Different geometries for varying coupling  $Q$

In the fabricated devices I have made, the pins were arranged in a hexagonal lattice with  $r = 0.76\text{mm}$  and  $d = 1.4\text{mm}$ , and the bandgap was designed to block light up to 150 GHz. In order to feed the light in and out of the resonator, some pins are taken out to form a waveguide inside of the PC structure, as seen in Fig. 4.20. There are several parameters we can change here to control the frequency, mode volume, and coupling  $Q$ :

1. The number and radii of coupling pins can change the coupling  $Q$ .
2. The gap  $dH$  between the top plate and the pins can change the mode volume. In general, we try to minimize this to zero to avoid accidental leakage.
3. The height of the pins changes the mode volume.
4. The defect size changes the frequency of the mode
5. The ratio  $\frac{r}{d}$  changes the bandgap

The fabrication process is shown diagrammatically in Fig. 4.24. I start with a  $500\mu\text{m}$  thick Si wafer, use the thickest photoresist available, followed by lithography using the Heidelberg machine. The cylindrical pins are produced using the Deep Si etch. After thorough cleaning and removal of the PR, the wafer is sputtered with Nb. The photos of the fabrication process are shown in Fig. 4.21

These devices produced reasonable results, but the best  $Q$  I was able to measure was around 40,000, as shown in Fig. 4.22. There could be several reasons for it: the quality and uniformity of the sputtered Nb, dielectric losses on the Nb, and, finally, the seam.

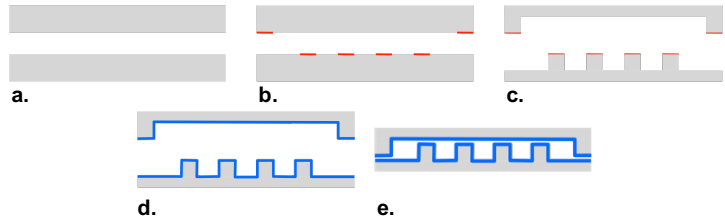


Figure 4.24: Diagram of the fabrication sequence: **a.**  $500\mu\text{m}$  Si wafer, **b.** Patterning the PR using Heidelberg lithography, **c.** Deep Si etch, **d.** Sputtering Nb, **e.** Assembling (snapping two pieces together).

The seam in this design is at the heart of the low-loss “box” idea with the meta-material surfaces. Even as a photonic crystal, without the defect cavity, a truly high- $Q$  photonic band block would be incredibly useful not only for circuit-QED but also many other efforts in THz chemistry and detectors for astrophysics research. However, it is hard to predictably create this seam. My simulations predict that we can tolerate many configurations: the

bottom and top perfectly sealed and in electrical contact, a small uniform gap between the lid and the top of the pins, and even a nonuniform gap, where some pins touch and some don't. But even with that surprising flexibility, it is hard to know how to seal the two pieces together to maintain performance during the cooldown. It's a challenge, but I don't think it's insurmountable.

### 4.6.3 *Machined cavities*

After the impressive internal Q performance of the seamless Nb cavity, I decided to try to make the PC by machining it out of the bulk Nb. Similar to the fabricated version, the cavity consists of the bottom part with the pins and the defect and a flat top part that acts as a cap for the PC. I started by designing and machining 13GHz and 26GHz devices out of aluminum and measuring them at room temperature as shown in Fig. 4.25. As expected for the aluminum, the best room temperature quality factors we measured were around 10000.

The machining of this device out of Nb at 100 GHz turned out to be quite difficult. The machining company I have contacted refused to make it due to the unusual material and small features. As a result, together with my undergraduate researchers, I had to figure out how to make it in-house.

I have gone through a few iterations of the design, but the latest one is shown in Fig. 4.26 with pin size  $r = 0.4$  mm and the distance between the pins  $d = 0.7$  mm. A photonic crystal with such parameters has a transmission in the WR-10 band shown in Fig. 4.28a. Unlike the fabricated chips, where the photons were coupled through the rectangular waveguide engineered into the PC, in the machined design, the light is coupled through an evanescent cylindrical waveguide perpendicular to the PC plane. This is possible in the machined design due to the availability of the third dimension. It is important to note that since the electric field of the PC mode is perpendicular to the TE<sub>10</sub> mode of the coupling waveguide, the

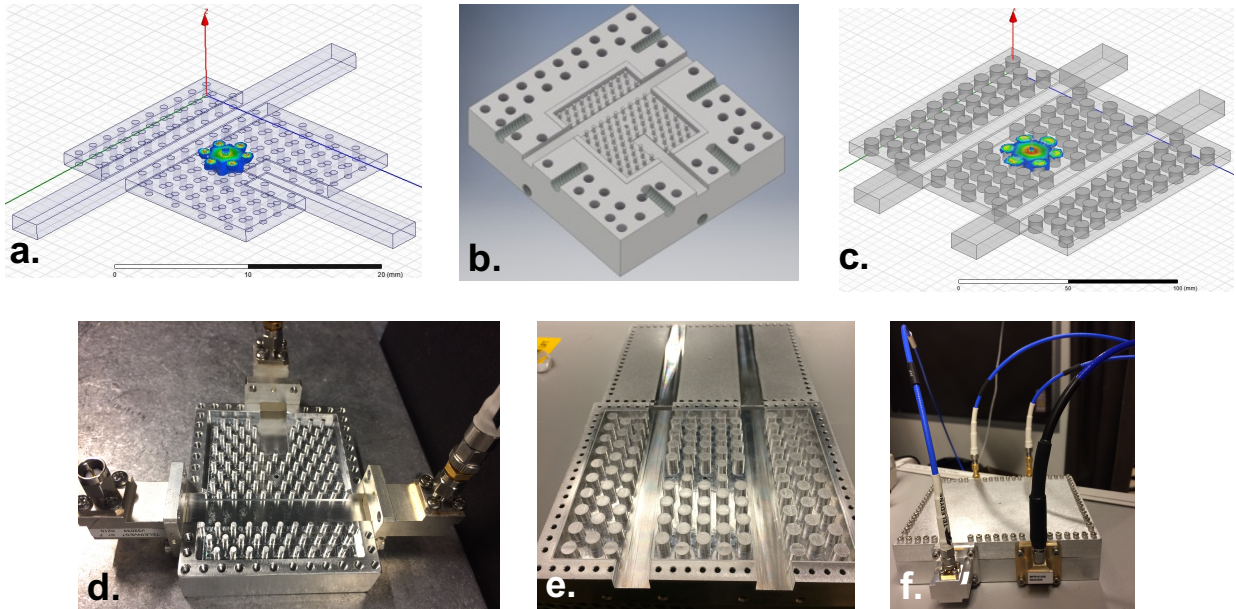


Figure 4.25: *26 GHz machined Aluminum PC*: **a.** HFSS simulation of the lowest mode of the PC, **b.** AutoCad model of the device, **d.** Machined Al device; *13GHz machined Aluminum PC*: **c.** HFSS simulation of the lowest mode of the PC, **e,f.** Machined Al device: hooked up for the measurement and separated bottom part.

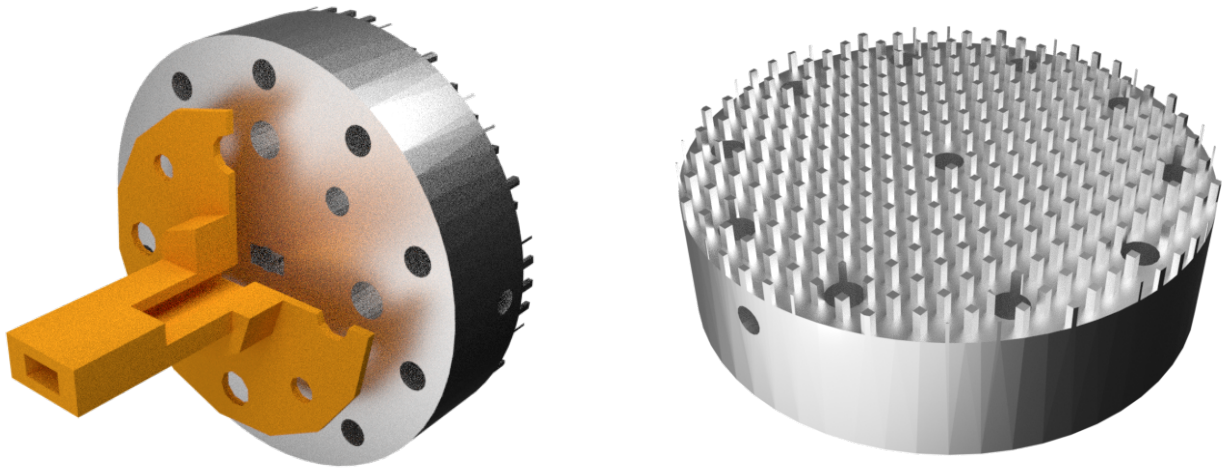


Figure 4.26: Design of a machined Nb photonic crystal cavity

coupling  $Q$  of the PC mode is really high unless the waveguide is very short.

To test the ability of this design to suppress photon leakage, I made a few cavities that combine a seamless cavity and a PC, as shown in Fig. 4.28b/c. The neat idea behind this

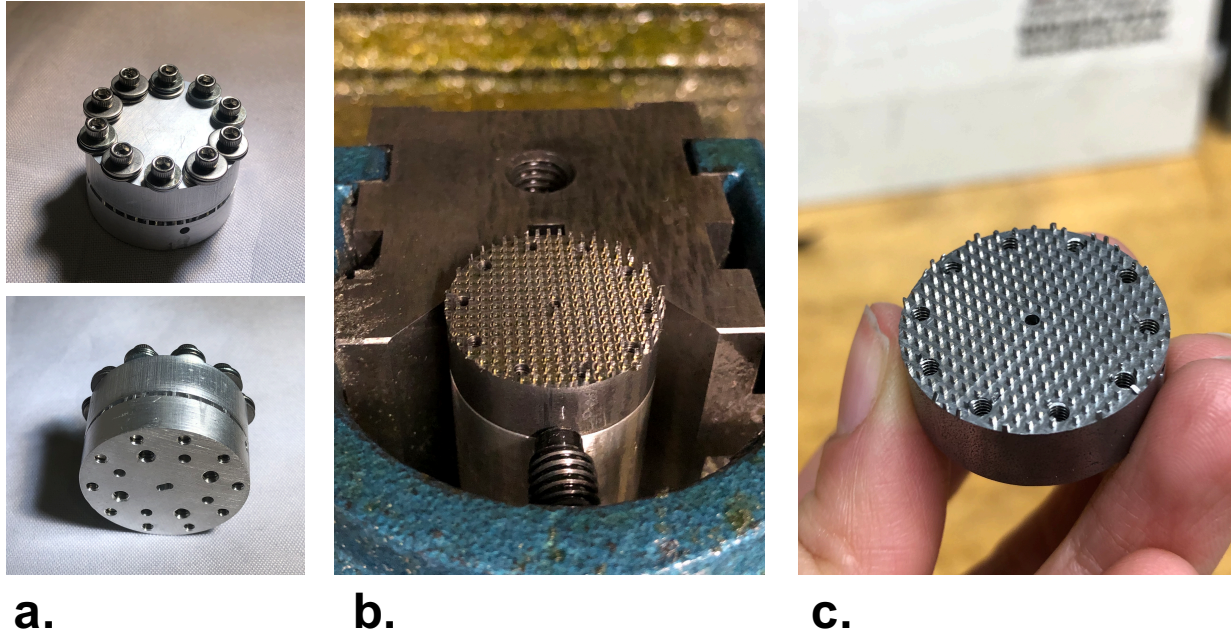


Figure 4.27: Photos of a machined mm-wave photonic crystal cavity: **a.** The assembled aluminum cavity for room temperature measurement, **b.**, **c.** The machined Nb cavity before the etch

cavity is that we can make the seamless cavity extremely leaky by shortening the top cylinder. This, in turn, pushes the mode volume towards the surface of the photonic crystal. If the PC works well in a cryogenic environment, this device could have several important applications. First, it can act as an empty box for wafer chips with 2D mm-wave circuits, such as our linear and nonlinear resonators and potentially Josephson junctions. Unlike our seamless cavities, the PC can protect the 2D devices from stray mm-wave photons while allowing convenient chip swapping and mounting. Second, if we can engineer high-Q modes, we can use it for hybrid mm-wave experiments involving both atoms and 2D circuits. Third, the PC allows for flexible incorporation of lattices of modes and other devices inside its structure. So once we can input photons into and output photons out of the device with high control and coherence, there is a variety of geometries to explore.

After machining on the CNC, both top and bottom parts of the cavities were etched in the 2:1:1 solution of  $H_3PO_4$ :  $HNO_3$  :  $HF$ . This process is significantly more sensitive than

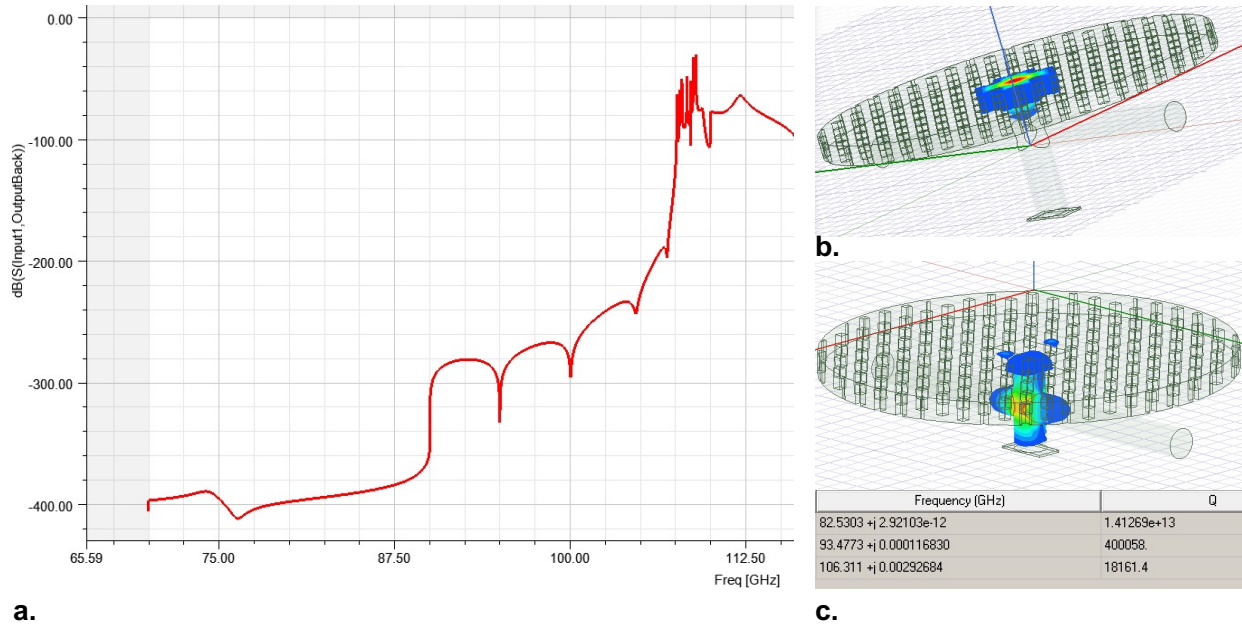


Figure 4.28: HFSS simulation of the PC cavity

the one with regular seamless cavities since long exposure to acids can reduce the size of the pins in the PC and void its functionality. Then the PC cavity was assembled using ten 2-56 screws and molybdenum washers to avoid loosening during the cooldown. The mode we were trying to measure was simulated to be around 94 GHz, as shown in Fig. 4.28c. The actual data of the measured reflection from one of the PC cavities at 1K is shown in Fig. 4.29.

The internal quality factor of the cavity with the cap attached is  $Q_{int} \approx 1.8 \times 10^6$ . This quality factor includes both leakage through the seam of the PC and the internal material losses. The same exact cavity with the cap removed has the measured  $Q_{int} \approx 3.4 \times 10^4$ . This internal Q has similar if not the same material loss, but now with no leakage suppression from the photonic crystal. As we can see, we achieve at least two orders of magnitude suppression from the PC. More work needs to be done to conclude whether our  $Q_{int}$  is dominated by the PC seam or the material losses. But we can conclude that this device is a promising tool for future hybrid platforms at mm-wave frequencies.

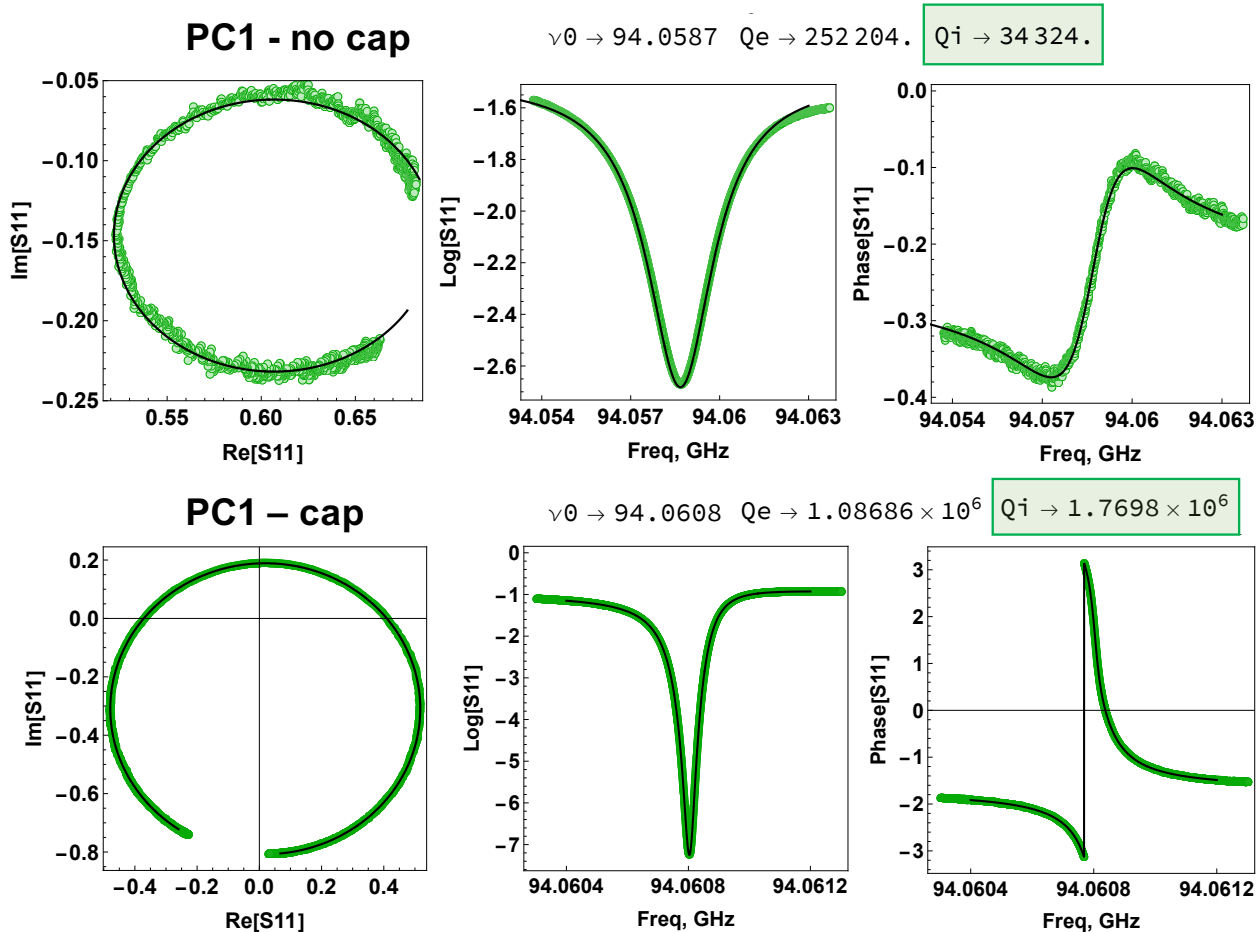


Figure 4.29: Reflection data from the leaky seamless cavity without the PC and with the PC

## 4.7 Mm-wave circuit-QED

### 4.7.1 Background

Superconducting circuit-QED in the microwave band is a compelling platform not only for quantum computation but also for photonics and many-body quantum simulations. The circuits have many advantages for engineering quantum systems [123]:

- **Flexible design:** circuit-QED allows one to design, simulate and fabricate arbitrary quantum Hamiltonians. Using Josephson junctions, resonators, and waveguides, we

can make artificial atoms, guide and trap photons and even imbue matter-like qualities on them such as mass and locality

- **Available infrastructure:** the manufacturing of circuit-QED systems, even though complex, is based on the existing micro-and nanofabrication processes. This means that superconducting circuit QED uniquely benefits from advancements in the chip-making industry while also being beneficial to those industries in return.
- **Flexible connectivity:** As mentioned above, circuit-QED systems allow for designing custom Hamiltonian. This, in part, is enabled by the relative ease of a couple of different elements to each other. The connectivity allows for exotic geometries and topologies that can benefit quantum technology.
- **Available microwave control:** circuit-QED platform uses the microwave band of the electromagnetic radiation due to the combination of factors. Transmission lines and lumped element superconducting circuits easily interface with microwave photons. Microwave technology is a highly developed tech industry with an enormous variety of commercially available equipment to aid circuit-QED platforms. And, finally, the cryogenic temperature required to operate at a zero thermal background level is available using dilution refrigerator technology.

There are disadvantages tied to short coherence times, the difficulty of error correction, the limited cooling power of cryogenic refrigerators, and the fact that microwave photons are quite lossy as long-distance information buses. However, all of these are being currently being addressed by efforts in academic institutions and industry.

In our lab, during my Ph.D., we started exploring the potential of the mm-wave superconducting circuit-QED platform. I am happy to say the effort has been successful and is still ongoing, past my graduation. I started exploring the mm-wave spectrum in 3D and quasi-2D for photonic crystals. With the addition of my labmate A. Anferov, we started looking into

truly 2D circuits in the mm-wave spectrum.

The high frequencies can bring many opportunities to circuit-QED:

- As I mentioned in Section.4.2, mm-wave circuit QED only requires modest cryogenic temperatures for low thermal photon background. Quantum technology at 100 GHz can be maintained at a few K temperatures. Not only this alleviates requirements for dilution refrigerators but also allows us to build larger fridges with enough cooling power for millions of qubits.
- Higher frequencies of nonlinear elements also imply faster gates.
- The smaller wavelength means the components are smaller in size. This especially becomes useful for waveguide-QED, wherein the microwave regime, the elements tend to be quite long or require Josephson junction.

Even though, currently, my primary interest lies in high-frequency mm-waves around 100 GHz, operating circuit-QED platforms at 20-30 GHz could already be significantly beneficial for quantum technology. Until very recently, the commercially available mm-wave technology was either scarce or non-existent. With the recent move of the TELECOM industry into 5G/6G, the mm-wave band has become more widely utilized. It's important to note that commercial availability of devices is not the only challenge for mm-wave quantum technology:

- The higher frequency of the photon means that we have to use superconductors with higher energy gap or equivalently higher  $T_c$ . This limits materials to Nb, TiN, NbN, and so on. Even though there are many possibilities for high-Q resonators, it makes the development of Josephson junctions tricky. The usual design of a junction uses aluminum due to its single insulating oxide, which can be grown uniformly in a predictable manner. The Nb is a significantly harder material to make Josephson junctions out of since it has many oxides, only some of them are insulating.

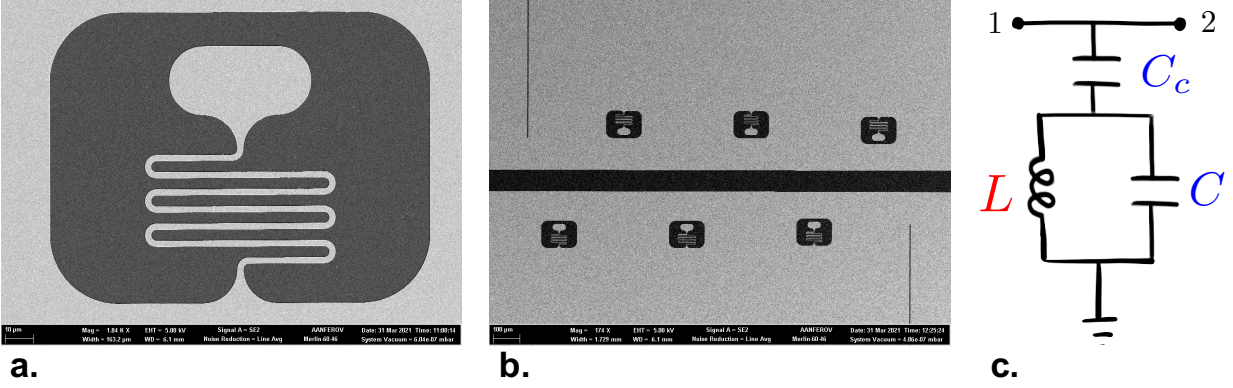


Figure 4.30: SEM images of a mm-wave lumped element Nb resonator made by A.Anferov and K-H. Lee: **a.** a single resonator zoomed in, **b.** A chain of six resonators on one chip, **c.** lumped element circuit of the device

- If the  $T_c$  of the material is too close to the frequency, the devices become lossy due to the breakage of cooper pairs.
- Circuit-QED chips are usually enclosed in a box or a cavity, which shield the qubits inside from interacting with stray E and B fields of the world.

#### 4.7.2 Planar mm-wave devices

In the quest to find out whether mm-wave frequency band could be practical for circuit-QED devices, we started looking for a high-Q linear resonator and the most nonlinear 2D device. The mm-wave linear device with the highest internal Q we have made so far is a high-impedance lumped element resonator in Fig. 4.30. For this 100 nm wide eBeam Nb on C plane sapphire, we get  $Q_i \approx 2 \cdot 10^5$  consistently. The sapphire chip is placed inside of a high purity grade copper box with WR10 waveguide input and output, similar to one shown in Fig. 4.31a. This is a good performance for a high-frequency Nb device, but we are currently working on tracking the loss mechanisms and improving the quality.

A good controllable nonlinear device is significantly harder to make than a linear device.

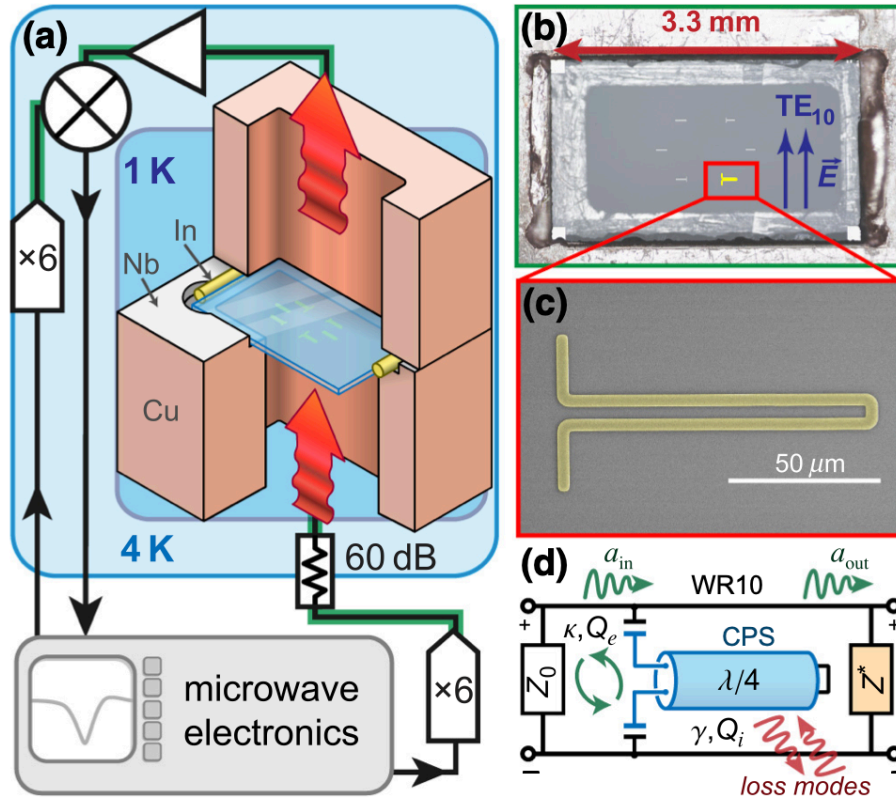


Figure 4.31: 2D nonlinear device for mm-wave para-amp. The figure is taken from [3] made by A.Anferov: **a.** mm-wave measurement setup with a copper box for the sapphire chip, **b.** Image of a mounted chip with the top waveguide removed, **c.** SEM image of one NbN resonator: wire width  $4 \mu\text{m}$  and film thickness, **d.** RLC diagram of the device with the coupling impedance included

Since the conventional Josephson junction is hard to make at 100 GHz with widely used materials, we started from Kerr nonlinearities generated from the kinetic inductance of electron cooper pairs in the superconductor. Here we used atomic layer deposition of NbN since it has a high intrinsic sheet inductance [124] and a high  $T_c = 14 - 18 \text{ K}$  [125]. With this device for film thicknesses  $> 20 \text{ nm}$ , we measure  $Q_i \approx 6 \cdot 10^4$ . Finally, using two-tone measurements, we showed the first degenerate parametric conversion at 95GHz with a forward efficiency up to +16 dB [3].

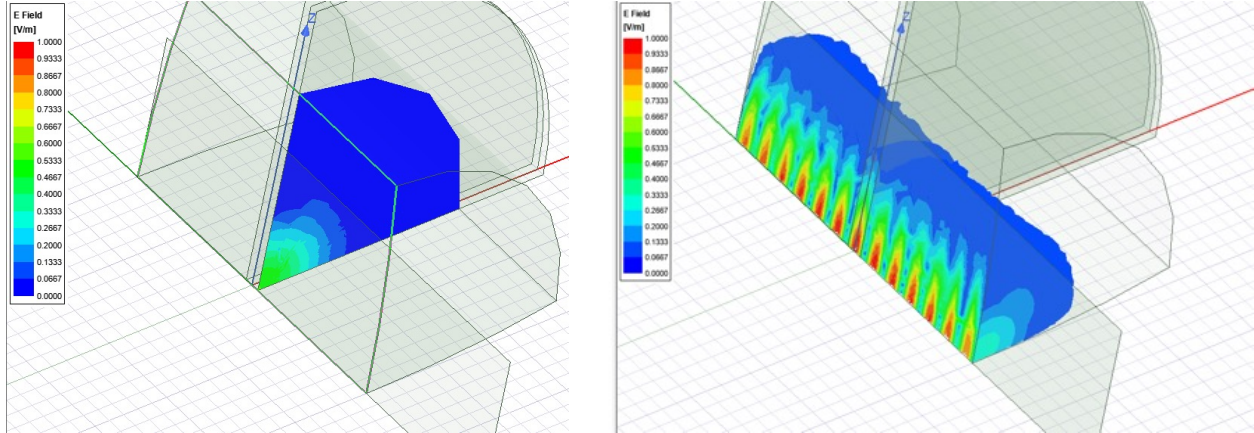


Figure 4.32: HFSS simulation of a mm-wave Fabry-Perot with a Gaussian excitation: **a.** transverse slice of the mode, **b.** axial slice

### 4.7.3 Outlook on 2D mm-wave circuits

There is a wide variety of projects to pursue in the planar mm-wave paradigm. Currently, our lab (our team with K-H Lee and A. Anferov) is working on developing strongly nonlinear devices or Josephson junctions at 100 GHz, potentially using weak link junctions made of granular aluminum or GAAL. We are also looking into mm-wave and microwave hybrid systems in 2D for inter-conversion of microwave to mm-wave photons and effectively cooling microwave resonators using mm-wave modes at 1K. I am hopeful and enthusiastic about the future of high-frequency circuit-QED. Whether it will be the next quantum platform or a unique playground for scientific explorations, I am excited to see future developments.

## 4.8 Mm-wave Fabry-Perot Cavity

Finally, while working with optical cavities, I got interested in the potential of mm-wave Fabry-Perot (FP) cavities. Heroche's [126] experiments have already demonstrated ultra high-Q FP at 50 GHz, and at this point, we knew that high Qs are possible at 100 GHz with bulk niobium. My main interest is in the possibility of machining arbitrary phase profiles on top of Nb mirrors to manipulate the geometry and topology of photons in superconducting

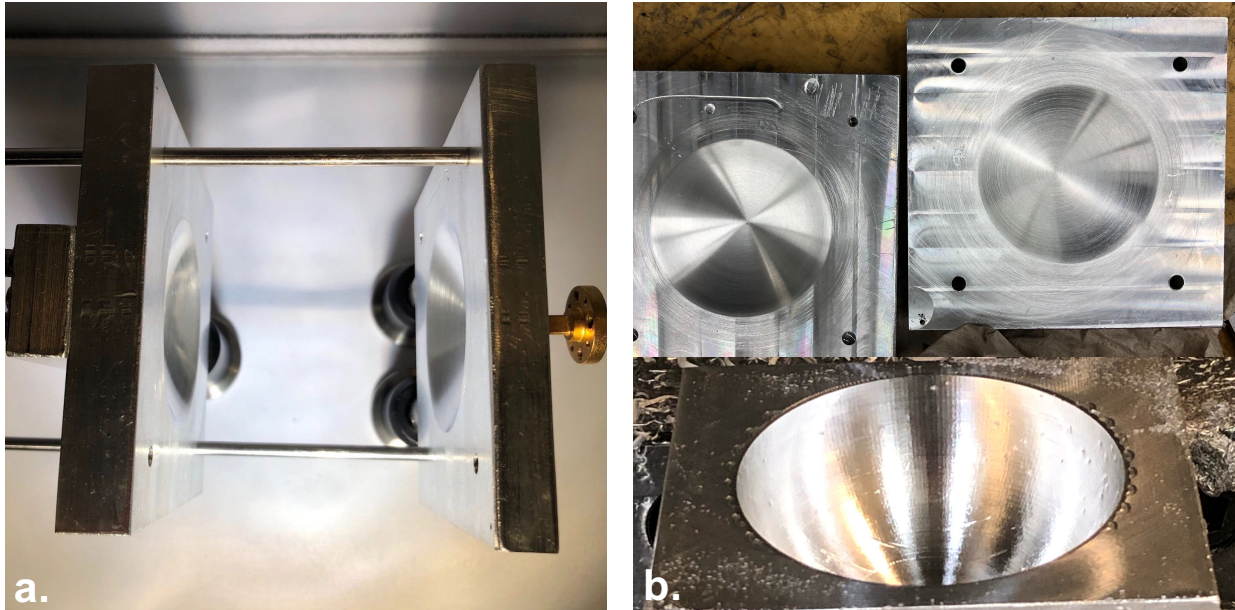


Figure 4.33: Photos of a machined mm-wave Fabry-Perot cavity: **a.** The assembled aluminum cavity for room temperature measurement, **b.** The machined Al mirrors

mm-wave cavities.

I have only done some exploratory work on room temperature mm-wave FP cavities made of aluminum. In the optical regime, we rarely calculate the exact frequencies of FP resonators since the axial mode number is extremely high. Here, in the mm-wave regime, a 40 mm diameter mirror with a 40 mm radius of curvature make the FP nearly paraxial, which means the mode waist is 2-5 times larger than the wavelength. This also means that the axial mode number is comparable to the transverse mode number, which is quite odd compared to the optical regime. This is why I usually calculate the frequencies of the modes analytically and simulate them in HFSS. Fig. 4.32 shows a more conventional  $TEM_{13,0,0}$  mode for mm-wave cavity at 100 GHz.

The machined FP is pictured in Fig. 4.33. The first project I worked on together with my talented undergrad Jasmine Kalia was coupling the light in and out of this cavity through an aperture hole. We measured the reflection and transmission of the modes in the cavity at room temperature with  $Q_i \approx 30000$ . It is also really convenient to sweep the cavity through

confocality and see modes pass through degeneracy. This works quite well, but since metal mirrors don't transmit light, it's hard to image the shapes of the modes. And for exotic FP designs, it's helpful to image the modes.

Inspired by the fiber SNOM technique in the optical regime, I made a similar setup where I could scan a thread of Nylon fishing line through the mode volume of the cavity using automated translation stages and record either the frequency shift of the mode (by parking on the slope of the Lorentzian) or the loss induced by the electric field passing through the Nylon thread. Since Nylon

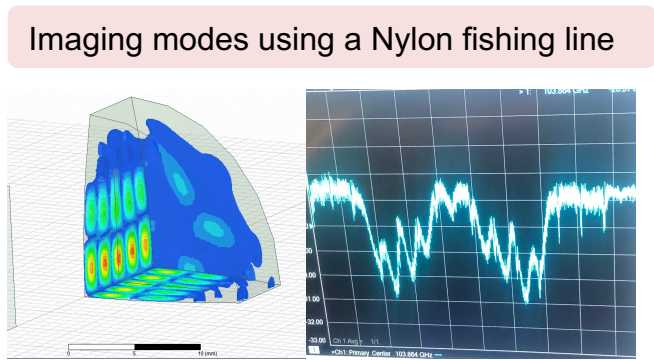


Figure 4.34: A preliminary scan of one of the modes of the FP. The image on the right shows a there-and-back scans through the cavity mode volume in the radial direction

has reasonable loss at 100 GHz compared to internal losses of the room temperature Al FP cavity and the thread width is a few mills - I got quite a good spatial resolution of mode imaging of the mm-wave FP. Some crude images of the scans are shown in Fig. 4.34.

#### 4.8.1 Outlook

It would be really interesting to optimize this imaging technique and see how well the measured mode shapes and frequencies match the simulations. From there, the goal is to engineer phase imprints on the mirrors by machining meta-material structures using simple milling tools. Another possibility would be to fabricate nonlinear circuits on top of flat metal mirrors to create monolithic hybrid systems. It's exciting to push the limits of the available materials, nanofabrication, machining, and ray optics to develop novel quantum systems. These experiments could provide different parameter spaces for interaction strength, nonlocality,

geometry, and topology of quantum systems. I hope to continue pursuing the development of these systems in the future.

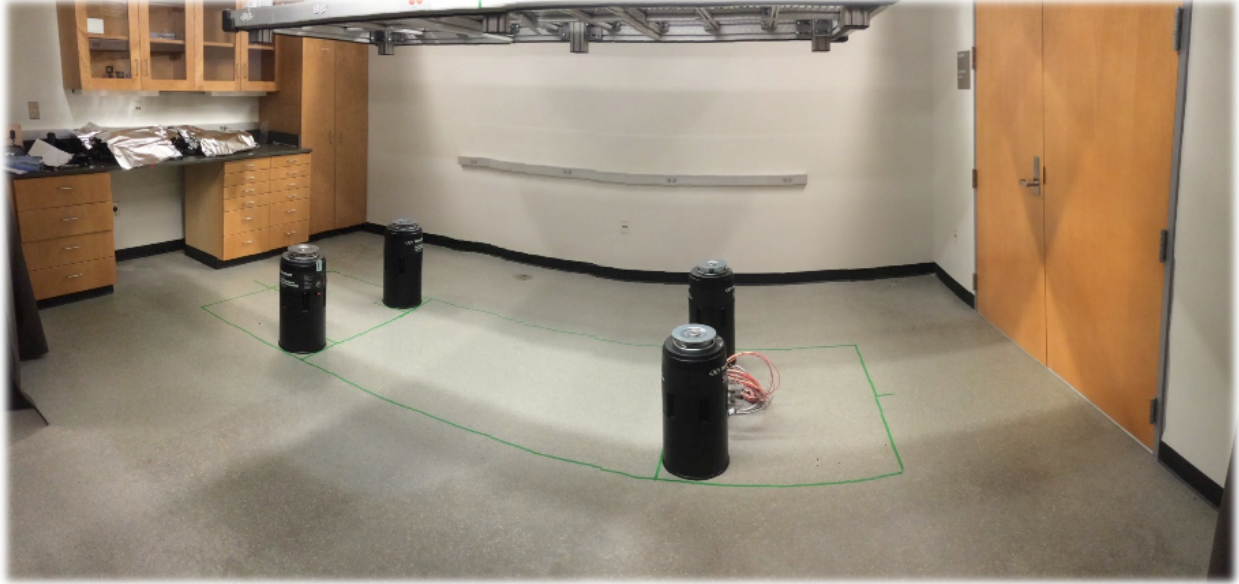


Figure 5.1: How it began...

## CHAPTER 5

### APPARATUS: HOW TO BUILD A HYBRID QUANTUM SYSTEM FROM SCRATCH?

The benefits of hybrid quantum experiments from harnessing mutual advantages of different quantum platforms come with a huge obstacle - the enormous technical complexity. In this chapter, I give an overview of my journey from an empty room to a fully built hybrid quantum system together with the greatest group of undergraduate students and talented lab-mates.

#### 5.1 System requirements

Before designing the experiment, it is important to clarify the key requirements and functionalities it needs to perform. Since our goal was to hybridize a superconducting circuit-QED platform with a Rydberg cavity-QED platform these were the minimal requirements we had:

Requirement	Range	Reason
Cryogenic temperature	$\leq 6K$	temperatures below $T_c = 9.2K$ required to access superconducting regime for Niobium; low thermal occupation of mm-wave photons for quantum measurements; cold surfaces adsorb background gases leading to lower vacuum pressure
Ultra-high Vacuum (UHV)	$\leq 10^{-9}$ mBar	low background pressure for cold atoms to have long lifetimes; low pressure aids the faster and more efficient cooldown of the cryogenic system
Low vibrations		stability of the narrow lines of the optical (predominantly) and mm-wave cavities
Optical access		many laser beams enter the chamber for trapping and manipulating the atomic cloud; probing and locking the optical cavity; imaging the atomic cloud
Atomic sources	$^{85}\text{Rb}$	the sources emit atomic vapor $\geq 150$ C, but need to be kept inside of the cryostat
Mm-wave circuitry	input and output lines	to manipulate Rydberg states, populate the mm-wave cavity with photons, measure the response of the mm-wave resonator
Optics	inside outside	to guide the light inside of the chamber a setup for regular cold atoms control and experiments
DC Wiring	cryo/low current high current	thermometers, piezo actuators MOT coils, atom sources

Table 5.1: System requirement

## 5.2 Building components

### 5.2.1 Optical Tables

Every optics lab needs optical tables. They are sturdy, patterned with 1/4-20 (M6 in metric) holes for optical mounts and come with legs, which can be pressurized to “float” the whole table and mechanically isolate the systems from the environment.<sup>1</sup> The optical table we use for the main chamber is 5' × 12' × 12" *Newport RS-2000 series* with an 18" square hole shown in Fig. 5.2.<sup>2</sup> The rest of the optics is mounted on the second optical table 5' × 10' × 18" *TMC 784-775-02R*. This table is 1.5 tones! The constant air pressure required to “float” this table is [127]:

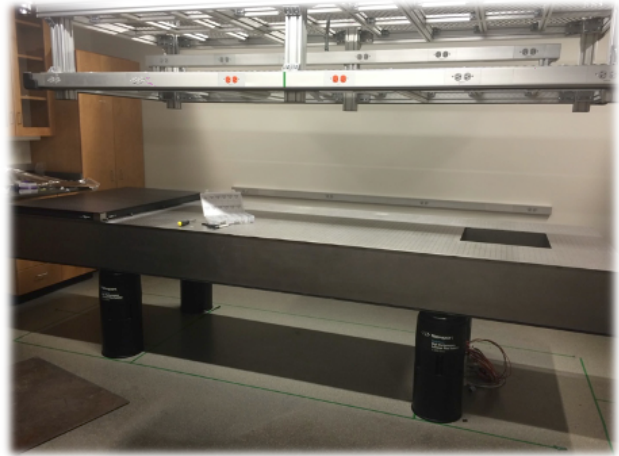


Figure 5.2: Newport optical table with an 18" hole

$$P = \frac{\text{Total table weight} + \text{load}}{\text{Total surface area of the isolated legs}} + 10 \text{ psi} = \frac{2973 \text{ lb} + 200 \text{ lb}}{4 \times 25.9 \text{ in}^2} + 10 \text{ psi} = 40.6 \text{ psi} \quad (5.1)$$

---

1. We didn't use this feature

2. This optical table was donated to us from a retired research group, so the table is over 25 years old.

## 5.2.2 Cryostat

Ideally, we would have liked to operate at temperatures around 1-2 K, but for the first iteration of the experiment, we decided to start with 4 K since 4 K refrigerators are commercially available, easier to install in hybrid systems, and provide a lot of cooling power. We use *Cryomech PT410 CPA289C series* dry pulse tube refrigerator, which has 1.0 W of cooling power at 4.2 K and 40 W at 45 K.

Pulse tube cryogenic (PTC) refrigerators are fascinating and complex inventions that provide cooling power through a closed-loop expansion of very pure (99.999%) Helium 4. One of the main advantages of using a PTC is that it is dry and uses a fixed amount of He that it constantly recycles. Here is a very cursory overview of the mechanism, which is most pertinent to our model, that could be helpful for a first-time user. As shown in Fig. 5.3, the cryostat has two major units: the compressor, which compresses the gas and removes heat from the system, and the cold head, which takes the gas through additional expansion cycles to reach cryogenic temperatures. The compressor is a loud machine with water cooling and oil filtering that we keep away from the experiment in a sound-isolated closet. As shown in Fig. 5.3a, it has two He lines: one at high pressure, which delivers He to the cold head, and one at low pressure, which returns the used He back into the compressor box. At the top of the cold head, there is a motor that switches the valve between the high-pressure input and low-pressure output. The top of the cold head also has two He reservoirs, one for each cooling stage, that are connected to the system through orifices.

Unlike original PTCs and regular refrigerators/heat pumps, the orifice PTC doesn't rely purely on surface heat pumping for cooling, which is when the cooling is achieved by a working gas transferring heat against a temperature gradient. In OPTC, the cooling results from enthalpy flow through the pulse tube in one oscillation of the pressure wave.<sup>3</sup>

---

3. It's important to note that the cooling here is maximized if the elements of the circuit are ideal, wherein the surface pump the cooling happens due to deviation of the elements from the ideal gas/regenerator

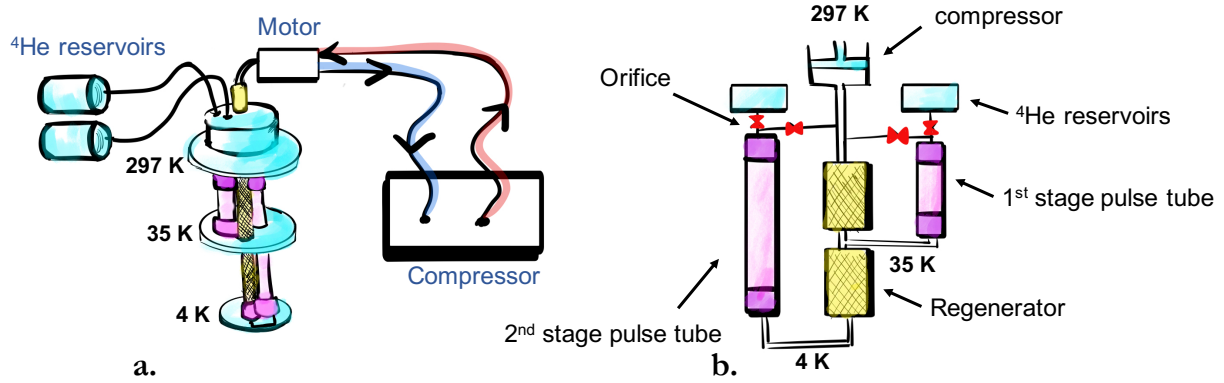


Figure 5.3: A two-stage pulse tube refrigerator: **a.** drawing **b** diagram

From the compressor, the high pressure He goes through the regenerator, which is usually made from a high heat capacity porous material such as stainless steel mesh or a magnetic granular material. The gas leaves the regenerator at a lower temperature leaving the heat inside of the regenerator. Next, the gas enters the pulse tube through the cold stage heat exchanger at  $T_{cold}$ . During the second half of the cycle, the motor opens the valve to the low-pressure flex line (or equivalently, the pistol in the diagram goes up) - and the gas that just entered the pulse tube cools down. This happens since the pulse tube is thermally isolated or adiabatic, which means the temperature follows the pressure directly. Since the pressure is lower, the gas goes back through the heat exchanger back into the regenerator. But now, since the temperature is lower than  $T_{cold}$  upon entry to the exchanger, the gas absorbs heat from the cold stage. The rate of thermal heat absorption in one cycle is what we call the cooling power  $\dot{Q}_c$  [128, 129]:

$$\begin{aligned} \dot{Q}_c &= \langle \dot{H}_{pulsetube} \rangle = \langle P\dot{V} \rangle + T_0 \langle \dot{S} \rangle \\ &\approx \langle P\dot{V} \rangle = \frac{1}{2} P_0 \dot{V} \cos \theta \end{aligned} \tag{5.2}$$

---

behavior.

where  $P = P_0 \sin \omega t$  is the pressure oscillations in the pulse tube,  $\dot{V} = \dot{V}_0 \sin(\omega t + \theta)$  is the gas volume flow oscillations in the pulse tube and  $\theta$  is the phase angle between them [130]. It is clear that  $\theta$  dramatically affects the performance of the cryocooler. The orifices that connect the reservoirs to the cold head are critical in providing a knob for tuning this phase between the pressure oscillations and volume flow at the cold plate by adding an impedance mismatch to the “circuit”. The cooling efficiency is maximized when this phase, at the cold end, is zero.

The pulse tube cryostat is yet another driven damped harmonic oscillator system from Chapter. 2. After several cycles, it reaches the steady-state periodic motion with a set temperature difference. The single-stage orifice PTC can be represented by an effective RLC circuit where voltage corresponds to pressure and current to volume flow. The capacitance,  $C$ , is the “compliance”, which is proportional to the volume of the reservoir. The inductance is the inertness of the gas, and the resistance,  $R$ , is the flow impedance of the orifice.

### 5.3 Two-chamber design

We designed and home-built the cryogenic system for our hybrid cavity-QED experiments. The design includes two chambers: the fridge chamber and the science chamber shown in Fig 5.4. The fridge chamber contains the dry pulse tube refrigerator, attached turbopump, and vibration isolation system to decouple the vibrations from the experiment. The Science chamber contains mm-wave circuitry, atom sources, viewports, and optics needed to perform the experiments. The two chambers are connected at room temperature solidly to each other through mechanical flanges of the chamber walls. The room temperature vacuum system is bolted to the optical table. The internal subsystems at cryogenic temperatures (both 35 K and 4 K) are attached through a cylindrical cold arm with flexible copper braids and foil connectors.

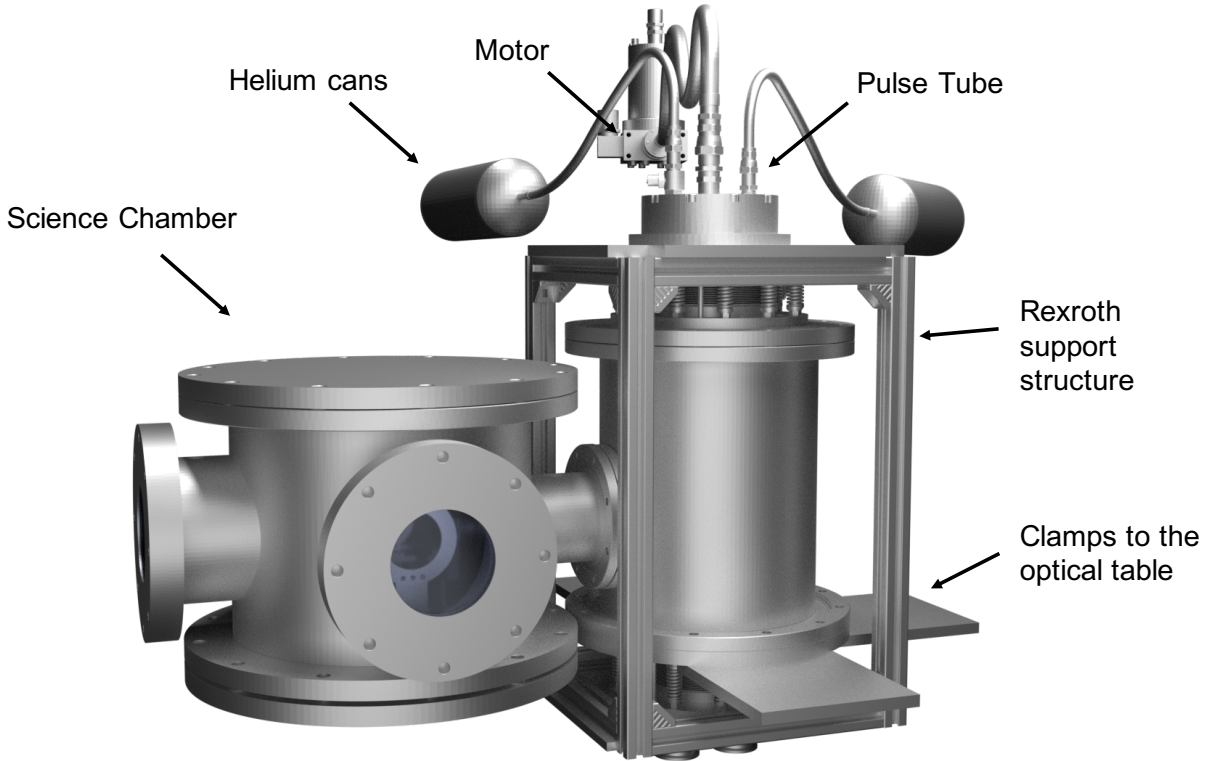


Figure 5.4: The design of the overall two-chamber system

### 5.3.1 Cryogenic Requirements

Our cooling power budget from the PTC is 1 W at 4.2 K and 40 W at 45 K. To stay at these temperatures it is crucial to ensure that the system's "thermal expenses" will be below these values as demonstrated by the capacity curve in Fig. 5.5. There are three main heat flows that the cryogenically cooled interior of the experiment will experience: convection, conduction, and radiation.

#### Convection:

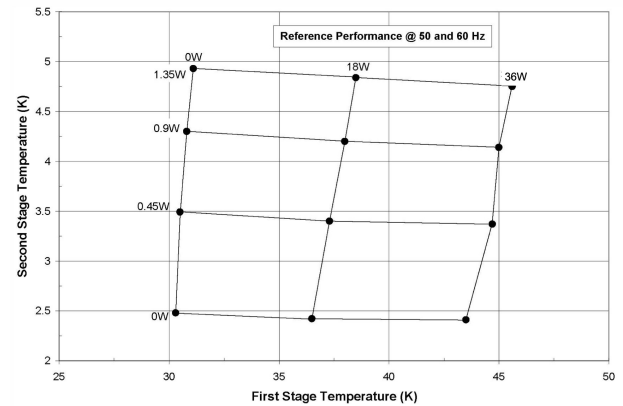


Figure 5.5: Cryomech PT410 CPA289C series capacity curves.

Gasses in air, listed in Table. 5.3.1, transfer

heat through convection in regular conditions. Convection heat flow from temperature  $T_1$  to the body at  $T_2$  with surface area  $A$  and convection heat transfer coefficient  $h_c$  can be determined using the following formula:

$$Q_{conv} = h_c A (T_1 - T_2) \quad (5.3)$$

For our 45 K stage in the Science chamber, which is a cylindrical shield with radius  $R_{45} = 12.7$  cm and height  $H_{45} = 19$  cm, the heat transfer would be:

$$Q_{conv35} = h_c (2\pi R_{35} H_{35} + 2(\pi R_{35}^2)) (300K - 45K) > 100W \quad (5.4)$$

for the modest value of  $h_c \approx 2W/m\ K$ . This means even at 45 K, the thermal load from the air is too high.

This is why an Ultra High Vacuum is necessary. At UHV pressures  $\leq 10^{-5}$  mBar, the conduction flow of gas turns into a free molecular flow, where the mean free path of gas molecules becomes larger than the chamber size. In this regime, the convection heat transfer becomes negligible. In our system, we start with room temperature pressure of  $10^{-6}$  mBar using a turbopump, and after the cryostat is cold, we reach  $10^{-8}$  mBar at the room temperature stage. We estimate the vacuum pressure at the 4K to be significantly lower due to cryo-pumping, see Table. 5.1. The only pressure measure we have at lower temperature stages are atoms, and the cold cloud's lifetime indicates an Ultra High Vacuum pressure regime.



Figure 5.6: 35K shield: **a.** First, we drill hole patterns in the aluminum sheet and roll it into a cylinder, **b.** we cover the surface of the shield with several repeated layers of Mylar and insulator

Gas	Mean Velocity [m s <sup>-1</sup> ], 300K	Partial Pressure [of 1 atm], 300K	T condensation at 10 <sup>-8</sup> mBar
Air	464	100%	
- Hydrogen, H <sub>2</sub>	1754	0.001%	3.5 K
- Oxygen, O <sub>2</sub>		21%	32 K
- Helium, He	1245	0.0005%	≪ 1 K
- Water vapor, H <sub>2</sub> O	585	<2% (varies)	140 K
- Nitrogen, N <sub>2</sub>	470	77%	24 K
- Argon, Ar	394	0.9%	27 K

- Carbon Dioxide, $CO_2$	375	0.003%	80 K
--------------------------	-----	--------	------

Table 5.2: Gas composition of air [5]

### Radiation:

Radiation heat flow occurs through electromagnetic waves, mostly in the infrared region due to blackbody radiation. The radiation emitted by a body at  $T$  with surface area  $A$  and the Stefan-Boltzmann Constant  $\sigma$  can be determined using the following formula:

$$Q_{rad} = \sigma AT^4 \quad (5.5)$$

Our room temperature Science chamber has a radius  $R_{300} = 19$  cm and height  $H_{300} = 30$  cm, so the radiation heat from it is:

$$Q_{rad}^{300} = \sigma(2\pi R_{300}H_{300} + 2(\pi R_{300}^2))(300K)^4 \approx 272W \quad (5.6)$$

which is a lot of power to be absorbed by the 45 K stage which only has 40 W. In contrast, the 35 K stage emits:

$$Q_{rad}^{45} = \sigma(2\pi R_{45}H_{45} + 2(\pi R_{45}^2))(45K)^4 \approx 0.06W \quad (5.7)$$

Of course, our chamber walls are not perfectly black, so with the emissivity of the stainless steel around  $\epsilon \approx 0.05$ , the actual heat emitted from the room temperature is:

$$Q_{rad}^{300} = \epsilon \cdot 272W = 13.6W \quad (5.8)$$

This is still a lot of power. In order to further reduce the heat absorbed by the 35 K stage, we cover its surface with multiple layers of extra shiny *Mylar/MLI from OxfordICE* and Spun Woven Polyester Holytex from Talas as shown in Fig. 5.6.

Another heat load to consider is the radiation coming from the room temperature blackbody and passing onto the 4K through the viewports of the 35K stage. We picked *UV-fused Silica* for window substrates since they do not let below 60 THz, though, which is where most of the blackbody radiation lies.

### **Conduction:**

Conduction is the hardest heat flow source to limit since the cryogenic stages need to be connected mechanically but decoupled thermally. Heat flow through an object with cross-section area  $A$ , length  $l$ , thermal conductivity  $k$  from a point 1 at temperature  $T_1$  to point 2 at temperature  $T_2$  is:

$$Q_{con} = kA(T_1 - T_2)/L \quad (5.9)$$

To mechanically connect different temperature stages we would like to thermally isolate, we use parts made of low conductivity material, small cross-sectional area, and long length. As

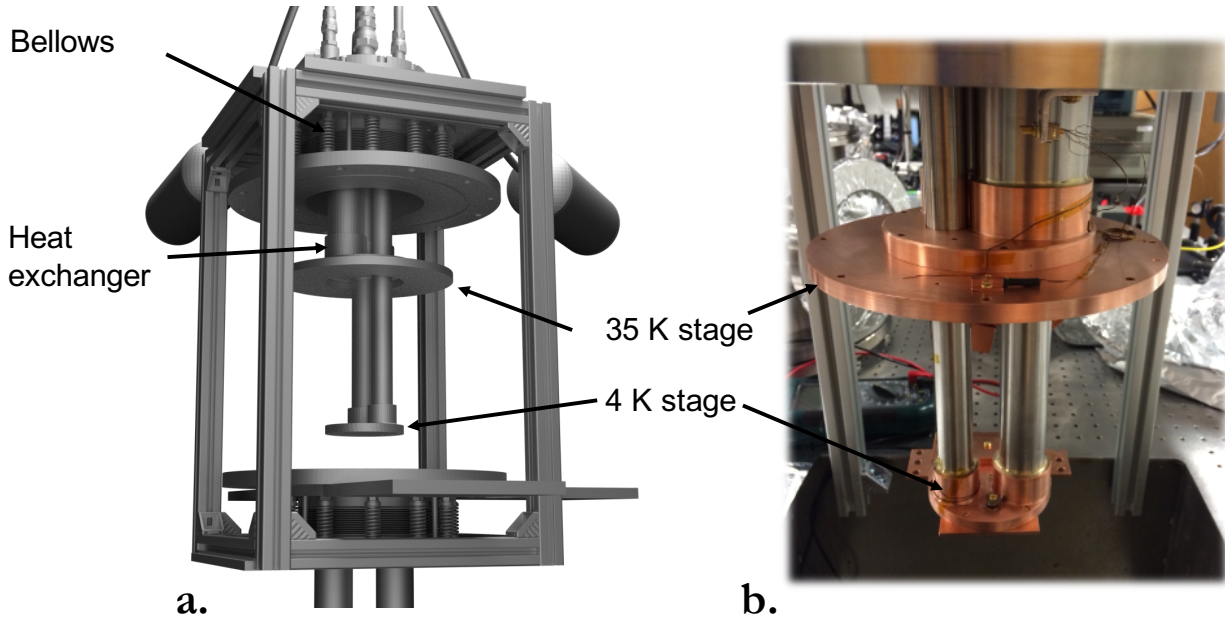


Figure 5.7: The Fridge chamber: **a.** design, **b.** picture of the internal structure

an example we use *Kevlar* thread or *G10* hollow rods. The *G10* rods are holding a 35K plate on top of the room temperature plate in the Science chamber, shown in Fig. 5.8.

On the other hand, to thermally short parts, we mostly use short pieces of copper with a high cross-sectional area. To thermalize the inside of the Science chamber, we use a large hollow copper tube at 45 K, which connects the Fridge 45 K plate in Figure. room 5.7 to the Science Chamber 45 K plate in Figure. 5.8. Similarly, the 4K is shorted using a solid Copper 101 cylinder which is inside of the hollow 45 K. The combined 45 K and 4 K cold arm which connects Science and Fridge Chambers is shown in Fig. 5.9.

To minimize mechanical vibrations, we connectorize the cold arm to the Fridge and Science Chamber plates using soft copper braids and foils. The

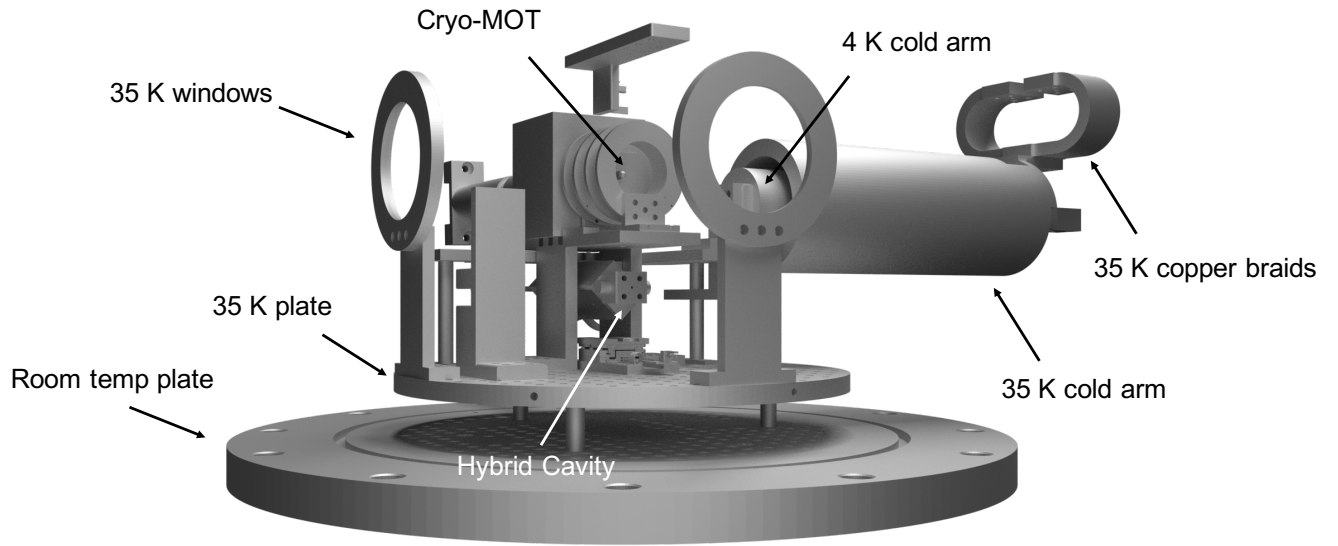


Figure 5.8: Internal design of the Science chamber

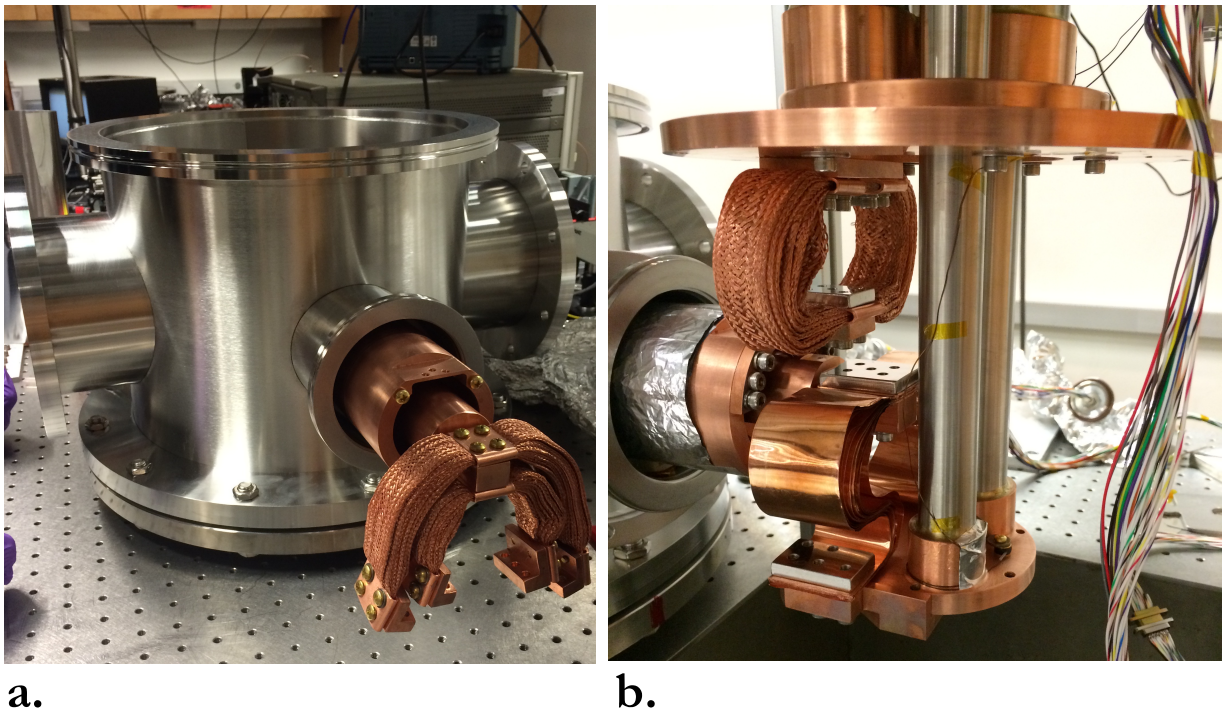


Figure 5.9: Thermal connectors: **a.** Science chamber with the cold arm and copper braids connectors, **b.** Fridge chamber connected to the cold arm of the Science chamber through braids connectors, 45 K, and copper foil connectors, 4K

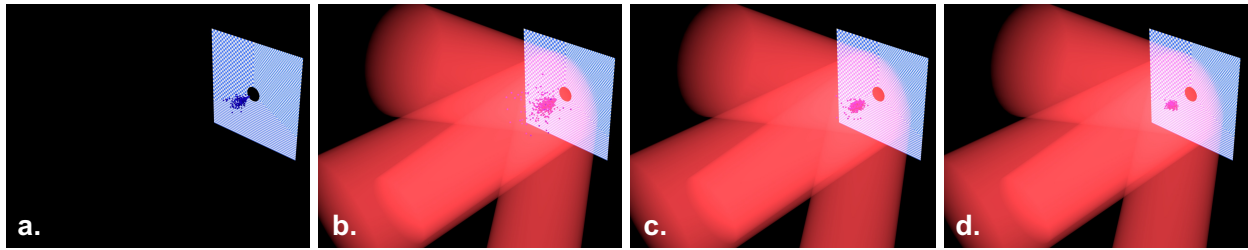


Figure 5.10: Animation of a grating MOT: **a.** Atoms are released from the source behind the getter, **b, c, d** Atoms are loaded, trapped and cooled in the trap

## 5.4 Cryogenic Magneto Optical Trap (MOT)

Magneto-Optical traps are an essential part of any cold atoms experiment. By combining laser beams and magnetic fields, MOTs trap and cool atoms using Zeeman and Doppler shifts in a small volume where the radiation pressure is zero [131]. Normally MOTs are formed using six beams counter-propagating along x,y,z axes to trap and cool atoms along these axes. These conventional MOTs are very good at trapping large numbers of atoms, but they require three optical axes into the chamber. As we have discussed above, cryogenic systems have limited cooling power, so it is beneficial to limit the number of windows as much as possible.

In order to avoid adding too many windows to our system, we decided to use a grating MOT. It consists of one incoming beam reflected off three blazed gratings at a specific angle [132, 133, 134]. The four beams form a volume with a zero radiation pressure at the centroid of the tetrahedron where the atoms are trapped and cooled, as shown in Fig. 5.10.

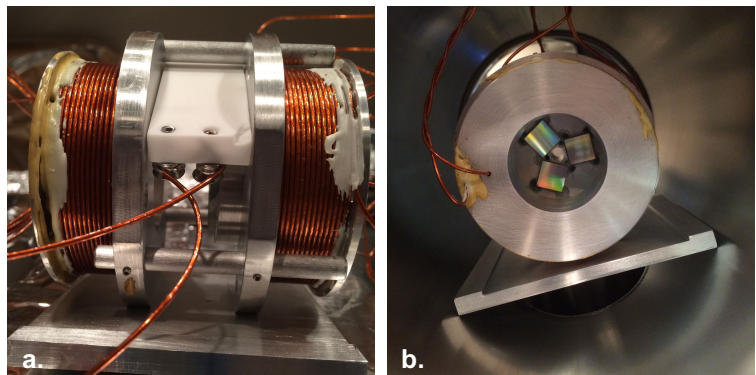


Figure 5.11: Homemade grating Mot with commercial gratings, Rb atom sources and magnetic coils attached

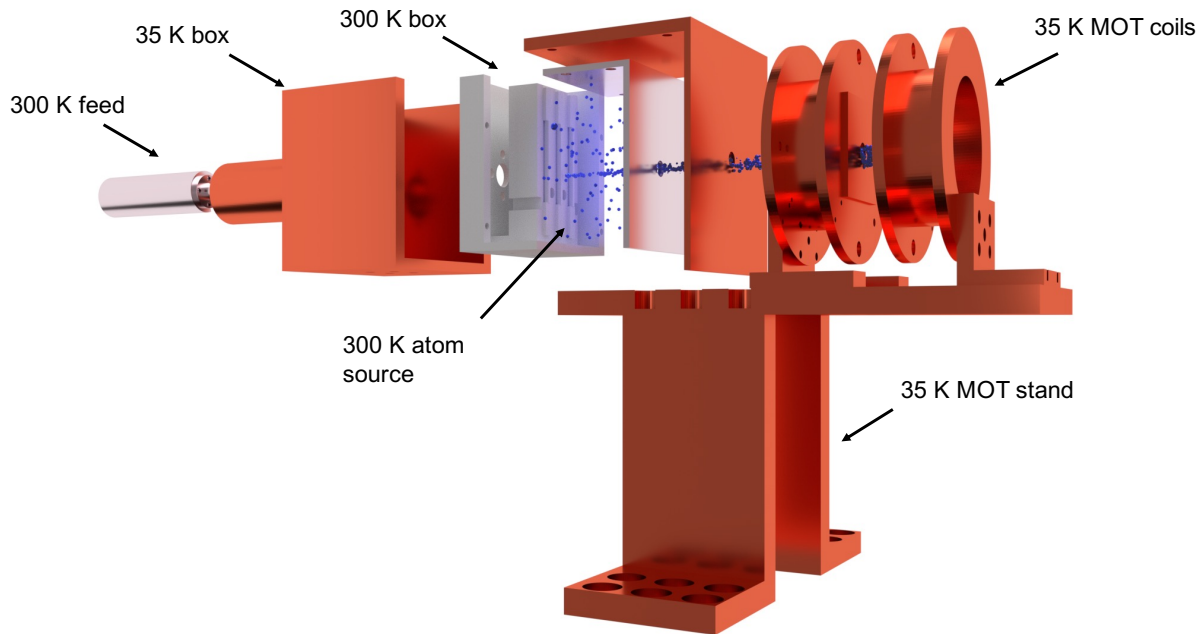


Figure 5.12: Cryogenic GMOT assembly including the atom source box and the atomic beam

As a first test, I made a room temperature setup using three commercially available blazed gratings, Rb sources attached to a Maycore piece located between two spools of magnetic coils in Helmholtz configuration. The setup is extremely easy to make and assemble, as shown in Fig. 5.11, and can be placed in any vacuum chamber that can reach  $10^{-8}$  mBar. Using a one inch input beam, a cloud of  $10^5$  atoms were trapped  $\approx 7$  mm off the surface of the plane of the gratings.

Before developing an analogous system in a cryostat, a few technological challenges have to be considered.

#### 5.4.1 Atom sources

The biggest challenge to trapping atoms at cryogenic temperatures is the temperature of the atom sources. We use *SAES getters* as the Rubidium source, which is an alkali metal dispenser, which requires a few A of current to run through the source and maintain it at a

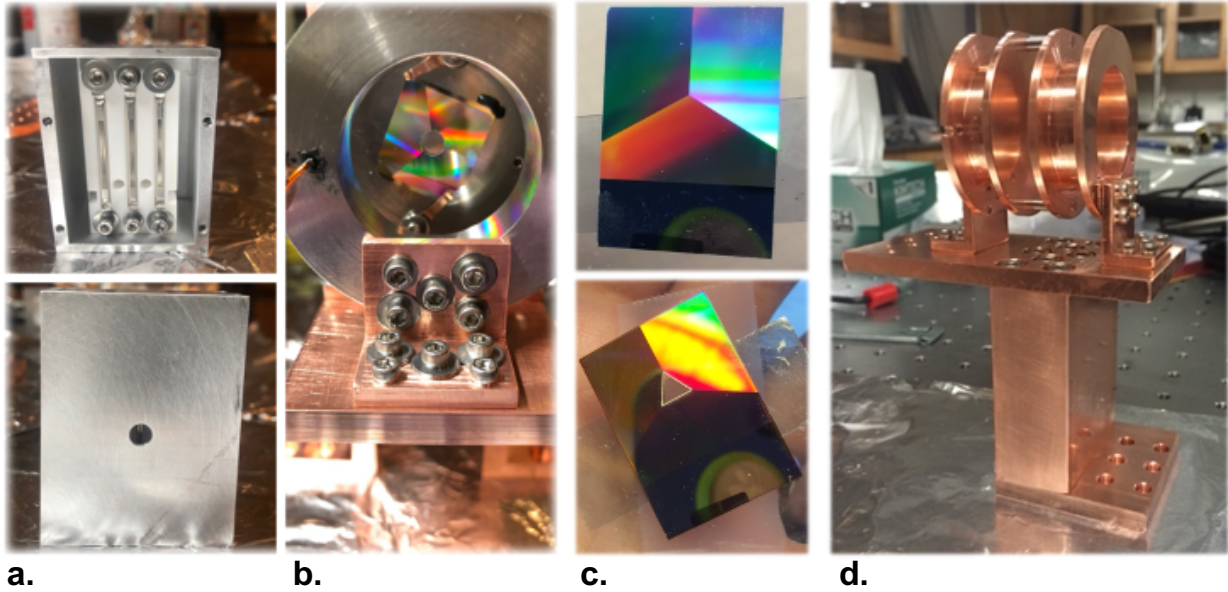


Figure 5.13: Pictures of the GMOT assembly: **a.** getters mounted on maycore inside of the room temperature aluminum box, **b** Assembled MOT with a grating (here the coil spools are made of stainless steel, later they were updated to copper)

high temperature of up to 150 C. This meant that we could not place the sources at either of the cold stages. At the same time, we wanted to keep the system compact and avoid adding another chamber for the oven and additional Zeeman slower to guide and slow atoms into the MOT.

The Fig. 5.12 shows the design of the solution I came up with. The getters are mounted on a Maycore ceramic piece to insulate current passing through the source. The Maycore mount is placed inside an aluminum box with an aperture for atoms to escape through, as shown in Fig. 5.13a. This aluminum box is thermalized to room temperature using a feedthrough arm attached to the outside of the vacuum chamber. This box is placed inside of a 35K box, without contact, which also has an aperture for the beam of atoms. This Russian “*Matryoshka doll*” is placed behind the MOT assembly so that the atomic beam can escape the getter, pass through apertures at 4K and 35 K, and load the MOT volume.

The layered design provides the shielding from high-temperature radiation of the atomic

source and cooling power of the lab at room temperature to the atomic dispenser. At the same time, it allows atoms to be emitted from the dispenser and thermalize to the room temperature box by continuously colliding with the walls of the inner box. This is important for the efficiency of trapping since GMOT has a specific range of velocities of atoms it can capture. If the atoms are emitted at 150 C, only a tiny fraction of that Boltzmann distribution is captured in the MOT. But if the atoms can cool down by bouncing off the aluminum box, there are more atoms at the capture velocity loaded into the MOT volume. In regular room temperature UHV experiments, the loading efficiency is either maximized using a slower (e.g., a Zeeman slower) or by using the room temperature chamber walls as a thermalizing box. So there is constant vapor pressure of the gas even if the sources are turned off. In the cryogenic case, our surface is perfect adsorber, and once the atoms hit the cold wall, they stick to it permanently.

### 5.4.2 Grating Chip

For the final cryogenic system, we used a surface patterned grating chip manufactured by the group in Strachlyde [132, 133] specifically to trap Rubidium. The single chip contains three regions for reflecting the input beam into the tetrahedral pattern as shown in Fig. 5.13c. This chip is 20×20 cm lithographically patterned grating with a pitch  $d = 1400$  nm, which corresponds to the first-order reflection at 34 degrees. This meant that the trapped volume is around 5 mm off the surface of the grating. The etched wafer

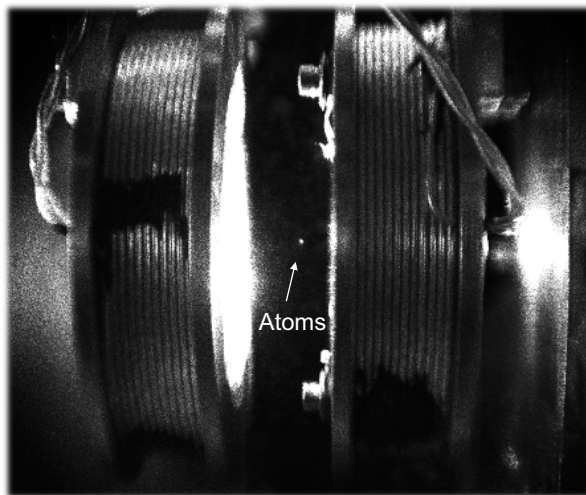


Figure 5.14: A fluorescence image of the GMOT structure with the trapped atoms inside of the cryostat

material is Silicon coated with Aluminum for optimal reflectivity. [135] To our pleasant surprise, the device performed well even at cryogenic temperatures. In order to avoid excessive heating and loss, the source box is placed behind the grating. Because of that, we laser-cut a hole in the middle of the grating after receiving the device, as shown in Fig. 5.13c. A 5 mm diameter hole did not degrade the performance of the grating since the reflected light at the center of the chip does not participate in the trapping and cooling of the atomic cloud.

### 5.4.3 Accessories

We decided to place the entirely MOT assembly on 35K for several reasons.

- None of the components needs to be at 4 K.
- Since we only have 4 K and 35 K stages, we would not need to shield the MOT structure from the superconducting cavity at 4 K.
- There is ample cooling power at 35 K.
- The resistivity of the copper wires at 35 K is significantly lower than at room temperature, so the heat load is significantly lower than at room temperature.
- We can use thick copper wires without worrying about the heat transferring through them from room temperature.
- The cold surfaces provide pumping to maintain low pressure around the grating.

Finally, we had to figure out how to image the atoms. We decided to image them from the side perpendicular to the direction of the B field coil system as shown in Fig. 5.14 It was critical to put a flat piece of copper thermalized at 4K and covered in activated charcoal at the back of the imaging plane. It provides a black/absorptive backdrop for imaging the

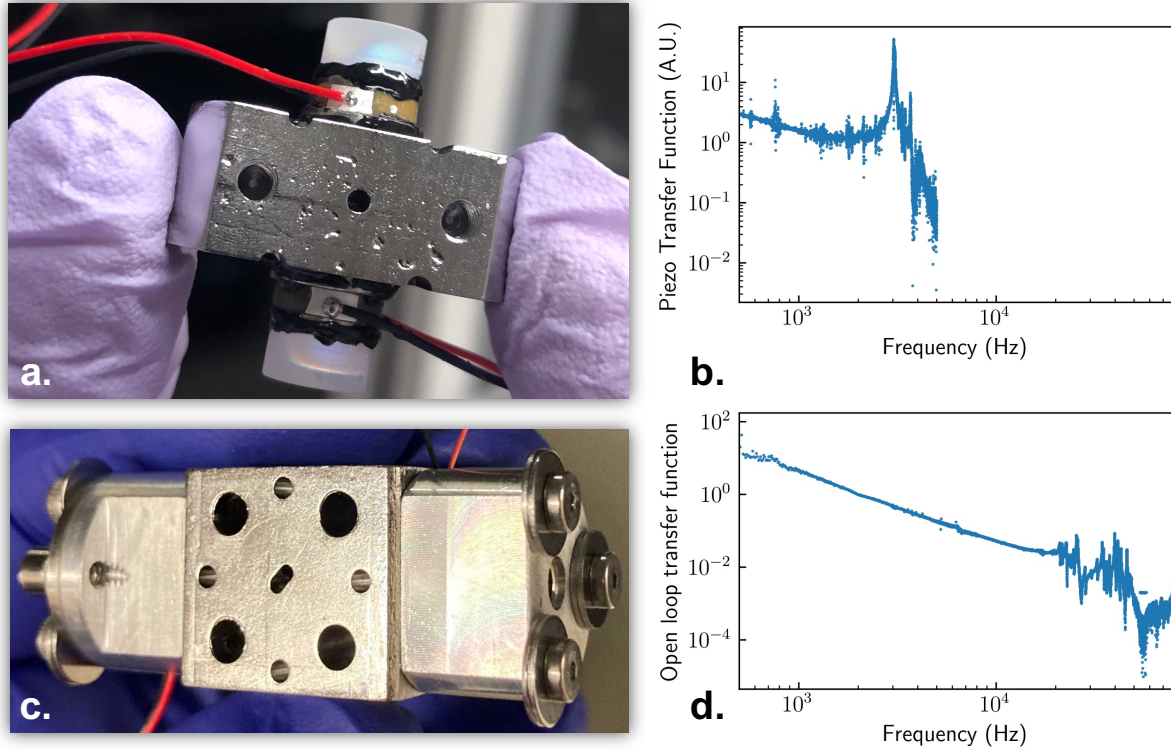


Figure 5.15: Upgrade of the hybrid cavity: **a.** The old hybrid cavity with mirrors and piezos glued to the Nb cavity, **b.** Frequency response of the mechanical vibrations of the optical cavity with dramatic resonances at low frequencies, **c.** New hybrid cavity with mirrors spring-loaded to the Nb cavity, without glue, **d.** Frequency response of the mechanical vibrations of the new optical cavity with significantly improved performance.

atoms and acts as an extra vacuum pump to lower the pressure around the GMOT. The Fig. 5.14 shows a fluorescent image of the full cryogenic GMOT structure with the trapped atomic cloud.

## 5.5 Hybrid Cavity

The crossed Hybrid device at the heart of our experiment consists of a superconducting mm-wave cavity described in Chapter. 4, and a Fabry-Perot cavity mounted onto the Nb structure.

As shown in Fig. 5.15, the optical cavity has been upgraded to the glue-less design to reduce vibrations coming from the degraded glue at cryogenic temperatures. These vibrations tend to worsen after each successive thermal cycling leading to the deterioration in performance. The new optical cavity is made of two 7.75 mm diameter mirrors 26.22 mm apart. It has a waist of about 60  $\mu\text{m}$  and Finesse of 4000.

The superconducting mm-wave cavity is an Nb box with three perpendicular tubes drilled into it. As shown in Fig. 5.17, we use an auxiliary mode of the superconducting cavity to tune the Rydberg state into the resonance with the lowest mode of the cavity, which we use for science. In order to minimize this tuning, we strive to machine the cavity as close to the resonance with the

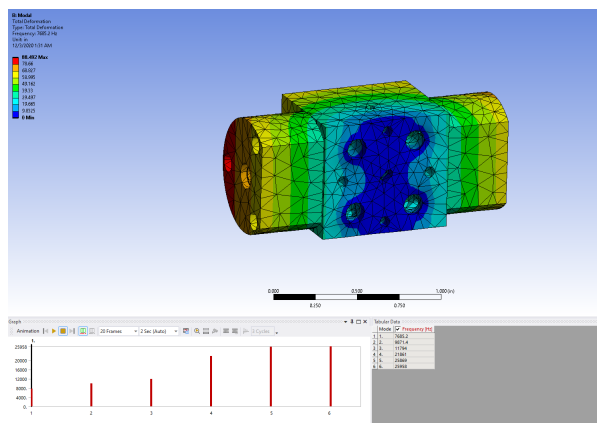


Figure 5.16: ANSYS mechanical vibrations simulation for the hybrid cavity structure

Rydberg transition as possible. Fig. 5.18 demonstrates how we were able to get from 108 GHz starting frequency to within 1 MHz of the transition at 99.429 GHz using acid etching and mechanical squeezing of the cavity. More data on squeezing and etching is presented in Appendix. B. The first generation hybrid cavity with the glue and with the frequency 85 MHz away from the  $|36S\rangle \rightarrow |35P\rangle$  transition was named HC1 and the current resonant model with the glue-less design is named “perfect pitch”.

## 5.6 Inside of the Science Chamber

After putting in the atomic sources, GMOT, hybrid cavity, optics necessary for guiding the light beams through the system, and all of the cryogenic wiring, the inside of the Science Chamber is very busy. Fig. 5.19 shows the interior of the Science Chamber I have designed

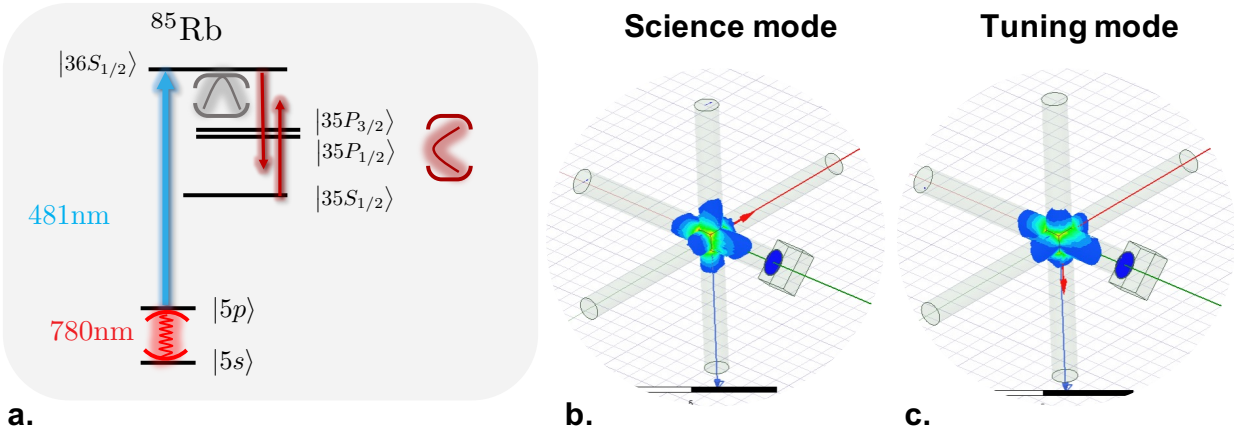


Figure 5.17: New superconducting cavity: **a.** The picture of the Nb cavity, **b.** Resonance frequency of the cavity after each subsequent etches and squeezes, **c.** Reflection measurement of the final cavity at 1K

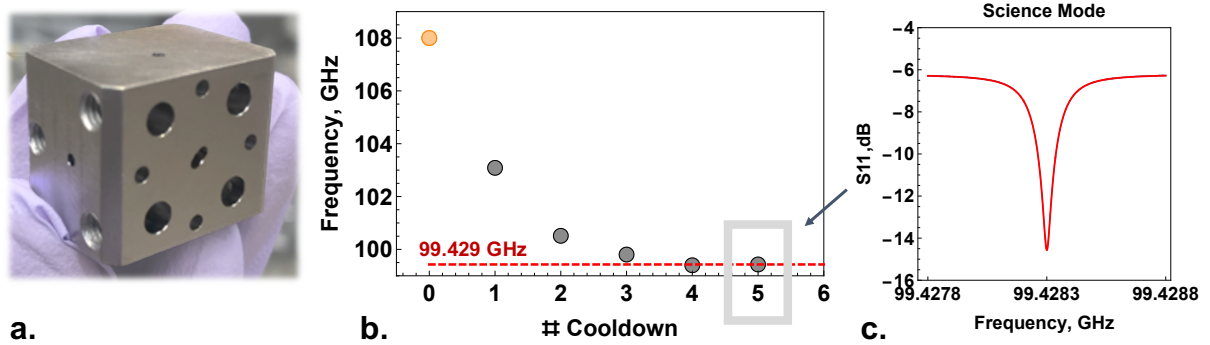


Figure 5.18: New superconducting cavity: **a.** The picture of the Nb cavity, **b.** Resonance frequency of the cavity after each subsequent etches and squeezes, **c.** Reflection measurement of the final cavity at 1K

and put together: with and without all of the ingredients of the experiment. Even though it looks extremely non-UHV compatible, our system maintains a high level of vacuum due to cryogenic surfaces acting as adsorption pumps. This comes with the bonus of not having to bake our vacuum system. And, it means we can open and close the chamber every week, sometimes even twice a week. As challenging as it was to figure out the right materials and geometries for the AMO experiments to function properly in cryo - it ended up being an extremely powerful tool. I hope the future generations of AMO experiments wishing to go cryo will benefit from our technical experience.

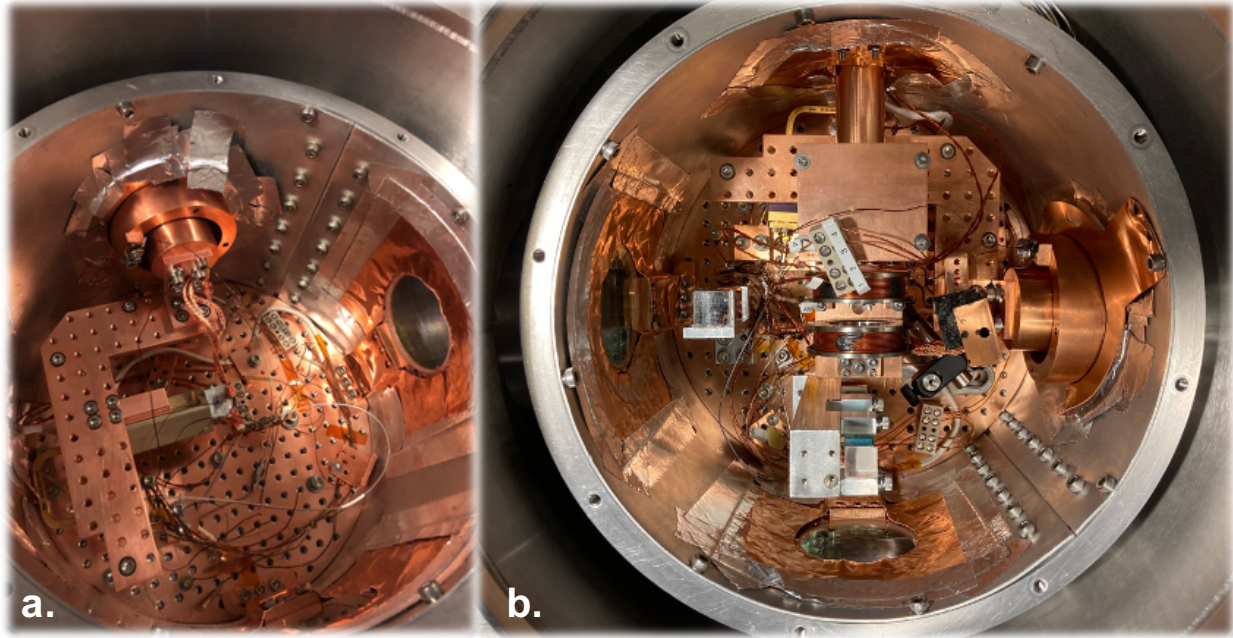


Figure 5.19: Interior of the Science Chamber: **a.** only including the mm-wave circuitry, **b.** with everything inside

## 5.7 Optical Setup

Our experiment requires a sophisticated system of many lasers beams. This includes the MOT and Repump lasers offset-locked to a reference Rb vapor cell, shown in Fig. 5.20. These lasers are home-made systems with the commercial *Eagleyard* DFB diode in them. In addition to the optical elements shown in Fig. 5.20, we also use a high power EOM on the MOT beam path for generating a phase-coherent repump beam for the Gray Molasses cooling.

Our science optical cavity is locked using the PDH system with a 1560 nm laser. Furthermore, the blue 485 nm *Toptica* and infrared 780 nm narrow laser (doubled using the SHG) are locked to the transmission of the cavity. So the laser beams follow whatever the residual shaking of the optical cavity we have left after the PDH locking. This “following” of the cavity by the lasers is necessary due to the high level of vibrations in our cryogenic system. The diagram of the system, built by Mark Stone, is shown in Fig. 5.21. Note that this schematic does not

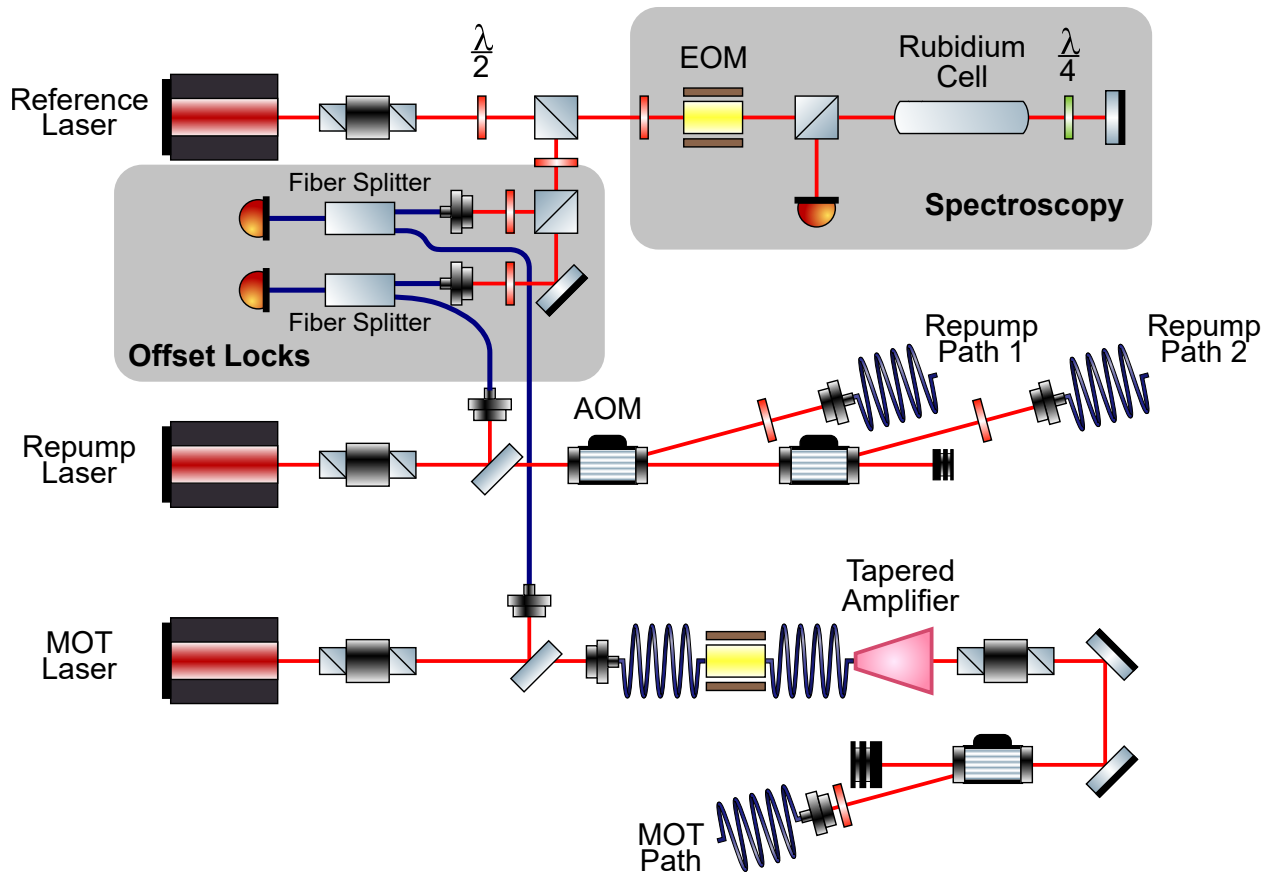


Figure 5.20: Diagram of the MOT laser setup (the figure is made by M.Stone )

include the UV laser, which also “follows” the cavity. Fig. 5.21 shows images of the main optical table with the hybrid chamber and laser setups involved in the mm-wave and optical interface system.

## 5.8 MM-wave setup for hybrid experiments

Fig. 5.23 shows the circuit, and Fig. 5.24 shows the schematic of the overall mm-wave circuit I have set up for measuring our hybrid cavity-QED experiment. We have used a very similar setup for measuring most of our devices at 100 GHz. I also included a list of devices with the company name and part number for anyone interested in using mm-wave circuitry in their experiment. In Appendix. C I attached notes on the mm-wave VNA I have made to

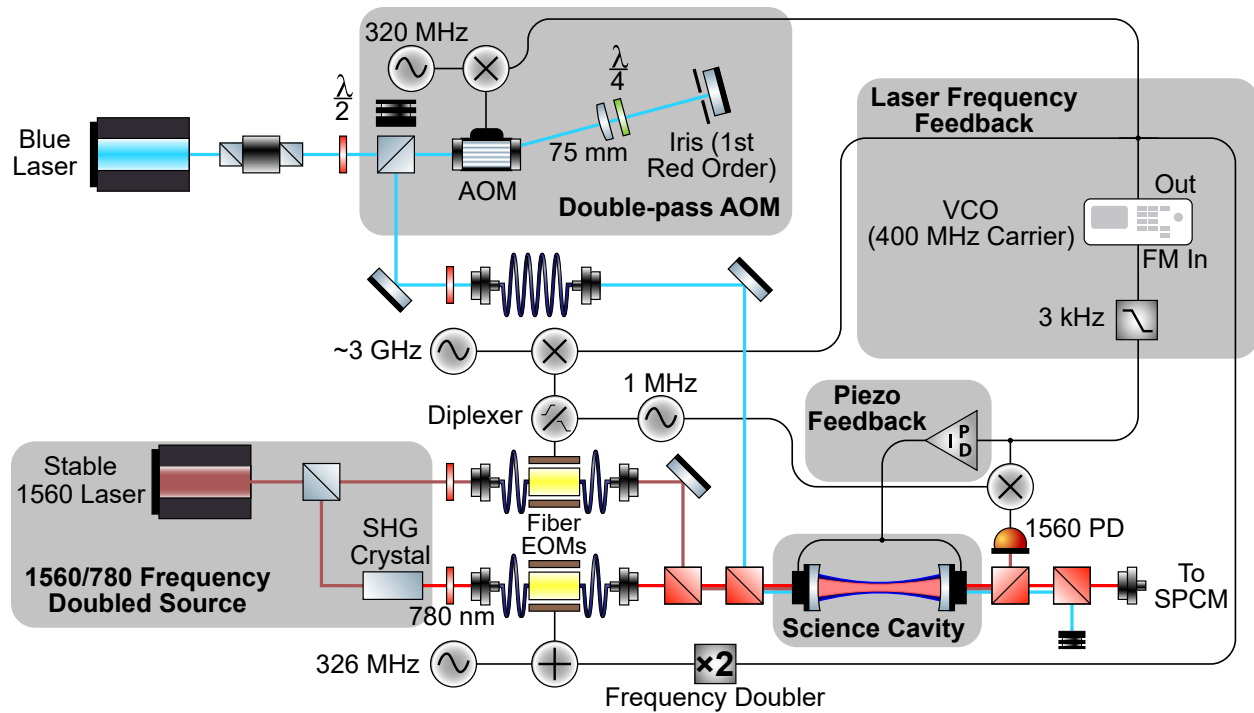


Figure 5.21: Diagram of the setup for locking 780 nm laser for optical cavity probe (the figure is made by M.Stone )

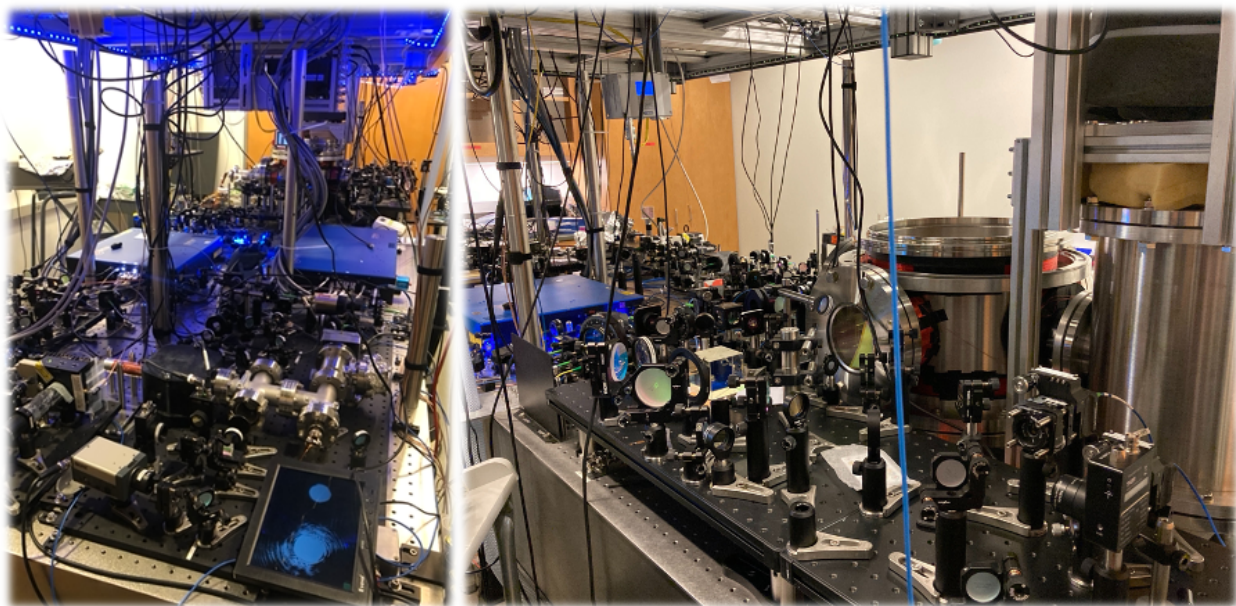


Figure 5.22: Images of the main optical table with the hybrid experiment

do simple phase and magnitude measurements of the mm-wave devices using *Signal Core* frequency sources and *VDI* frequency multipliers.

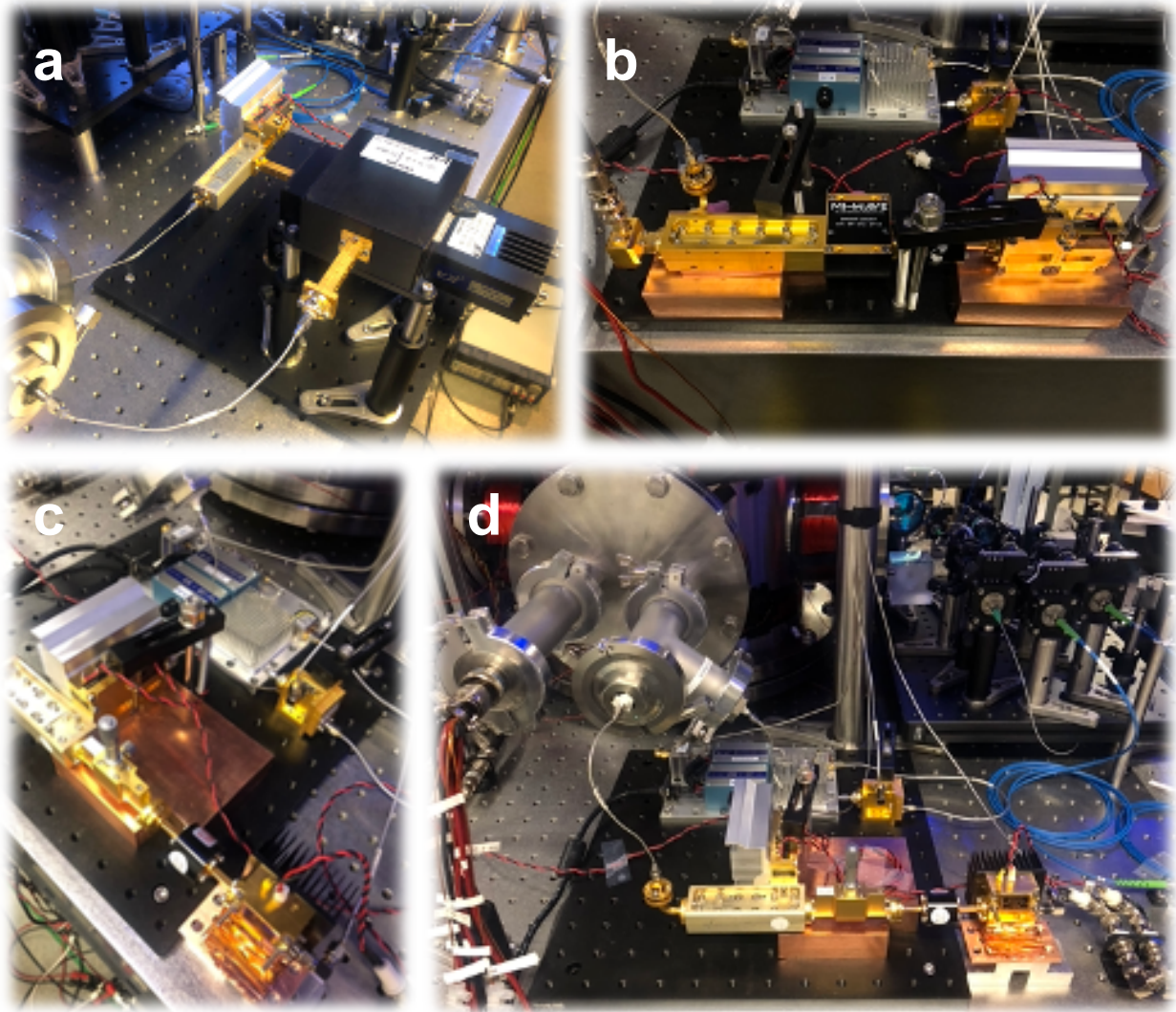


Figure 5.23: MM-wave measurement setup for our hybrid experiment:**a.** using VDI TRx modules, **b,c,d** using VDI AMC modules

Device	Description	Company	Part number
<b>Vector Network Analyzer</b>	Generates and measures coherent microwave signals up to 26GHz	Keysight	N5242A

Device	Description	Company	Part number
<b>WR-10 Multiplier VNAX</b>	x6 multiplier/mixer chain for up-converting the signal at 12.5-18.3GHz to 75-110GHz	VDI	VNAX WR-10 Mini TxRx
<b>WR-10 Multiplier/Amplifier chain</b>	x6 multiplier for up-converting the signal at 12.5-18.3GHz to 75-110GHz and a 21dB Gain amplifier	Quantum Microwave Components	QMC-MX6-10F21HS
<b>WR-10 Directional Coupler</b>	Precision high directivity, 20dB Directional Coupler, directivity 35dB	Quinstar	QJR-W20R00
<b>WR-10 Waveguide to coax adapters</b>	WR-10 Waveguide to coax adapters with 1-3dB insertion loss	Mi-wave	411W-387-1mmF/M
<b>WR-10 Cryogenic Attenuator</b>	WR-10 Waveguide 10dB attenuator	Quinstar	QCX-W10000
<b>1mm coaxial cable</b>	1mm coax cable for 75-110GHz	RF cable	W047MM-6R
<b>WR-10 E-plane 45° bend</b>	WR-10 E-plane 45° bend	Sage	SWB-10045-EB
<b>WR-10 Custom waveguide</b>	WR-10 Custom waveguide with 45° twist and U-shape bend	Sage	QAC -W0045T90BUOC

Device	Description	Company	Part number
<b>WR-10 Cryogenic Directional Coupler</b>	Cryogenic precision high directivity, 10dB Directional Coupler, directivity 35dB	Quinstar	QJR-W10R0ZCT
<b>WR-10 Cryogenic LNA Amplifier</b>	25dB Gain amplifier, PSAT +12dBm for 80-105GHz	Quantum Microwave Components	QMC-AMP10-93352512C
<b>WR-10 Multiplier/Mixer chain</b>	x6 multiplier/mixer for down-converting the signal at 75-110GHz to 12.5-18.3GHz and reading out the measurement through IF=279MHz	VDI	VNAx WR-10 Mini Rx

Table 5.3: MM-wave measurement circuit components

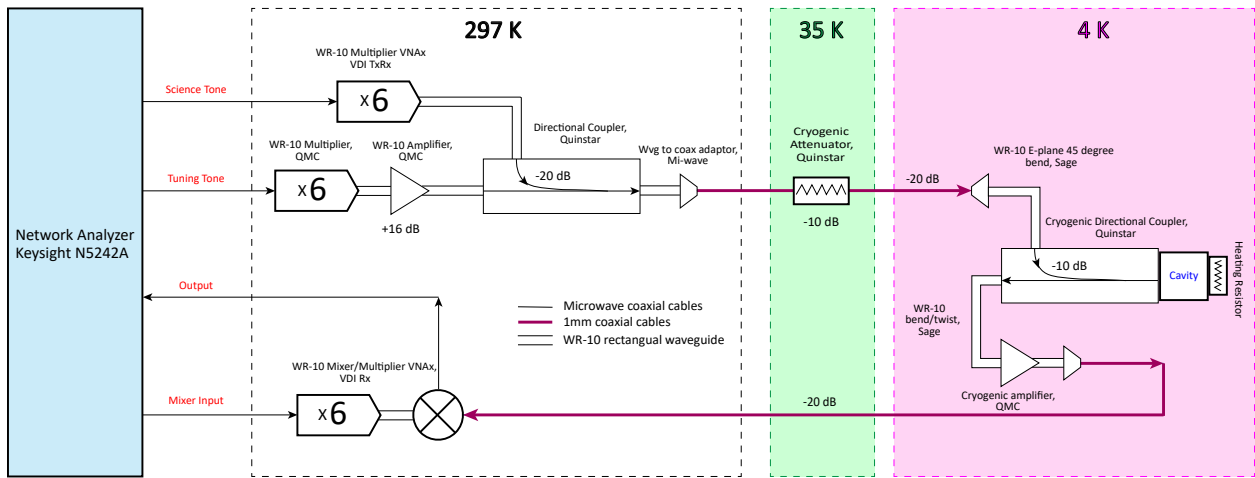


Figure 5.24: The schematic for the MM-wave measurement setup for our hybrid experiment.

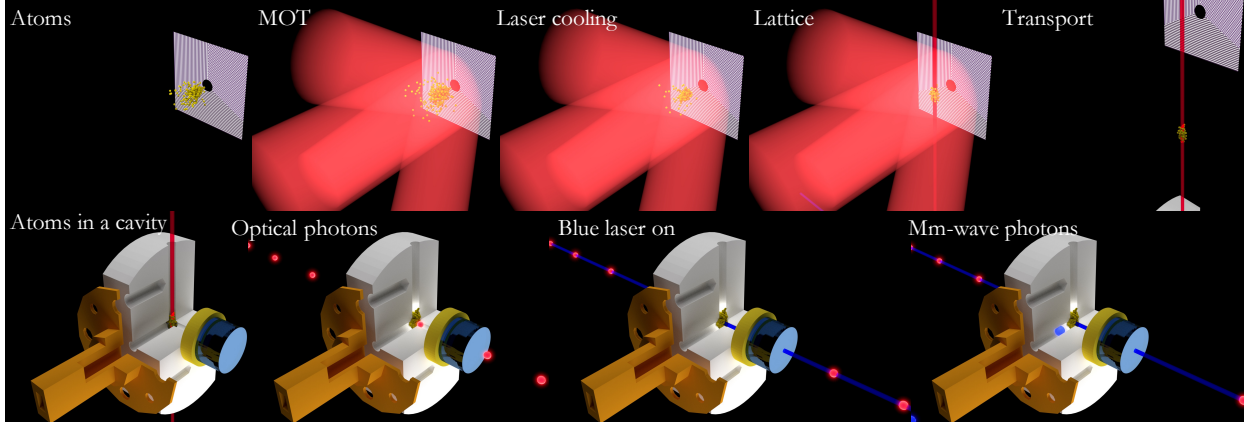


Figure 6.1: Our experimental sequence for interfacing mm-wave and optical photons using cold atoms.

## CHAPTER 6

### EXPERIMENT: INTERFACING OPTICAL AND MM-WAVE PHOTONS USING RYDBERG ATOMS

In this chapter I will go over the first measurements on our fully built hybrid system. Since it's a novel platform, I will start by describing in detail the experimental sequence. And then will proceed towards our most recent results that show: efficient interface between optical and mm-wave photons and an observed nonlinearity in the number of photons. Our novel platform combines tools from cold atoms, circuit-QED and Rydberg cavity-QED fields into one unique hybrid experiment. We have just began to explore the capability of our machine, and thrilled to see where the science could takes us.

#### 6.1 Experimental Sequence

The majority of our experimental sequence consists of steps for trapping, cooling and loading  $^{85}\text{Rb}$  atoms into the Hybrid cavity. Then, there is a sequence of steps to prepare the cloud in the correct atomic state. And, the final step in which we probe the cloud and detect

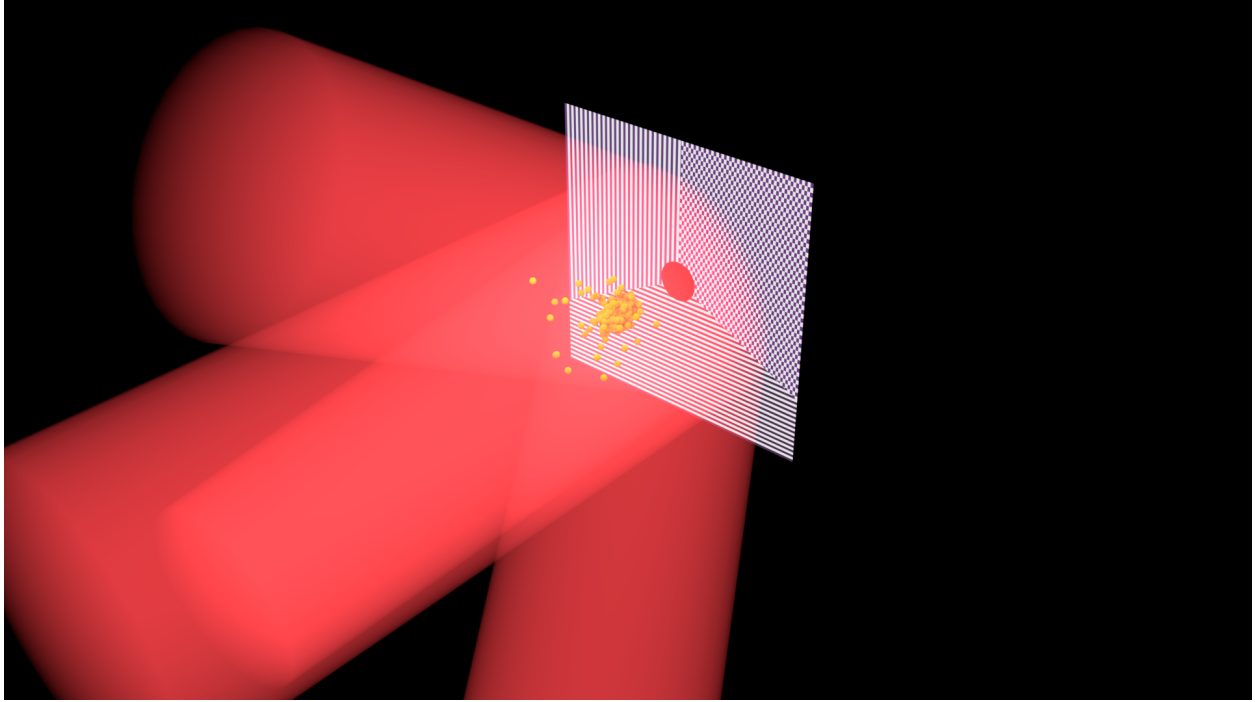


Figure 6.2: Grating MOT and laser cooling

the transmitted signal through the hybrid cavity using single photon detectors *SPCM from Exelitas*. We have derived the spectra for this transmitted signal using the non-Hermitian perturbation theory and other methods in Chapter. 3, and will be using it for fitting the experimental data. Fig. 6.1 shows cartoon snapshots of a routine sequence in our experiment.

### 6.1.1 Trapping and cooling of $^{85}\text{Rb}$

We turn up the  $^{85}\text{Rb}$  sources in the morning. While the entire laser system is warming up, the getters populate a significant partial pressure in the room temperature  $^{85}\text{Rb}$  box. By the time the system is ready to run, both atoms and lasers reach their peak performance. In order to have consistence in atom number and speedy system warm up in the mornings we don't turn getters completely off at the end of the day. Instead, we keep them at low 1 A current when the system is not running, as opposed to 3.5 A when the machine is running.

First step is the grating Magneto-Optical Trap (MOT) for 250 ms. The MOT beam is

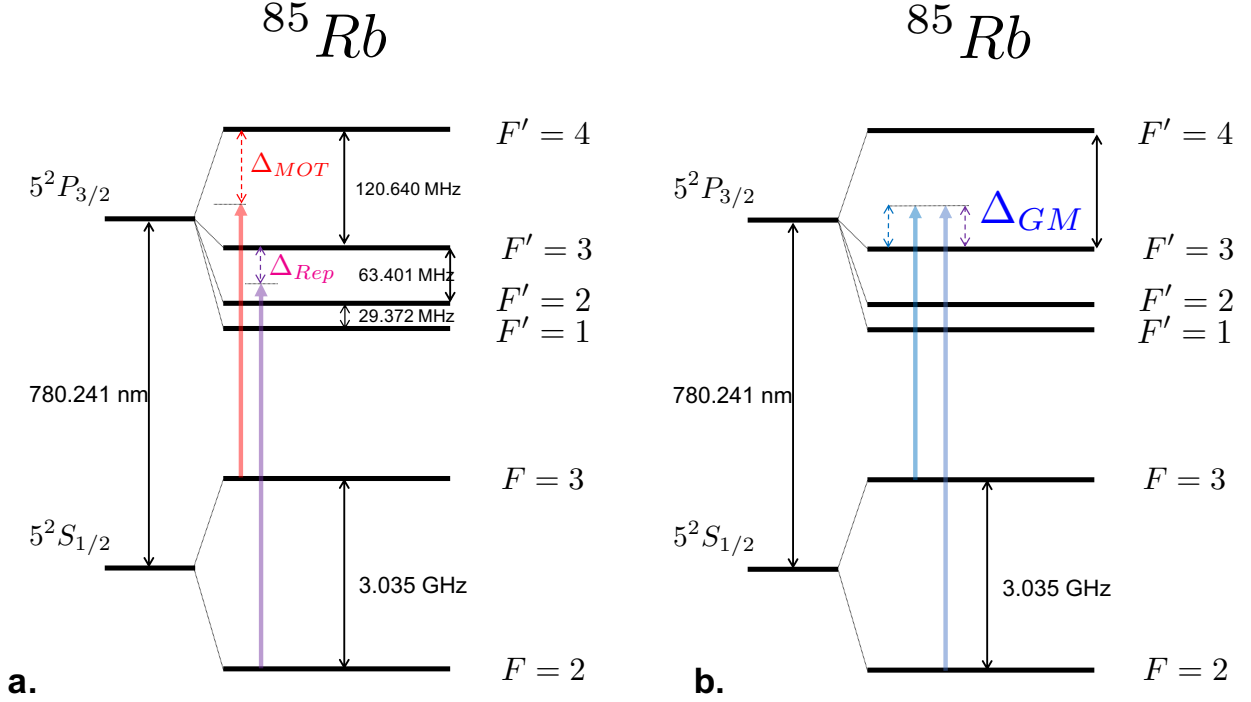


Figure 6.3:  $^{85}\text{Rb}$   $D_2$  line energy levels used in: **a.** MOT and PGC cooling, **b.**  $\lambda$ -enhanced Gray Molasses.

$\Delta_{MOT} \approx 4\Gamma$  red-detuned from the  $|F = 3\rangle \rightarrow |F' = 4\rangle$  transition, and the repump beam is  $\Delta_{Rep} \approx 0.8\Gamma$  red detuned from the  $|F = 2\rangle \rightarrow |F' = 3\rangle$  transition, as shown in Fig. 6.3a. The regular MOT is followed by the EndMOT stage for 30 ms which we introduced to optimize for the best transition into Polarization Gradient Cooling, PGC. Note that usually the endMOT in cold atoms experiments is used to compress the atomic cloud after initial trapping. There, the detunings are decreased and magnetic fields are increased. This way the pre-captured atoms are more efficiently cooled and tightly trapped. In our case, however, the endMOT has a different purpose. In a cryogenic environment the B fields ring down for a long time. Because of this we introduce a "loose" endMOT, which has PGC-like detunings  $\Delta_{MOT} \approx 12.5\Gamma$  and  $\Delta_{Rep} \approx 0.8\Gamma$ , and 2/3 of the MOT B field gradient. By the end of the endMOT we get about  $10^7$  atoms at temperature  $T_{MOT} \approx 98\mu\text{K}$  and phase space density  $\rho_{MOT} \approx 1.8 \times 10^{-10}$ , as shown in Fig. 6.4.

Next, we have the laser cooling using Polarization Gradient Cooling (PGC) in two steps.

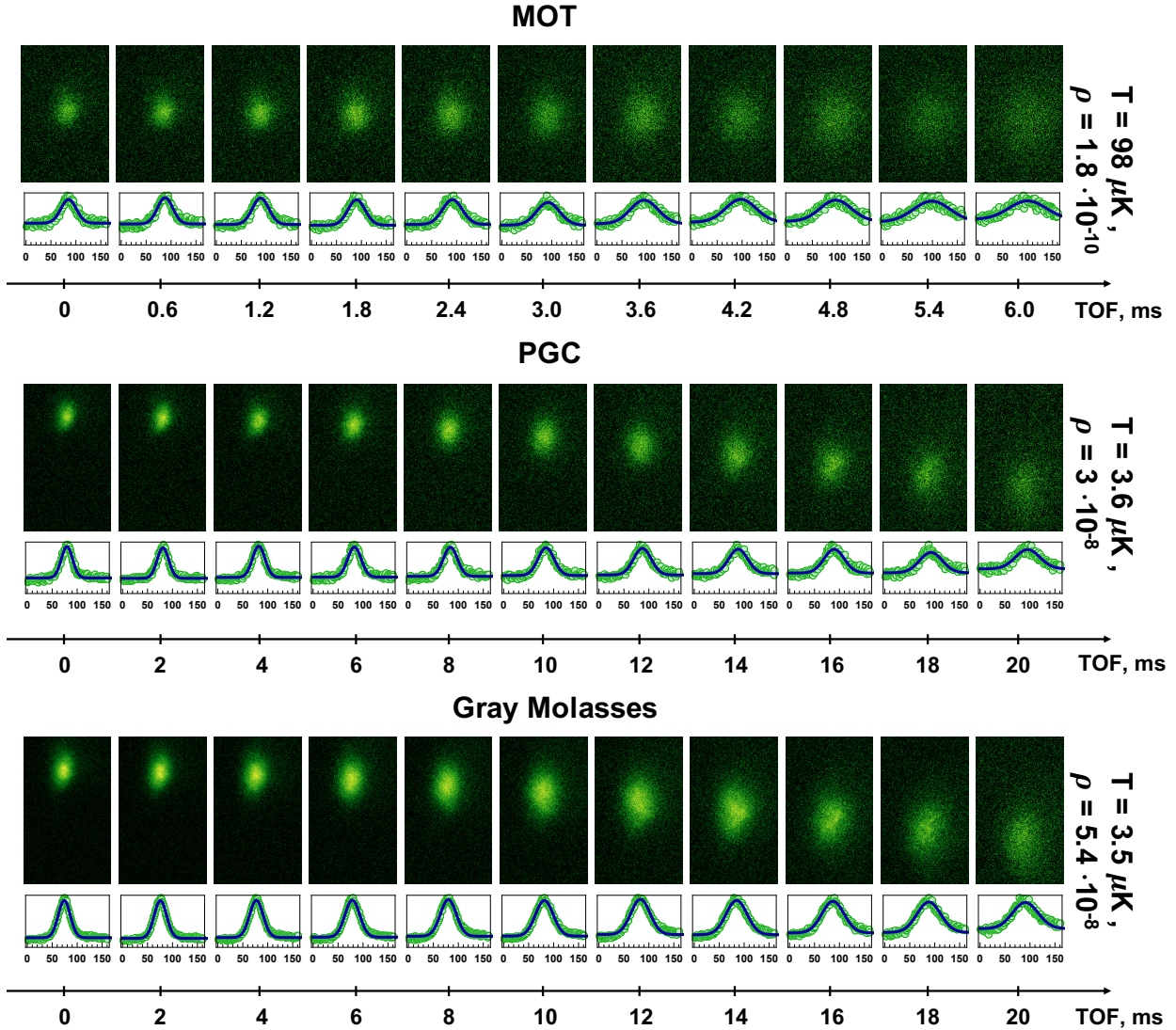


Figure 6.4: Time of flight fluorescence images of the atomic cloud after MOT, PGC and Gray molasses

The first step is 20 ms with  $\Delta_{MOT} \approx 14.1\Gamma$  and a resonant Repump beam. The second is a short 2.5 ms ramp-down of MOT's beam power to almost zero. Similar to the MOT optimization, the steps are a bit unusual for cold atoms experiments due to inability to turn off magnetic coils abruptly. After the PGC steps are done we get down to  $T_{PGC} \approx 3.6\mu K$  and phase space density  $\rho_{MOT} \approx 3 \times 10^{-8}$ , as shown in Fig. 6.4. This temperature is already quite good for just PGC cooling for  $^{85}\text{Rb}$ , which is not used very frequently in cold atoms experiments.

### 6.1.2 $\lambda$ -enhanced Gray Molasses $^{85}\text{Rb}$

Even though we are not limited by temperature after the PGC, it's always a good idea to get the highest possible phase-space density to load more atoms into the transport lattice. For that reason I tried  $\lambda$ -enhanced Gray Molasses cooling on the  $D_2$  transition, demonstrated before in  $^{87}\text{Rb}$  [136].

The idea behind higher phase-space density is cooling using dark states of atoms, which are decoupled from light, created by two coherent laser beams in a  $\lambda$  configuration. As shown in Fig. 6.3b., unlike regular MOT, we use open transition  $|F = 3\rangle \rightarrow |F' = 3\rangle$  and repump  $|F = 2\rangle \rightarrow |F' = 3\rangle$  both blue detuned from the excited state. The coherent repump beam is generated using a fiber coupled high-power EOM (phase modulator) from *AvdR*.

As far as we know,  $^{85}\text{Rb}$   $\lambda$ -enhanced Gray Molasses cooling on the  $D_2$  transition has not been demonstrated before, especially in a grating cryogenic MOT. At  $\Delta_{GM} \approx 5.8\Gamma$  we achieve  $T_{GM} \approx 3.5\mu\text{K}$  and phase space density  $\rho_{GM} \approx 5.4 \times 10^{-8}$ , as shown in Fig. 6.4. The temperature difference is not a significant win compared to our regular PGC, but we see a factor improvement in phase space density. The coherent signature of Fano resonance in Fig. 6.5 shows that we, indeed, have cooling using a coherent superposition of states. The coldest temperature achieved is a bit off the Raman condition  $\delta = 0$  due to an imperfect compensation of stray magnetic fields.

### 6.1.3 Lattice and transport

Since our MOT is mechanically mounted to a 35 K stage and the hybrid cavity is at the 4 K stage, the two are spatially separated to shield the 4 K from the scattered light, high pressure and radiated heat from the atomic sources. The center of the crossed cavity is located 64 mm directly below the MOT volume. To transport precooled and trapped atoms inside the

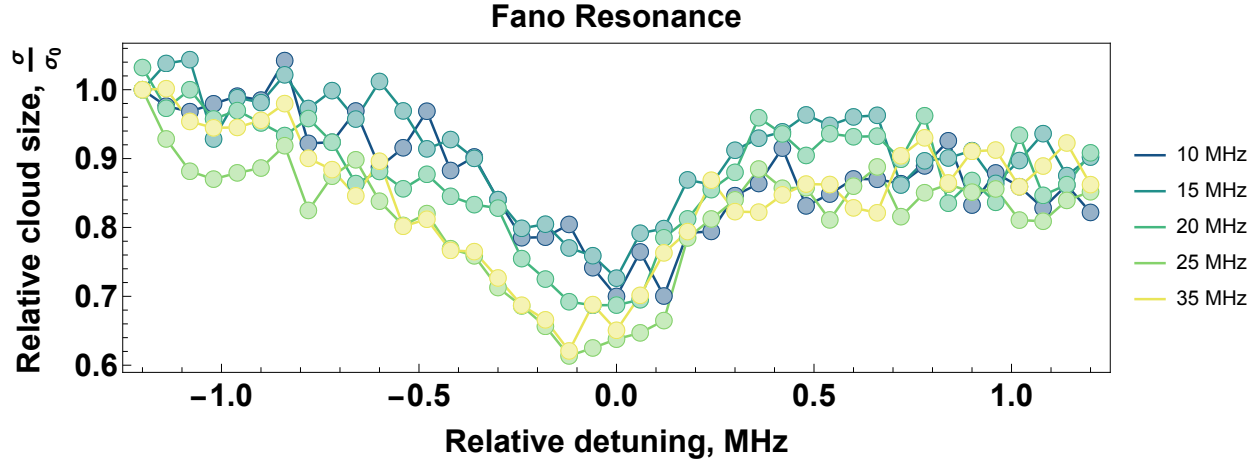


Figure 6.5: Fano signature of Gray Molasses cooling at different  $\Delta_{GM}$

cavity we use 1D optical lattice. It is made of two counter-propagating 785 nm laser beams. The large detuning and high power of the beams create a standing wave pattern, which traps atoms using a dipole force. Both beams pass through a double-pass AOM for controlling the power and frequency of the beams. By changing one of the frequencies of the beams using an RF port of the AOM we can control the velocity of the peaks and troughs of the standing wave. As the wave pattern moves, so do the atoms.

We load a fraction of the cloud into the optical lattice and transport it downwards by 64mm. Empirically, we found that the most amount of atoms is retained if we accelerate out for 5 ms, coast at a fixed velocity for 5 ms and decelerate into the crossed cavity for 5 ms. An example of tightly trapped atoms in a lattice compared to a falling under the gravity MOT cloud is shown in

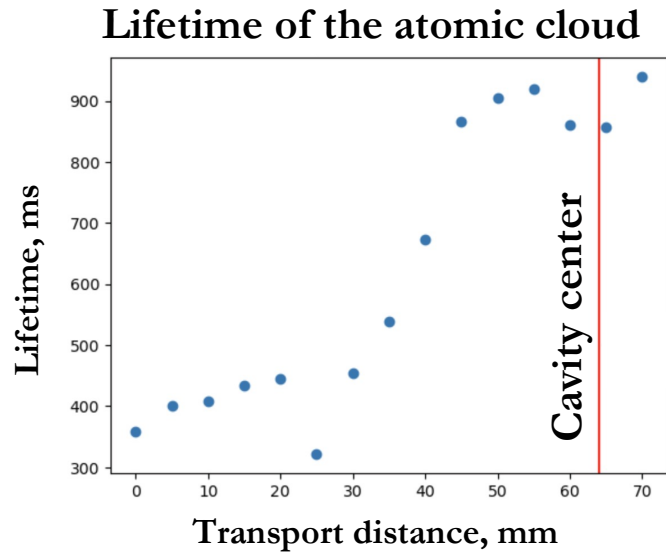


Figure 6.6: Lifetime of the atomic cloud in a lattice as a function of the transport distance from the MOT

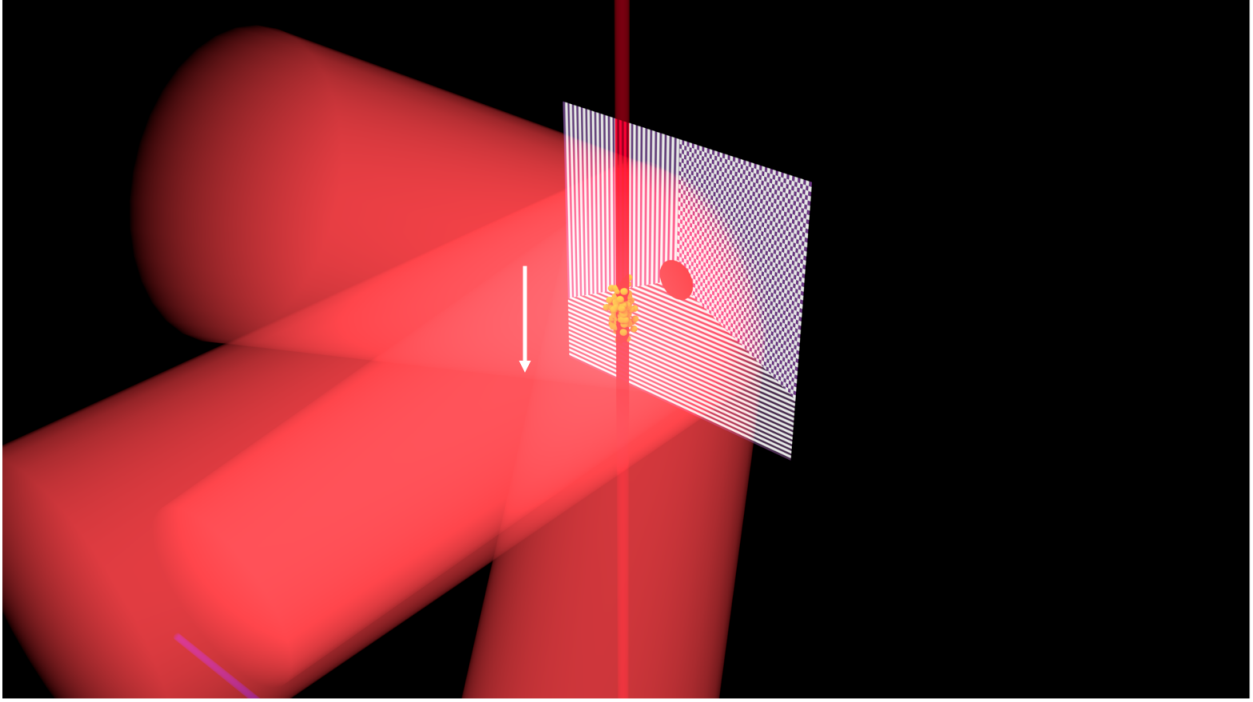


Figure 6.7: Transport of the atoms in the lattice

Fig. 6.8. It is important to note that the measured lifetime of the atoms in a trap varies depending on the location of the atoms. The data in Fig. 6.6 shows clearly that the atoms live longer in the lattice trap when they are located inside of the hybrid cavity,  $\approx 1$  s, compared to when they are held at the location of the MOT,  $\approx 350$  ms. This indicates lower background pressure inside of the 4 K cavity, which we expected and hoped for. This is another unique feature of our system - the ability to use cold surfaces to control the pressure experienced by the atomic cloud.

## 6.2 Hybrid Interface for mm-wave and optical photons

Now that the atoms are inside of the hybrid cavity, we can start testing our system. The data presented below is for the 1st generation cavity HC1, an earlier design 85 MHz detuned from the  $|36S\rangle \rightarrow |35P\rangle$  transition.

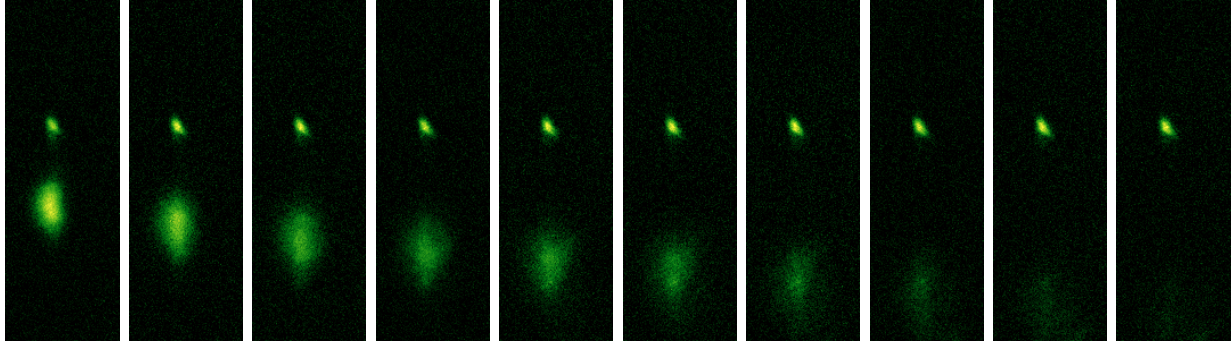


Figure 6.8: Fluorescent images of atoms trapped in a lattice with a falling under gravity MOT

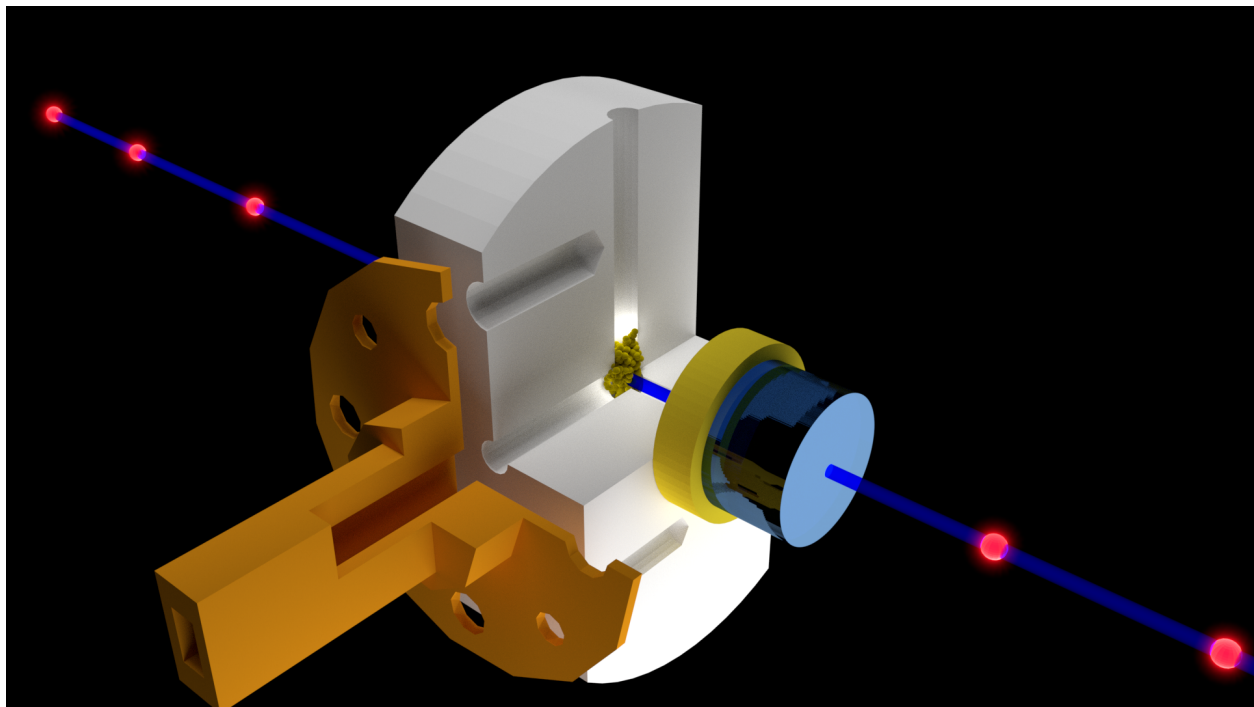


Figure 6.9: Interfacing optical and mm-wave photons with Rydberg atoms

First, we measured the transmission of the bare optical cavity, by probing it with resonant optical photons. The probe duration was around 1 ms, and to produce plot in Fig. 6.10 we averaged over 100 sample points. From the Lorentzian fit, we get linewidth of the optical cavity  $\kappa_{opt} \approx 3.9$  MHz.

Second, we measured the cavity transmission with the atomic cloud inside the cavity mode and observed the Vacuum Rabi Splitting spectrum in Fig. 6.11. From the fit, we get  $g_{opt} \approx 16$

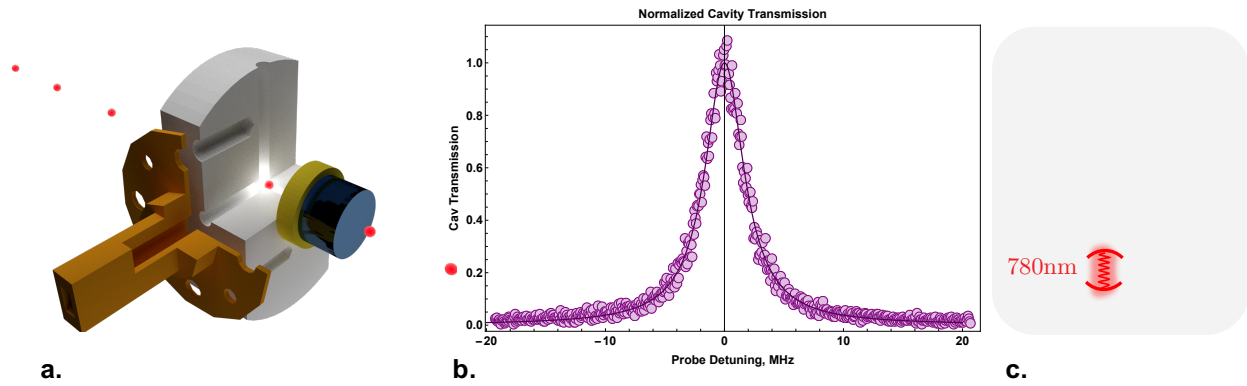


Figure 6.10: Bare optical cavity transmission measurement: **a.** Cartoon of the system, **b.** Data and fit, **c.** The excitations involved in the spectrum

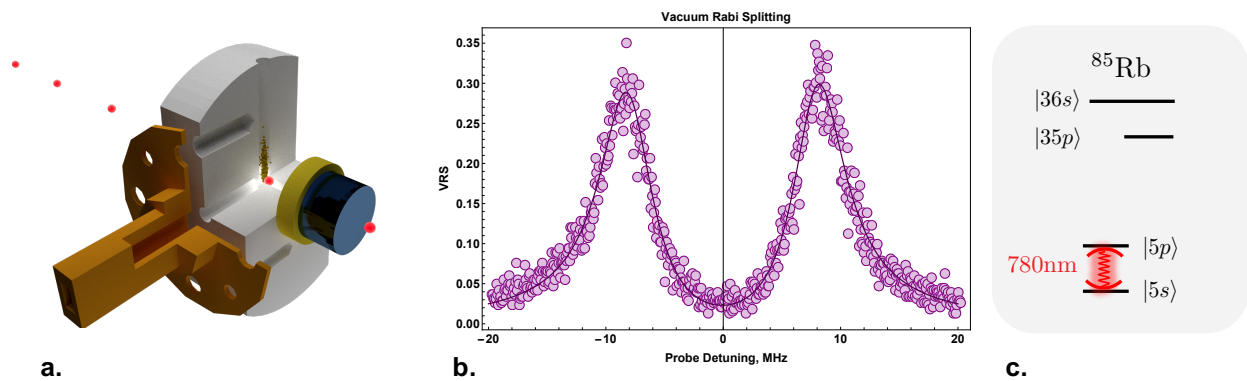


Figure 6.11: Vacuum Rabi splitting measurement: **a.** Cartoon of the system, **b.** Data and fit, **c.** The excitations involved in the spectrum

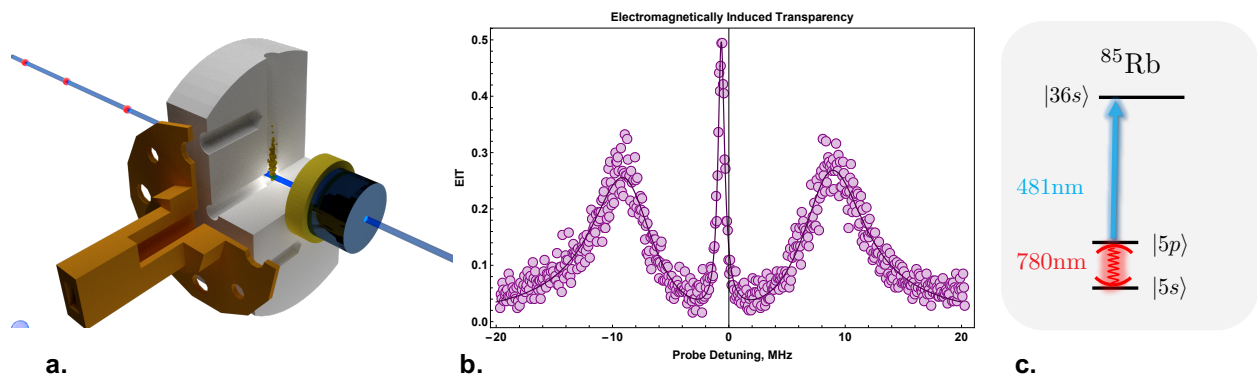


Figure 6.12: Electromagnetically Induced Transparency measurement: **a.** Cartoon of the system, **b.** Data and fit, **c.** The excitations involved in the spectrum

MHz.

Then, we turn on the blue 485 nm laser beam and measure a narrow transparency window

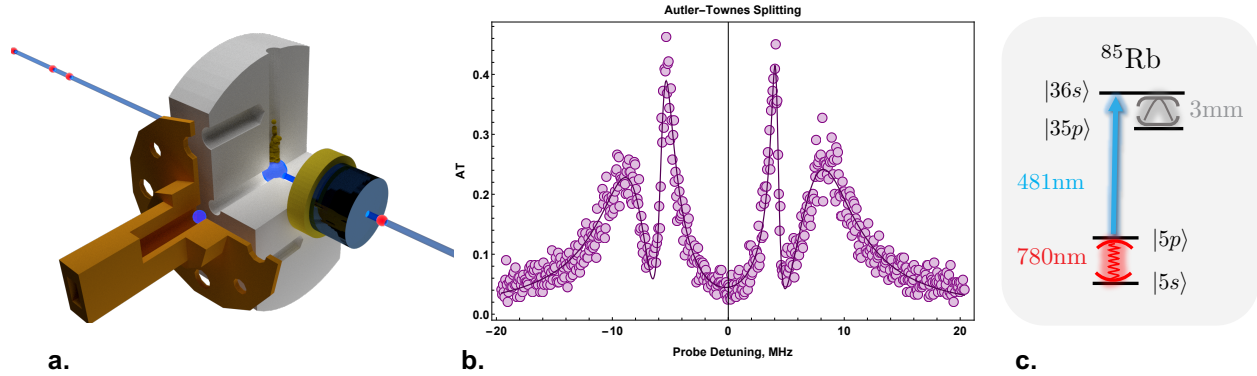


Figure 6.13: Autler-Townes splitting due to mm-wave photons in the superconducting cavity: **a.** Cartoon of the system, **b.** Data and fit, **c.** The excitations involved in the spectrum

at zero detuning, characteristic of the cavity EIT in Fig. 6.12. Here, from the fit, we get the linewidth of the Rydberg state to be  $\Gamma_R \approx 0.486$  MHz.

Finally, we measured the Autler-Townes splitting of the EIT peak due to the coupling of the Rydberg state to the mm-wave photons, shown in Fig. 6.13. Here, we sent a few mm-wave photons inside of the superconducting cavity and locked the power of the mm-wave source to keep the coupling strength constant. Even though we were operating off the resonance, the coupling between the Rydberg state and the mm-wave photons is very strong.

These measurements showed that we have, indeed, built a hybrid machine that is able to interface mm-wave and optical photons using Rydberg atoms. The next step was to tune the mm-wave cavity frequency to the  $|36S\rangle \rightarrow |35P\rangle$  atomic transition. This maximizes the coupling strength between a single mm-wave photon and Rydberg atom to its designed value. With the designed strong coupling we would be able to observe the splitting of the EIT peak due to the vacuum state of the mm-wave cavity without the need to populate the superconducting cavity with mm-wave photons. And, finally, we would be able to observe the photon nonlinearity in the second order correlation function.

As was mentioned in the Chapter 5, I have designed an auxiliary mm-wave mode to tune the Rydberg states into the resonance with the cavity, since it is significantly easier than to

machine a 100 GHz cavity with 100 kHz accuracy in frequency. We were able to tune the Rydberg states into the resonance with the cavity, however it came at a cost to the EIT linewidth. By 30 MHz tuning, the EIT linewidth would grow up to 1-2 MHz which is not acceptable for our parameter regime. Therefore, I have made another cavity HC2, also known as “perfect pitch”, which as name suggests the is extremely close to its bare atomic transition frequency. See Chapter. 5 and App. B for more details on how this became possible.

Now, with a resonant cavity at hand, we had one more mystery to solve - the broad linewidth of the EIT peak without any tuning. The natural linewidth of the  $|36s\rangle$  state is around 5 kHz. The  $\Gamma_R \approx 0.486$  MHz measured from Fig. 6.12 even with the blackbody radiation included is significantly broadened. And since we need to be able to resolve a splitting of order  $g_{mm}$ , this broadening had to be corrected. This is where we discovered an issue which eventually became a useful tool in our system - the Meissner effect for optical pumping.

### 6.3 Optical Pumping and Meissner effect

Accurate control of atomic levels and magnetic sub-levels is crucial for our experiments. Without any intervention, atoms at temperature  $T$  occupy energy levels  $E_1$  and  $E_2$  according to the Boltzmann distribution:

$$\frac{n_1}{n_2} \propto \exp \frac{E_2 - E_1}{k_B T} \quad (6.1)$$

This means that if the energy differences are small or comparable to thermal energy  $k_B T$ , atoms are spread across many sub-levels. If we have many nearly-degenerate  $m_F$  states, with small energy deviations due to stray fields, this could lead to the broadening of the effective linewidth of the dark polariton in our EIT spectrum as discussed in Chapter. 3. To eliminate

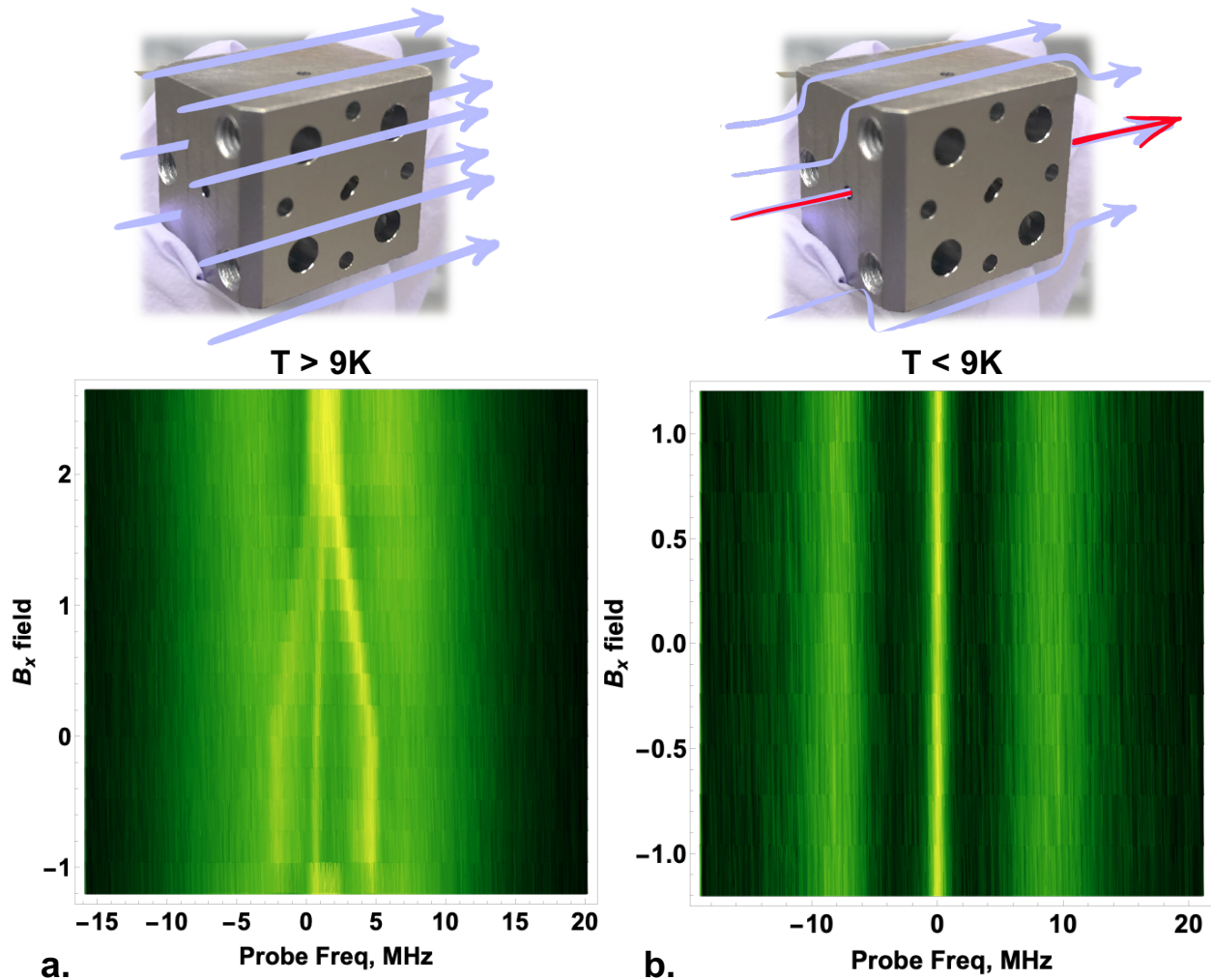
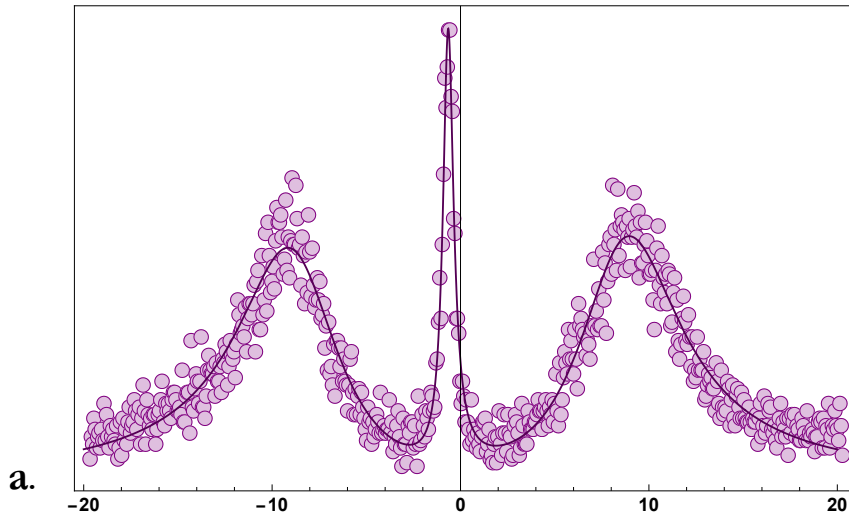


Figure 6.14: EIT spectrum as a function of B field: **a.** Above  $T_c$ , **b.** Below  $T_c$

this effect cold atoms experiments use optical pumping, which splits the magnetic sub-levels along one axis using an external B field and selectively pumps atoms into a particular  $m_F$  sub-level using a laser beam of chosen polarization.

It turns out that in our system the optical pumping needs to be optimized before the cavity is cooled down below the  $T_c = 9.2K$  of Nb due to Meissner effect. The Meissner effect is responsible for expelling the B fields out of the bulk of the superconductor and freezing B field lines in the holes of our cavity as we cool through the critical point. Once the B fields are frozen the optical pumping cannot be modified. To test this hypothesis, we performed

### EIT not compensated for the Meissner Effect



### EIT compensated for the Meissner Effect

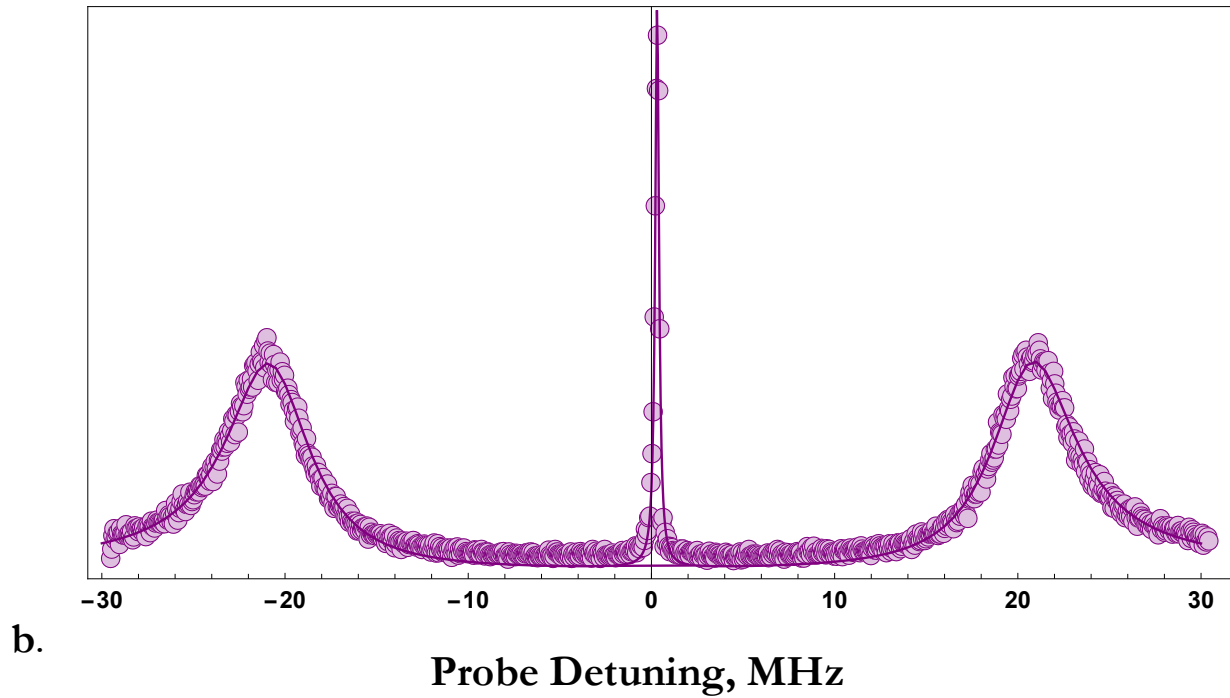


Figure 6.15: EIT spectrum: **a.** Before optimizing optical pumping above  $T_c$ , **b.** After optimizing the optical pumping

a 2D scan of the EIT spectra as a function of magnetic field. One of the 2D scans for the x-axis B field is shown in Fig. 6.14. It is clear how the B field affects the EIT, normally,

in the cold atoms experiments by broadening and eventually splitting the peak into sub-peaks corresponding to the different atomic sublevels. For us this is observable above  $T_c$  in Fig. 6.14a. However, we operate below  $T_c$  where the B fields don't make any difference to the spectra as shown in Fig. 6.14b. Note that this is only true once the atomic cloud is transported into the superconducting cavity. At the location of the MOT our system resembles the conventional cold atoms experiments with the a longer ring down time for the B fields due to a large amount of high-Q copper.

So in order to optimize the EIT spectra we had to optimize the optical pumping above  $T_c$  then cool the system down. The results of the B field optimization are shown in Fig. 6.15. Not only were we able to increase the  $g$  by a factor of 2, but we were able to decrease the EIT linewidth from  $\Gamma_R \approx 486$  kHz down to 30 kHz! This is a huge win towards reaching the strong coupling regime. At 1K we would be deep in the strong coupling regime, at 5K we are about to cross the strong coupling threshold.

## 6.4 The first nonlinear signals from our hybrid system

Finally, with the nearly-resonant cavity, “perfect pitch”, and the narrow EIT we can start to explore the parameter regime of our quantum system. Here, I present the most recent data, which shows the mean field nonlinearity in photon number in our system and potential signs for the quantum photon nonlinearity we are striving towards. The data is preliminary and there are still many questions to answer, but this is truly the highlight of my PhD experience.

The Fig. 6.16a shows multiple curves of  $\Gamma_R$  vs mm-wave detuning from the cavity resonance. The data was acquired by using the tuning mode of the mm-wave cavity to shift the  $|36S\rangle$  state. The EIT spectrum was re-centered by changing the frequency of the blue laser beam. This leads to some detuning  $\delta_{mm} = \omega_{mm} - \omega_{R \rightarrow R2}$ , between the science cavity mode and the desired Rydberg transition. The EIT data was taken at various detunings. The  $\Gamma_R$  is

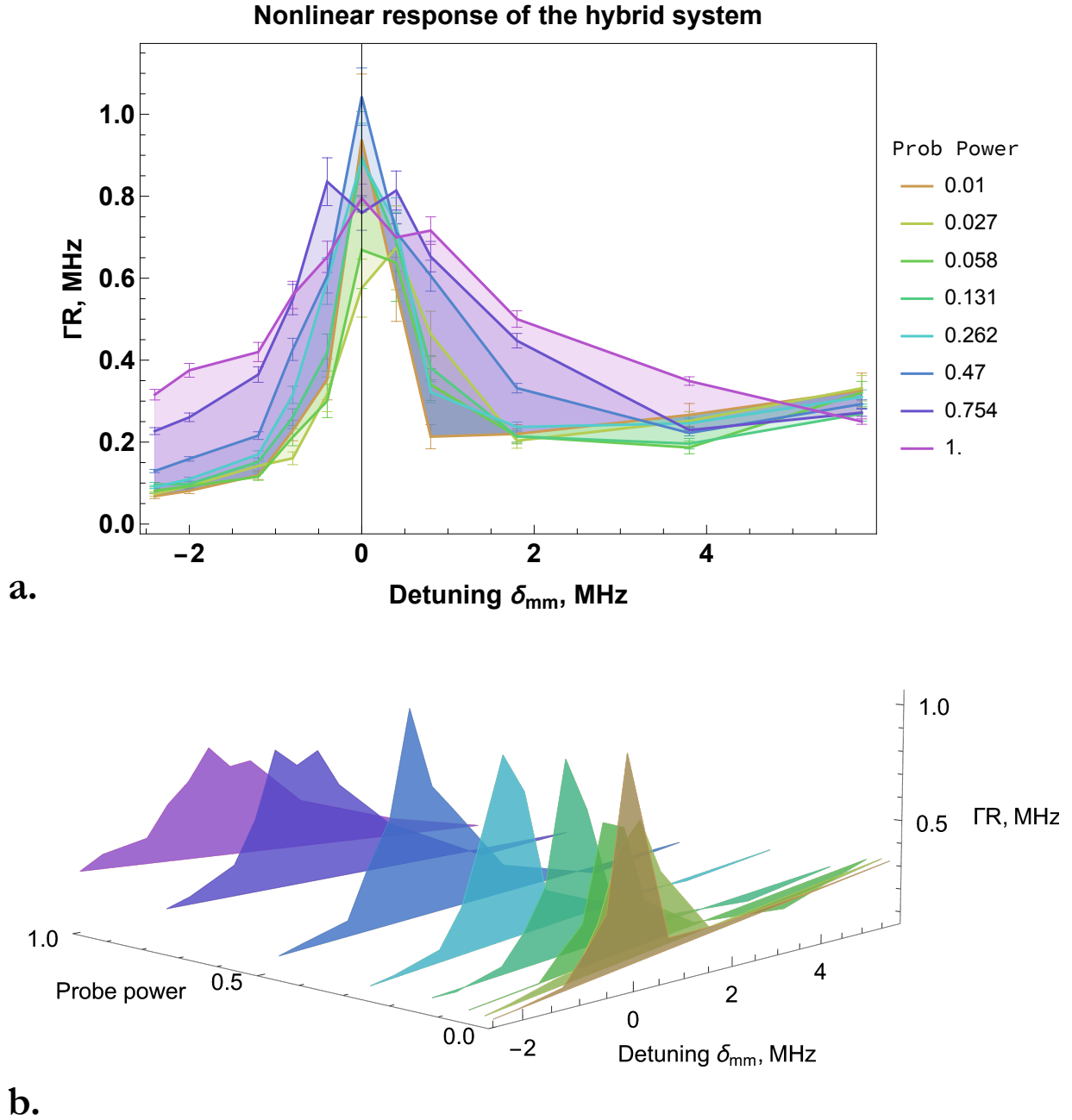


Figure 6.16: EIT spectrum: **a.** Before optimizing optical pumping above  $T_c$ , **b.** After optimizing the optical pumping

a fit parameter from the non-Hermitian perturbation theory covered in Chapter. 3. As we shift the atomic transition through the resonance with the superconducting mm-wave cavity the  $\Gamma_R$  and the EIT linewidth increase dramatically, since  $\delta_{mm} = 0$  the effective coupling is at its maximum. This was expected from the previous data that showed AT splitting

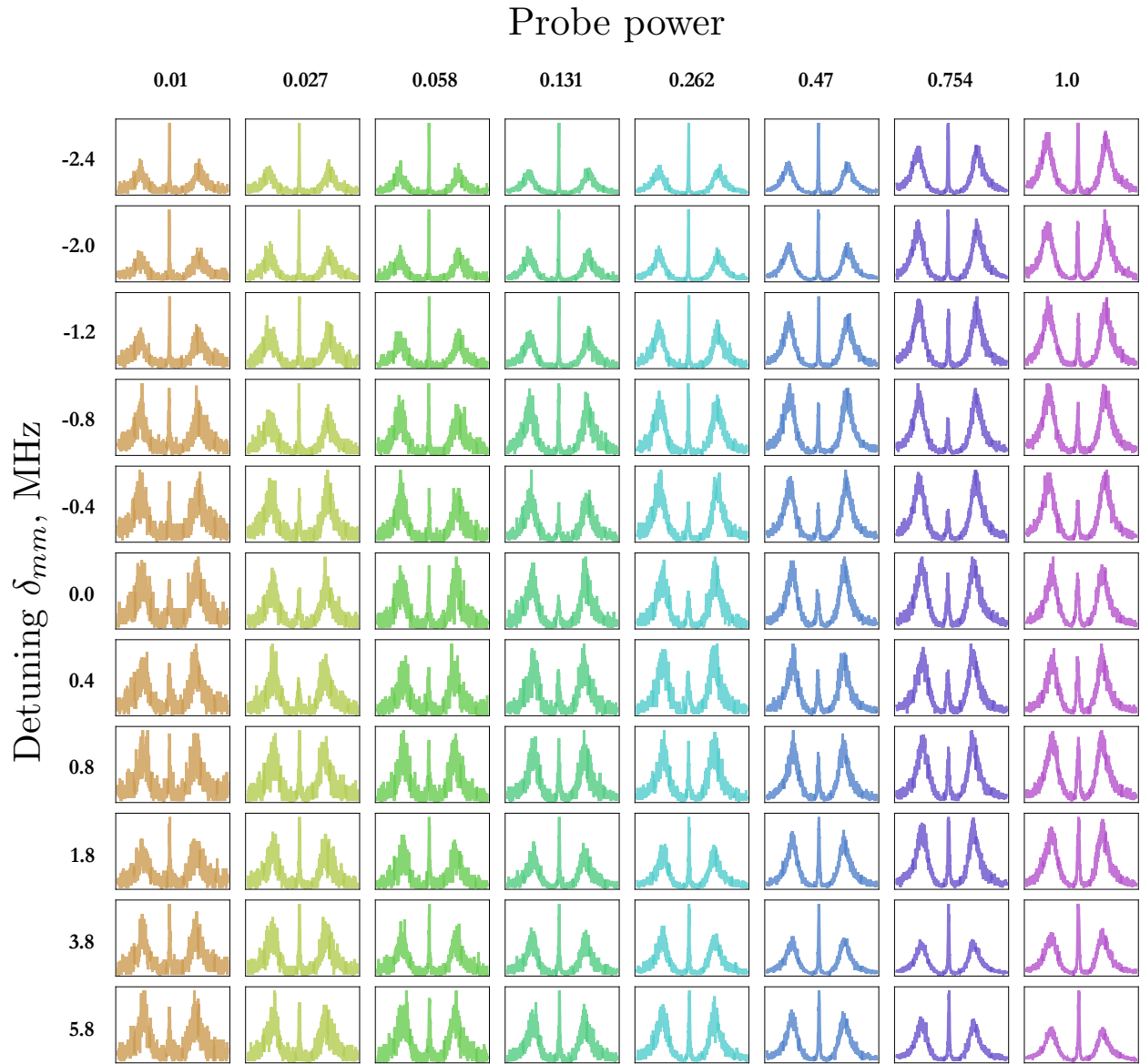


Figure 6.17: Raw data

with the cavity mm-wave photons. The most exciting part about this data is that there is a nonlinear dependence of the EIT broadening on the optical probe power.

The Fig. 6.16 and Fig. 1.11 show that at lower power the broadening feature is significantly narrower. This is a clear signature of the mean-field nonlinearity which comes from coupling more than one polaritons to the cavity. It is also possible that in the low probe power data we are seeing the quantum photon-photon nonlinearity. But some more work needs to be

done to confirm this observation. Note that in these plots the power is in some arbitrary but linear power scale. And the  $\delta_{mm} = 0$  is at 2.4 MHz AC stark shift. This means that after the installment in our hybrid system, the cooldown and the magnetic field effects there is a 2.4 MHz frequency difference between the “perfect pitch” and  $|36S\rangle \rightarrow |35P\rangle$  transition. Luckily, it is not detrimental to our system, since the little power needed to tune the atomic state by 2.4 MHz doesn’t broaden the EIT feature. At higher detunings  $\delta_{mm} > 0$  (higher tuning powers) the inhomogenous broadening of the EIT line can be seen in Fig. 6.16.

## 6.5 Conclusion

In conclusion, at the time of the submission of this thesis we have observed the first clear evidence of the mean-field nonlinearity in our hybrid optical to mm-wave CQED system with Rydberg atoms. We are currently working on multiplying the data rate on our experiment by a factor of  $> 20$  to be able to resolve the nonlinearities at a few photon level. At the same time we are working on determining the precise thermal occupation number at 100 GHz in our cavity, since that affects the observation of the nonlinearity. In Chapter. 7, I will give a quick overview of the near- and long-term goals we are pursuing on our hybrid quantum system.

## CHAPTER 7

### OUTLOOK

In this thesis, I described my PhD work on hybrid quantum systems with mm-wave photons. I have had the privilege of starting two efforts from their beginnings. First is the exploration of the mm-wave frequency band for quantum technology. And the second is developing a novel hybrid cavity QED system for interfacing single mm-wave and optical photons using Rydberg atoms. Both of these projects have only started to reveal their full potential.

#### 7.1 Mm-wave quantum platforms

Mm-wave photons offer unique advantages for quantum technology: mild cryogenic requirement, length-scale flexibility, and abundance of possible qubits. Once more widely incorporated, mm-wave frequencies could allow large-scale quantum hybrid platforms that are not accessible in other frequency domains. At the same time, mm-waves could become a more scalable alternative for microwave-based superconducting circuits quantum platforms.

In our lab, there are several short-term projects we are excited about in the mm-wave band. First, we are working on developing a complete circuit-QED platform in the mm-wave band. We hope to make devices with stronger nonlinearity. One direction we are pursuing is through leveraging the kinetic inductance of superconducting materials. And the other one is through a development of a Josephson junction that can operate at 100 GHz. In parallel with these efforts, we are incorporating the nonlinear devices in the microwave to mm-wave hybrid experiments. These include a potential for inter-conversion of quantum information between single mm-wave and microwave photons [68] and dissipative cooling of microwave resonators using mm-wave photons.

Second, I hope further to develop the ray optics limit of mm-wave photonics. Specifically, I hope to finish my work on imaging Fabry-Perot modes in mm-wave bands. And start to work on designing topologically nontrivial potentials for mm-wave photons using both machining and nano-fabrication tools.

Finally, there is a vast opportunity to build novel hybrid quantum computing platforms in the mm-wave band. These could incorporate cold atoms, nonlinear circuit-QED, and 3D cavity QED platforms into one integrated cryogenic 3D system.

During my PhD, due to rising interest in the industry, the mm-wave technology has become more widely accessible and affordable. I hope that this trend will continue in the future and enable other labs to utilize the mm-wave frequency band in their quantum platforms. After a few years of our work, there is already more interest in mm-wave quantum technology and mm-waves for entangling atoms in different labs at Stanford and JILA.

## **7.2 Hybrid Cavity-QED systems with mm-wave photons**

Mm-wave photons have enabled us to build a novel hybrid cavity-QED system with a unique parameter space. We built an experiment that combined tools from cold atoms physics, optical cavity-QED, and superconducting circuit-QED to achieve novel functionalities inaccessible to each paradigm. Using Rydberg excitations of our atomic cloud, we can generate a coherent and strongly nonlinear interface for single optical and mm-wave photons. While working on the system, we have also innovated many new pieces of technology that would have an impact beyond our scientific goals. These include seamless superconducting cavities, mm-wave circuitry, glue-less optical cavities and optics, and cold atoms inside the cryogenic environment.

There is a tremendous amount of science to explore using our system. A few short time-scale

projects are as follows. Firstly, we want to measure the strength of nonlinear interactions between optical and mm-wave photons in our systems and show sub-Poissonian statistics of the second-order correlation function for photons. Secondly, we are excited to demonstrate the first inter-conversion between mm-wave and optical photons using Rydberg atoms as mediators. We have just upgraded our system to be UV compatible and incorporated the brand new 297 nm *Toptica* UV laser, shown in Fig. 7.1, to start measuring the inter-conversion.

Finally, we would like to start exploring the full potential of our ultra-high cooperativity on the mm-wave transition. For this, we need to upgrade our experimental setup. In particular, we are working on designing the best cryogenic solution to reaching 1 K temperatures. One option would be to add an additional cryo stage, a Joule Thompson adsorption cooler, to our existing experiment. Another one is to design a new cryogenic system with a commercial 1

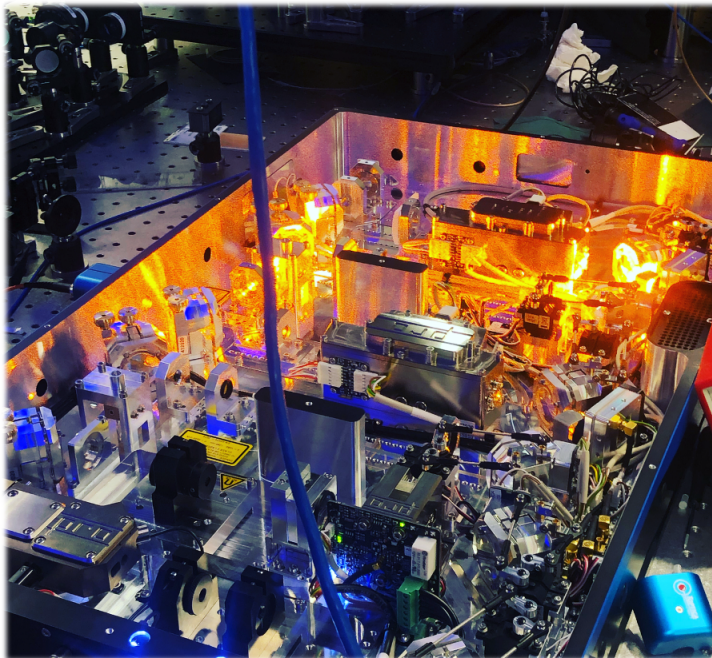


Figure 7.1: The 297 nm UV laser for the mm-wave to optical inter-conversion

K cryostat while the current system is running and exploring its parameter space. With this upgrade, we will reach the  $\eta > 22000$  cooperativity limit at measured mm-wave cavity Qs of  $3 \times 10^7$ . In this regime, we have access not only to strong nonlinearity between optical and mm-wave photons but also the ability to generate spin squeezed states of atoms. Using "all-to-all" interactions between the mm-wave photons in the superconducting cavity and the atomic cloud, we can generate many-body entangled states of atoms. This would create squeezed states at low cooperativities, but with  $\eta > N$  atoms, we can start generating

large Cat states for quantum computing and metrology. Moreover, inducing several Rydberg excitations would enable us to explore a regime with two types of interactions: Rydberg-Rydberg interaction and cavity-induced atom interaction. The interplay of both could lead to some exotic and unexplored phenomena. It has been a great excitement to be part of the development of new platforms for quantum technology. My experience as a Ph.D. student has been very reminiscent of our systems - very hybrid and interdisciplinary. I am excited for the future expansions of our photonic platforms and the adoption of some tools and ideas we have developed beyond our lab. I hope to continue to work on new technologies and harness quantum platforms for exploring new science.

# Appendices

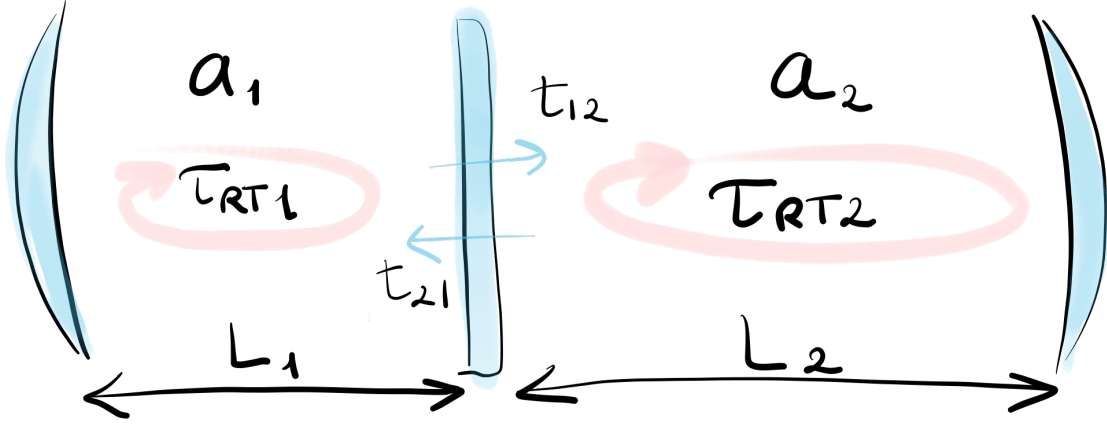


Figure A.1: Coupled cavities

## APPENDIX A

### INPUT/OUTPUT THEORY

#### A.1 Quantized Coupled Cavities

I will start by setting up two perfectly mode-matched (areas,  $A$ , of the modes are the same) coupled cavities with quantized fields  $a_1$ ,  $a_2$  and parameters shown in Fig.1. In rotating frame the bare and interaction Hamiltonians are

$$H_0 = \hbar\omega_1(a_1^\dagger a_1 + \frac{1}{2}) + \hbar\omega_2(a_2^\dagger a_2 + \frac{1}{2}) \quad (\text{A.1})$$

$$H_{12} = \hbar g(a_1 a_2^\dagger + a_2 a_1^\dagger) \quad (\text{A.2})$$

respectively. The  $g$ , classically, is  $i \frac{t_{12}}{\tau_{rt2}}$ , and since in the E field quantization process we get a prefactor  $\mathcal{E}_j = \sqrt{\frac{\hbar\nu_j}{\epsilon_0 V}}$ , in the quantized form the coupling constant is:

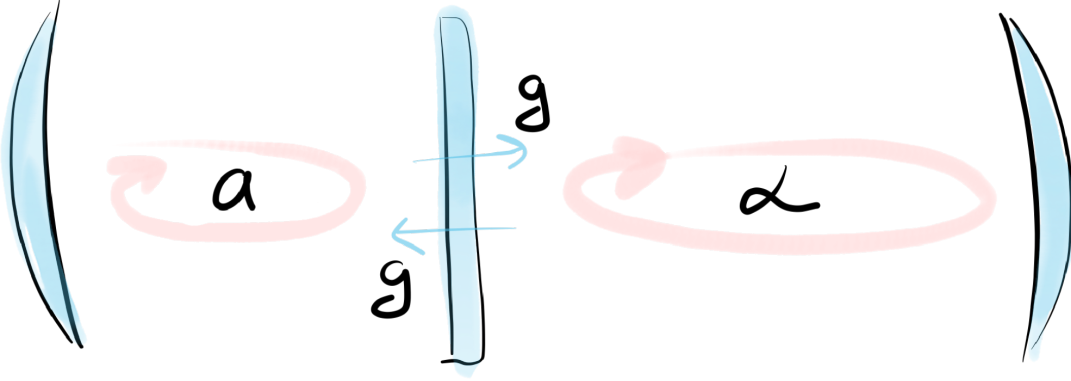


Figure A.2: A cavity with quantized field coupled to one with classical field inside

$$g = i \frac{t_{12}}{\tau_{rt2}} \sqrt{\frac{w_1 V_2}{w_2 V_1}} = i \frac{ct_{12}}{2\sqrt{L_1 L_2}} = i \frac{t_{12}}{\sqrt{\tau_{rt1} \tau_{rt2}}} \quad (\text{A.3})$$

where we set the frequencies to be equal  $w_1 = w_2 = w$ , otherwise we would get two different dressed modes, and used the mode-matching condition  $V_1 = AL_1$  and  $V_2 = AL_2$ .

The toy model of quantized coupled cavities is very useful for derivation of familiar cavity dynamics but in a quantized form [137].

### A.1.1 Coherent driving of a perfect cavity

If we set the field inside the cavity 2 to be classical, as shown in Fig. A.2, we can write down a Hamiltonian for a classically driven quantum harmonic oscillator:

$$H_0 = \hbar w_1 (a^\dagger a + \frac{1}{2}) \quad (\text{A.4})$$

$$H_{12} = \hbar \mathcal{E} (a e^{i w L t} + a^\dagger e^{-i w L t}) \quad (\text{A.5})$$

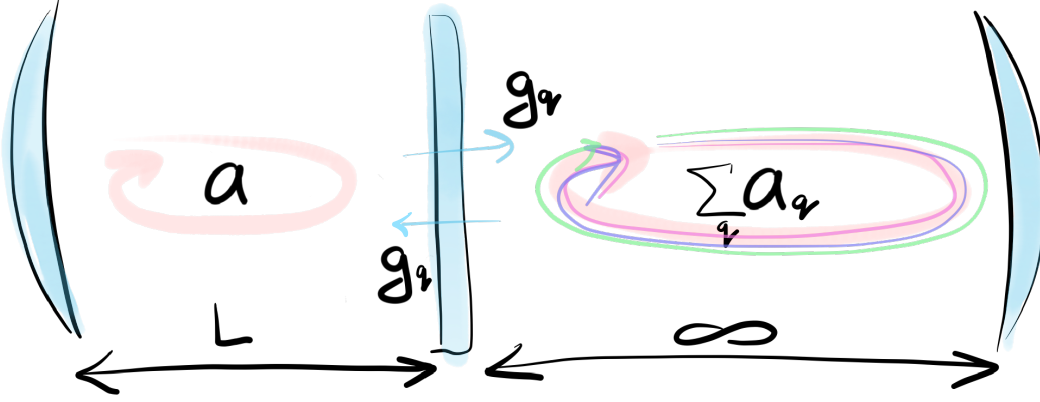


Figure A.3: A cavity coupled to a bath

where  $\mathcal{E} = \alpha g = \alpha i \frac{t_{12}}{\sqrt{\tau_{rt1}\tau_{rt2}}}$ . The circulating power in the cavity 2 is  $P = \frac{|\alpha|^2 \hbar \omega_2}{\tau_{rt2}}$ , so we can express the new coupling constant between the cavities as:

$$\mathcal{E} = \alpha g = \sqrt{\frac{P}{\hbar \omega_L}} \frac{|t_{21}|}{\sqrt{\tau_{rt1}}} = \sqrt{\frac{P}{\hbar \omega_L}} \frac{|t_{21}|}{\sqrt{\tau_{rt1}}} = \sqrt{\frac{P \kappa}{\hbar \omega_L}} \quad (\text{A.6})$$

where we have defined a cavity 1 leakage rate to be  $\kappa = \frac{|t_{21}|^2}{\tau_{rt1}}$ .

### A.1.2 Cavity decay into the bath

Another neat trick is to increase the length of the cavity 2 to a point where it holds almost a continuum of modes, as shown in Fig. A.3, resembling a coupling to a bath with operators  $a_q$ , where  $q$  is a mode index of the bath cavity. In this case, the Hamiltonian becomes

$$H_0 = \hbar \omega_1 \left( a^\dagger a + \frac{1}{2} \right) + \hbar \sum_q w_q \left( a_q^\dagger a_q + \frac{1}{2} \right) \quad (\text{A.7})$$

$$H_{int} = \hbar \sum_q g_q (a a_q^\dagger + a_q a^\dagger) \quad (\text{A.8})$$

where, if we assume that our cavity mode couples equally to all external modes,  $g_q = \sqrt{\frac{\kappa}{\tau_{rt2}}}$ .

For both the classically driven cavity as well as a cavity coupled to a bath with continuum of modes, we can solve the problem using the Heisenberg equation of motion. Instead of doing that here, we will do the full derivation using the Input-Output formalism while, explicitly, keeping track of input and output operators which will be useful to directly calculate quantum expectation values of the measurements we have derived classically in Chapter. 2.

## A.2 Input-Output theory of a cavity coupled to a bath

First, using Fig. A.3, we will derive the input and output operators to the cavity from the creation and annihilation operators of the bath/vacuum. We will use the analogy to a very common procedure used to derive the spontaneous emission of a two level system coupled to the environment.

Since the cavity now has infinitely many modes, we can write the external bare and interaction Hamiltonians of our system as integrals instead of sums, by using:  $\sum_q |g_q|^2 \rightarrow \frac{\tau_{rt2}}{2\pi} \int_0^\infty dw' \frac{\kappa}{\tau_{rt2}} = \int_0^\infty dw' \frac{\kappa}{2\pi}$  and  $a_q \rightarrow b(w')$ :

$$H_0 = \hbar \omega a^\dagger a \quad (\text{A.9})$$

$$H_{bath} \approx \hbar \int_{-\infty}^{+\infty} dw' (w' b(w')^\dagger b(w')) \quad (\text{A.10})$$

$$H_{int} \approx \frac{\hbar}{\sqrt{2\pi}} \int_{-\infty}^{+\infty} dw' (ab(w')^\dagger + a^\dagger b(w')) \quad (\text{A.11})$$

where we used took  $\int_0^{+\infty} \rightarrow \int_{-\infty}^{+\infty}$  for convenience, since only frequencies  $w'$  around cavity  $w$  contribute significantly, and dropped the zero point average for  $H_{bath}$  and  $H_0$ .

Now, we use Heisenberg equation of motion to find a time evolution of operators  $a$  and  $b(w')$ :

$$\partial_t c = -\frac{i}{\hbar}[c, H] \quad (\text{A.12})$$

$$\partial_t a = -\frac{i}{\hbar}[a, H_0] - \frac{i}{\hbar}[a, H_{int}] = -i\omega a(t) - \frac{i}{2\pi} \int_{-\infty}^{+\infty} dw' w' \sqrt{\kappa} b(w') \quad (\text{A.13})$$

and

$$\partial_t b(w') = -\frac{i}{\hbar}[b, H_{bath}] - \frac{i}{\hbar}[a, H_{int}] = -i\omega' b(w') - i\sqrt{\frac{\kappa}{2\pi}} a(t) \quad (\text{A.14})$$

where we assumed that around resonance  $\kappa$  is frequency independent.

In a frame rotating with  $w'$  Eq. A.14 becomes

$$\partial_t [b(w') e^{i\omega' t}] = -i\sqrt{\frac{\kappa}{2\pi}} a(t) e^{i\omega' t} \quad (\text{A.15})$$

Now this is an important part, we will integrate Eq. A.15 from some past  $t_0$  to time  $t$  and call  $b_0(w') = b(w')|_{t=t_0}$

$$b(w') e^{i\omega' t} - b_0(w') e^{i\omega' t} = -i\sqrt{\frac{\kappa}{2\pi}} \int_{t_0}^t a(t') e^{i\omega' t'} \quad (\text{A.16})$$

$$b(w') = b_0(w')e^{iw'(t-t_0)} - i\sqrt{\frac{\kappa}{2\pi}} \int_{t_0}^t a(t')e^{iw'(t-t')} \quad (\text{A.17})$$

We plug Eq. A.17 into Eq. A.13 and get

$$\partial_t a = -iwa(t) - \frac{i}{2\pi}\sqrt{\kappa} \int_{-\infty}^{+\infty} dw' b_0(w')e^{iw'(t-t_0)} - \frac{1}{2\pi}\kappa \int_{-\infty}^{+\infty} dw' \int_{t_0}^t dt' a(t')e^{iw'(t-t')} \quad (\text{A.18})$$

$$\partial_t a = -iwa(t) - \frac{\kappa}{2}a(t) - \sqrt{\kappa}a_{in}(t) \quad (\text{A.19})$$

which is known as the *Quantum Langevin Equation* where

$$a_{in} = \frac{i}{2\pi} \int_{-\infty}^{+\infty} dw' b_0(w')e^{-iw'(t-t_0)} \quad (\text{A.20})$$

Analogously, if we integrate Eq. A.15 from time  $t$  to some time in the future  $t_1$  and call  $b_1(w') = b(w')|_{t=t_1}$  we get the *time-reversed Langevin Equation*

$$\partial_t a = -iwa(t) + \frac{\kappa}{2}a(t) - \sqrt{\kappa}a_{out}(t) \quad (\text{A.21})$$

where

$$a_{out} = \frac{i}{2\pi} \int_{-\infty}^{+\infty} dw' b_1(w')e^{-iw'(t-t_1)} \quad (\text{A.22})$$

Input-Output Relation between the operators is:

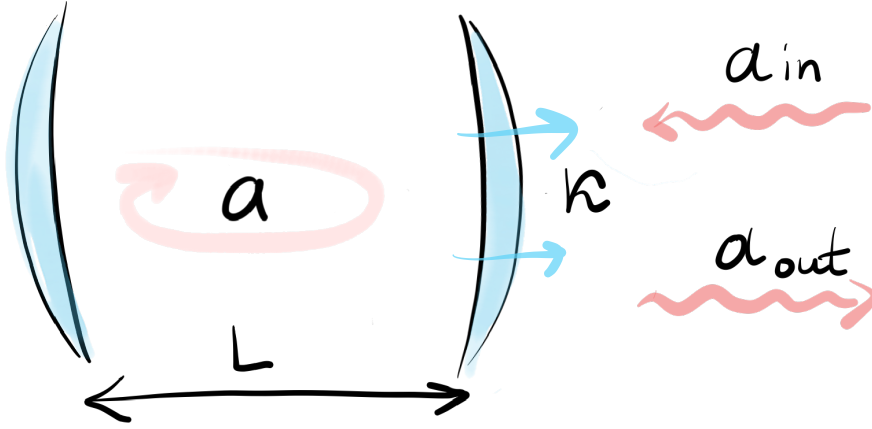


Figure A.4: A cavity with one port with a decay rate  $\kappa$

$$\boxed{a_{out}(t) = a_{in}(t) + \kappa/2a(t)} \quad (\text{A.23})$$

### A.2.1 Cavity Reflection

With these new input/output operators we can simplify our picture from Fig. A.3 to Fig. A.4.

The commutator relationships of  $a_{in}$  and  $a_{out}$  are the same:  $[a_{in}(t), a_{in}^\dagger(t')] = [a_{out}(t), a_{out}^\dagger(t')] = \delta(t - t')$  which indicates that they have a spectra of white noise. So over long times the average of input operators go to 0, but since the fluctuations are not zero the  $a$  operator still has a meaningful commutator relationship at all times.

In Fourier space Eq. A.19 and Eq. A.21 becomes

$$-iw'a(w') = -iwa(w') - \frac{\kappa}{2}a(w') - \sqrt{\kappa}a_{in}(w') \quad (\text{A.24})$$

$$-iw'a(w') = -iwa(w') + \frac{\kappa}{2}a(w') - \sqrt{\kappa}a_{out}(w') \quad (\text{A.25})$$



Figure A.5: A cavity with two ports with decay rates  $\kappa/2$

which after combining give us the expected, from Chapter. 2, result for the reflection from a one-sided cavity coupled to a bath:

$$\boxed{a_{out}(w) = \left( \frac{i(w' - w) + \kappa/2}{i(w' - w) - \kappa/2} \right) a_{in}(w')} \quad (\text{A.26})$$

### A.2.2 Cavity Transmission

Similarly, if we have a two-sided cavity and total each mirror leaks at  $\kappa$ , then we have  $\overrightarrow{a_{in}}$  and  $\overleftarrow{a_{out}}$  on each side.

If we assume  $\overleftarrow{a_{in}} = 0$  (or we could have assumed that  $\overleftarrow{a_{in}} = \overrightarrow{a_{in}}$ ), we get:

$$\boxed{\overrightarrow{a_{out}}(w') = \left( \frac{\kappa/2}{i(w' - w) - \kappa/2} \right) \overrightarrow{a_{in}}(w')} \quad (\text{A.27})$$

$$\boxed{\overleftarrow{a_{out}}(w') = \left( \frac{i(w' - w)}{i(w' - w) - \kappa/2} \right) \overrightarrow{a_{in}}(w')} \quad (\text{A.28})$$

$$\boxed{a(w') = \left( \frac{\sqrt{\kappa/2}}{i(w' - w) - \kappa/2} \right) \vec{a}_{in}(w')} \quad (\text{A.29})$$

### A.2.3 Driven cavity

For a driven cavity, we can either include  $H_{driven} = \hbar\mathcal{E}(ae^{i\omega t} + a^\dagger e^{-i\omega t})$ , but we instead will include it in the input operator:

$$a_{in}(t) \longrightarrow \frac{i\mathcal{E}}{\sqrt{\kappa}} e^{-i\omega t} + a_{in}(t) \quad (\text{A.30})$$

In a frame rotating with a laser frequency, the Langevin equation becomes:

$$\partial_t \tilde{a} = i(\omega_l - w)\tilde{a}(t) - \frac{\kappa}{2}\tilde{a} - i\mathcal{E} - \sqrt{\kappa}\tilde{a}_{in}(t) \quad (\text{A.31})$$

In a steady state

$$\boxed{\langle a \rangle = \frac{i\mathcal{E}}{i(\omega_l - w) - \kappa/2}} \quad (\text{A.32})$$

on resonance the amplitude is

$$|\alpha|^2 = \frac{4\mathcal{E}^2}{\kappa^2} = \frac{4P}{\kappa\hbar\omega} = \frac{2\mathcal{F}P}{\pi\nu_{FSR}\hbar\omega} \quad (\text{A.33})$$

### A.3 Atom in a cavity

Now let's say we have an atom in a cavity. The relevant Hamiltonians are  $H_{cav} = \hbar w(a^\dagger a)$ ,  $H_{driven} = \hbar \mathcal{E}(ae^{i\omega t} + a^\dagger e^{-i\omega t})$ ,  $H_A = \hbar w_A \sigma^\dagger \sigma$  and  $H_{int} = \hbar g(\sigma a^\dagger + \sigma^\dagger a)$ . And quantum Langevin equations in a rotating frame are:

$$\partial_t \tilde{a} = i(\omega_l - w)\tilde{a}(t) - \frac{\kappa}{2}\tilde{a} - ig\sigma^\dagger(t) - i\mathcal{E} - \sqrt{\kappa}\tilde{a}_{in}(t) \quad (\text{A.34})$$

$$\partial_t \tilde{\sigma} = i(w - w_0)\tilde{\sigma}(t) - ig[\tilde{\sigma}(t), \tilde{\sigma}^\dagger(t)]a(t) - \frac{\Gamma}{2}\tilde{\sigma}(t) - \sqrt{\Gamma}\tilde{\sigma}_{in}(t) \quad (\text{A.35})$$

the latter in the the weak excitation limit becomes

$$\partial_t \tilde{\sigma} = i(w - w_0)\tilde{\sigma}(t) - iga(t) - \frac{\Gamma}{2}\tilde{\sigma}(t) - \sqrt{\Gamma}\tilde{\sigma}_{in}(t) \quad (\text{A.36})$$

Following [138, 139]

## APPENDIX B

### SEAMLESS MM-WAVE CAVITIES

#### B.1 Etching of Nb seamless cavities

Here I will present some etch data, which I used to calibrate etch rates for our cavities. I usually design the cavity to be 4-5 GHz higher than the desired frequency. The machining usually decreases the frequency a little bit at first. Then, the first round of etching usually takes off 1-2 GHz. This initial violent etch rate could be due to sharp edges left from the machining. After the second etch, the rate is relatively constant. The average etch rate I used for our cavities is 7-11 MHz/s or  $6\mu\text{m}/\text{min}$ . The Fig. B.1 shows some calibration data.

#### B.2 Mechanical squeezing of Nb seamless cavities

Another mechanism I use for tuning mm-wave cavities is through mechanical deformation.

#### B.3 Room temperature filter cavity

The Fig. B.4 shows the filter cavities used as room temperature band passes in our mm-wave circuitry.

#### B.4 High-Tc superconductor seamless cavities

The Fig. B.5 shows the few high-Tc superconductor cavities I have machined. Both BSCCO and YBCO samples didn't show high-Q mm-wave resonances at 1K.

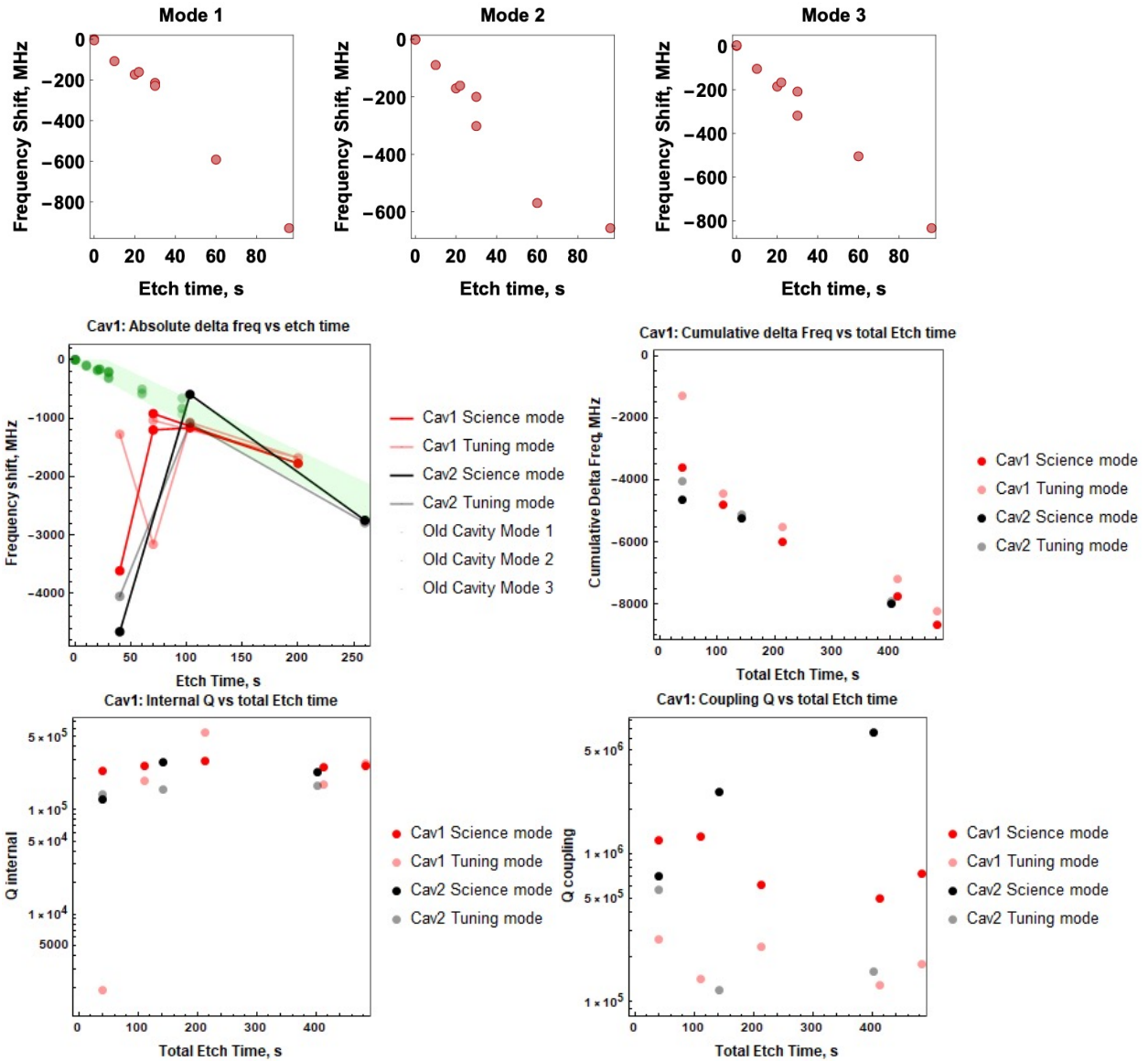


Figure B.1: Data from several etching calibration runs

## B.5 Etching Cavities

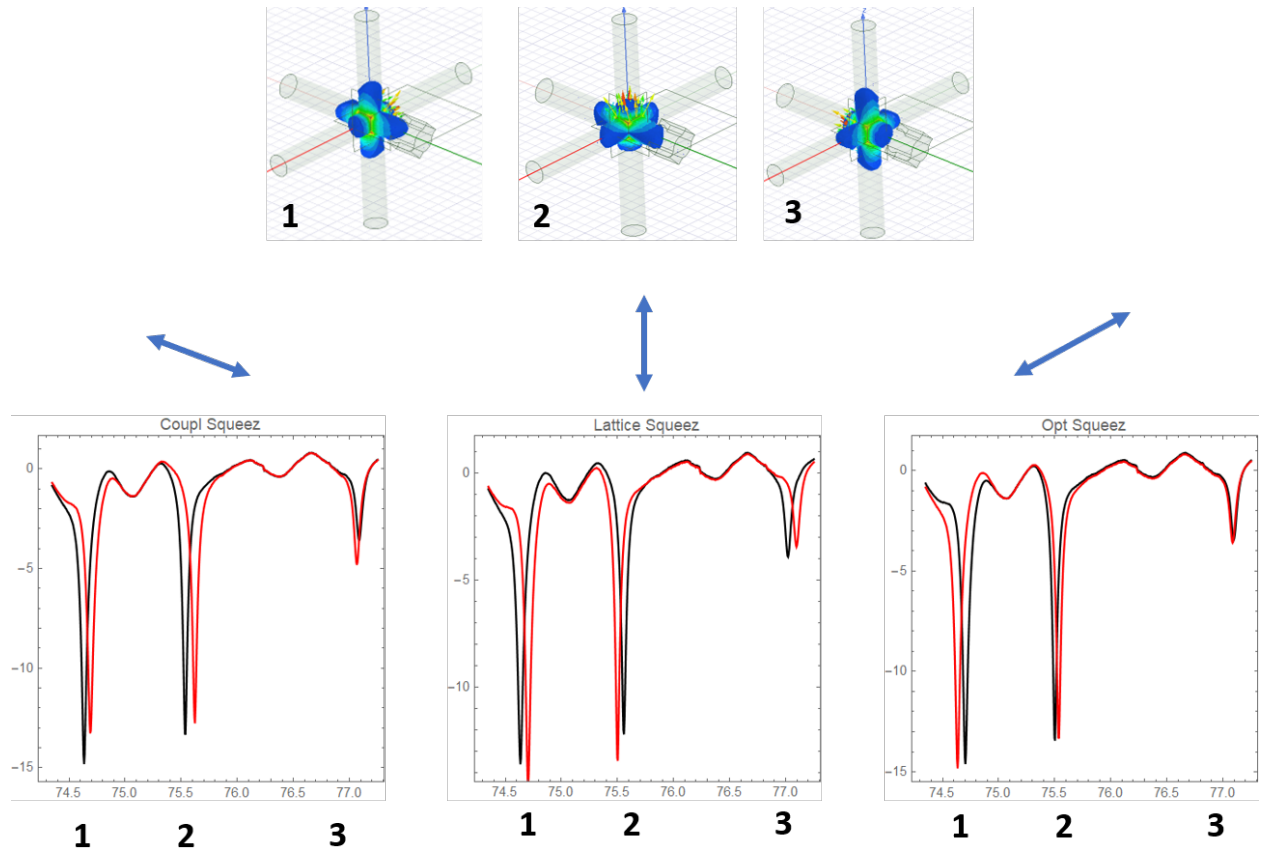


Figure B.2: Mechanical deformation in different direction corresponds to different signs of frequency shifts for different modes.

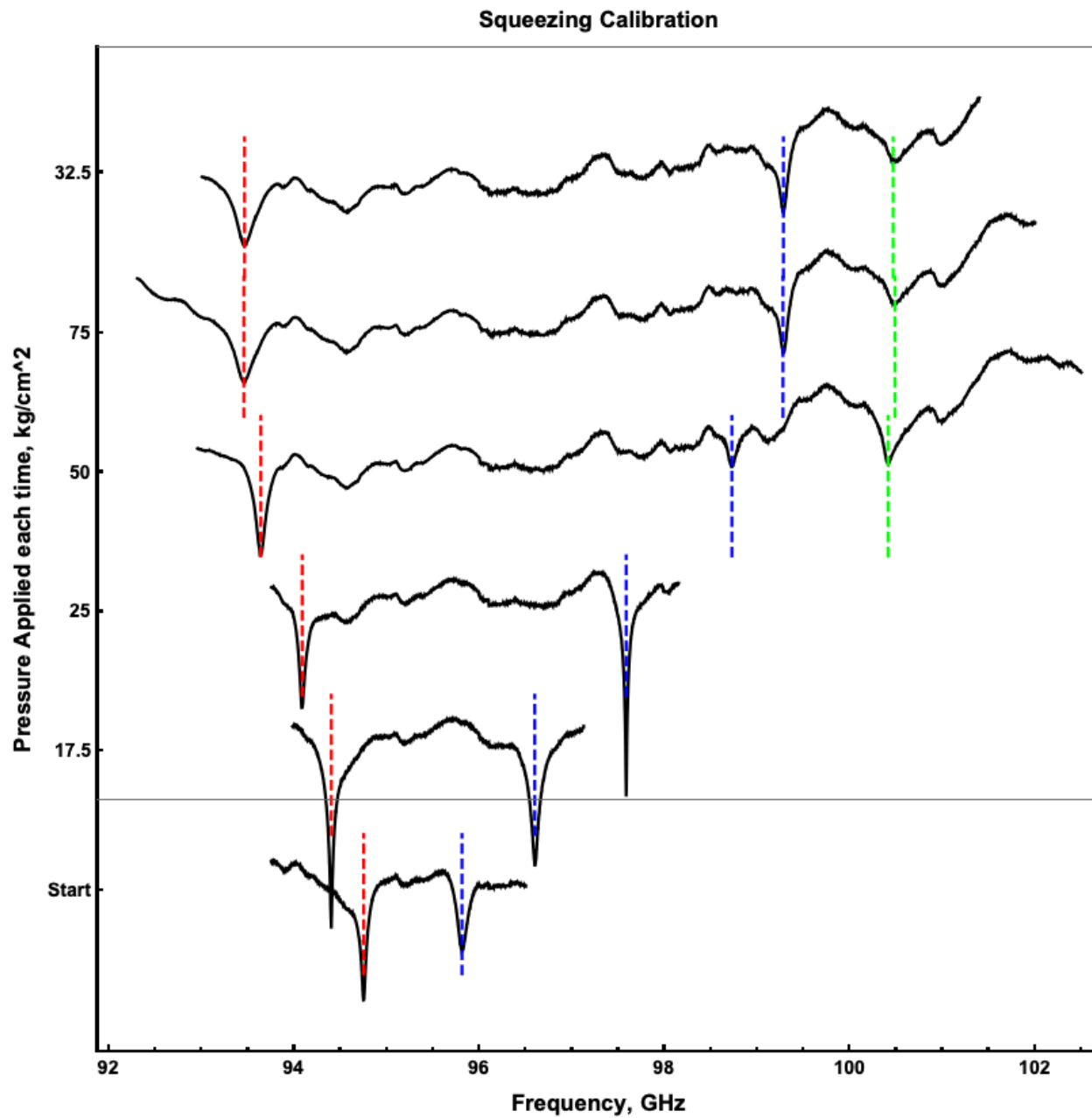


Figure B.3: Mechanical deformation calibration.

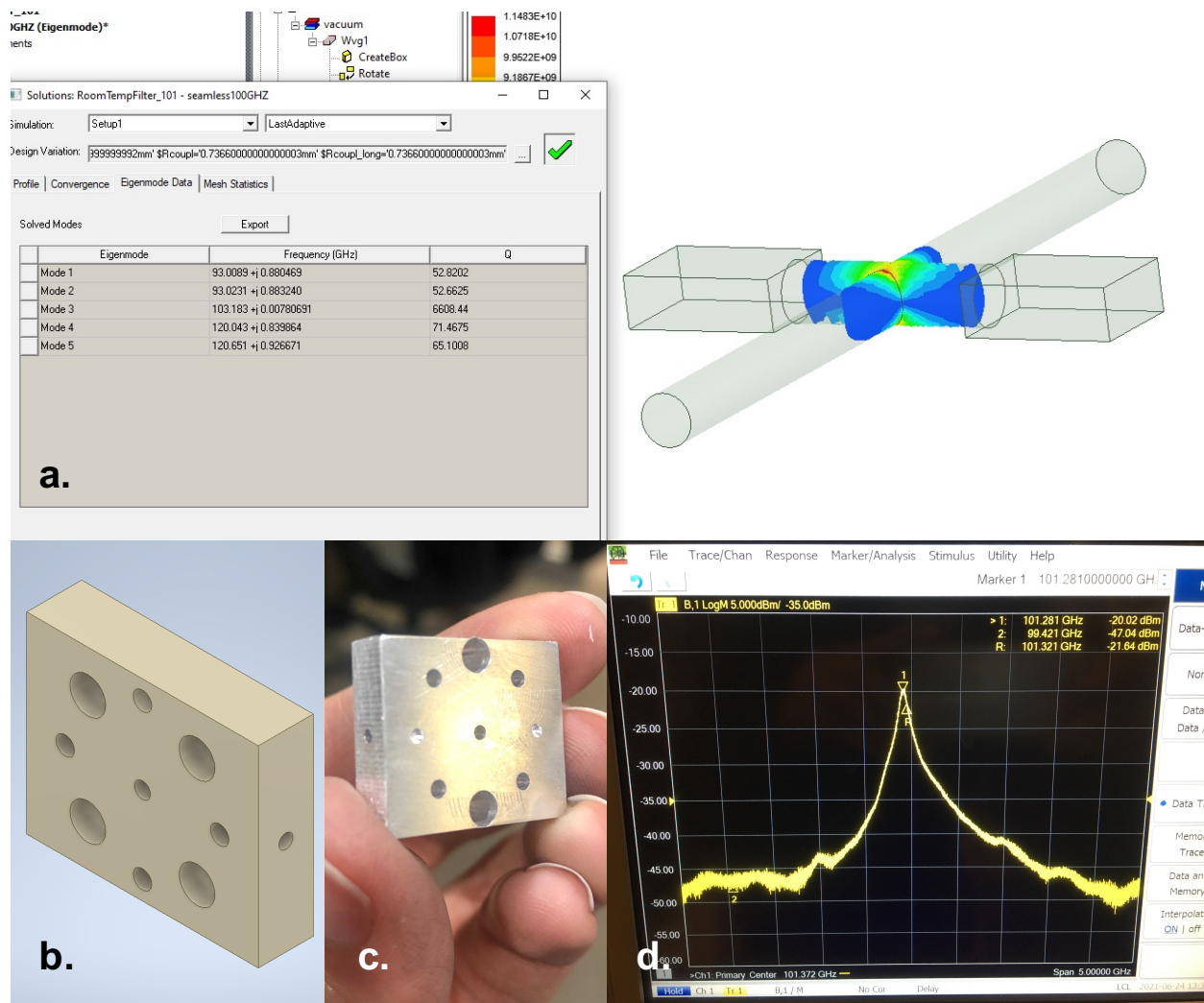


Figure B.4: Room temperature seamless cavity used as a band-pass filter: **a.** HFSS simulation of the filter mode, **b.** CAD 3D, model, **c.** Machined Al cavity, **d.** A typical transmission through the cavity

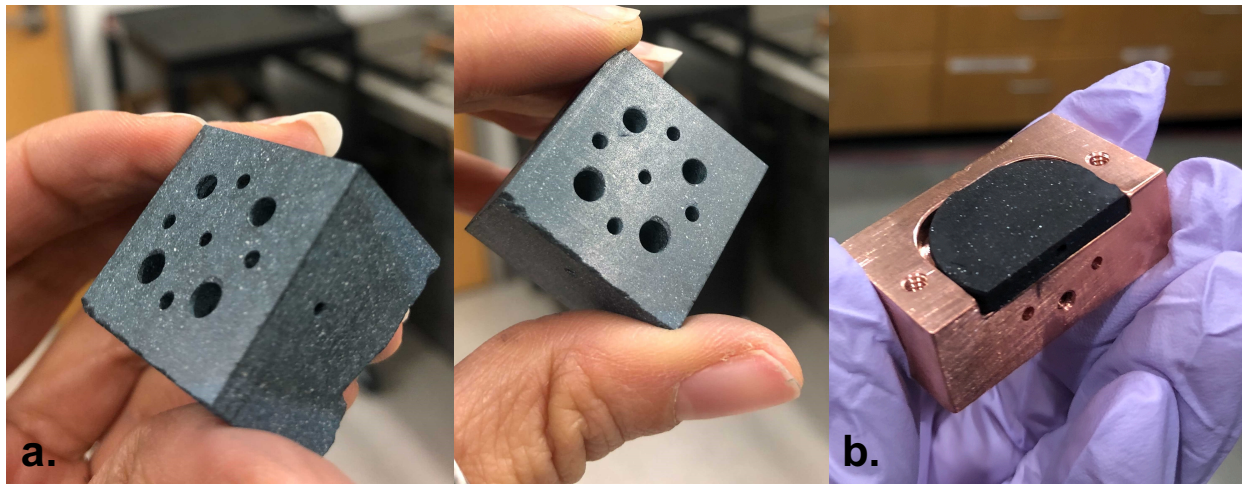


Figure B.5: High-T<sub>c</sub> superconductor seamless cavities: **a.** YBCO, **b.** BSCCO

## APPENDIX C

### MM-WAVE VECTOR NETWORK ANALYZER

Most of the time we need to scan through the resonances of the cavity and measure the reflection and transmission spectrum. The PNAX together with the up-converter + down-converter modules are very powerful and flexible set of tools. However, it is convenient to have a permanent and lower cost setup that is continuously attached to the system. This is why I have build a home-made mm-wave Vector Network Analysers using Signal Core signal generators as RF sources, up- and down-converters from the VDI to change from RF frequency to the WR-10 mm-wave band and a Red Pitaya for triggering, measuring and storing the measuring data. This is by no means an ideal setup, but it was easy to build and the parts were available in the lab at the time.

#### C.1 Schematic

The Fig. C.1 shows the schematic of the VNA setup. The Signal Core modules are used to generate RF signals up to 20 GHz that can be swept automatically through the required range. The SC source modules are linked to each other and to an external 10 MHz external clock. The input RF signal passes through a VDI up-converter where the frequency is multiplied by six. After the input mm-wave signal passes through the device, the signal get down-converted in a VDI multiplier-mixer chain. This down-converter has input  $LO = RF - IF/6$  which is the same signal fed into the input up-converter, but shifted by the  $IF/6$ . This helps to maintain the phase coherence of the signal. The IF output of the down-converter is used as the measurement output. To get the phase and magnitude from the transmitted signal this IF signal is mixed with another coherent tone from a Signal Core source in an IQ mixer. It's important to note that while the RF signals are swept in a range

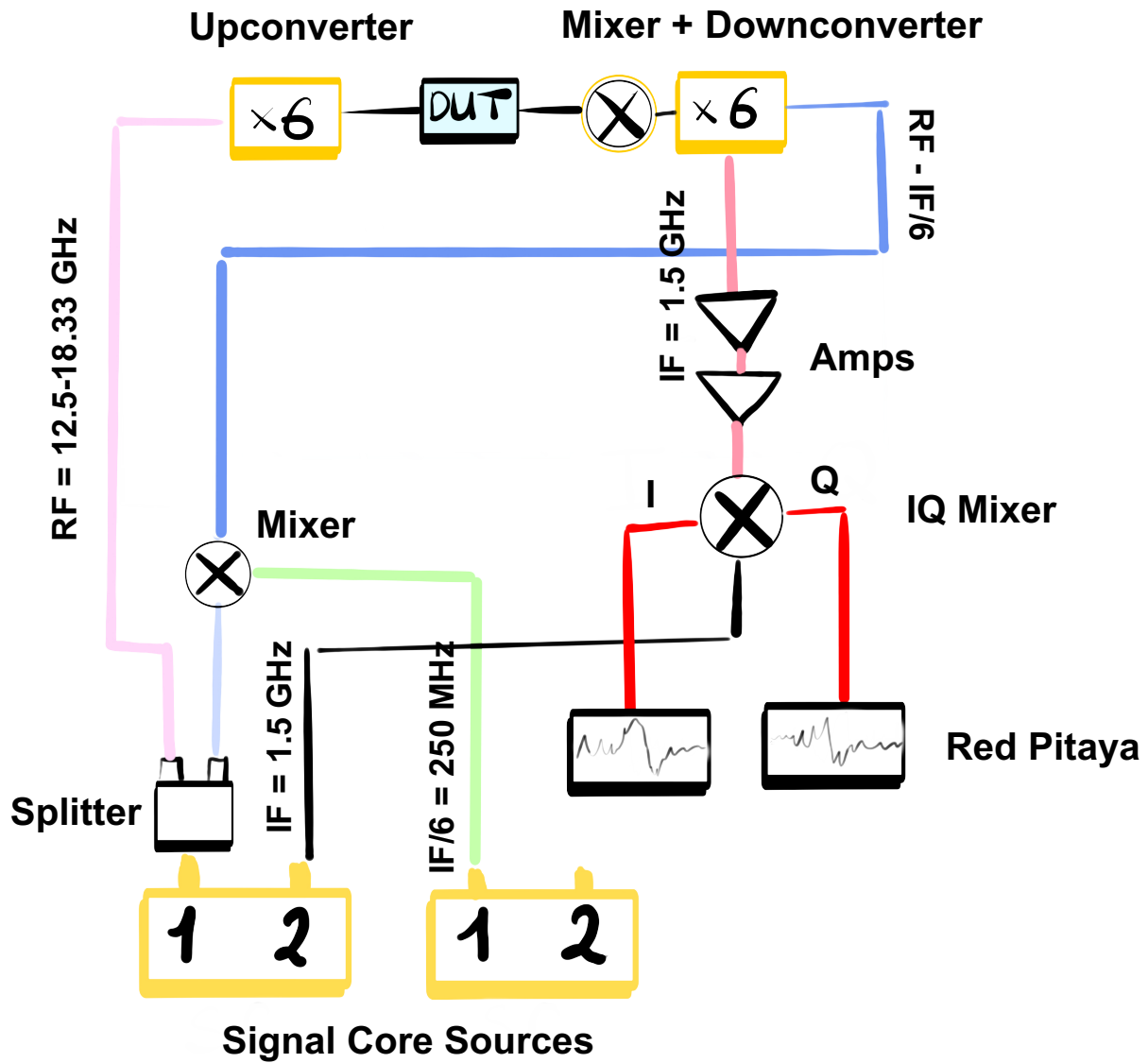


Figure C.1: Mm-wave VNA schematic

of frequencies, the IF output is a constant frequency tone. The only change is an amplitude. The output of the IQ mixer is DC, and both I and Q quadrature data are fed into a Red Pitaya device. From Red Pitaya the data is retrieved, displayed and permanently stored on the experiment PC computer.



Figure C.2: Mm-wave VNA GUI before the measurement

## C.2 GUI

The source code for the GUI as well as for operating the Signal Core Sources and the Red Pitaya can be found here: [140]. The GUI allows for specifying the range for the sweep, trigger and reflection fit using the specified parameters.

The Fig. C.3 shows a sample from an early iteration of the VNA. The raw data is saved as I, Q quadrature of the complex data, and then displayed together with the magnitude and phase derived from the raw data. The data is noisy and the signal seems to be running into the noise floor. All of this could be improved dramatically by choosing a better IQ mixer at the output and adding low pass filters.

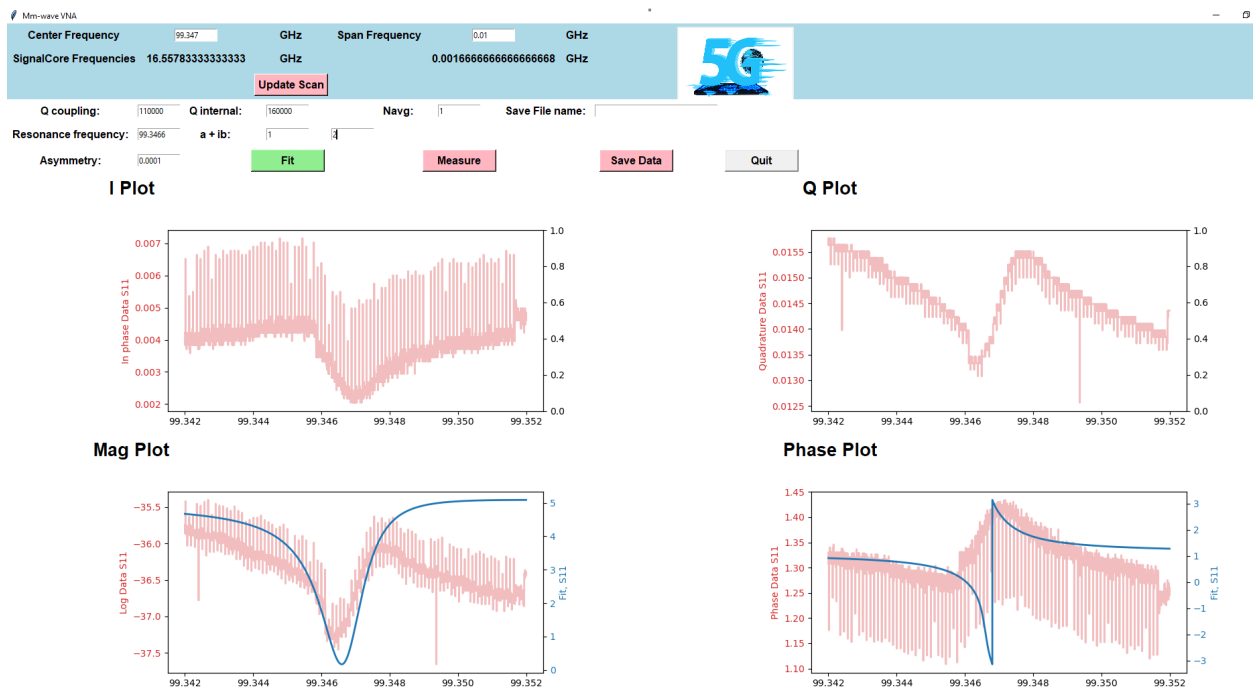


Figure C.3: Mm-wave VNA GUI with the loaded data right after the measurement

## REFERENCES

- [1] Darrick E Chang, Vladan Vuletić, and Mikhail D Lukin. Quantum nonlinear optics—photon by photon. *Nature Photonics*, 8(9):685, 2014.
- [2] Luca Pezze, Augusto Smerzi, Markus K Oberthaler, Roman Schmied, and Philipp Treutlein. Quantum metrology with nonclassical states of atomic ensembles. *Reviews of Modern Physics*, 90(3):035005, 2018.
- [3] Alexander Anferov, Aziza Suleymanzade, Andrew Oriani, Jonathan Simon, and David I. Schuster. Millimeter-Wave Four-Wave Mixing via Kinetic Inductance for Quantum Devices. *arXiv:1909.01487 [cond-mat, physics:physics, physics:quant-ph]*, September 2019. arXiv: 1909.01487.
- [4] Teresa Brecht, Wolfgang Pfaff, Chen Wang, Yiwen Chu, Luigi Frunzio, Michel H Devoret, and Robert J Schoelkopf. Multilayer microwave integrated quantum circuits for scalable quantum computing. *npj Quantum Information*, 2(1):1–4, 2016.
- [5] Pfeiffer vacuum. <https://www.pfeiffer-vacuum.com/en/know-how/lists/literature/lit-8>.
- [6] Cliff Burgess and Guy Moore. *The standard model: A primer*. Cambridge University Press, 2007.
- [7] Alán Aspuru-Guzik and Philip Walther. Photonic quantum simulators. *Nature physics*, 8(4):285–291, 2012.
- [8] Jeremy L O’Brien, Akira Furusawa, and Jelena Vučković. Photonic quantum technologies. *Nature Photonics*, 3(12):687–695, 2009.
- [9] Sbastien Tanzilli, Wolfgang Tittel, Matthaeus Halder, Olivier Alibart, Pascal Baldi, Nicolas Gisin, and Hugo Zbinden. A photonic quantum information interface. *Nature*, 437(7055):116–120, 2005.

- [10] Patricia Fara. Newton shows the light: a commentary on newton (1672)‘a letter... containing his new theory about light and colours...’. *Philosophical Transactions of the Royal Society A: Mathematical, Physical and Engineering Sciences*, 373(2039):20140213, 2015.
- [11] Alan E Shapiro. Kinematic optics: A study of the wave theory of light in the seventeenth century. *Archive for history of exact sciences*, 11(2-3):134–266, 1973.
- [12] Bruce J Hunt. *The maxwellians*. Cornell University Press, 2005.
- [13] James Clerk MAXWELL. Maxwell, james clerk. a treatise on electricity and magnetism. vol. i. oxford: Clarendon press series, 1873. preface, pv-xiv. 1873.
- [14] Max Planck. On the law of distribution of energy in the normal spectrum. *Annalen der physik*, 4(553):1, 1901.
- [15] Louis De Broglie. The wave nature of the electron. *Nobel lecture*, 12:244–256, 1929.
- [16] Michael Bordag, Umar Mohideen, and Vladimir M Mostepanenko. New developments in the casimir effect. *Physics reports*, 353(1-3):1–205, 2001.
- [17] Hendrik BG Casimir and Dirk Polder. The influence of retardation on the london-van der waals forces. *Physical Review*, 73(4):360, 1948.
- [18] Paul R Berman. *Cavity quantum electrodynamics*. 1994.
- [19] David Isaac Schuster. *Circuit quantum electrodynamics*. Yale University, 2007.
- [20] Ruichao Ma, Brendan Saxberg, Clai Owens, Nelson Leung, Yao Lu, Jonathan Simon, and David I Schuster. A dissipatively stabilized mott insulator of photons. *Nature*, 566(7742):51–57, 2019.
- [21] Eliot Kapit, Mohammad Hafezi, and Steven H Simon. Induced self-stabilization in fractional quantum hall states of light. *Physical Review X*, 4(3):031039, 2014.

- [22] Thibault Peyronel, Ofer Firstenberg, Qi-Yu Liang, Sebastian Hofferberth, Alexey V Gorshkov, Thomas Pohl, Mikhail D Lukin, and Vladan Vuletić. Quantum nonlinear optics with single photons enabled by strongly interacting atoms. *Nature*, 488(7409):57–60, 2012.
- [23] Sebastien Gleyzes, Stefan Kuhr, Christine Guerlin, Julien Bernu, Samuel Deleglise, Ulrich Busk Hoff, Michel Brune, Jean-Michel Raimond, and Serge Haroche. Quantum jumps of light recording the birth and death of a photon in a cavity. *Nature*, 446(7133):297–300, 2007.
- [24] Logan W Clark, Nathan Schine, Claire Baum, Ningyuan Jia, and Jonathan Simon. Observation of Laughlin states made of light. *Nature*, 582(7810):41–45, 2020.
- [25] Andreas Wallraff, David I Schuster, Alexandre Blais, Luigi Frunzio, R-S Huang, Johannes Majer, Sameer Kumar, Steven M Girvin, and Robert J Schoelkopf. Strong coupling of a single photon to a superconducting qubit using circuit quantum electrodynamics. *Nature*, 431(7005):162–167, 2004.
- [26] Carlo Bradac, Weibo Gao, Jacopo Forneris, Matthew E Trusheim, and Igor Aharonovich. Quantum nanophotonics with group IV defects in diamond. *Nature communications*, 10(1):1–13, 2019.
- [27] Mihir K Bhaskar, Ralf Riedinger, Bartholomeus Machielse, David S Levonian, Christian T Nguyen, Erik N Knall, Hongkun Park, Dirk Englund, Marko Lončar, Denis D Sukachev, et al. Experimental demonstration of memory-enhanced quantum communication. *Nature*, 580(7801):60–64, 2020.
- [28] Gary Wolfowicz, F Joseph Heremans, Christopher P Anderson, Shun Kanai, Hosung Seo, Adam Gali, Giulia Galli, and David D Awschalom. Quantum guidelines for solid-state spin defects. *Nature Reviews Materials*, pages 1–20, 2021.

- [29] Hanhee Paik, D. I. Schuster, Lev S. Bishop, G. Kirchmair, G. Catelani, A. P. Sears, B. R. Johnson, M. J. Reagor, L. Frunzio, L. I. Glazman, S. M. Girvin, M. H. Devoret, and R. J. Schoelkopf. Observation of High Coherence in Josephson Junction Qubits Measured in a Three-Dimensional Circuit QED Architecture. *Physical Review Letters*, 107(24):240501, December 2011.
- [30] Kerry J Vahala. Optical microcavities. *nature*, 424(6950):839–846, 2003.
- [31] Bharath Kannan, Max J Ruckriegel, Daniel L Campbell, Anton Frisk Kockum, Jochen Braumüller, David K Kim, Morten Kjaergaard, Philip Krantz, Alexander Melville, Bethany M Niedzielski, et al. Waveguide quantum electrodynamics with superconducting artificial giant atoms. *Nature*, 583(7818):775–779, 2020.
- [32] Nathan Schine, Albert Ryou, Andrey Gromov, Ariel Sommer, and Jonathan Simon. Synthetic landau levels for photons. *Nature*, 534(7609):671–675, 2016.
- [33] Alicia J Kollár, Mattias Fitzpatrick, and Andrew A Houck. Hyperbolic lattices in circuit quantum electrodynamics. *Nature*, 571(7763):45–50, 2019.
- [34] Ningyuan Jia, Nathan Schine, Alexandros Georgakopoulos, Albert Ryou, Logan W Clark, Ariel Sommer, and Jonathan Simon. A strongly interacting polaritonic quantum dot. *Nature Physics*, 14(6):550–554, 2018.
- [35] Ofer Firstenberg, Thibault Peyronel, Qi-Yu Liang, Alexey V Gorshkov, Mikhail D Lukin, and Vladan Vuletić. Attractive photons in a quantum nonlinear medium. *Nature*, 502(7469):71–75, 2013.
- [36] Mohammad Hafezi, Mikhail D Lukin, and Jacob M Taylor. Non-equilibrium fractional quantum hall state of light. *New Journal of Physics*, 15(6):063001, 2013.
- [37] S Haroche, M Brune, and JM Raimond. From cavity to circuit quantum electrodynamics. *Nature Physics*, 16(3):243–246, 2020.

- [38] Edward Mills Purcell. Spontaneous emission probabilities at radio frequencies. In *Confined Electrons and Photons*, pages 839–839. Springer, 1995.
- [39] Ph Goy, JM Raimond, M Gross, and S Haroche. Observation of cavity-enhanced single-atom spontaneous emission. *Physical review letters*, 50(24):1903, 1983.
- [40] Vahid Sandoghdar, CI Sukenik, EA Hinds, and Serge Haroche. Direct measurement of the van der waals interaction between an atom and its images in a micron-sized cavity. *Physical review letters*, 68(23):3432, 1992.
- [41] M Brune, P Nussenzveig, F Schmidt-Kaler, F Bernardot, Abdelhamid Maali, JM Raimond, and S Haroche. From lamb shift to light shifts: Vacuum and subphoton cavity fields measured by atomic phase sensitive detection. *Physical review letters*, 72(21):3339, 1994.
- [42] Y Kaluzny, P Goy, M Gross, JM Raimond, and S Haroche. Observation of self-induced rabi oscillations in two-level atoms excited inside a resonant cavity: The ringing regime of superradiance. *Physical review letters*, 51(13):1175, 1983.
- [43] D Meschede, Herbert Walther, and G Müller. One-atom maser. *Physical review letters*, 54(6):551, 1985.
- [44] M. Brune, F. Schmidt-Kaler, A. Maali, J. Dreyer, E. Hagley, J. M. Raimond, and S. Haroche. Quantum Rabi Oscillation: A Direct Test of Field Quantization in a Cavity. *Physical Review Letters*, 76(11):1800–1803, March 1996.
- [45] G. Rempe, F. Schmidt-Kaler, and H. Walther. Observation of sub-Poissonian photon statistics in a micromaser. *Physical Review Letters*, 64(23):2783–2786, June 1990.
- [46] J M Raimond, M Brune, S Haroche, and Laboratoire Kastler Brossel. Colloquium: Manipulating quantum entanglement with atoms and photons in a cavity. *Rev. Mod. Phys.*, 73(3):18, 2001.

- [47] Frank Arute, Kunal Arya, Ryan Babbush, Dave Bacon, Joseph C Bardin, Rami Barends, Rupak Biswas, Sergio Boixo, Fernando GSL Brandao, David A Buell, et al. Quantum supremacy using a programmable superconducting processor. *Nature*, 574(7779):505–510, 2019.
- [48] Rami Barends, Julian Kelly, Anthony Megrant, Andrzej Veitia, Daniel Sank, Evan Jeffrey, Ted C White, Josh Mutus, Austin G Fowler, Brooks Campbell, et al. Superconducting quantum circuits at the surface code threshold for fault tolerance. *Nature*, 508(7497):500–503, 2014.
- [49] Christian Kraglund Andersen, Ants Remm, Stefania Lazar, Sebastian Krinner, Nathan Lacroix, Graham J Norris, Mihai Gabureac, Christopher Eichler, and Andreas Wallraff. Repeated quantum error detection in a surface code. *Nature Physics*, 16(8):875–880, 2020.
- [50] JM Pino, JM Dreiling, C Figgatt, JP Gaebler, SA Moses, MS Allman, CH Baldwin, M Foss-Feig, D Hayes, K Mayer, et al. Demonstration of the trapped-ion quantum ccd computer architecture. *Nature*, 592(7853):209–213, 2021.
- [51] Hannes Bernien, Sylvain Schwartz, Alexander Keesling, Harry Levine, Ahmed Omran, Hannes Pichler, Soonwon Choi, Alexander S Zibrov, Manuel Endres, Markus Greiner, et al. Probing many-body dynamics on a 51-atom quantum simulator. *Nature*, 551(7682):579–584, 2017.
- [52] H-J Briegel, Tommaso Calarco, Dieter Jaksch, Juan Ignacio Cirac, and Peter Zoller. Quantum computing with neutral atoms. *Journal of modern optics*, 47(2-3):415–451, 2000.
- [53] JM Arrazola, V Bergholm, K Brádler, TR Bromley, MJ Collins, I Dhand, A Fumagalli, T Gerrits, A Goussev, LG Helt, et al. Quantum circuits with many photons on a programmable nanophotonic chip. *Nature*, 591(7848):54–60, 2021.

- [54] Han-Sen Zhong, Hui Wang, Yu-Hao Deng, Ming-Cheng Chen, Li-Chao Peng, Yi-Han Luo, Jian Qin, Dian Wu, Xing Ding, Yi Hu, et al. Quantum computational advantage using photons. *Science*, 370(6523):1460–1463, 2020.
- [55] Amir H Safavi-Naeini, Dries Van Thourhout, Roel Baets, and Raphaël Van Laer. Controlling phonons and photons at the wavelength scale: integrated photonics meets integrated phononics. *Optica*, 6(2):213–232, 2019.
- [56] Paul Magnard, Simon Storz, Philipp Kurpiers, Josua Schär, Fabian Marxer, Janis Lütolf, T Walter, J-C Besse, M Gabureac, K Reuer, et al. Microwave quantum link between superconducting circuits housed in spatially separated cryogenic systems. *Physical Review Letters*, 125(26):260502, 2020.
- [57] JD Pritchard, JA Isaacs, MA Beck, R McDermott, and M Saffman. Hybrid atom-photon quantum gate in a superconducting microwave resonator. *Physical Review A*, 89(1):010301, 2014.
- [58] Moritz Forsch, Robert Stockill, Andreas Wallucks, Igor Marinković, Claus Gärtner, Richard A Norte, Frank van Otten, Andrea Fiore, Kartik Srinivasan, and Simon Gröblacher. Microwave-to-optics conversion using a mechanical oscillator in its quantum ground state. *Nature Physics*, 16(1):69–74, 2020.
- [59] Mohammad Mirhosseini, Alp Sipahigil, Mahmoud Kalaei, and Oskar Painter. Quantum transduction of optical photons from a superconducting qubit. *arXiv preprint arXiv:2004.04838*, 2020.
- [60] Reed W Andrews, Robert W Peterson, Tom P Purdy, Katarina Cicak, Raymond W Simmonds, Cindy A Regal, and Konrad W Lehnert. Bidirectional and efficient conversion between microwave and optical light. *Nature Physics*, 10(4):321–326, 2014.
- [61] David Petrosyan, Klaus Mølmer, József Fortágh, and Mark Saffman. Microwave to

- optical conversion with atoms on a superconducting chip. *New Journal of Physics*, 21(7):073033, 2019.
- [62] Timothy P McKenna, Jeremy D Witmer, Rishi N Patel, Wentao Jiang, Raphaël Van Laer, Patricio Arrangoiz-Arriola, E Alex Wollack, Jason F Herrmann, and Amir H Safavi-Naeini. Cryogenic microwave-to-optical conversion using a triply resonant lithium-niobate-on-sapphire transducer. *Optica*, 7(12):1737–1745, 2020.
- [63] Joerg Bochmann, Amit Vainsencher, David D Awschalom, and Andrew N Cleland. Nanomechanical coupling between microwave and optical photons. *Nature Physics*, 9(11):712–716, 2013.
- [64] Nicholas J Lambert, Alfredo Rueda, Florian Sedlmeir, and Harald GL Schwefel. Coherent conversion between microwave and optical photons—an overview of physical implementations. *Advanced Quantum Technologies*, 3(1):1900077, 2020.
- [65] Edwin T Jaynes and Frederick W Cummings. Comparison of quantum and semiclassical radiation theories with application to the beam maser. *Proceedings of the IEEE*, 51(1):89–109, 1963.
- [66] Andrew D Greentree, Jens Koch, and Jonas Larson. Fifty years of jaynes–cummings physics. *Journal of Physics B: Atomic, Molecular and Optical Physics*, 46(22):220201, 2013.
- [67] Hubert Stokowski, Marek Pechal, Emma Snively, KS Kevin Multani, Paul B Welande, Jeremy Witmer, Emilio A Nanni, and Amir H Safavi-Naeini. Towards millimeter-wave based quantum networks. In *2019 44th International Conference on Infrared, Millimeter, and Terahertz Waves (IRMMW-THz)*, pages 1–2. IEEE, 2019.
- [68] Marek Pechal and Amir H. Safavi-Naeini. Millimeter-wave interconnects for microwave-frequency quantum machines. *Physical Review A*, 96(4):042305, October 2017. arXiv: 1706.05368.

- [69] Ian D Leroux, Monika H Schleier-Smith, and Vladan Vuletić. Implementation of cavity squeezing of a collective atomic spin. *Physical Review Letters*, 104(7):073602, 2010.
- [70] Zilong Chen, Justin G Bohnet, Joshua M Weiner, Kevin C Cox, and James K Thompson. Cavity-aided nondemolition measurements for atom counting and spin squeezing. *Physical Review A*, 89(4):043837, 2014.
- [71] Zilong Chen, Justin G Bohnet, Shannon R Sankar, Jiayan Dai, and James K Thompson. Conditional spin squeezing of a large ensemble via the vacuum rabi splitting. *Physical review letters*, 106(13):133601, 2011.
- [72] JA Souza, L Cabral, RR Oliveira, and CJ Villas-Boas. Eit-related phenomena and their mechanical analogs.
- [73] Joshua Harden, Amitabh Joshi, and Juan D Serna. Demonstration of double eit using coupled harmonic oscillators and rlc circuits. *European journal of physics*, 32(2):541, 2011.
- [74] Stefan Weis, Rémi Rivière, Samuel Deléglise, Emanuel Gavartin, Olivier Arcizet, Albert Schliesser, and Tobias J Kippenberg. Optomechanically induced transparency. *Science*, 330(6010):1520–1523, 2010.
- [75] Otto Redlich. Intensive and extensive properties. *Journal of Chemical Education*, 47(2):154, 1970.
- [76] Howard Georgi. *The physics of waves*. Prentice Hall Englewood Cliffs, NJ, 1993.
- [77] CL Garrido Alzar, MAG Martinez, and P Nussenzevig. Classical analog of electromagnetically induced transparency. *American Journal of Physics*, 70(1):37–41, 2002.
- [78] <https://lpsa.swarthmore.edu/Analog/ElectricalMechanicalAnalog.html>.
- [79] David M Pozar. *Microwave engineering*. John wiley & sons, 2011.

- [80] George Barbastathis. Fabry-perot interferometers. <http://web.mit.edu/2.710/Fall06/2.710-wk8-a-ho.pdf>, 2005.
- [81] Nicolas Joly. Laser course 2011, chapter 3. <http://www.mpl.mpg.de/personal/njoly/pdf/Laser/chap3.pdf>, 2005.
- [82] Markus Aspelmeyer, Tobias J Kippenberg, and Florian Marquardt. Cavity optomechanics. *Reviews of Modern Physics*, 86(4):1391, 2014.
- [83] Stephan Welte, Bastian Hacker, Severin Daiss, Stephan Ritter, and Gerhard Rempe. Photon-mediated quantum gate between two neutral atoms in an optical cavity. *Physical Review X*, 8(1):011018, 2018.
- [84] Matthew Reagor, Wolfgang Pfaff, Christopher Axline, Reinier W Heeres, Nissim Ofek, Katrina Sliwa, Eric Holland, Chen Wang, Jacob Blumoff, Kevin Chou, et al. Quantum memory with millisecond coherence in circuit qed. *Physical Review B*, 94(1):014506, 2016.
- [85] Mark Stone, Aziza Suleymanzade, Lavanya Taneja, David I Schuster, and Jonathan Simon. Optical mode conversion in coupled fabry–perot resonators. *Optics Letters*, 46(1):21–24, 2021.
- [86] R. W. Andrews, R. W. Peterson, T. P. Purdy, K. Cicak, R. W. Simmonds, C. A. Regal, and K. W. Lehnert. Bidirectional and efficient conversion between microwave and optical light. *Nature Physics*, 10(4):321–326, April 2014.
- [87] Michael Tavis and Frederick W Cummings. Exact solution for an n-molecule—radiation-field hamiltonian. *Physical Review*, 170(2):379, 1968.
- [88] Jonathan Simon. *Cavity QED with atomic ensembles*. Harvard University, 2010.
- [89] Gershon Kurizki, Patrice Bertet, Yuimaru Kubo, Klaus Mølmer, David Petrosyan,

- Peter Rabl, and Jörg Schmiedmayer. Quantum technologies with hybrid systems. *Proceedings of the National Academy of Sciences*, 112(13):3866–3873, 2015.
- [90] AA Clerk, KW Lehnert, P Bertet, JR Petta, and Y Nakamura. Hybrid quantum systems with circuit quantum electrodynamics. *Nature Physics*, 16(3):257–267, 2020.
- [91] Drew B Branden, Tamas Juhasz, Tatenda Mahlokozera, Cristian Vesa, Roy O Wilson, Mao Zheng, Andrew Kortyna, and Duncan A Tate. Radiative lifetime measurements of rubidium rydberg states. *Journal of Physics B: atomic, molecular and optical physics*, 43(1):015002, 2009.
- [92] Anton Frisk Kockum, Adam Miranowicz, Simone De Liberato, Salvatore Savasta, and Franco Nori. Ultrastrong coupling between light and matter. *Nature Reviews Physics*, 1(1):19–40, 2019.
- [93] Marlan O Scully, M Suhail Zubairy, et al. Quantum optics cambridge university press. *Cambridge, CB2 2RU, UK*, 1997.
- [94] A Ruschhaupt, F Delgado, and JG Muga. Physical realization of-symmetric potential scattering in a planar slab waveguide. *Journal of Physics A: Mathematical and General*, 38(9):L171, 2005.
- [95] Ali Mostafazadeh. Pseudo-hermiticity versus pt symmetry: the necessary condition for the reality of the spectrum of a non-hermitian hamiltonian. *Journal of Mathematical Physics*, 43(1):205–214, 2002.
- [96] Markus Müller and Ingrid Rotter. Exceptional points in open quantum systems. *Journal of Physics A: Mathematical and Theoretical*, 41(24):244018, 2008.
- [97] Hichem Eleuch and Ingrid Rotter. Exceptional points in open and pt symmetric systems. *arXiv preprint arXiv:1311.6320*, 2013.

- [98] Fabio Bagarello, Francesco Gargano, Margherita Lattuca, Roberto Passante, Lucia Rizzuto, and Salvatore Spagnolo. Exceptional points in a non-hermitian extension of the jaynes-cummings hamiltonian. In *Non-Hermitian Hamiltonians in Quantum Physics*, pages 83–95. Springer, 2016.
- [99] Thomas Frith. Exotic entanglement for non-hermitian jaynes-cummings hamiltonians. *Journal of Physics A: Mathematical and Theoretical*, 53(48):485303, 2020.
- [100] KB Whaley and JC Light. Rotating-frame transformations: A new approximation for multiphoton absorption and dissociation in laser fields. *Physical Review A*, 29(3):1188, 1984.
- [101] MH Devoret, Steven Girvin, and Robert Schoelkopf. Circuit-qed: How strong can the coupling between a josephson junction atom and a transmission line resonator be? *Annalen der Physik*, 16(10-11):767–779, 2007.
- [102] Serge Haroche and J-M Raimond. *Exploring the quantum: atoms, cavities, and photons*. Oxford university press, 2006.
- [103] Robert H Dicke. Coherence in spontaneous radiation processes. *Physical review*, 93(1):99, 1954.
- [104] Aziza Suleymanzade. G2 hybrid cavity-qed calculations. <https://github.com/AzizaSuleyman/HybridCavityQED.git>, 2021.
- [105] Claude Cohen-Tannoudji, Jacques Dupont-Roc, and Gilbert Grynberg. *Atom-photon interactions: basic processes and applications*. 1998.
- [106] Alexandros Georgakopoulos, Ariel Sommer, and Jonathan Simon. Theory of interacting cavity rydberg polaritons. *Quantum Science and Technology*, 4(1):014005, 2018.
- [107] P.U. Jepsen, D.G. Cooke, and M. Koch. Terahertz spectroscopy and imaging - Modern techniques and applications. *Laser & Photonics Reviews*, 5(1):124–166, January 2011.

- [108] F Sizov. Terahertz radiation detectors: the state-of-the-art. *Semiconductor Science and Technology*, 33(12):123001, December 2018.
- [109] Jane S Greaves, Anita MS Richards, William Bains, Paul B Rimmer, Hideo Sagawa, David L Clements, Sara Seager, Janusz J Petkowski, Clara Sousa-Silva, Sukrit Ranjan, et al. Phosphine gas in the cloud decks of venus. *Nature Astronomy*, pages 1–10, 2020.
- [110] Jane S Greaves, Anita Richards, William Bains, Paul B Rimmer, David L Clements, Sara Seager, Janusz J Petkowski, Clara Sousa-Silva, Sukrit Ranjan, and Helen J Fraser. Re-analysis of phosphine in venus’ clouds. *arXiv preprint arXiv:2011.08176*, 2020.
- [111] J. E. Carlstrom, P. A. R. Ade, K. A. Aird, B. A. Benson, L. E. Bleem, S. Busetti, C. L. Chang, E. Chauvin, H.-M. Cho, T. M. Crawford, A. T. Crites, M. A. Dobbs, N. W. Halverson, S. Heimsath, W. L. Holzapfel, J. D. Hrubes, M. Joy, R. Keisler, T. M. Lanting, A. T. Lee, E. M. Leitch, J. Leong, W. Lu, M. Lueker, D. Luong-Van, J. J. McMahon, J. Mehl, S. S. Meyer, J. J. Mohr, T. E. Montroy, S. Padin, T. Plagge, C. Pryke, J. E. Ruhl, K. K. Schaffer, D. Schwan, E. Shirokoff, H. G. Spieler, Z. Staniszewski, A. A. Stark, C. Tucker, K. Vanderlinde, J. D. Vieira, and R. Williamson. The 10 Meter South Pole Telescope. *Publications of the Astronomical Society of the Pacific*, 123(903):568–581, May 2011.
- [112] J. D. Vieira, T. M. Crawford, E. R. Switzer, P. A. R. Ade, K. A. Aird, M. L. N. Ashby, B. A. Benson, L. E. Bleem, M. Brodwin, J. E. Carlstrom, C. L. Chang, H.-M. Cho, A. T. Crites, T. de Haan, M. A. Dobbs, W. Everett, E. M. George, M. Glad-  
ders, N. R. Hall, N. W. Halverson, F. W. High, G. P. Holder, W. L. Holzapfel, J. D. Hrubes, M. Joy, R. Keisler, L. Knox, A. T. Lee, E. M. Leitch, M. Lueker, D. P. Mar-  
rone, V. McIntyre, J. J. McMahon, J. Mehl, S. S. Meyer, J. J. Mohr, T. E. Montroy, S. Padin, T. Plagge, C. Pryke, C. L. Reichardt, J. E. Ruhl, K. K. Schaffer, L. Shaw, E. Shirokoff, H. G. Spieler, B. Stalder, Z. Staniszewski, A. A. Stark, K. Vanderlinde, W. Walsh, R. Williamson, Y. Yang, O. Zahn, and A. Zenteno. EXTRAGALAC-

TIC MILLIMETER-WAVE SOURCES IN SOUTH POLE TELESCOPE SURVEY DATA: SOURCE COUNTS, CATALOG, AND STATISTICS FOR AN 87 SQUARE-DEGREE FIELD. *The Astrophysical Journal*, 719(1):763–783, August 2010.

- [113] T. S. Rappaport, S. Sun, R. Mayzus, H. Zhao, Y. Azar, K. Wang, G. N. Wong, J. K. Schulz, M. Samimi, and F. Gutierrez. Millimeter Wave Mobile Communications for 5g Cellular: It Will Work! *IEEE Access*, 1:335–349, 2013.
- [114] W. Roh, J. Seol, J. Park, B. Lee, J. Lee, Y. Kim, J. Cho, K. Cheun, and F. Aryanfar. Millimeter-wave beamforming as an enabling technology for 5g cellular communications: theoretical feasibility and prototype results. *IEEE Communications Magazine*, 52(2):106–113, February 2014.
- [115] Wenhui Li, I Mourachko, MW Noel, and TF Gallagher. Millimeter-wave spectroscopy of cold rb rydberg atoms in a magneto-optical trap: Quantum defects of the ns, np, and nd series. *Physical Review A*, 67(5):052502, 2003.
- [116] Yan Zhou, David D Grimes, Timothy J Barnum, David Patterson, Stephen L Coy, Ethan Klein, John S Muentner, and Robert W Field. Direct detection of rydberg–rydberg millimeter-wave transitions in a buffer gas cooled molecular beam. *Chemical Physics Letters*, 640:124–136, 2015.
- [117] Denis D Sukachev, Alp Sipahigil, Christian T Nguyen, Mihir K Bhaskar, Ruffin E Evans, Fedor Jelezko, and Mikhail D Lukin. Silicon-vacancy spin qubit in diamond: a quantum memory exceeding 10 ms with single-shot state readout. *Physical review letters*, 119(22):223602, 2017.
- [118] Teresa Brecht, Matthew Reagor, Yiwen Chu, Wolfgang Pfaff, Chen Wang, Luigi Frunzio, Michel H Devoret, and Robert J Schoelkopf. Demonstration of superconducting micromachined cavities. *Applied Physics Letters*, 107(19):192603, 2015.

- [119] Aziza Suleymanzade, Alexander Anferov, Mark Stone, Ravi K Naik, Andrew Oriani, Jonathan Simon, and David Schuster. A tunable high-q millimeter wave cavity for hybrid circuit and cavity qed experiments. *Applied Physics Letters*, 116(10):104001, 2020.
- [120] Chenglong Xie, Chun-Ping Chen, and Tetsuo Anada. 2d microwave metallic photonic crystal point-defect-cavity resonator. *Microwave and optical technology letters*, 59(10):2547–2551, 2017.
- [121] Arthur R McGurn and Alexei A Maradudin. Photonic band structures of two- and three-dimensional periodic metal or semiconductor arrays. *Physical Review B*, 48(23):17576, 1993.
- [122] DR Smith, S Schultz, N Kroll, M Sigalas, KM Ho, and CM Soukoulis. Experimental and theoretical results for a two-dimensional metal photonic band-gap cavity. *Applied Physics Letters*, 65(5):645–647, 1994.
- [123] He-Liang Huang, Dachao Wu, Daojin Fan, and Xiaobo Zhu. Superconducting quantum computing: a review. *Science China Information Sciences*, 63(8):1–32, 2020.
- [124] Yachin Ivry, Chung-Soo Kim, Andrew E Dane, Domenico De Fazio, Adam N McCaughan, Kristen A Sunter, Qingyuan Zhao, and Karl K Berggren. Universal scaling of the critical temperature for thin films near the superconducting-to-insulating transition. *Physical Review B*, 90(21):214515, 2014.
- [125] Mark J Sowa, Yonas Yemane, Jinsong Zhang, Johanna C Palmstrom, Ling Ju, Nicholas C Strandwitz, Fritz B Prinz, and J Provine. Plasma-enhanced atomic layer deposition of superconducting niobium nitride. *Journal of Vacuum Science & Technology A: Vacuum, Surfaces, and Films*, 35(1):01B143, 2017.
- [126] Stefan Kuhr, Sébastien Gleyzes, Christine Guerlin, Julien Bernu, Ulrich Busk Hoff, Samuel Deléglise, Stefano Osnaghi, Michel Brune, Jean-Michel Raimond, Serge

Haroche, E. Jacques, P. Bosland, and B. Visentin. Ultrahigh finesse Fabry-Perot superconducting resonator. *Applied Physics Letters*, 90(16):164101, April 2007. arXiv: quant-ph/0612138.

[127] <https://www.newport.com/medias/sysmaster/images/images/hf3/h8e/8797226106910/Optical-Table-Pre-installation-Checklist.pdf>.

[128] C Wang. Extracting cooling from the pulse tube and regenerator in a 4 k pulse tube cryocooler. *Cryocoolers*, 15:177–184, 2009.

[129] N Almtireen, JJ Brandner, and JG Korvink. Pulse tube cryocooler: Phasor analysis and one-dimensional numerical simulation. *Journal of Low Temperature Physics*, pages 1–19, 2020.

[130] <http://large.stanford.edu/courses/2007/ph210/bert2/>.

[131] Christopher J Foot et al. *Atomic physics*, volume 7. Oxford University Press, 2005.

[132] James P McGilligan, Paul F Griffin, Erling Riis, and Aidan S Arnold. Phase-space properties of magneto-optical traps utilising micro-fabricated gratings. *Optics express*, 23(7):8948–8959, 2015.

[133] James P McGilligan, Paul F Griffin, Rachel Elvin, Stuart J Ingleby, Erling Riis, and Aidan S Arnold. Grating chips for quantum technologies. *Scientific reports*, 7(1):1–7, 2017.

[134] Matthieu Vangeleyn, Paul F Griffin, Erling Riis, and Aidan S Arnold. Single-laser, one beam, tetrahedral magneto-optical trap. *Optics express*, 17(16):13601–13608, 2009.

[135] CC Nshii, Matthieu Vangeleyn, Joseph P Cotter, Paul F Griffin, EA Hinds, Charles N Ironside, Patrick See, AG Sinclair, Erling Riis, and Aidan S Arnold. A surface-patterned chip as a strong source of ultracold atoms for quantum technologies. *Nature nanotechnology*, 8(5):321–324, 2013.

- [136] Sara Rosi, Alessia Burchianti, Stefano Conclave, Devang S Naik, Giacomo Roati, Chiara Fort, and Francesco Minardi.  $\lambda$ -enhanced grey molasses on the d 2 transition of rubidium-87 atoms. *Scientific reports*, 8(1):1–9, 2018.
- [137] Daniel A Steck. Quantum and atomic optics. <https://atomoptics.uoregon.edu/dsteck/teaching/quantum-optics.pdf>, 2007.
- [138] Scott Parkins and Takao Aoki. Microtoroidal cavity qed with fiber overcoupling and strong atom-field coupling: A single-atom quantum switch for coherent light fields. *Physical Review A*, 90(5):053822, 2014.
- [139] Cristiano Ciuti and Iacopo Carusotto. Input-output theory of cavities in the ultrastrong coupling regime: The case of time-independent cavity parameters. *Physical Review A*, 74(3):033811, 2006.
- [140] Aziza Suleymanzade. Mm-wave vector network analyzer. <https://github.com/AzizaSuleyman/mmwave-vna-gui.git>, 2021.